Keele University

The aggregation and reduction of iron minerals by the Alzheimer's disease peptide ß-amyloid (1-42): an X-ray absorption study

James Everett

PhD Thesis in Biomedical Engineering

March 2015

School of Postgraduate Medicine

Institute for Science and Technology in Medicine

Abstract

Iron is vital for healthy brain function. However when present in a redox-active form or in excess concentrations it can be toxic. Interestingly, increased levels of *redox-active* iron biominerals have been shown to exist in Alzheimer's disease (AD) tissues, including lesions comprised of the AD peptide β-amyloid (Aβ). These iron phases are capable of producing reactive oxygen species, resulting in the generation of oxidative stress manifesting as neuronal injury. As oxidative stress and the accumulation of iron are recognised as early stage events in AD, the presence of redox-active iron may prove fundamental in the development of AD pathology. The origin of these redox-active iron biominerals is unclear but recent studies suggest their formation may involve the interaction of Aβ with unbound brain iron and/or the malfunction of the iron storage protein ferritin.

Despite these observations, the relationship between Aβ and iron is poorly understood, and the products of Aβ/iron interaction remain unknown. In this thesis, synchrotron-based x-ray techniques are combined with traditional biological approaches to examine the interactions between Aβ and various synthetic and naturally occurring iron forms. Through this methodology Aβ is shown to incorporate ferric iron phases into its fibrillar structure *in vitro,* with this interaction resulting in the chemical reduction of iron into a redox-active state. Further to this, Aβ is demonstrated to disrupt ferritin structure resulting in the chemical reduction of its redox-inactive iron core *in vitro*. Additionally the interaction of Aβ with crystalline iron phases is shown destroy iron crystal structure.

Finally, redox-active iron is shown to be associated with regions of AD pathology, including fibrillar Aβ-like structures, within a transgenic mouse model of AD *in situ.* These findings suggest an origin for the redox-active iron forms and oxidative stress previously witnessed in AD tissue, thereby shedding light on the process of AD pathogenesis.

Table of Contents

List of Figures

Chapter 1. Introduction: Iron biominerals in Alzheimer's disease

Chapter 2. Material and methods

Chapter 3. Ferrous iron formation following the co-aggregation of ferric iron and the Alzheimer's disease peptide Aβ (1-42)

Chapter 4. Evidence of redox-active iron formation following aggregation of ferrihydrite and the Alzheimer's disease peptide β-amyloid

Chapter 5. Interactions between the Alzheimer's disease peptide β-amyloid and the iron storage protein ferritin

Chapter 6. Disruption of magnetite crystal structure by the Alzheimer's disease peptide β-amyloid (1-42)

Chapter 7. Associated investigation: Observation of iron bearing fibrillar aggregates and redox-active biominerals in Alzheimer's disease transgenic mouse cortex

List of Tables

Chapter 5. Interactions between the Alzheimer's disease peptide β-amyloid and the iron storage protein ferritin

Acknowledgments

Firstly, I would like to thank my supervisor Dr Neil Telling who has been a constant source of support and advice throughout this project. I will be forever thankful to Neil for providing me with the opportunity to experience exciting new techniques at the forefront of modern science, and the chance to travel to multiple research institutes at home and abroad. I feel privileged to have worked so closely with Neil over the last three and a half years. The advice and lessons I have learnt from him will undoubtedly stand me in good stead for my future career, whatever direction that may take. At this point I also wish to thank Diamond Light Source for providing my doctoral training position, and the EPSRC for funding this project.

I would like to thank my co-supervisor Prof Gerrit van der Laan of Diamond Light Source, whose expertise in synchrotron techniques has proved invaluable to this research effort. I also wish to thank my co-supervisors Dr Joanna Collingwood and Prof Jon Dobson, and also Prof Chris Exley for their input into this project, and their insights into the ever changing field of dementia research. I thank Karen Walker for her teaching and support at the electron microscopy unit, and Eva Céspedes for her tireless efforts during synchrotron beamtimes.

To the guys at the ISTM thank you for your friendship. I would also like to acknowledge my childhood friends Rich, James and Dale, who have provided a constant source of amusement throughout the last 15 years. To my parents who have respected and backed my choices in life, providing unwavering support, I am eternally grateful. And to Natalie thank you. Your companionship has made my time at Keele so enjoyable.

Finally, thanks to Eoin and Rory, for getting me through the writing of this thesis

Author Contributions

James Everett – Author, sample preparation, data collection, data analysis.

Neil Telling – Data collection (XAS, XMCD, STXM, TEM (Chapter 7)), sample preparation (Chapter 7), data analysis (Chapter 7).

Eva Céspedes – Data collection (XAS, XMCD, STXM).

Leigh Shelford – Data collection (XAS, XMCD).

Clare Hoskins – Data collection (AFM).

Associated Publications

Chapter 3: J. Everett, E. Céspedes, L. R. Shelford, C. Exley, J. F. Collingwood, J. Dobson, G. van der Laan, C. A. Jenkins, E. Arenholz and N. D. Telling. "Ferrous iron formation following the co-aggregation of ferric iron and the Alzheimer's disease peptide Aβ (1-42)". *Journal of the Royal Society Interface*. **11**, 20140165 (2014).

Chapter 4: J. Everett, E. Céspedes, L. R. Shelford, C. Exley, J. F. Collingwood, J. Dobson, G. van der Laan, C. A. Jenkins, E. Arenholz and N. D. Telling. "Redox-Active Iron Formation Following Aggregation of Ferrihydrite and the Alzheimer's Disease Peptide β‑Amyloid". *Inorganic Chemistry*. **53**, 2803−2809 (2014)

Chapter 5: J. Everett, J. F. Collingwood, C. Exley, J. Dobson, G. van der Laan, and N. D. Telling. "Interactions between the Alzheimer's disease peptide β-amyloid and the iron storage protein ferritin". Manuscript in preparation for submission to *Journal of Biological Chemistry* (anticipated date of submission Nov 2014).

Chapter 7: N. D. Telling, J. Everett, J. Collingwood , J. Dobson, G. van der Laan, J. Gallagher, J. Wang and A. Hitchcock. "Nanoscale correlation of iron with amyloid plaque morphology in Alzheimer's disease transgenic mouse cortex". Manuscript in preparation for submission to *Proceedings of the National Academy of Sciences of the United States of America* (anticipated date of submission Oct 2014).

Abbreviations

AC	Alternating current
AD	Alzheimer's disease
AFM	Atomic force microscopy
APP	Amyloid precursor protein
ATP	Adenosine triphosphate
Aβ	β-amyloid
DNA	Deoxyribonucleic acid
EELS	Electron energy loss spectroscopy
ERK	Extracellular signal-regulated kinase
FAD	Familial Alzheimer's disease
Glt	Glucose transporter
HFE	Haemochromatosis
H-ferritin	Heavy-chain ferritin
HNE	4-hydorxynoneal
IRE	Iron responsive element
IRP	Iron regulatory protein
KH	Krebs Henseleit
LCP	Left circularly polarized photons
L-ferritin	Light-chain ferritin
LTP	Long-term potentiation
mRNA	Messenger RNA
MRI	Magnetic resonance imaging
NFT	Neurofibrillary tangle
NMDA	*N*-Methyl-D-aspartic acid
NMR	Nuclear magnetic resonance

OD	Optical density
PSEN	Presinilin
PSP	Progressive supranuclear palsy
RCP	Right circularly polarized photons
Redox	Reduction-oxidation
ROI	Regions of interest
ROS	Reactive oxygen species
RNA	Ribonucleic acid
SP	Senile plaque
STXM	Scanning transmission x-ray microscopy
SQUID	Superconducting quantum interference device
TEM	Transmission electron microscopy
TEY	Total electron yield
XAS	X-ray absorption spectroscopy
XMCD	X-ray magnetic circular dichroism
8-OHG	8-hydroxyguanosine

Chapter 1

Introduction: Iron biominerals in Alzheimer's disease

1.1 Introduction to Alzheimer's disease

Alzheimer's disease (AD) is a fatal progressive neurodegenerative disorder that is the most common cause of dementias amongst the elderly population (60-80% of cases) [1]. Disease onset is directly correlated to age, with 45% of those over 85 years being diagnosed with AD compared to ca. 5% of those aged 65-74 [2]. AD incidence is approximately 95% sporadic (a.k.a late-onset AD) and 5% familial (inherited predisposition to the disease) [1]. For those who develop familial AD (FAD), disease onset is typically under the age of 65, an age criteria commonly referred to as early-onset AD [1,3]. FAD is inherited in an autosomal dominant manner, arising through mutations in the genes encoding the amyloid precursor protein (APP), Presinilin 1 (PSEN1) and PSEN2 [4,5]. However the majority of AD cases (sporadic AD) are attributed to genetic factors such as possession of the E4 allele of apolipoprotein E [4,6,7], single nucleotide polymorphisms (as identified through genome-wide association studies) [7,8], and also epigenetic factors (long-term DNA methylation, histone modification) suggesting genetic and environmental factors to influence the occurrence of AD [9]. Due to an ever aging population, cases of AD are projected to significantly increase over the next 50 years, thereby placing an increasing burden upon world health organisations [1,3].

AD is characterized by extensive widespread neuronal loss in the higher brain centres responsible for memory and learning, resulting in memory loss, cognitive decline and psychosis [10-12]. This pattern of neurodegeneration is both spatially and temporally complex, and therefore disease pathogenesis is poorly understood and no cure currently exists [10,12]. However, it is becoming accepted that the accumulation (and in FAD cases, the overproduction) of the peptide β-amyloid (Aβ) within brain tissues may be fundamental to the disease process [13-17]. Aβ is formed through the sequential cleavage of the

transmembrane amyloid precursor protein by proteolytic secretase enzymes [14-16,18,19]. The peptide goes on to form dysfunctional insoluble protein aggregates with a β-pleated structure (a protein confirmation comprised of multiple polypeptide chains connected laterally by 2 or more hydrogen bonds). These aggregates are deposited extracellularly, manifesting as senile plaques (SPs), a hallmark lesion of AD (Figure 1.1) [14,18,20].

Aβ has also been shown to induce the formation of intracellular neurofibrillary tangles (NFTs) comprised of hyperphosphorylated tau filaments [21], resulting in diminished energy production, activation of the immune system and disturbances to normal neuronal function that ultimately result in cell death [22]. Additionally Aβ has been shown to be directly neurotoxic through its ability to induce oxidative stress, promote excitotoxicity, disrupt synaptic networks, and cause significant increases in intracellular calcium(II) (Ca^{2+}) concentrations [16,23-25].

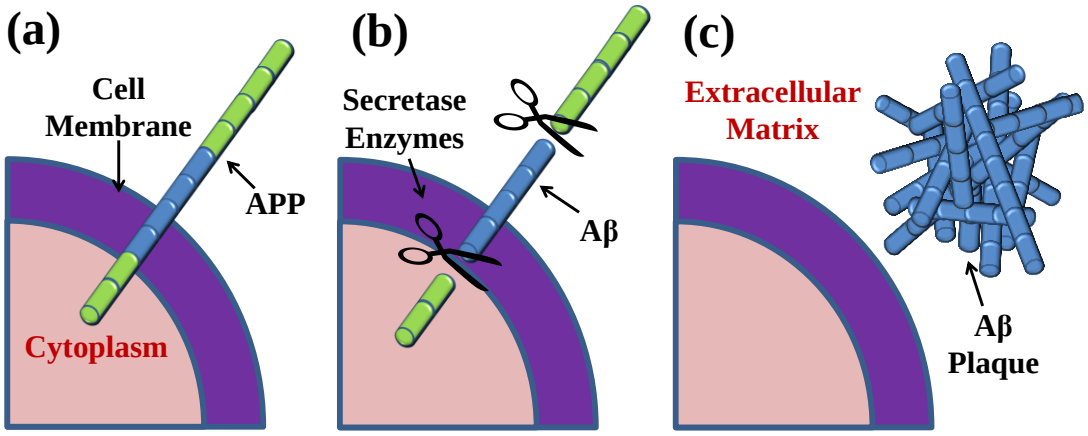

Figure 1.1. The amyloid cascade hypothesis. **(a)** Amyloid precursor protein (green/blue), a transmembrane protein is **(b)** proteolytically cleaved by secretase enzymes to form the β-amyloid (Aβ) peptide fragment (blue). **(c)** Aβ fragments assemble into insoluble extracellular plaque structures, recognised as senile plaques, a hallmark lesion of Alzheimer's disease.

A number of Aβ isoforms are produced varying from 39-43 amino acid residues in length, with the 40 and 42 base forms being the dominant species [25-28]. The base length of Aβ affects the ability of the peptide to form fibrillar structures, a trait that is thought to influence the toxicity of Aβ [16,25,29]. The 42 base isoform of Aβ (Aβ(1-42); Figure 1.2) is the most fibrillogenic, and is therefore commonly associated with AD traits, such as SPs [29]. Typical Aβ fibrils are comprised of a cross-β structure, characterized by elongated unbranched protein chains, with a substructure composed of β-sheets and protofilament strands perpendicular to the long fibril axis [30]. However, the result of Aβ conformational state upon its neurotoxic properties is hotly debated. Both soluble Aβ oligomers and insoluble Aβ fibrils have been shown to induce neuronal dysfunction, suggesting that multiple amyloid confirmations may act in equilibrium to induce the progressive neurodegeneration characteristic of AD [15,25,31-33]. Although typically associated with disruptions to neuronal function, Aβ accumulation is also seen to alter the structure and function of astrocytes, microglia and the endothelial and muscle cells of cerebral blood vessels [16]. (For a review of Aβ neurotoxicity see Mucke and Selkoe (2012) [16]).

Figure 1.2. The 42 base amino acid sequence of β-amyloid(1-42)

Interestingly, evidence of iron accumulation has been observed in areas of AD pathology, including NFTs, and Aβ containing SPs [12,31,34-45]. These observations have led to the theory that Aβ may act as a "sink" for iron accumulation within the AD brain. Although vital for

healthy brain function [46,47], when stored incorrectly or present in excessive concentrations, iron can be toxic [12,43,48]. This toxicity arises through iron's valence chemistry, enabling it to participate in Fenton chemistry, leading to the generation of toxic free radicals [37,38,49-51]. These reactive oxygen species (ROS) go on to cause oxidative stress, a process resulting from the inability of a biological system to detoxify peroxides and free radicals, manifesting in the damage of cellular components causing neuronal injury [37,38,42,48,49,52-55]. With the accumulation of iron within brain structures and the occurrence of oxidative stress being recognized as early stage events in Alzheimer's disease pathogenesis, the role played by iron may be key in the development of AD [40,48,56,57].

1.2 Iron accumulation and oxidative stress in AD

1.2.1 Iron in the human brain

Iron is distributed throughout the human body, and the brain is no exception [43,46,58,59]. Iron is fundamentally involved in multiple processes within the human brain and therefore a basal level of iron is required for healthy function [47,59]. It is a key component of multiple biological structures involved in ATP (energy) production, such as cytochromes a, b and c, and cytochrome oxidase [43,46,60]. This essential role in energy production coupled with the high energy demands of the brain, result in high iron concentrations within brain tissues relative to the other organs of the human body. In addition to the production of ATP, iron is fundamentally involved in neurotransmitter synthesis acting as a cofactor for the enzymes tyrosine hydroxylase and tryptophan hydroxylase [43,46]. Furthermore, iron is required in the formation of myelin sheaths through its ability to biosynthesise lipids and cholesterol, important substrates of myelin; thus becoming indirectly involved in the transmission of neuronal signals in the human brain [43,46]. Finally iron is involved in

hippocampal long-term potentiation (LTP) through its essential role in ryanodine receptor-mediated Ca release following *N*-Methyl-D-aspartic acid (NMDA) receptor stimulation. NMDA receptor stimulation results in extracellular signal-regulated kinase (ERK) 1/2 phosphorylation, a key step in the signalling cascade required for sustained hippocampal LTP [61,62]. In light of these roles, it is clear that disruptions to iron homeostasis will have an extremely deleterious effect upon healthy brain function, with both iron deficiency and iron excess resulting in negative consequences [47,59].

The functions of iron as described above are made possible through iron's ability to change oxidative state. It is also iron's oxidative (redox) state that determines its ability to form ROS, and induce oxidative stress. When in a ferric (Fe^{3+}) state, iron is redox-inactive and thus incapable of partaking in reduction-oxidation (redox) reactions [63]. However when in a redox-active form (such as ferrous, Fe^{2+}) iron can participate in redox reactions (see *Section 1.2.2*) that result in the generation of potentially neurotoxic free radicals[48,50,63].

In the human brain, iron is stored as ferrihydrite ($(Fe^{3+})_2O_3 \bullet 0.5H_2O$), a poorly crystalline *redox-inactive* ferric oxyhydroxide, within the storage protein ferritin [46,58,60,64,65]. This form of storage prevents iron-associated ROS production, thereby protecting neurons (and associated microglia, astrocytes, endothelial and smooth muscle cells) from detrimental free radical burdens. Structurally, ferritin is comprised two subunits: heavy (H) and light (L) chain ferritin, which assemble into a 24 subunit protein complex, 450 kDa in molecular weight (Figure 1.3a) [46,65,66]. The protein is 12 nm in diameter, containing an 8 nm hollow core capable of storing approximately 4500 Fe atoms (Figure 1.3b) [58,60,65,66]. Both H-ferritin and L-ferritin subunits have distinct functions. H-ferritin (21 kDa) contains a di-iron binding site, and possesses ferroxidase activity, catalyzing the conversion of redox-active Fe^{2+} into a redox-inactive Fe^{3+} state. L-ferritin (19 kDa) does not convey any enzymatic activity, but does contribute to long term iron storage, by accelerating the

transfer of iron from the ferroxidase centre to the ferritin core, whilst also stabilizing ferritin complex structure [46,64,65]. Thus ferritin provides an efficient means by which to store large volumes of iron safely in brain tissue.

The transportation of iron within the brain is largely regulated by the extracellular transferrin protein, with multiple neuron types expressing transferrin mRNA [46,67]. Neurons acquire their iron via the interaction between transferrin and transferrin receptors found on the neuron surface [46,67]. Moreover transferrin is implicated with the transportation of iron over the blood brain barrier and is therefore required for iron's entry into the brain [68]. An additional level of control in maintaining iron homeostasis comes through the action of iron regulatory proteins (IRPs). These intracellular proteins, found in the cytoplasm, are responsible for regulating cellular iron, by binding to the iron-responsive element (IRE) in the 5' untranslated region of ferritin and transferrin receptor mRNA, thereby regulating their expression [46,59,69]. In turn this dictates how much iron enters a cell, and the amount of this iron that is free or stored within ferritin.

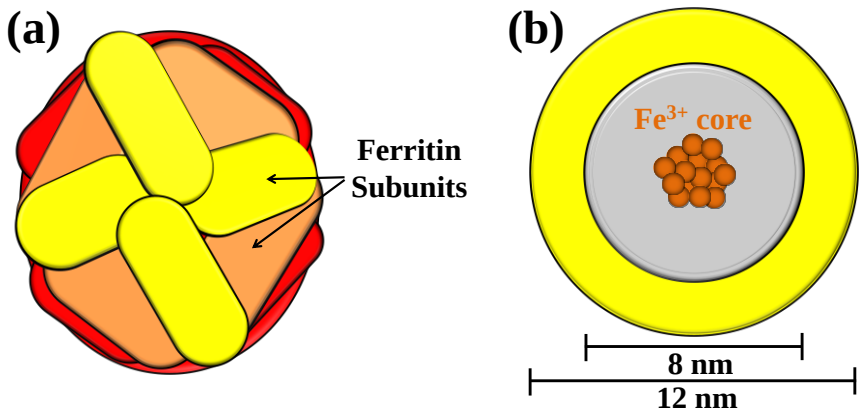

Figure 1.3. Illustrated representation of the ferritin protein. **(a)** The assembly of ferritin subunits (yellow, orange and red) into a 24 subunit protein-complex. **(b)** A cross section of (a) displaying the 12 nm diameter ferritin cage (yellow) and the 8 nm core of ferritin (grey) containing ferrihydrite particles (brown; Fe^{3+})

1.2.2 Iron accumulation in AD

Despite the regulatory systems described in the previous section, increased brain iron loads have been observed in AD tissues [12,31,34,35,37,39,42,43,48,55,56,59,70]. The association of iron accumulation and the development of AD lesions were first suggested by Louis Goodman in 1953 following a case study of 23 AD subjects [34]. Through histological staining techniques, localized iron foci were observed in glial cells, NFTs and SPs, the pathological hallmarks of AD [34]. From these initial observations, a variety of approaches have been utilized to probe the relationship between iron and AD, and it is now widely accepted that iron homeostasis is disrupted in diseased individuals.

Iron accumulation has been observed in brain structures known to be vulnerable to AD including the hippocampus and cerebral cortex [55]. Through the use of micro particle-induced x-ray emission analysis, iron levels have been shown to be locally increased within SP material compared to surrounding AD brain tissue [35], whilst MRI of APP/PS1 transgenic mice displaying AD pathology have demonstrated iron accumulation within SPs in mouse models of the disease [71]. Increased concentrations of iron have been shown to accumulate to areas of AD pathology in mice overexpressing Aβ, suggesting an affiliation of Aβ for iron [31]; and in *C.elegans* models of AD, increased Aβ production is associated with an increase in cellular iron content and oxidative stress [72]. Further to this, chemical and laser microprobe studies of AD tissues have demonstrated the occurrence of iron within both SP and intracellular NFT material *in situ* [35,44]. Further evidence from transgenic PSAPP mouse models of AD indicates iron accumulation to be an early stage event in AD, and that iron accumulation coincides with the formation of SP material [40]. Moreover, recent studies suggest that APP may be involved in iron exportation, explaining iron accumulation in FAD cases where APP mutations occur [73]. Taken together this

evidence demonstrates increased iron levels in lesions associated with AD, coupled with neurons and tissues vulnerable to AD neurodegeneration, suggesting iron to play a significant role in the pathogenesis of the disorder.

Surprisingly, in the brains of AD patients, increased iron levels are not correlated with increased ferritin expression [74]. Moreover the expression and distribution of iron regulatory proteins have also been shown to be disrupted in the AD brain, resulting in an increased uptake of cellular iron, and also a decreased expression of ferritin mRNA[75]. In addition, iron regulatory protein-iron responsive element (IRP-IRE) complexes have been shown to be more stable in AD patients compared to healthy controls [69]. This increased IRP-IRE stability results in a decrease in ferritin synthesis coupled with a concurrent stabilization of transferrin receptors, again resulting in the accumulation of iron within neuronal bodies [59,69,75,76]. Interestingly, a link between AD and haemochromatosis (HFE; also referred to as congenital iron overload) has been demonstrated [43]. The presence of HFE mutations in AD patients further suggests that disruptions to iron homeostasis may be influential in the development of AD.

Increases in intracellular iron content without an appropriate increase in ferritin to detoxify said iron would leave neurons vulnerable to ROS formation and oxidative stress [75]. ROS production arises through the ability of poorly liganded, labile iron to partake in Fenton chemistry; a set of redox reactions (chemical reactions whereby electrons are transferred between atoms), culminating in the generation of free radicals [48,56,63]. During these reactions, ferrous iron is oxidized by hydrogen peroxide (produced by mitochondria) to create ferric iron, a hydroxyl radical ($OH\cdot$) and a hydroxyl anion (OH^-) (equation 1). The ferric iron is then reduced back to ferrous iron by the action of hydrogen peroxide, to form a peroxide radical ($OOH\cdot$) and a proton (H^+) (equation 2). Thus the net products of these reactions are two free radical molecules, and one molecule of water. Further to this, ferric

iron can react with the superoxide anion ($O_2^{\bullet-}$, also produced by the mitochondria), to re-form ferrous iron, facilitating the redox cycling of iron (equation 3)[48]. The consequence of ROS production and the resulting oxidative stress are covered in more detail in *Section 1.2.3*

$$Fe^{2+} + H_2O_2 \longrightarrow Fe^{3+} + OH^{\bullet} + OH^{-} \quad \textbf{(1)}$$

$$Fe^{3+} + H_2O_2 \longrightarrow Fe^{2+} + OOH^{\bullet} + H^{+} \quad \textbf{(2)}$$

Fenton-chemistry involving iron, resulting in the production of ROS

$$O_2^{\bullet-} + Fe^{3+} \longrightarrow O_2 + Fe^{2+} \quad \textbf{(3)}$$

Superoxide reduction of iron

Further to a direct toxicity caused through iron-mediated ROS production, disruptions to iron homeostasis may also have downstream effects, such as blockage of mitochondrial aconitase synthesis, resulting in pathophysiological energy metabolism in AD tissues [75].

1.2.3 Oxidative stress and AD

ROS are a natural by-product of healthy brain functions, and thus high levels of anti-oxidant defences are employed within the nervous system to maintain oxidative balance. However oxidative imbalance is observed in multiple neurodegenerative disorders resulting in oxidative stress and tissue damage [55].

Considerable evidence of oxidative damage in AD is provided through the observations of lipid peroxidation products and the presence of oxidatively modified proteins and nucleic

acids [55,57,77-80]. Markers for oxidative stress are seen to rise in multiple transgenic models of AD (see Belkacemi (2012) for a recent review on these animal models [77]). Examples include elevated levels of cholesterol oxidation products and hippocampal protein carbonyls, in Tg2576 transgenic AD mice compared to wild type controls [80]. Similarly, multiple studies have reported increased levels of protein carbonyls in autopsy studies of AD patients [80].

8-hydroxyguanosine (8-OHG), an oxidized nucleoside primarily formed through the reaction of hydroxyl radicals with RNA (thus acting as an indicator of intracellular oxidative damage), is known to be greatly increased in the cytoplasm of neurons vulnerable to AD [38,81]. Moreover the oxidized amino acid nitrotyrosine has also been located within such vulnerable neurons [82,83]. These oxidative modifications were found to be greatest during the earliest stages of disease progression, suggesting oxidative damage to be an early event in AD pathogenesis [57,84]. HFE mutations (associated with AD; as described in *Section 1.2.2*) are also correlated to increased oxidative stress, thus contributing to the severity of AD [43]. The deposition of SP material in AD tissues has been shown to activate microglia/reactive astrocytes [85]. These activated cell lines secrete cytokines, which when extensively produced result in the activation of macrophages that generate large amounts of ROS. Furthermore, activated microglia have been demonstrated to induce lipid peroxidation by releasing iron from ferritin in a superoxide dependent fashion [86].

Comparisons of AD brains to age-matched disease free controls have also revealed increases in the lipid peroxidation product 4-hydroxynoneal (HNE), in the ventricular fluid and multiple areas of the diseased brain [12,80,87,88]. HNE conveys toxicity to neurons both *in vitro* and *in vivo*, by inducing free radical attack of arachionic acid, a cell membrane component abundant in brain tissues. HNE is further implicated in the disruption of

multiple biological processes vital for survival such as DNA and RNA synthesis, mitochondrial activity, Ca homeostasis and energy production [12,80,87]. Moreover, HNE has been shown to cause excitotoxicity, the pathological process in which neurons are damaged by over activation of excitatory neurotransmitter receptors [80].

A number of oxidatively modified proteins can be seen in AD tissues compared to disease-free controls. Examples of affected proteins include: β-actin, the glucose transporter Glt-1, glutamine synthase, transferrin, hemopaxin and anti-trypsin [12,79,89]. These oxidative modifications of proteins in the AD brain may result in negative disturbances to neuronal processes such as uncoupling of the electron transport chain, loss of synaptic plasticity, excitotoxicity, neuronal communication and alterations in the properties of the blood brain barrier [79].

Finally the process of protein turnover in neurons by the ubiquitin-proteasomal system may be disturbed by the presence of HNE-modified or oxidized proteins in the AD brain [89]. This is turn may lead to protein aggregation, tau hyperphosphorylation and disrupted axonal transport, all manifesting in neuronal damage.

1.2.4 Effects of iron interaction upon β-amyloid configuration and toxicity

As mentioned in *Section 1.1*, Aβ appears to be both directly and indirectly toxic to neurons. Existing evidence shows Aβ to be capable of inducing membrane peroxidation, protein oxidation, and the inhibition of oxidatively sensitive enzymes, implicating Aβ in ROS production [16,17,23,29,42,50,72,90]. Moreover multiple anti-oxidants have been shown to reduce β-amyloid associated neurotoxicity, protecting neurons from damage[12]. Further indirect Aβ toxicity arises through its ability to induce the formation of NFTs [21], detrimentally

effecting cellular transport and energy production, and through the activation of the immune response [12] and ROS producing macrophages. Thus the accumulation of Aβ in the AD brain appears to contribute to the catastrophic levels of ROS production and oxidative stress observed in AD tissues, as described in the previous section.

Despite this established toxicity, studies examining free radicals produced directly by Aβ have provided inconsistent results. Initial findings indicated towards Aβ being capable of spontaneously generating free radicals [50,51], whereas other lines of evidence show β-amyloid to be incapable of forming peptide-derived free radicals [91]. The effect of Aβ conformational state upon its ability to form ROS is also disputed. Evidence suggests both soluble (small oligomers) and insoluble (mature fibril and plaque structures) Aβ forms contribute to neuronal dysfunction in AD tissues (Figure 1.4) [15,16]. However for the purpose of this thesis, emphasis will be placed upon the effect of Aβ aggregation (formation of insoluble fibrils) upon amyloid toxicity.

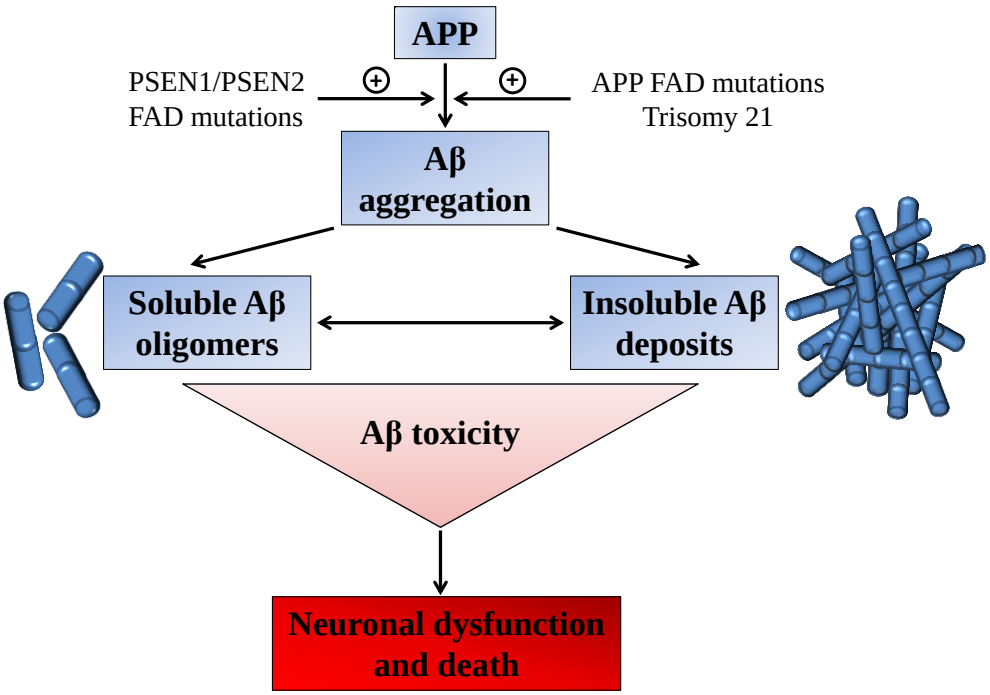

Figure 1.4. Implication of Aβ production upon neuronal health in AD (modified from Karran *et al*. 2011 [15]).

Investigations conducted by Monji *et al*. provided *in vitro* evidence directly correlating the formation of Aβ fibril structures to the generation of free radicals using electron spin resonance spectroscopy [32]. Indeed, freshly solubilized synthetic Aβ monomers have been demonstrated as non-toxic to cultured neurons, whereas high molecular mass aggregates of Aβ were found to induce neurotoxic effects [25,92,93]. These findings support investigations by Hensley *et al.* who demonstrated areas of Aβ deposition to be hotbeds of protein oxidation in AD tissues using biomarkers for neuronal protein oxidation [94]. Similar patterns can be seen in transgenic mice models of AD, where immunohistochemical studies showed anti-oxidant (superoxide dismutase and heme oxygenase) levels to be increased in the immediate vicinity of Aβ plaques [80]. Furthermore, oxidative stress is seen to induce the production and aggregation of Aβ into insoluble forms, in a positive feedback mechanism resulting in perpetuated ROS production [77,90].

Findings in this field led to the proposal of a mechanochemical mechanism for peptidyl free-radical generation, [Kay (1997) FEBS Letters [24]] based upon the cross β-sheet structure of Aβ fibrils (Figure 1.5):

(i) During the process of amyloid fibrillogenesis (Figure 1.5a), there exists a small probability of β-amyloid monomer mispacking leading to abnormal fibril formation (Figure 1.5b).

(ii) As fibrillogenesis continues, the packing defect is trapped within the β-sheet conformation of the protein. The surrounding protein structure resists distortion, and the abnormally packed peptide is strained (Figure 1.5c).

(iii)The strain placed upon the abnormal peptide leads to mechanically activated thermal decomposition, causing the production of peptidyl free radicals and homolytic bond scission (Figure 1.5d).

(iv) Further reaction with oxygen produces peroxy free radicals, promoting the production of ROS (Figure 1.5e).

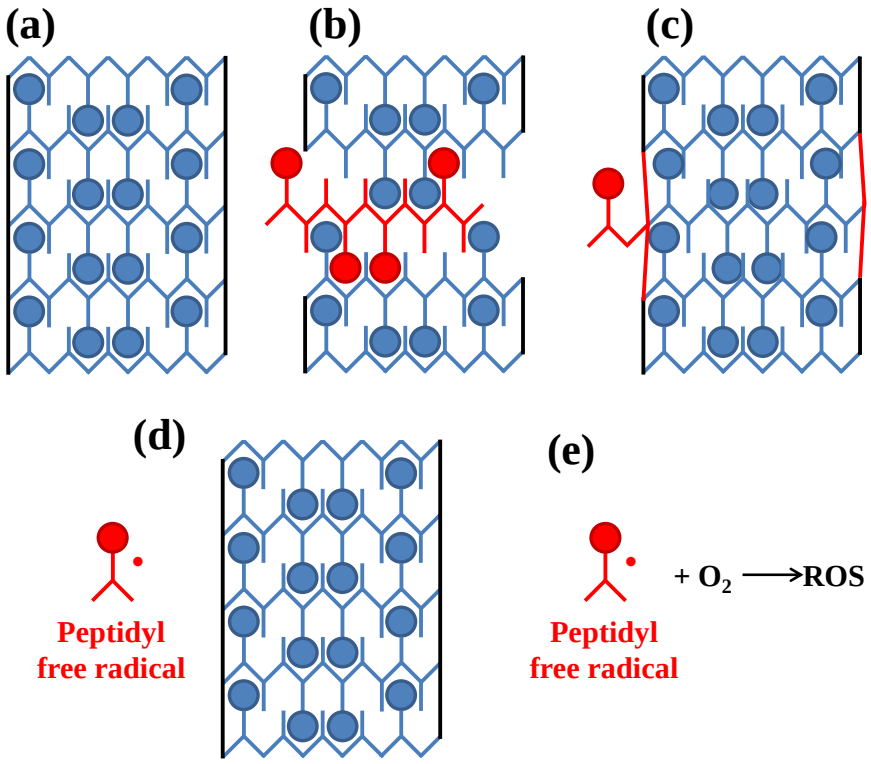

Figure 1.5. Peptidyl free radical production through the mispacking of Aβ fibrils. **(a)** Normal Aβ fibrillogenesis. **(b)** Addition of a polypeptide with abnormal hydrogen bond alignment (red). **(c)** Continued fibril growth around this packing abnormality resulting in mechanical strain on the fibril (red). **(d)** Mechanically activated thermal decomposition of the strained fibril produces peptidyl free radicals which interact with oxygen **(e)** to induce free radical production. [Interpreted from Kay *et al.* 1997 [24]]

Intriguingly, the aggregation of Aβ into fibril structures has been shown to be greatly accelerated in the presence of iron (known to accumulate within Aβ structures *in vivo*). Transmission electron microscopy and ThT fluorescence studies conducted by House *et al.* and Khan *et al.* revealed significant aggregation of synthetic Aβ fragments following the addition of iron(III) *in vitro* [95,96]. The effect of iron upon Aβ aggregation is suggested to be so dramatic that even trace metal contaminants within solution media are believed to induce its aggregation[97]. A potential mechanism for iron mediated Aβ aggregation involves

the formation of intermolecular crosslinks in the β-pleated structure of amyloid by the atoms of the metal [96]. Recent evidence suggests that this aggregation process may involve the binding of iron by Aβ, with amyloid potentially acting as a metalloprotein [98-100]. Evidence suggests this binding domain to consist of three histidine residues at positions 6, 13 and 14, and a further tyrosine residue at position 10 located at the N-terminus of Aβ [55,101,102].

Further to inducing aggregation of amyloid into fibril structures, the interaction of Aβ with iron has been shown to increase ROS production and oxidative stress. *In vitro* examination of iron(II) sulphate ($FeSO_4$) incubated with Aβ revealed ROS production to be markedly increased to where Aβ or $FeSO_4$ were incubated alone[103]. *In vitro* studies conducted by Liu *et al.* indicate that iron specifically enhances Aβ toxicity when present throughout the aggregate process, by impeding its ordered aggregation into cross β-fibrils [104]. These findings are consistent with models proposed by Kay, where imperfections in cross β-structures are identified as potential sources of ROS production [24]. Moreover, the integration of iron into amyloid fibril structures may act to mediate Aβ toxicity via the ability of amyloid to transport iron into the vicinity of cellular membranes, inducing lipid peroxidation and cellular death (Figure 1.6) [54].

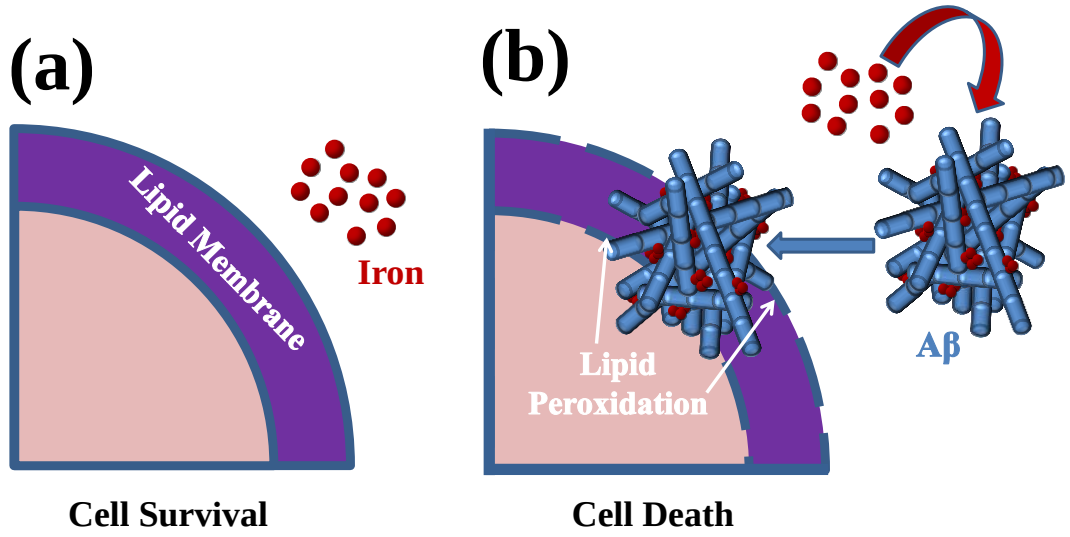

Figure 1.6. Iron mediated Aβ toxicity as described by Rottkamp *et al.* [54]. **(a)** In the absence of Aβ, iron (red) does not induce lipid peroxidation, due to its distance from the lipid membrane and the short lived nature of iron-associated ROS. **(b)** Aβ (blue) incorporates iron into its fibrillar structure, transporting iron into the immediate vicinity of the lipid membrane, resulting in iron-induced lipid peroxidation and cell death.

1.3 Redox-active iron and AD

From the literature examined in *Section 1.2.4* it is apparent that Aβ-associated toxicity is increased in the presence of iron. As Aβ is known to act as a "sink" for iron deposition, this interaction process is likely to influence ROS production within AD tissues. However, significant evidence also suggests there to be increased levels of redox-active iron in regions of AD pathology including SPs [36-38,49,52,58,60,70,105-109]. These iron phases would themselves be a source of free radical production and could therefore be pathologically relevant to AD.

1.3.1. Ferrous iron in AD tissues

Associations between the occurrence of ferrous (redox-active) iron and AD pathology were initially observed using modified histochemical techniques, allowing the visualisation of both iron(III) and iron(II) content within AD brain tissues [37]. Iron(II) was closely associated with SPs NFTs and neuropil threads in AD tissues, compared to disease free control tissues where no specific structures were positively stained for ferrous iron [37]. This, combined with observations that iron chelators ameliorate Aβ-induced toxicity to neurons [54], suggests Aβ-associated iron rather than the peptide itself to be the predominant source of ROS in Aβ-induced toxicity [49,53]. Further histochemical studies show iron(II) levels to be significantly increased in hippocampal AD neurons compared to disease free controls, resulting in increased redox activity and RNA damage [110]. These findings also indicate ribosomal RNA (rRNA) to possess a binding site for redox-active iron, suggesting that redox-active iron specifically, is a source of oxidative stress in AD tissues [110].

1.3.2. Iron(II)-bearing biominerals in AD

Initial observations of iron(II)-bearing minerals within tissues of subjects suspected to have AD were made by Kirschvink *et al*. in 1992 [111]. In this study, superconducting magnetometry and high resolution electron microscopy techniques identified the mixed-valence iron mineral magnetite (Fe_3O_4) within a variety of brain tissues [111]. These findings were built upon by Dobson (2002), who observed age related increases in biogenic magnetite levels within hippocampal tissues from male subjects, suggesting magnetite to play a role in the neurophysiology of aging [112]. Preliminary superconducting magnetometry evaluation of magnetite levels from tissues confirmed to contain AD pathology, demonstrated increased biogenic magnetite levels in AD subjects compared to age and sex-matched disease-free controls [105]. These results suggest that increases in magnetite levels

contribute to the increased iron loads observed in AD patients [105]. Evidence of increased < 20 nm diameter magnetite nanoparticle loads in AD tissues compared to sex-matched disease-free controls has also been demonstrated [113]. Moreover, increased levels of magnetite and a cubic iron phase consistent with the pure iron(II) mineral wüstite, have been recorded in pathological ferritin removed from AD tissues but not in physiological ferritin, using election nanodiffraction and high resolution electron microscopy [108]. This was coupled with a decrease in ferritin ferrihydrite content, suggesting the conversion of ferritin's ferrihydrite core into a redox-active state [108,109].

Recently, *in situ* mapping and characterization of iron minerals within AD tissues has been achieved through the use of synchrotron-based x-ray techniques. Through x-ray fluorescence microanalysis, Collingwood *et al.* demonstrated the presence of multiple iron deposits within tissue sections taken from the frontal gyrus of an AD patient [106]. X-ray absorption levels from these iron regions demonstrated the presence of an iron mineral consistent with magnetite. Again these results demonstrate a link between increased iron loads, and the presence of redox-active iron phases within AD tissues. Further to this the same group applied a multidisciplinary approach incorporating high resolution TEM, energy dispersive x-ray spectroscopy, electron energy-loss spectroscopy, electron tomography and electron diffraction, to image an AD plaque core in three-dimensions [36]. This three-dimensional tomographic imaging revealed the presence of an iron deposit approximately 8 nm in diameter (equivalent to the core size of ferritin) with a crystalline structure consistent with magnetite or maghemite (Fe_2O_3, the oxidation production of magnetite), to be located within AD plaque material [36].

The presence of redox-active iron minerals in AD tissues may prove to be of pathological significance, through the ability of these phases to partake in Fenton chemistry, resulting in the generation of neurotoxic ROS [114,115]. In particular, magnetite is known to promote free

radical production not only through Fenton reactions [116-118] but also the stabilization of triplet states (formed during biochemical reactions). This triplet state stabilization is a result of magnetite's ability to form strong local magnetic fields [60,113], dramatically increasing ROS production, thereby conveying toxic effects *in vitro* [119 120].

1.3.3 Possible origins of redox-active iron phases

1.3.3.1 Ferritin malfunction

Despite the numerous occasions on which iron(II)-bearing phases have been recorded in AD tissues, the exact origins of these minerals remains unclear. The increased levels of iron(II)-bearing minerals located within pathological ferritin [108,109] suggest that the storage protein may act as a nucleation site for redox-active iron formation, putatively through the conversion of its ferric core into a ferrous phase. Indeed, the < 10 nm and < 20 nm magnetite nanoparticles observed in AD tissues (Collingwood *et al.* [36] and Pankhurst *et al*. [113]) are in a size range consistent with the core of ferritin. Moreover, through the use of TEM, EELS, x-ray absorption spectroscopy, superconducting magnetometry and x-ray scattering, low levels of magnetite have been recorded within physiological ferritin [121]. Should ferritin function become compromised in AD, this physiological magnetite may act as a seed for further magnetite formation, resulting in increased magnetite burdens, such as those observed in superconducting magnetometry measurements of AD tissues [105,113]. A loss of ferritin function in this manner would be extremely detrimental to neuronal health due to extensive and widespread ROS production through inappropriate iron storage (and redox-active iron formation). Recent findings have shown ferritin function to be compromised when exposed to ROS [66]. Thus the increased levels of ROS observed in AD tissues may act to disrupt ferritin function through oxidative modifications to the protein. It

should also be noted that ferritin dysfunction is observed in multiple neurodegenerative disorders, emphasising the importance of ferritin function to brain health [122,123].

1.3.3.2 Iron reduction by Aβ

The identification of redox-active iron, and iron(II)-bearing biominerals in the immediate vicinity of Aβ deposits is also of great intrigue [36,42,45]. As mentioned previously, iron is capable of influencing Aβ fibril conformation and aggregation state. However, this interaction process is also seen to have an effect on iron chemistry by altering the valence state of iron, indicating that Aβ may contribute to the formation of redox-active iron species.

In 1999 Huang *et al.* demonstrated Aβ to have a strong reductive capacity for transition metals including Fe^{3+}. This reduction was found to be followed by the trapping of molecular oxygen (O_2) to generate H_2O_2 which was then converted to a hydroxyl radical (OH•) as per the Fenton reaction. It was found that Aβ itself became oxidized during this process, therefore acting as a direct reducing equivalent [45,50,51]. This process is outlined in the panel below.

Aβ reacts with a metal ion (M) resulting in a reduced metal ion and radicalized Aβ:

$$(A\beta)_2 + M^{(n+1)+} \longrightarrow A\beta: A\beta^{+\cdot} + M^{n+} \quad \textbf{(4)}$$

The reduced metal ion reacts with molecular oxygen to generate a superoxide anion (O_2^-):

$$M^{n+} + O_2 \longrightarrow M^{(n+1)+} + O_2^- \quad \textbf{(5)}$$

The superoxide anion undergoes dismutation to generate hydrogen peroxide and molecular oxygen:

$$O_2^- + O_2^- + 2H^+ \longrightarrow H_2O_2 + O_2 \quad \textbf{(6)}$$

The ability of β-amyloid to reduce iron is highly dependent upon its isoform. Where the β-amyloid peptide was shortened to 28 amino acids in length (Aβ 1-28) the ability to reduce iron was lost. This observation suggested that it is the hydrophobic carboxyl-terminal domain of β-amyloid that provides the peptide with its reductive properties, whilst N-terminal of Aβ provides iron binding sites [51,101,102]. Furthermore, the addition of two extra hydrophobic amino acid residues (Ile and Ala) to the 40 amino acid fragment of β-amyloid (creating Aβ 1-42), resulted in a significant rise of the reduction properties of the peptide compared to the 40 amino acid fragment (Aβ1-40) [51]. These initial findings suggest that the 42 base isoform of the peptide possesses the most reductive potential, whilst also being the most fibrillogenic.

Further findings by Huang's group also revealed the amount of hydrogen peroxide produced by the Aβ-iron complex is in great molar excess of the amount of metal ions present [50]. It has been suggested that these excessive hydrogen peroxide concentrations are a result of iron redox cycling by β-amyloid, thus creating a mechanism by which the repeated transfer of electrons to multiple O_2 molecules can occur. In theory, two moles of Fe^{2+} are required to generate one mole of O_2^-, and as two moles of Aβ are required to create one mole of Fe^{2+}, four moles of Aβ are needed to generate one mole of H_2O_2. In reality it was found that 25μM of H_2O_2 could be produced by only 10μM of β-amyloid peptide when under high O_2 tensions, providing evidence that multiple cycles of Fe^{3+} reductions must occur [51]. The potential of Aβ to produce extracellular H_2O_2 may help to explain the high intracellular H_2O_2 burdens seen in AD, due to the ability of hydrogen peroxide to pass over lipid boundaries [51].

Further evidence of Aβ-mediated iron reduction and redox cycling was provided by *Khan et al*. (2006)[96]. Using *in vitro* spectrophotometric techniques, iron(III) suspensions were found to become chemically reduced following incubation with Aβ. This was accompanied by a delayed precipitation of iron as redox-inactive iron hydroxide, enabling extended Fe^{2+}/Fe^{3+} redox cycling. In addition, increased Aβ β-sheet formation was correlated to increased Fe^{2+} content, again suggesting Aβ aggregation to increase its reductive capacity. This led to the proposal of a three step mechanism (Khan *et al.*) suggesting a role for Aβ in the reduction and oxidation of iron (Figure 1.7):

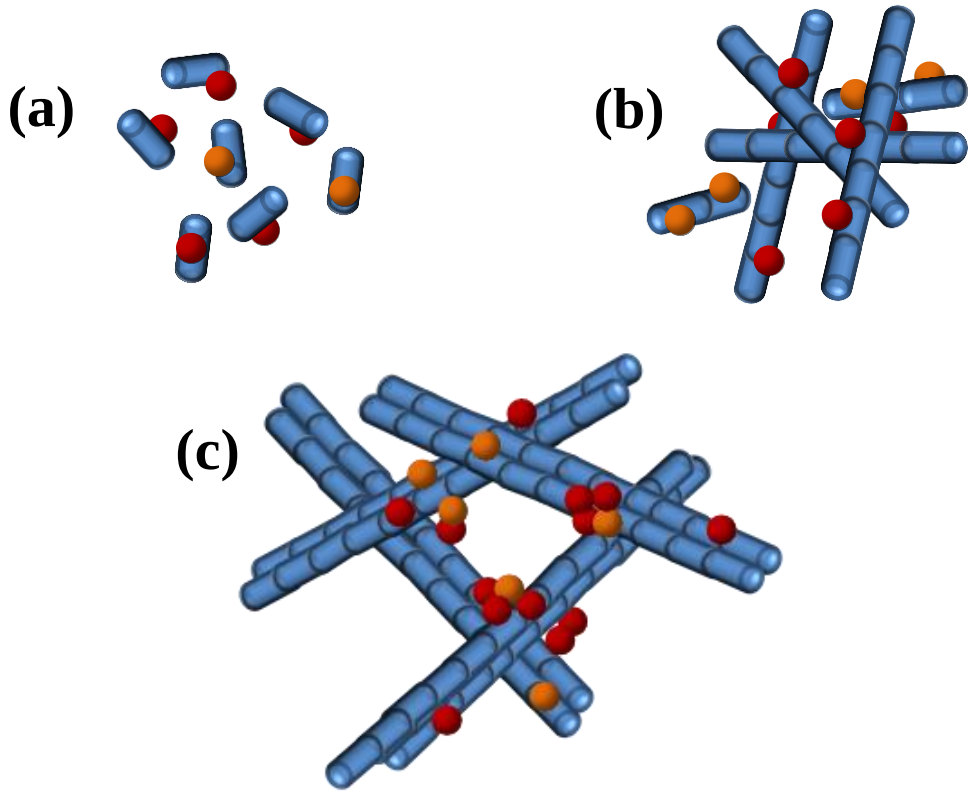

Figure 1.7. Redox cycling of iron by Aβ as described in Khan *et al.*[96] **(a)** Fe^{2+} (red) and Fe^{3+} (brown) are bound by monomeric Aβ (blue), inducing the reduction of Fe^{3+}. **(b)** Monomers of Aβ assemble into oligomers which may include bound iron. This oligomerisation process may also serve to bring iron atoms into closer proximity. Redox reaction rates are accelerated and the deleterious effects of Fe^{2+} are increased compared to where the peptide is in its monomeric form. **(c)** Oligomers assemble into immature and mature β-pleated fibrils. Iron may be retained by or released from newly formed fibrils. Any free iron could then be bound by newly formed fibrils [96].

Similarly, β-amyloid is shown to be capable of stabilizing ferrous iron by decreasing its rate of oxidation. This stabilization effect extends the time with which ferrous iron can interact with ROS and partake in Fenton chemistry [124]. Several β-amyloid fragments including Aβ 25-35, Aβ 1-40 and Aβ 1-42 were found to be capable of stabilizing ferrous iron, with stabilization effects appearing similar to those observed in preparations containing iron and ascorbic acid, a compound known to inhibit the oxidation of Fe^{2+} [124].

Curiously, the presence of aluminium has been shown to increase the reductive capacity of Aβ upon iron [96,103]. Aluminium is known to accumulate in AD tissues [125], and is implicated as a promoting factor in the development of the disease. It is possible that synergies between these metals exist, and that aluminium may influence AD pathogenesis through catalysing the formation of redox-active (toxic) iron biominerals within AD tissues [103].

From the studies highlighted above, it is apparent that Aβ is capable of inducing redox-active iron formation following interaction with ferric precursors. This interaction process may be involved in the increase of iron(II)-bearing biominerals observed in AD tissues thereby contributing to free radical burden and AD pathology. The ability of Aβ to chemically reduce iron also provides explanations to the histochemical observations of ferrous iron associated with SP material in AD tissues [35-37,42]. In light of the ferritin core-sized magnetite deposit found within AD plaque material (Collingwood *et al.* [36]) the formation of redox active biominerals may involve the interaction of Aβ with the iron storage protein ferritin. In fact ferritin has been observed to accumulate within SP material in AD tissues, suggesting that Aβ and ferritin are co-localized in the diseased brain [126].

1.3.4 The amyloid paradox

Aside from the pro-oxidative effects mentioned above, the interaction between brain iron and β-amyloid (in particular, fibrillar forms of Aβ) may also lead to anti-oxidative effects under certain conditions [12,127,128]. In this scenario, excess iron could be sequestered (chelated) by Aβ, thereby preventing iron from taking part in the Fenton like reactions responsible for the production of ROS, and thus creating an "amyloid paradox" where Aβ can act to both increase and decrease iron-associated toxicity [128]. These effects of Aβ upon iron chemistry may prove to be influenced by factors such as the conformational state of Aβ when the protein first comes into contact with the metal, or the crystal state of the iron phase being examined.

1.4. Synchrotron techniques for the characterization of iron phases associated with AD pathology

Following the discovery of increased levels of iron(II)-bearing biominerals in AD tissues, it is imperative to understand the nature of these phases. Iron exists in a wide variety of oxide states, with an array of crystal structures that ultimately govern the magnetic properties of the metal [129]. Determining these properties may prove vital in understanding the redox-activity (toxicity) of iron(II) biominerals and consequently their potential as targets for iron chelation therapies [12], and also the use of iron biominerals as a marker for the detection of early stage AD [60]. Furthermore, identifying the localization of these iron minerals within regions of AD pathology may prove vital in understanding their origin, and how they might contribute to the pattern of neurodegeneration witnessed in AD subjects.

Recent developments in advanced synchrotron-based x-ray absorption techniques have provided a powerful tool to examine these current gaps in our knowledge [130]. Indeed x-ray techniques have been successfully utilized to demonstrate the presence of magnetite-like deposits in AD tissues (Collingwood *et al.* 2005 [70]) and transgenic mouse tissue (Gallagher *et al.* [31]) as described in *Section 1.3.2.* However the precise nature *and* localization of this iron could not be definitively concluded from the techniques employed.

In this section, the two principal x-ray techniques used in this thesis will be introduced. The advantages of each approach will be covered, and I will discuss how these techniques can be employed (individually or in tandem) to improve our understanding of the role played by iron biominerals in AD.

1.4.1. X-ray absorption spectroscopy and x-ray magnetic circular dichroism

X-ray absorption spectroscopy (XAS) and x-ray magnetic circular dichroism (XMCD) are element specific synchrotron-based x-ray absorption techniques that probe the oxidation state, site symmetry and magnetic moments of -3d transition metal ions, including iron [131-133]. Differences in the elemental composition of iron phases result in alterations to XAS/XMCD features, thus these techniques can be utilized to characterize the iron species present in a given composite material. The energy of the soft x-rays used in this thesis (200-1000 eV) are considerably lower than the equivalent energy imparted in electron microscopy, making these techniques preferable for soft matter studies.

X-ray absorption occurs when the energy from an incident photon, generated from a synchrotron source, is absorbed by an inner-shell electron of an atom (1s, 2s, 2p, 3s etc.) which is excited to an empty higher energy orbital, leaving a core hole [132,133]. The photon

energy of the x-ray beam is tuned using a monochromator, to an energy range (or "edge") where core electrons of the material of interest become excited. In this thesis the predominant energy range examined is 700-740 eV, corresponding to the iron *L*-edges, in which 2*p* electrons are excited to unfilled 3*d* orbitals. The precise absorption energy spectrum is sensitive to the oxidation state of the cation that absorbs the x-ray. Thus by detecting and recording x-ray absorption events across the iron *L*-edge, x-ray absorption spectra characteristic of the oxidation state of a given iron material can be created [132,133].

X-ray absorption events result in the emission of both photoelectrons and Auger electrons. Photoelectrons are core-electrons ejected following absorption of the x-ray beam, whereas Auger electrons are emitted where higher-orbital electrons fill the core-hole left by the photoelectron [132,133]. In total electron yield (TEY) detection methods, the current from both photoelectrons and Auger electrons that escape the sample surface is recorded, providing a signal that is proportional to the x-ray absorption.

Further, probing the magnetic properties of 3*d* transition elements can be achieved through XMCD. This method exploits differences in the x-ray absorption of a magnetically polarized material when illuminated with circularly polarized photons. When an atom absorbs a circularly polarized photon, the angular momentum of this photon will transfer to the excited electron spin through spin-orbit coupling. Reversing the polarization reverses the angular momentum of the photon, transferring the opposite momentum to the electron spin. Thus photoelectrons of opposing spins (i.e. spin up and spin down) will be created in response to illumination with left circularly polarized photons (LCP) and right circularly polarized photons (RCP). If an equal number of empty spin up and spin down orbitals exist in the valence state, then LCP and RCP will be absorbed identically, as is the case in non-magnetic materials (Figure 1.8a). However in magnetic materials, there is an imbalance of spin-up and spin-down valence holes, and therefore absorption intensities in response to

LCP and RCP differ (Figure 1.8b). The difference (dichroism) between the two absorption spectra is referred to as the XMCD, and reveals the magnetic moment of the atom which has absorbed the x-rays [132,133].

The combination of XAS and XMCD provides a probe of element-specific oxidation and magnetic properties. Typical x-ray probing depth for XAS/XMCD techniques operating in TEY mode is approximately 5 nm; meaning that information regarding oxidation and magnetic state is obtained from the outermost 5nm of a sample material. Thus for large iron deposits, say several microns in diameter, XAS/XMCD will provide information regarding the surface oxidation/magnetic state. Conversely for nanoscale iron structures (such as ferritin, 12 nm in diameter), 5nm probing depth is sufficient to gain an overall picture of the oxidative/magnetic properties of this nanoscale iron.

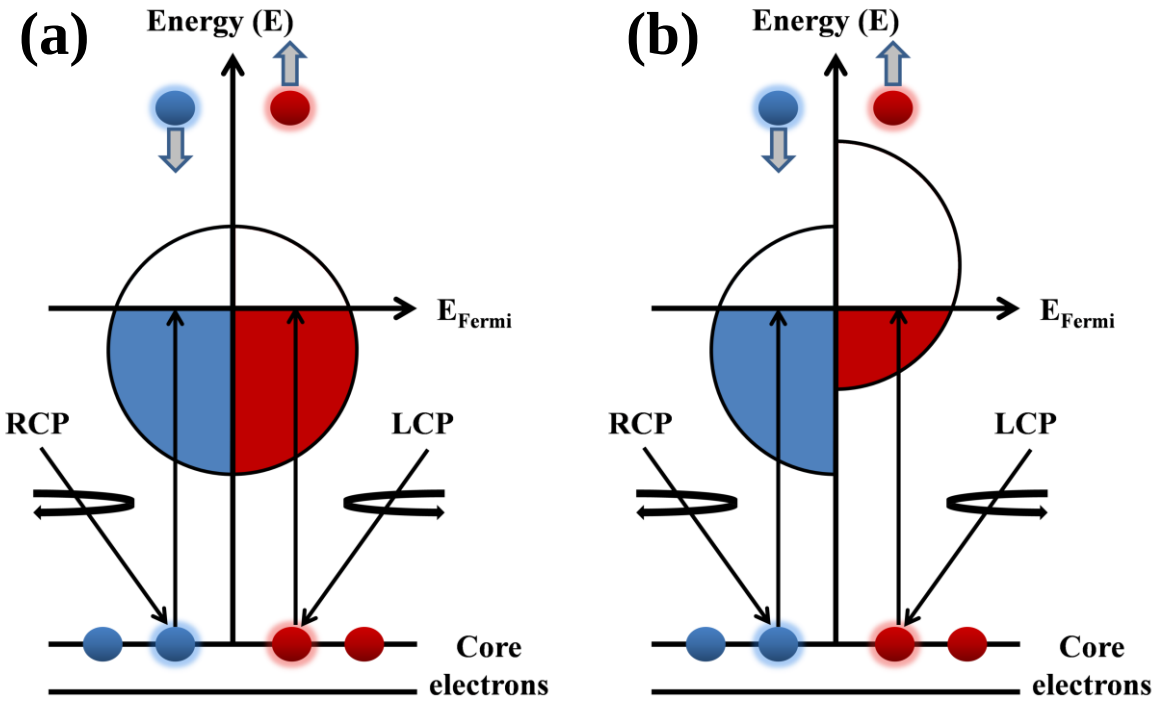

Figure 1.8. The principals of XMCD. **(a)** In a non-magnetically polarized material, excited spin up and spin down electrons occupy an equal number of valence states in response to polarized light. **(b)** In a magnetically polarized material, an imbalance in the number of spin up and spin down valence states results in an altered absorption levels in response to oppositely circularly polarized light [132,133].

1.4.1.1 Applications

XAS and XMCD allow the characterization of iron oxidative and magnetic state, enabling us to distinguish between multiple, similar iron oxide phases [131]. The sensitivity of these techniques [132,133], combined with traditional approaches such as electron diffraction could allow potentially pathological iron phases associated with AD to be separated from physiological iron, as explained below.

As described in *Section 1.2.1*, within the human brain, iron is predominantly stored as the redox-inactive iron oxyhydroxide, ferrihydrite [46,64]. Ferrihydrite is a ferric, poorly crystalline material [129,134-136], with antiferromagnetic spin ordering at room temperature such that the atomic magnetic moments are anti-aligned and thus cancel each other. XAS spectra from pure iron(III) minerals (Figure 1.9; blue) are characterized at the L_3 absorption edge by a dominant peak at 709.5 eV and a low energy shoulder at 708 eV, both arising from Fe^{3+} cations [131]. At the L_2 edge two low intensity peaks are observed at 721 eV and 723 eV again arising from Fe^{3+} cations. The low energy Fe^{3+} feature at 708 eV resides at the same energy as the Fe^{2+} cation peak, thus increases in Fe^{2+} content of an iron material manifest as an enhancement of this feature. Similarly at the L_2 edge increases in Fe^{2+} content result in an increase in Fe^{2+} cation feature at 721 eV with respect to the Fe^{3+} feature at 723 eV. In pure iron(II) minerals (Figure 1.9; red) the Fe^{2+} cation peak at 708 eV becomes dominant, and the Fe^{3+} cation feature at 709.5 eV disappears. This effect is mirrored at the L_2 absorption region [131].

The mixed valence iron oxide magnetite also provides distinguishable XAS spectrum (Figure 1.9; green). In magnetite, the L_3-edge Fe^{3+} cation feature at 709.5 eV is shifted slightly down in energy to 709.2 eV, and the Fe^{2+} cation feature at 708 eV appears as a shoulder on the L_3 Fe^{3+} peak. This Fe^{2+} shoulder is approximately two thirds the intensity

of the Fe^{3+} peak at 709.2 eV. At the L_2-edge, Fe^{2+} and Fe^{3+} cation features appear equal in intensity.

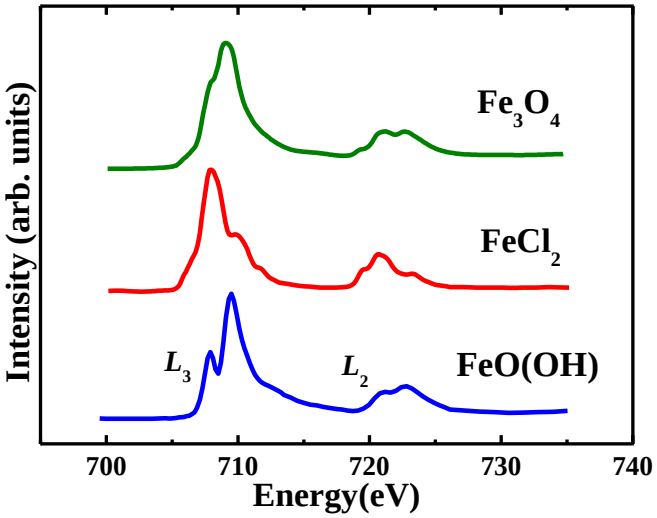

Figure 1.9. Iron $L_{2,3}$ absorption-edge XAS reference spectra. From bottom to top, iron(III) mineral (goethite, FeO(OH)), iron(II) chloride ($FeCl_2$), and magnetite (Fe_3O_4).

Differences in iron $L_{2,3}$-edge XAS spectra arising from an incremental increase in Fe^{2+} content (from 0-100%) with respect to Fe^{3+} content (100-0 %), reveal that even modest increases in Fe^{2+} content can significantly alter iron XAS spectra (Figure 1.10). This allows the identification of pure iron(II) phases such as wüstite (potentially found in pathological ferritin cores [108]), intermediate Fe^{2+}/Fe^{3+} phases, and iron(III) phases alike. Further to this elemental iron ($Fe^{(0)}$; Figure 1.11, grey) provides $L_{2,3}$-edge spectra distinct from pure ferrous materials as evidenced by the absence of iron oxide features (as indicated by the asterisks in Figure 1.11; red).

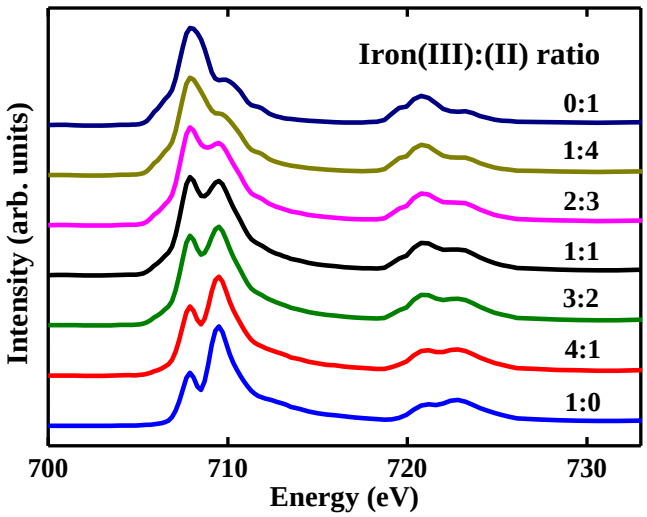

Figure 1.10. Iron $L_{2,3}$ absorption-edge XAS spectra displaying the effect of altered iron(III):(II) ratios upon absorption features. Iron ratios are displayed above each spectrum. Absorption spectra were created by adding weighted iron(II) and iron(III) reference spectra.

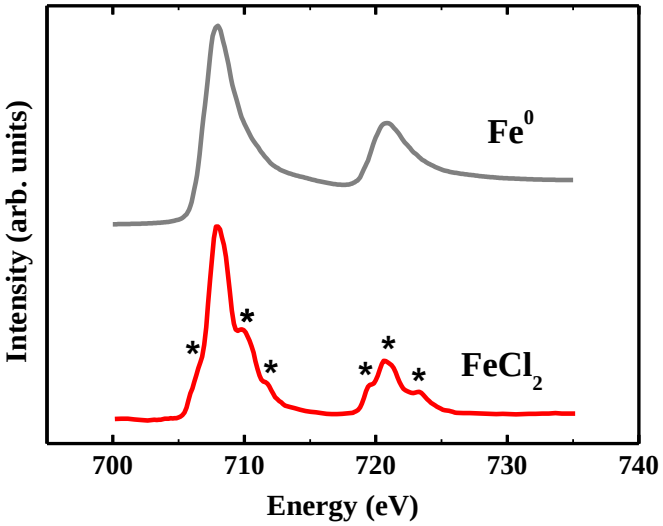

Figure 1.11. Iron $L_{2,3}$ absorption-edge XAS reference spectra of elemental iron (Fe^0; grey) compared to iron(II) ($FeCl_2$; red). Note the absence of the iron cation features (indicated by the asterisks in the iron(II) spectra), in the Fe^0 spectra.

Differences in the magnetic properties of iron minerals can also aid in distinguishing between iron phases. Magnetite is a ferrimagnetic iron oxide with alternating lattices of Fe^{2+} and Fe^{3+} which are antiferromagnetically coupled in a similar arrangement to ferrihydrite (Figure 1.12) [60]. However unlike ferrihydrite, magnetite has a large net

magnetic moment per lattice cell unit due to the atomic spin moments of the Fe^{2+} and Fe^{3+} ions not cancelling each other [60]. These differences in spin moments are manifested as a characteristic three-peak iron L_3-edge XMCD profile, corresponding to Fe^{2+} and Fe^{3+} cations occupying octahedral and tetrahedral crystal sites (Figure 1.13a) [137]. For titanomagnetite (a solid solution mineral complex of Ti cations within the magnetite crystal structure), an additional positive peak is observed because of Fe^{2+} cations occupying tetrahedral sites (Figure 1.13b) [138]. The sign of the XMCD peaks (positive or negative) indicates the relative alignment of the magnetic moments of the cations. Furthermore, the different crystal symmetry at octahedral and tetrahedral sites results in a small energy shift in the XMCD peak positions for Fe^{3+} cations. Thus, although the opposing Fe^{3+} magnetic moments cancel each other, their presence can still be detected by XMCD [132,133]. Dichroism effects of 10-15% are characteristic of magnetic iron phases such as magnetite, making them clearly discernible from non-magnetic iron phases such as hematite and goethite.

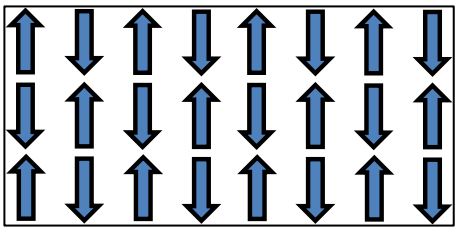

Figure 1.12. Antiferromagnetic ordering showing the anti-alignment of atomic spin moments (arrows)

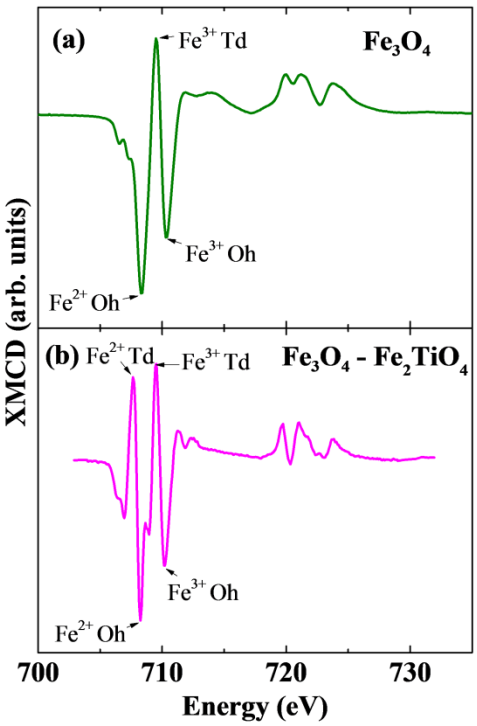

Figure 1.13. (a) Magnetite (Fe_3O_4) XMCD spectrum with labeled octahedral (Oh) and tetrahedral (Td) Fe cation contributions. **(b)** Titanomagnetite (Fe_3O_4-Fe_2TiO_4) XMCD spectrum [138].

Likewise, the oxidation product of magnetite, maghemite (Fe_2O_3) also displays large dichroism effects. Maghemite is a ferric mineral and provides an iron $L_{2,3}$-edge XAS profile indistinguishable from non-magnetic iron(III) phases. However differences in the dichroism effects of these minerals should allow the identification of maghemite from non-magnetic iron species. This is of particular importance due to the ease with which redox-active minerals become oxidized. For example AD tissue containing magnetite may become exposed to aerobic environments post mortem. This could in turn oxidize magnetite into maghemite, providing XAS spectra consistent with naturally occurring ferric iron phases. It would only be apparent upon XMCD examination that the formation of a (strongly) magnetic iron phase had occurred. An example of how XMCD can be used to distinguish between two iron phases with similar XAS profiles is shown in Figure 1.14.

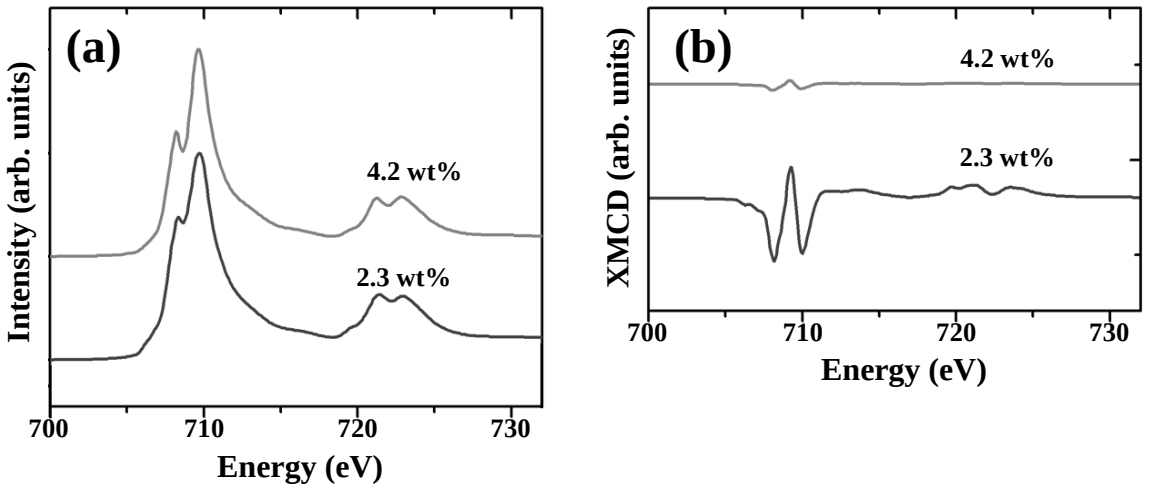

Figure 1.14. Comparisons of **(a)** XAS and **(b)** XMCD iron $L_{2,3}$-edge profiles from biogenic iron precipitates formed by incubating schwertmannite containing various levels of arsenic (shown as a wt% above each spectra), in the presence of the iron reducing bacterium *Geobacter sulfurreducens*. The two XAS spectra shown in (a) have similar features and are not easily distinguishable. However clear differences in the XMCD profiles are evident, with the iron phase formed under 4.2 wt% arsenic providing an XMCD curve reminiscent of a non-magnetic iron material (such as goethite); whereas the iron formed under 2.3 wt% arsenic provides an XMCD spectra consistent with magnetite/maghemite. Figure modified from Cutting *et al.* (2012) [139].

Thus XAS and XMCD used in tandem could allow the characterisation of iron biominerals within AD tissue to a greater level of detail than currently achieved. The ability of these techniques to determine both oxidation states and magnetic properties offers a clear advantage over electron based techniques such as EELS, where only oxidation state can be determined. However, due to a large x-ray beam size (ca. 100-200 μm diameter) these x-ray absorbance techniques do not allow the visualisation of localized structures. One technique allowing both the evaluation of iron oxidation state, and the imaging of biological structures is x-ray microspectroscopy, which is described in the following section.

1.4.2 Scanning transmission x-ray microscopy

Scanning transmission x-ray microscopy (STXM) is a synchrotron-based technique that enables the element-specific imaging of a given material to a spatial resolution of approximately 20 nm. It allows the imaging of structures, providing pictures reminiscent of those obtained via transmission electron microscopy (TEM), whilst simultaneously generating spectral information regarding the chemical composition of the material present, in a manner similar to nuclear magnetic resonance (NMR) spectroscopy. STXM thereby addresses limitations of both TEM (limited chemical sensitivity), and NMR (incapable of providing direct images of the sample material). Moreover STXM x-ray beam exposure does not induce chemical changes in the composition of iron materials as is often seen in electron-based techniques including EELS (for electron-beam induced iron reduction see [140]), and therefore is a more reliable tool to assess the chemical composition of structures.

The chemical imaging of a sample material is achieved by tuning soft x-rays to a desired single energy (typically ranging between 100-1600 eV) via the use of a monochromator. A zone plate is then used to focus coherent x-rays into a single spot (pixel) on the sample of interest, whilst an order sorting aperture (a pinhole-sized aperture) is used to filter any unwanted diffraction orders [141]. Once passed through the sample, the transmitted x-rays are recorded via the use of a detector (for a STXM schematic see Figure 1.15). Energy specific images are created by raster scanning the sample across the focus point of the x-ray beam. Absorbance spectra for a given x-ray focus point (pixel) are generated by recording the level of x-ray transmission across multiple energies through a desired energy range (e.g. the carbon *K*-edge 280-320eV) [141]. This approach allows the imaging of a structure in which each pixel provides an individual x-ray absorption spectrum.

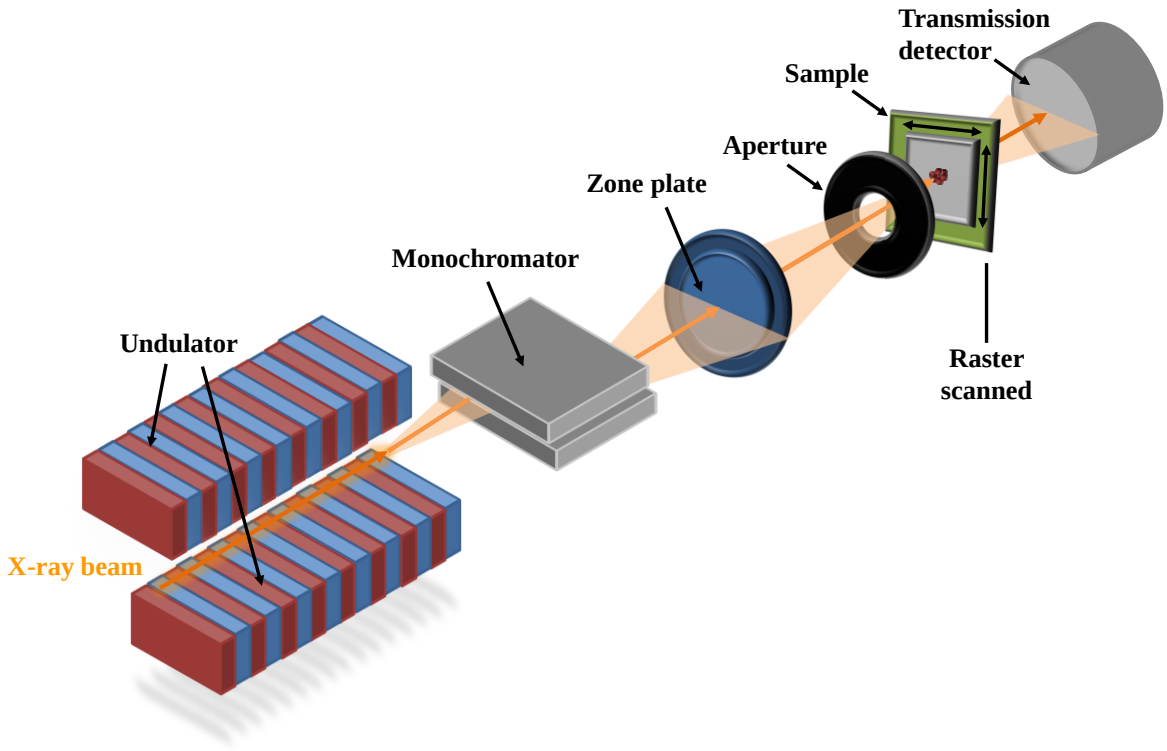

Figure 1.15. Schematic of a scanning transmission x-ray microscope

A variety of sample types (ranging from dry powders to encapsulated solutions) can be suitable for STXM examination, providing sample thickness is not too large. Maximum sample thickness depends upon the material being examined, and is ca. 300-500 nm for carbon studies, and 1-2 µm for higher energy edges (such as the iron *L*-edge). The ability to operate throughout much of the soft x-ray energy range enables the imaging of multiple different elements, potentially found within a single structure. Importantly this allows the examination of both metals and elements within the "water window" (the elemental building blocks of biology). Thus STXM provides a powerful means with which to examine the interactions between metals and biological structures. One such example of STXM application to characterize the metal content of a biological system is provided by Lam *et al.* (2010) who utilized said technique to characterize both the oxidative and

magnetic state of iron-bearing magnetosomes within the magnetotactic bacterium strain MV-1 [142]. This group provided images of MV-1 bacterium by scanning at the carbon *K*-edge, before repeating scans at the iron *L*-edges to reveal the iron content of the sample area. By overlaying these two scans, the authors created a colour composite that allowed the position of iron deposits (magnetosomes) within the bacterium to be identified (Figure 1.16). Iron $L_{2,3}$-edge x-ray magnetic circular dichroism probing of the magnetosomes (30 nm in size) showed these structures to possess oxidative and magnetic properties consistent with the crystalline iron-oxide magnetite (Figure 1.17) [142]. Hence STXM was used to assess both the biological content of a given sample, whilst also providing detailed information regarding the oxidative and magnetic properties of any metals present, to a 30 nm spatial resolution.

In addition to iron absorption spectra, STXM can be utilized to generate carbon *K*-edge spectra from the peptides of a biological structure. Following the extensive characterisation of x-ray absorption features generated from amino acid bases and peptide bonds, it is also possible to create theoretical carbon x-ray absorption spectra for a given peptide sequence (an example calculated spectra for Aβ(1-42) is shown in Figure 1.18) [143]. These theoretical spectra can be used as a reference to aid in the identification of protein based substances in a given sample (e.g. confirming the presence of Aβ in AD plaque material). Thus STXM provides a potential means to probe not only the oxidation state of AD-associated iron at a nanometer resolution, but also the localization of iron with regards to pathological AD structures.

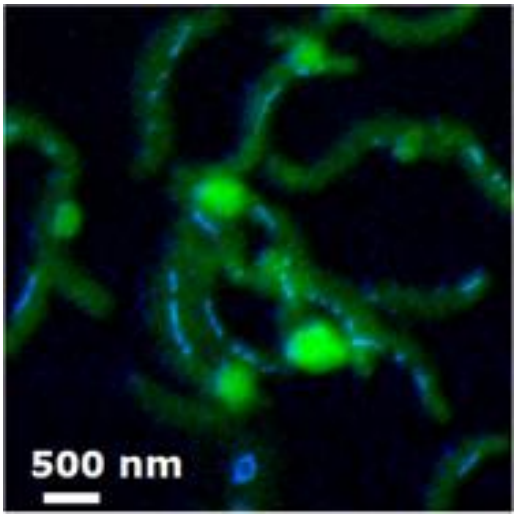

Figure 1.16. STXM composite image showing the organic (green) and iron (blue) content of MV-1 magnetotactic bacterium (from Lam *et al.* [142])

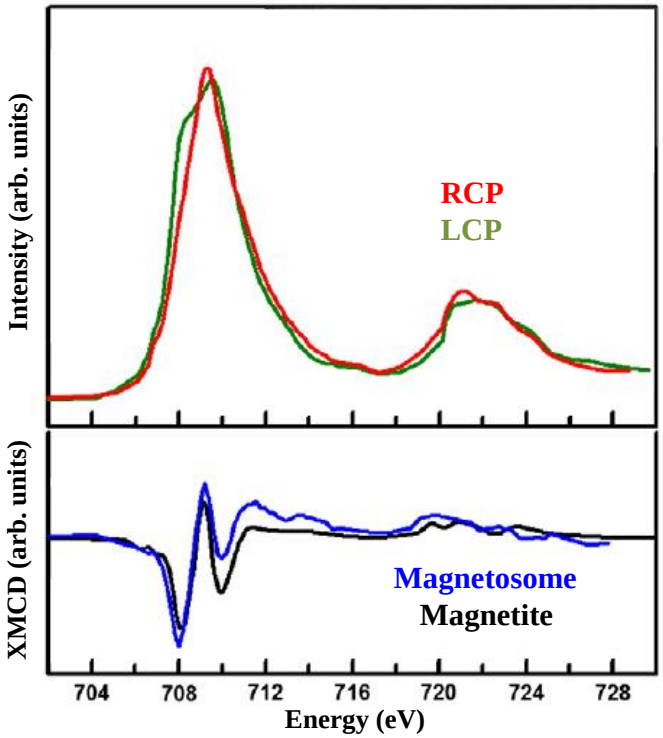

Figure 1.17. (Upper) Average XAS spectra from 9 magnetosomes located within MV-1 bacterium when illuminated with right circularly polarized (RCP) and left circularly polarized (LCP) x-rays. (Bottom) Comparison of the resulting magnetosome XMCD (blue) compared to a magnetite reference (black). (Figure modified from Lam *et al.* [142])

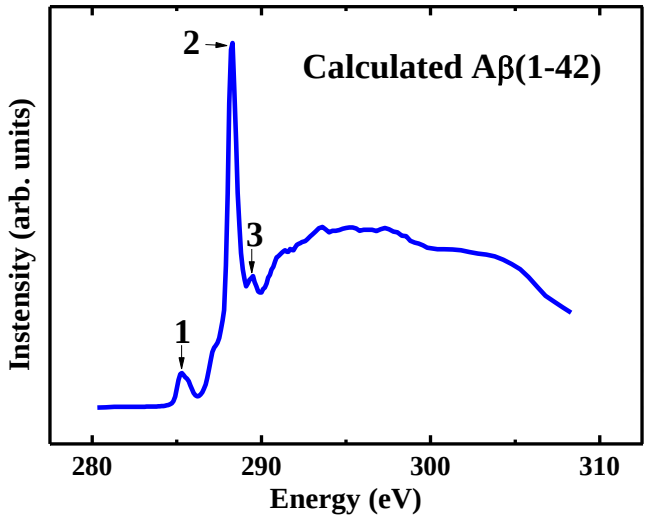

Figure 1.18. Calculated carbon *K*-edge absorption spectra for the amino acid sequence of Aβ(1-42). Absorption features labelled 1, 2 and 3 correspond to contributions from aromatic amino acid, the π* amide peak and arginine respectively. Calculations were performed following the methods described in Steward-Ornstein *et al.* [143].

Utilizing this technique to investigate the role of iron in AD may act to address current discrepancies in knowledge including (but not limited to): Aβ/iron binding, mechanisms behind iron accumulation in areas of AD pathology, and the origins of redox-active biominerals found in AD tissue. Therefore STXM may prove to be an invaluable tool in the understanding of AD pathology.

1.5 Summary

From the available scientific literature, it appears that the accumulation of brain iron and formation of redox-active iron biominerals is inherently linked to the development of AD pathology; including SPs comprised of Aβ. However how these redox-active minerals are formed, and their exact contribution to the process of AD pathogenesis remains elusive. To date, therapeutic measures intended to lower brain iron burdens in AD patients have provided encouraging results, with multiple studies showing a retardation of disease progression following drug administration [12,144-150]. These studies suggest that excess brain levels may directly contribute to the progression of AD, and therefore represent a target for preventative medicine. However due to poor drug specificity, detrimental side-effects following administration of these therapeutic agents have also been reported owing to disruptions in natural iron functions [146].

It is therefore imperative to distinguish "pathological" iron phases (i.e. iron species associated with the development of AD), from natural iron stores. By doing so, therapeutic treatments can be developed that specifically target toxic iron forms, whilst maintaining healthy brain functions. Furthermore by understanding the origins of redox-active iron phases, it may be possible to prevent their formation, further decreasing iron-associated toxicity in AD subjects. Finally it may be possible to utilize "pathological" iron as a bioinorganic marker for early-stage AD, long before the development of traditional clinical symptoms of the disorder.

1.6. Thesis aims and objectives

The overall aim of this thesis is to explore the origins and nature of redox-active iron biominerals associated with AD, in an attempt to further our understanding as to how iron contributes to the pathogenesis of AD. Investigations focus around the ability of Aβ to convert naturally occurring non-toxic ferric precursors, into potentially toxic redox-active iron phases, akin to those observed in AD tissues. Through the use of state-of-the-art synchrotron-based techniques, three key objectives are achieved as follows:

- The detailed chemical characterization of ferric iron materials following interaction with Aβ
- Examination of iron and Aβ co-localization to a nanometer scale
- The characterization of iron deposits associated with regions of AD pathology in transgenic AD tissues

It is hoped that the findings from these studies will contribute to the development of technologies intended to detect and prevent (inhibit) the progression of AD.

Chapter 2

Materials and methods

2.1 X-ray absorption spectroscopy (XAS) and x-ray magnetic circular dichroism (XMCD)

In order to determine the oxidative and magnetic state of the iron forms used in this thesis, x-ray absorption spectroscopy (XAS) and x-ray magnetic circular dichroism (XMCD) were performed at the iron *L*-edge. These techniques, introduced in *Section 1.4.1* were employed to characterize the oxidation state and magnetic properties of starting iron materials, and to monitor any changes to these iron phases once incubated in the presence of Aβ. Measurements were performed on beamline I10 at Diamond Light Source (Oxfordshire, UK), and beamline 4.0.2 at the Advanced Light Source (Berkeley Laboratory, USA)

2.1.1 Equipment development for XAS/XMCD examination

XAS and XMCD are techniques that are performed under a high vacuum, and direct imaging of samples to identify regions of interest (ROI) once under vacuum was not possible. Due to the inhomogeneous distribution of Aβ/iron materials examined in this thesis, efficiently identifying sample position and regions of iron accumulation was of paramount importance. To aid in sample location, aluminium probes (70 x 12 x 2 mm) were produced containing 2 mm diameter holes at 14 pre-determined co-ordinates (Figure 2.1a). The advantages of this probe were two fold. First, these holes gave a fixed position for sample mounting, allowing ROI to be readily located. Secondly these holes allow the position and dimensions of the aluminium probe to be defined (with regards to the computational software used to control the x-ray beam); whilst also aiding in the alignment of the aluminium probe which was required to be perpendicular to the incoming x-ray beam. For the probes to be utilized to their full advantage, additional detectors were

utilized to record transmitted x-rays (i.e. photons that pass through the holes in the aluminium probe), in addition to the sample drain current.

To further aid in sample preparation and location, copper plates were manufactured (8 x 12 x 2 mm), containing two, 2 mm diameter holes spaced 5mm apart, each located within a 4mm (diameter) recessed area (Figure 2.1b). The recessed areas of these grids acted as a point for copper TEM grids (3 mm diameter, carbon/formvar coated; 200 mesh) to be attached (Figure 2.1c), onto which sample solutions were deposited. By attaching TEM grids to the larger copper plates, the efficiency of sample preparation was significantly improved. In particular, TEM grids did not need to be directly handled when depositing sample solutions, a great advantage when working within a glove chamber (see *Section 2.1.2; Figure 2.4*), where dexterity is compromised.

The holes of the copper plates were aligned to the holes in the aluminium probe (Figure 2.1d), allowing transmission XAS/XMCD to be conducted (Figure 2.1e), further aiding in sample location. A maximum of seven copper plates (each containing two holes/ sample positions) could be mounted on a probe at a single time. By attaching TEM grids to copper plates rather than directly onto the aluminium probes, the samples mounted onto aluminium probes were easily interchangeable. This allowed a great level of flexibility with regards to sample selection, and enabled sample probes to be mounted quickly and efficiently. The ability to quickly mount/modify the samples on sample probes was of vital importance, as XAS/XMCD experiments were often time limited. The bottom two holes of the aluminium probe were often left free (Figure 2.1d) to aid in x-ray beam alignment.

To allow anoxic transportation of the aluminium probes (containing oxygen sensitive samples) to the XAS/XMCD beamline, Perspex O-ring sealed containers were produced, with a 14 mm diameter opening allowing the sample probe to be inserted (Figure 2.2).

These containers were filled with nitrogen (N_2) prior to sample probe insertion, within a N_2 filled glove chamber.

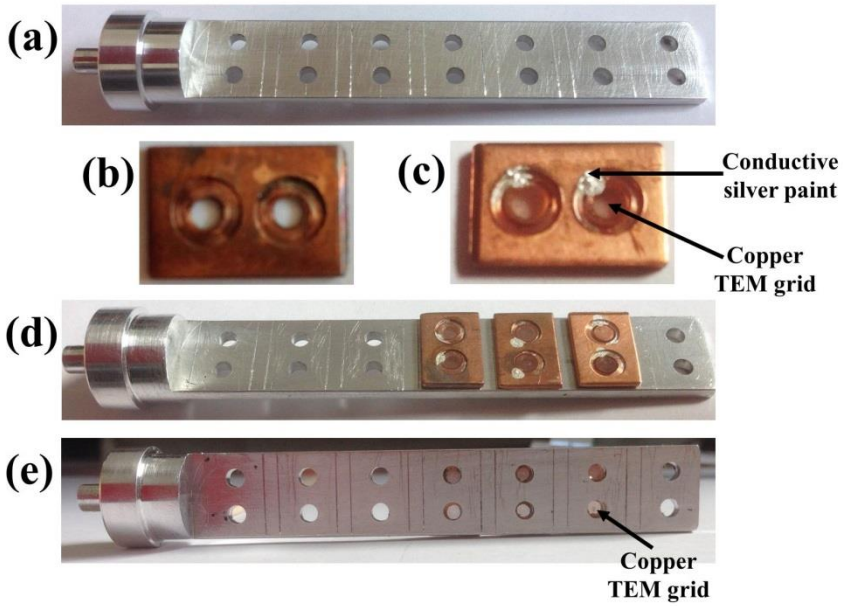

Figure 2.1. Aluminium probes and copper plates used in XAS/XMCD experiments. **(a)** Aluminium probe prior to sample loading. **(b)** Copper plates to which TEM grids were attached, as shown in **(c)**. **(d)** Aluminium probe loaded with 3 copper plates. **(e)** The underside of the loaded aluminium probe shown in (d), demonstrating the alignment of the 2 mm holes in the probe and copper grids, allowing x-ray transmission.

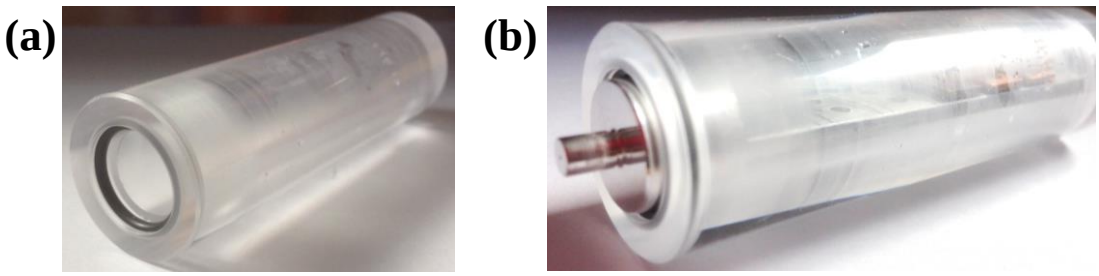

Figure 2.2. (a) O-ring sealed Perspex container used for the transportation of aluminium sample probes under anoxic conditions. **(b)** Aluminium probe inserted within the container shown in (a).

Finally, to concentrate any magnetic material that was present in sample solutions (therefore allowing easy location) a magnet array was created (Figure 2.3). This magnet was built with a recessed area matching the dimensions of the copper plates used for sample mounting (Figure 2.3b). Pin magnets were located under each of the two holes of the copper plate, creating a magnetic focal point at the centre of the each hole (Figure 2.3a). Upon sample deposition all magnetic material is drawn to this central point (Figure 2.3c). Thus once mounted on the aluminium probe, the exact location of any magnetic materials was known, prior to XAS/XMCD examination.

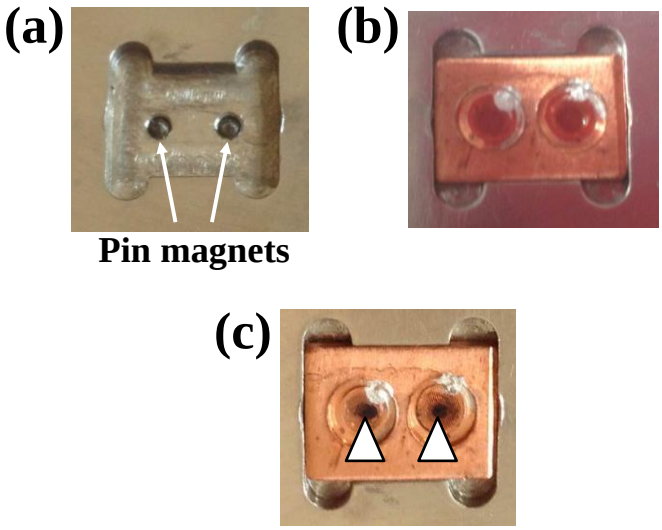

Figure 2.3. Magnet array used during sample preparation for XAS/XMCD experiments. **(a)** Unloaded magnet array, showing the location of the two pin magnets (arrows), located within the central recessed area. **(b)** Magnet array loaded with a copper plate containing two TEM grids, positioned directly above the pin magnets. **(c)** Example of the magnetic iron accumulation induced by the magnet array (white arrows), following the deposition of magnetite nanoparticles onto the TEM grids.

2.1.2 XAS/XMCD sample preparation

All sample preparation, transportation and examination was conducted under strictly anoxic conditions as to prevent any changes in iron oxidation state prior to XAS and XMCD examination. Such methodology has previously been successfully employed by Coker *et al.* (2009), where the technique was shown to prevent the surface oxidation of magnetite nanoparticles [151].

Copper TEM girds (carbon/formvar coated; 200 mesh) were attached to copper plates with conductive silver paint (Figure 2.1c), and placed within the magnetic array as described above (Figure 2.3b). Small sample volumes (15 µL) were then deposited onto the TEM grids, and excess liquid removed using filter paper, to prevent any artefacts that may occur due to the drying of the sample solution (such as salt crystal formation). Sampling was performed at Keele University, within a N_2 filled glove chamber as pictured in Figure 2.4. Once sample deposition was complete, copper plates were stored individually within plastic boxes, thus preventing sample cross-contamination. Whilst still within a N_2 filled glove chamber, plastic boxes (containing copper plates) were transferred into a N_2 filled, O-ring sealed container, for sample transportation to the synchrotron-light source (Figure 2.5).

Once at the synchrotron beamline, sample-loaded copper plates were mounted onto the aluminium probes with conductive carbon tape, within a N_2 filled glove chamber (Figure 2.1d). Conductive materials were used throughout, allowing an electron drain current to be established, enabling the detection of x-ray absorption events. Once mounted with samples, aluminium probes were inserted into N_2 filled Perspex containers, prior to their removal from the glove chamber. Aluminium probes were then attached to a larger XAS/XMCD probe (from which a drain current could be recorded), before being transported to the

synchrotron beamline chamber. Beamline chambers were backfilled with N_2 preventing iron oxidation once the probes had been inserted. Sample materials were exposed to oxygen for a maximum of one second whilst being lowered into the beamline chamber. An overview of the beamline chamber used in the XAS/XMCD experiments conducted at Diamond light Source is shown in Figure 2.6**.**

Figure 2.4. Nitrogen filled glove chamber used throughout the sampling process for XAS/XMCD and STXM experiments.

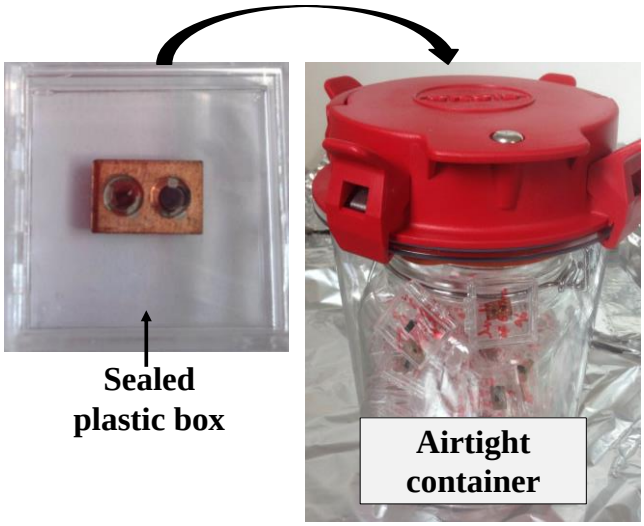

Figure 2.5. Methodology used for the storage and transport of XAS/XMCD samples. Individual copper plates containing TEM grids with deposited sample materials were stored within sealed plastic boxes. These plastic boxes were then transferred into an O-ring sealed airtight container. This process was conducted within a nitrogen filled glove chamber as shown in Figure 2.4.

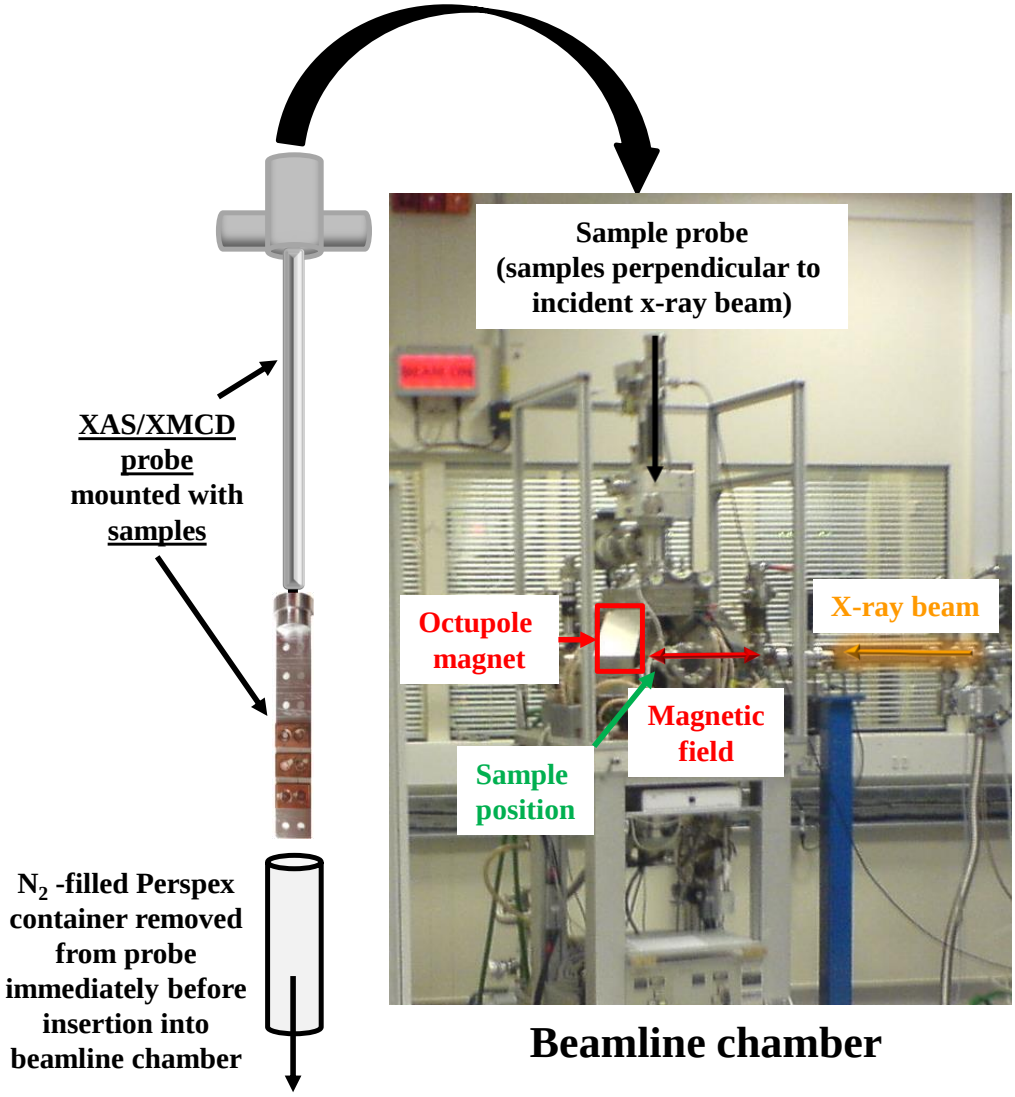

Figure 2.6. Illustration of the XAS/XMCD sample probe (left), and photograph of the octupole electromagnetic beamline chamber (right) used in XAS/XMCD experiments. Incident beam direction (orange), octupole magnet position and magnetic field direction (red), and sample position (green) are labelled on the beamline chamber. Beamline chamber is located at Diamond Light Source (Oxfordshire, UK).

2.1.3 Sample mapping and x-ray absorption spectra generation

After insertion of the sample probe into the beamline chamber, the position of the aluminium probe was determined, and the co-ordinates of the sample grids were defined. To visualize the iron content of the sample area under XAS/XMCD examination, two

dimensional maps revealing areas of iron accumulation were created. This was achieved by performing sample area scans just below (706 eV) and on the iron L_3 peak energies (710.5 eV) at a spatial resolution of 100 µm. Off peak x-ray absorption values were then subtracted from the equivalent peak iron x-ray absorption values, resulting in the removal of background absorption signals and highlighting areas of iron accumulation (Figure 2.7).

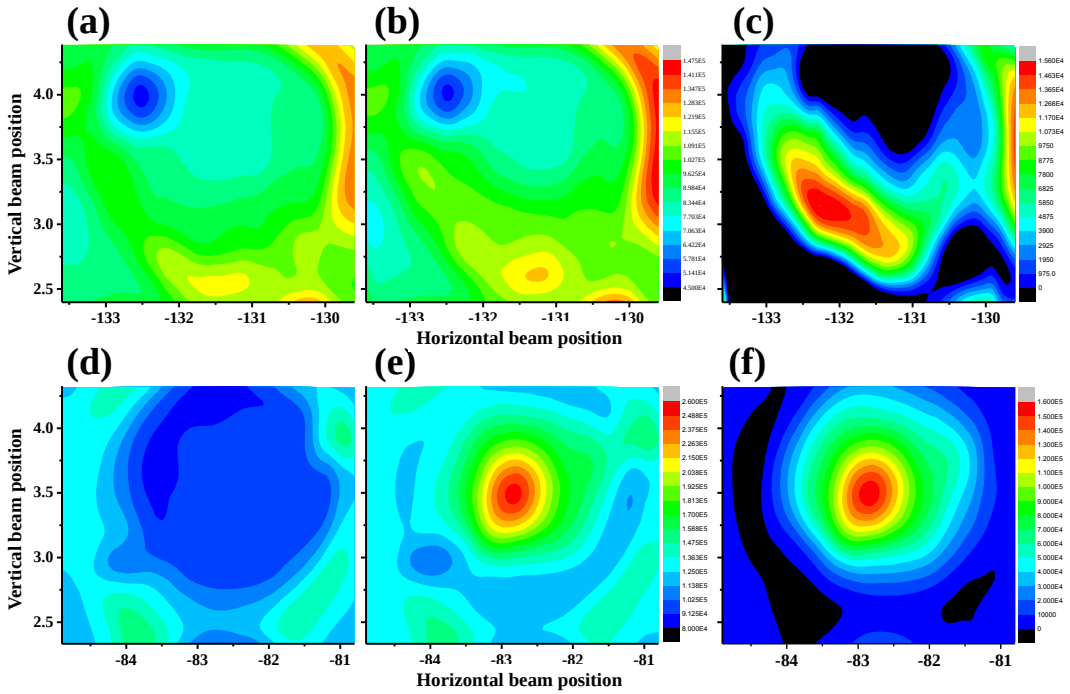

Figure 2.7. Typical x-ray absorption maps of sample grids containing (a-c) iron(III) and (d-f) magnetite. **(a)** And **(d)** off iron L_3 peak images (706 eV). **(b)** And **(e)** on-peak L_3 iron images (710.5 eV). **(c)** And **(f)** difference maps showing distribution of iron. Note the central dense accumulation of iron in (f) induced by the magnetic focal point produced by the magnetic array shown in Figure 2.3. Iron x-ray absorbance values are shown to the right of the images.

The x-ray beam position was then moved to areas of iron accumulation and swift, low (energy) resolution x-ray absorption scans were performed across the iron L_3-edge (700-716 eV; see Figure 2.8a). These preliminary scans provided an indication as to the oxidation state of the iron (Fe^{2+}, Fe^{3+} etc.) along with the strength of the iron signal (false positive readings were often displayed when producing iron maps from highly conductive

areas such as silver paint) whilst minimizing exposure time of iron to the x-ray beam. More detailed energy scans were then performed over the entire iron *L*-edge (700 – 740 eV; Figure 2.8b) to provide detailed information regarding iron oxidation state. Maximum energy resolution was typically 0.1 eV. XAS spectra were recorded using the TEY method (see *Section 1.4.1*).

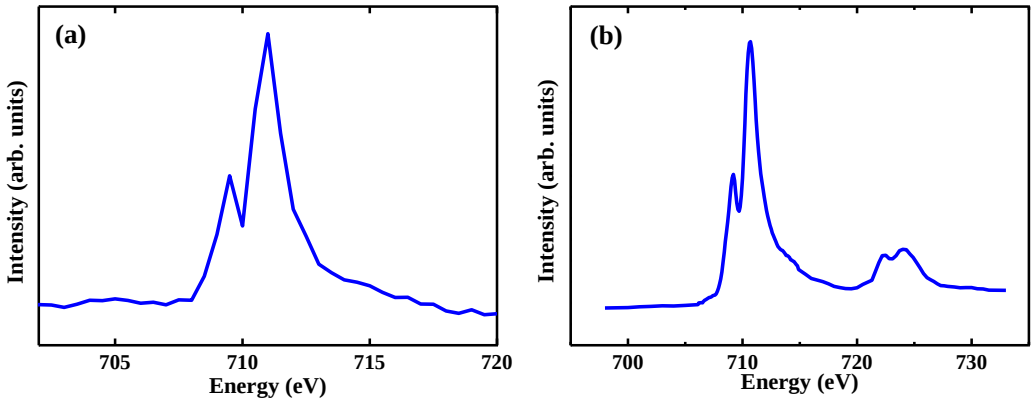

Figure 2.8. Example iron(III) *L*-edge XAS spectra at **(a)** low energy resolution, and **(b)** high energy resolution.

2.1.4 Recording XMCD spectra

XMCD spectra were obtained by recording two x-ray absorption spectra across the iron *L*-edge (as described above) with opposed 0.6 T magnetic fields orientated along the x-ray beam direction, induced by the octupole electromagnet beamline chamber (see Figure 2.6). The magnetic field was reversed at each photon energy point in the scan, to minimize x-ray beam drift effects between the two spectra. Differences (dichroism) between these two absorption spectra create XMCD spectra (Figure 2.9) allowing the magnetic properties of an iron-based material to be elucidated.

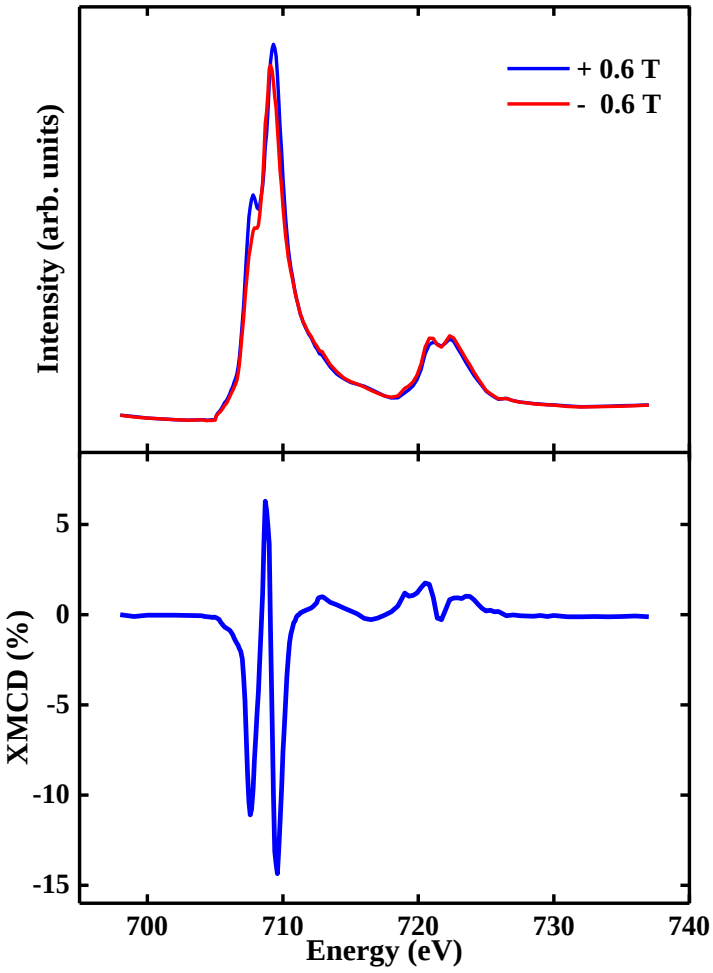

Figure 2.9. Example iron $L_{2,3}$-edge XAS spectra for maghemite, obtained in opposing 0.6 T magnetic fields (top). The differences between these spectra result in XMCD spectra (bottom).

2.1.5 Data reduction

X-ray absorption levels from sample materials were normalized to the incident beam intensity (recorded by thin *non*-iron-based foils) to remove background absorbance levels that were not attributable to the sample itself (thereby reducing the "noise" in x-ray the absorption spectra). Off resonance background absorbance levels were then subtracted. For XMCD spectra, x-ray absorption spectra obtained in opposing magnetic fields were scaled

to unity at the L_3 peak feature, and resonance background absorbance levels were subtracted. Data was averaged where applicable. Further smoothing of "noisy" x-ray absorption spectra was performed at the off-resonance energy regions, using a 3-5 point sliding window to improve spectra quality. No smoothing was performed over the peak iron *L*-edge features.

2.2 Scanning transmission x-ray microscopy (STXM)

As described in *Section 1.4.2*, scanning transmission x-ray microscopy (STXM) is a synchrotron-based microspectroscopy technique that provides element-specific images and x-ray absorbance information of a given sample to a spatial resolution of approximately 30 nm. In this thesis STXM was employed to examine the interaction between Aβ and various forms of iron *in vitro,* and also to investigate iron deposits within transgenic AD mice brain tissue *in situ.* By using this technique it is possible to attain images demonstrating the correlation between Aβ structures and areas of iron deposition, whilst also providing x-ray absorption data regarding the peptide structure of Aβ and the oxidation state of iron deposits. STXM was performed on the PolLux beamline at the Swiss Light Source (Villigen, Switzerland), and the Soft X-ray Spectromicroscopy beamline at the Canadian Light Source (Saskatoon, Canada).

2.2.1 Sample preparation

Small volumes (15 µL) of sample solutions were deposited onto silicon nitride (Si_3N_4) membranes (Figure 2.10; DuneSciences, 75 nm membrane thickness) by the use of a micropipette. Membranes were comprised of multiple 100 μm^2 Si_3N_4 windows etched from a silicon wafer base, with a hydrophilic coating encouraging the deposition of sample

material to the membrane surface. The use of Si_3N_4 membranes was preferential to that of carbon/formvar coated copper TEM grids (used elsewhere in this thesis), as their composition does not interfere with the generation of carbon images and carbon *K*-edge x-ray absorbance spectra. As STXM is a largely non-destructive imaging technique, complementary electron microscopy examination of these membranes was achievable following STXM analysis.

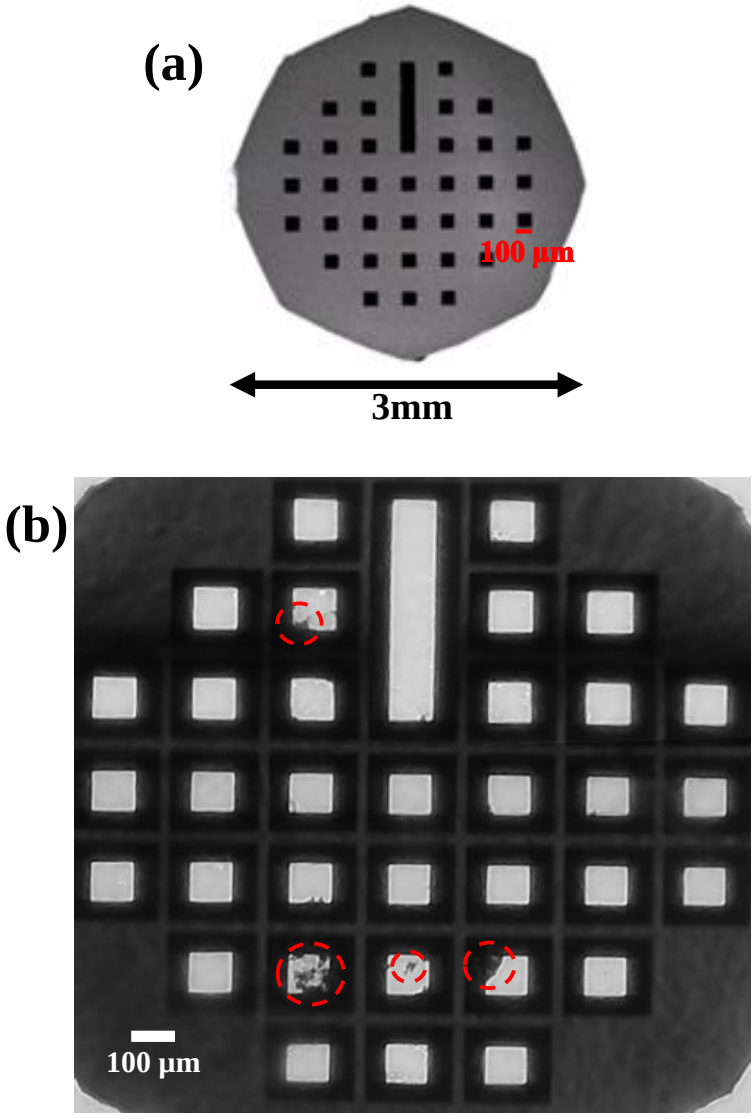

Figure 2.10. Silicon nitride membranes used for STXM studies. **(a)** Overview of the membrane structure, comprised of multiple 100µm^2 windows. **(b)** Optical microscopy image showing regions of dense aggregate deposition (regions of interest), highlighted by red dashed circles.

Si_3N_4 membranes were mounted onto stainless steel microspectroscopy plates for STXM examination (Figure 2.11) Examination of the sample membranes under optical microscopy was conducted prior to loading in the STXM chamber to identify ROI for STXM investigation (Figure 2.10b). Microscopy plates were then inserted into the STXM beamline chamber as shown in (Figure 2.11). For the STXM experiments described in *Chapter 5*, (and also for the Aβ structure shown in *Figure 3.9*) attempts were made to perform sample preparation and examination under anoxic conditions as to prevent changes in iron oxidation state. Sample deposition was conducted within a nitrogen filled glove bag as shown in Figure 2.4. Si_3N_4 membranes were kept under nitrogen within an O-ring sealed glass jar throughout transportation to the STXM beamline. Loading of the membranes onto spectromicroscopy plates, and preliminary optical microscopy were again conducted under anoxic conditions; and the STXM chamber was backfilled with nitrogen prior to sample transfer. However unlike the approaches outlined in *Section 2.1.2* these techniques have not been confirmed to strictly maintain anoxic environments.

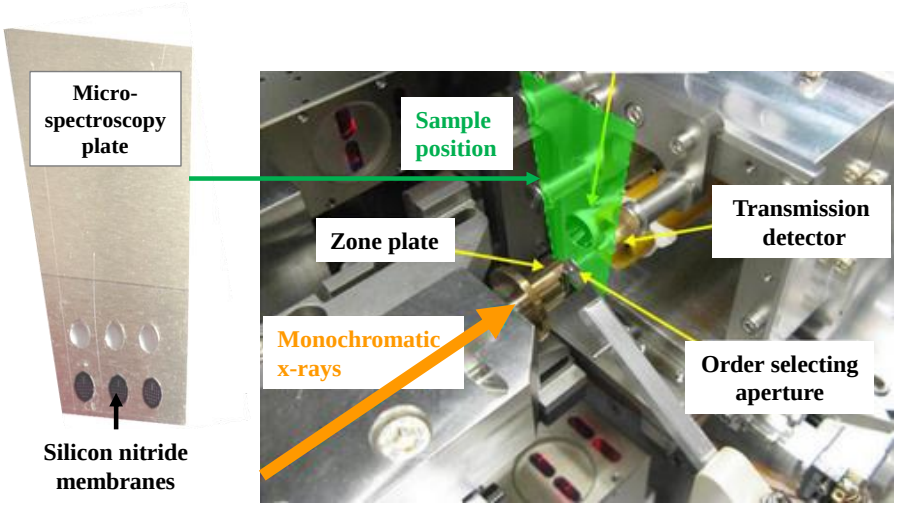

Figure 2.11. Schematic showing the loading of silicon nitride membranes onto stainless steel microspectroscopy plates (left), and the insertion of sample plates into the STXM beamline chamber (right; green region). X-ray beam direction, (orange), and STXM focussing/ detection equipment are labelled on the STXM beamline chamber. Photograph is of the PolLux beamline chamber at the Swiss Light Source. See also the STXM schematic in *Section 1.4.2 (Figure 1.15).*

2.2.2 Carbon and iron imaging and spectroscopy

Carbon *K*-edge (280-320 eV) mapping was conducted on the Si_3N_4 membranes to assess the biological content of the sample area. Coarse large scale (typically 2 mm^2) scans were conducted at 380 eV to gain an overview of the sample membrane, enabling the location of ROI as previously identified through optical microscopy (Figure 2.12a). These preliminary scans were conducted at energies above the carbon *K*-edge to provide higher levels of photon transmission, therefore aiding in the imaging process where the x-ray beam is not fully focussed onto the sample area (x-ray intensity is lost when at carbon absorption energies, due to the carbon content of the beamline optics).

More (spatially) detailed images of individual 100 μm^2 Si_3N_4 windows were then obtained revealing ROI (Figure 2.12b). Maps displaying the carbon content of these ROI were created by conducting scans at the peak carbon *K*-edge energy (288 eV) and off peak energy (286 eV), with differences between these absorbance values indicating areas of carbon (biological) material (Figure 2.12c). Carbon maps were conducted to a spatial resolution typically ranging between 30 – 60 nm and therefore enabled the location of Aβ aggregates whilst also providing detailed images revealing aggregate structure. By subtracting off resonance carbon *K*-edge absorption values from peak on resonance values, absorption artefacts (caused by, for example, salt crystal formation) are removed, providing artefact-free carbon images. This process is shown in Figure 2.13**,** where bright spots (formed through salt formation following the drying of KH buffer) can be seen in the off resonance (Figure 2.13a) and on resonance (Figure 2.13b) images taken at 286 eV and 288.5 eV respectively. By subtracting the absorption values taken at 286 eV from those taken at 288.5 eV, these spotted artefacts are removed (Figure 2.13c), resulting in an artefact free carbon image.

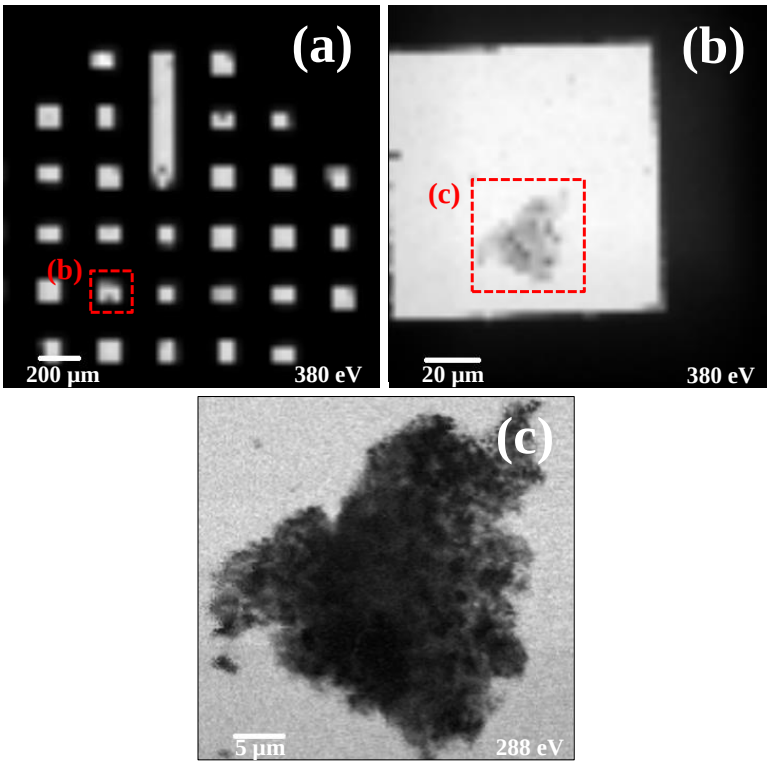

Figure 2.12. Identifying regions of interest in STXM experiments. **(a)** Course scan taken at an intermediate energy (380 eV), providing an overview of the sample membrane, **(b)** Scan of an individual 100 µm^2 membrane window, containing a large aggregate structure. **(c)** Carbon *K*-edge image (288 eV), of the dense carbon structure identified in (b).

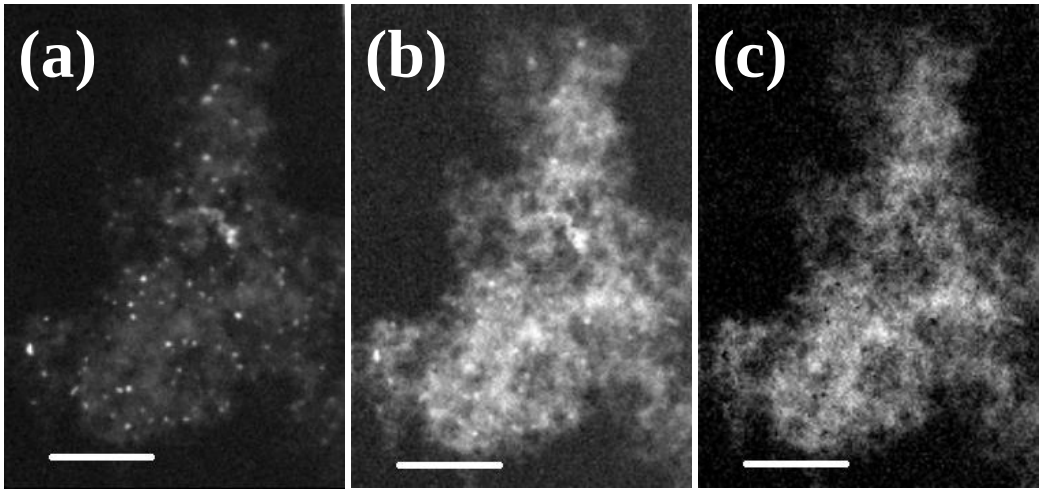

Figure 2.13. Example of the carbon mapping process. **(a)** Image taken at 286 eV showing absorption artefacts (bright spots). **(b)** Image taken at 288.5 eV showing carbon content and the artefacts shown in (a). **(c)** Carbon map created by subtracting image (a) from (b), providing carbon content without absorption artefacts. Scale bars = 5 µm.

X-ray absorption spectra for carbon regions were generated by taking images at multiple energies over the carbon *K*-edge to an energy resolution of 0.1 eV (Figure 2.14). These so called carbon "stacks" were typically conducted at a lower spatial resolution (around 100 nm) than the previously described carbon maps due to time limitations. This method of microspectroscopy allows x-ray absorption spectra to be generated from each pixel of a stack image, enabling carbon spectra for a highly specific region (e.g. a carbon area with a high iron content) to be created. Spatially dependent x-ray absorption data is of vital importance whilst examining inhomogeneous sample materials comprised of localised structures in the nanometer-micrometer size range.

Iron L_3-edge maps revealing the iron content were created in a similar manner as described above, by raster scanning across the sample area at the peak iron L_3 energy (709.5 eV) and off peak energy (705 eV) with differences in these scans displaying the location of iron deposits, whilst providing artefact-free iron images (Figure 2.15). Iron x-ray absorption spectra were created by conducting scans over at multiple energies over the iron *L*-edge. Again, due to the high level of spatial resolution of STXM, individual sub-micron iron aggregates can be examined. As the absorbance energies of iron are higher than those of carbon, STXM carbon analysis of Aβ structures was conducted prior to analysis of the iron content, in order to prevent any damage to carbon structure.

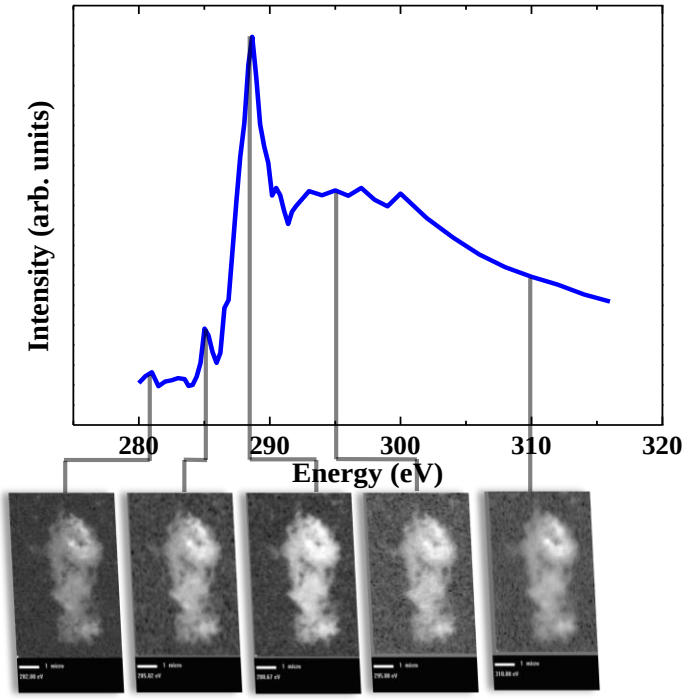

Figure 2.14. Carbon STXM spectra, created from carbon stacks performed over the carbon *K*-edge. Each energy point in the spectra corresponds to the absorption levels recorded in the STXM image taken at that energy (as shown below the spectra).

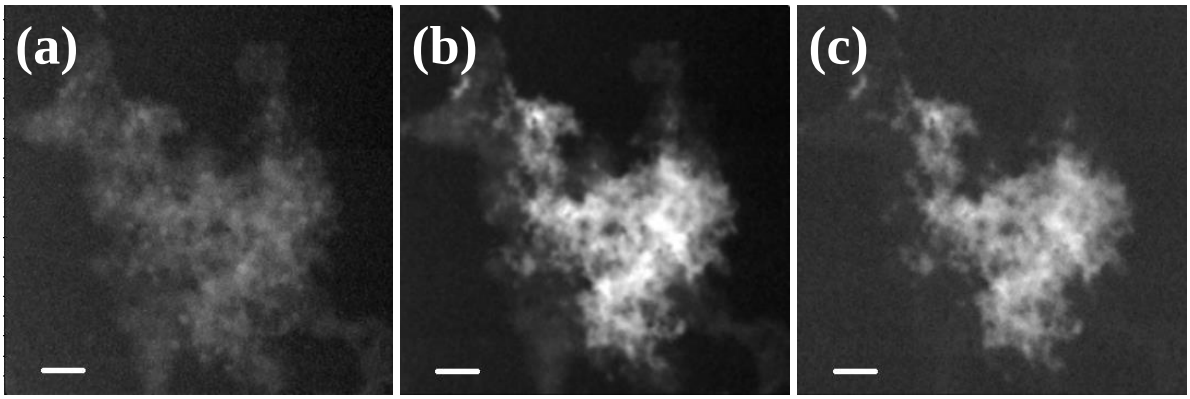

Figure 2.15. Example of the iron mapping process. **(a)** Image taken at 705 eV. **(b)** Image taken at 709.5 eV. **(c)** Artefact-free iron map created by subtracting image (a) from (b). Scale bar = 1 µm.

2.2.3 Data reduction

STXM data was analysed using AXIS (Analysis of X-ray Images and Spectra) 2000 imaging software, a programme specialized for the processing of STXM data (online resource [152]). To obtain quantitative carbon and iron images, transmitted x-rays were converted to optical density (OD), thereby removing background absorption noise attributable to the synchrotron beamline. The conversion of a transmitted signal to optical density is achieved according to:

$$OD = \ln (I_0/I) \quad \textbf{(7)}$$

Where I_0 is the incident x-ray beam flux, and I is the x-ray beam flux transmitted through the sample.

OD is in turn related to the sample properties by the following:

$$OD = \mu(E).\rho.t \quad \textbf{(8)}$$

Where $\mu(E)$ is the mass absorption coefficient for a given energy (E), ρ is sample density and t is the thickness of the sample.

To determine $I_{0,}$ absorption levels were recorded from regions of blank silicon nitride membrane, adjacent to carbon/iron regions of interest (Figure 2.16a). These absorption values were then used to convert those obtained from carbon/iron structures (Figure 2.16b) into OD (Figure 2.16c), according to equation 7.

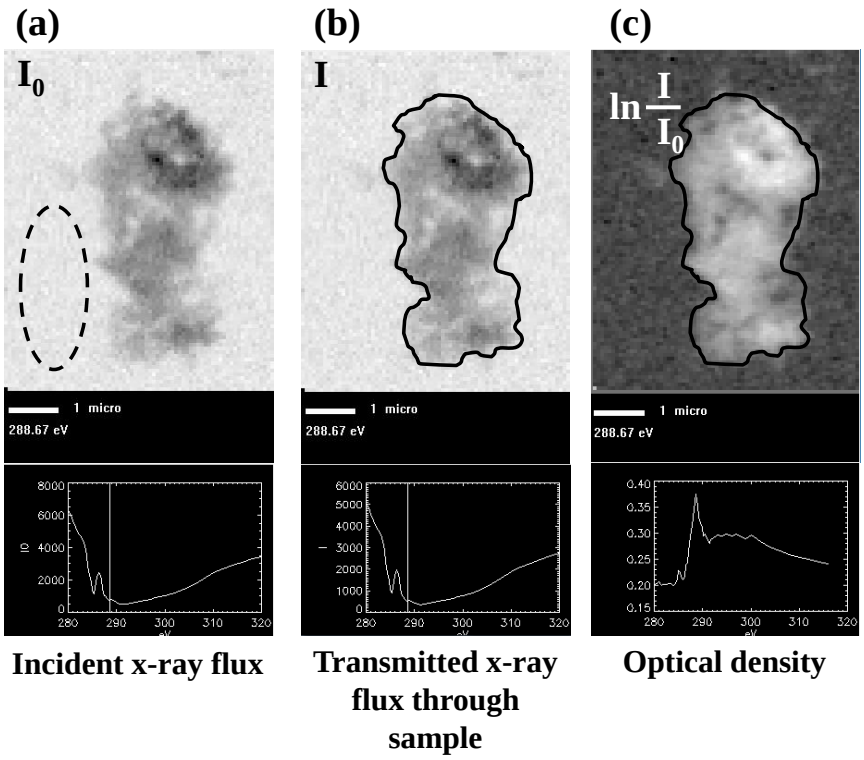

Figure 2.16. Converting STXM images to optical density. (**a)**The incident x-ray flux (I_0) is measured by recording transmitted x-ray levels through a blank region of silicon nitride membrane (highlighted by dashed region; top), providing an absorption spectrum for the incident x-ray beam (bottom). **(b)** Transmitted x-ray levels are recorded through the sample material (I; top) providing a spectrum for the sample (bottom). **(c)** The transmitted x-ray signal in (b) is converted to optical density according to equation 7, providing quantitative x-ray absorption spectra (bottom) for the sample material. This process was conducted for stacks taken over the carbon *K*-edge, and iron *L*-edge.

Where multiple images were taken at different energies (e.g carbon/iron stacks), images were aligned to a common feature, thereby compensating for any x-ray beam drift that may have occurred during scanning (scans can take anywhere up to 2 hours dependent upon the scan area). STXM-x-ray absorbance spectra were created by selecting areas (pixels) of interest from aligned stack images obtained over the carbon *K*-edge or iron *L*-edge.

Calculated carbon *K*-edge spectra for the amino acid sequence of Aβ (*see Section 1.4.2; Figure 1.18*), were created using AXIS 2000 software, through the "calculate peptide

spectra" function [143,152] This feature utilizes a database containing the carbon *K*-edge x-ray absorbance spectra of all known amino acids, to generate calculated carbon *K*-edge absorption spectra for a desired amino acid sequence. The effect of the peptide bonds upon these calculated spectra is also addressed by this function. This feature was developed from methodology described by Stewart-Ornstein *et al.* [143].

2.3 Electron microscopy

To generate high resolution images, and to ascertain the crystal structures of the Aβ /iron structures examined in the thesis, transmission electron microscopy (TEM) was performed. TEM was conducted on a JEOL 1230 microscope system operating at 100 kV.

Small volumes (15 µL) of sample solutions/suspensions were deposited onto carbon/formvar coated TEM grids (Agar Scientific; 200 mesh), and excess liquid was removed using filter paper. Sample preparation and TEM examination were performed in aerobic conditions.

Both bright field images and electron diffraction patterns were obtained from Aβ /iron structures. During electron diffraction examination, a selected area aperture was utilized to obtain diffraction patterns from selected areas of interest. Electron diffraction images were created by exposing the transmitted electron beam onto photographic film. Films containing diffraction patterns were developed and subsequently scanned to provide diffraction patterns in a digital format. The *d*-spacing values and lattice parameters of diffraction patterns were compared to mineral references from the American mineralogist crystal structure database, and Joint Committee on Powder Diffraction Standards (JCPDS) files.

2.4 Ferrozine assay

In order to assess the iron(II) content of sample solutions throughout this thesis, Ferrozine iron(II) quantification assays were performed. First described by Stookey in 1970 [153], Ferrozine is a compound that selectively binds to iron(II) ions in solution, with this binding resulting in the formation of a stable magenta-coloured complex. The intensity of this colouring is positively correlated to the concentration of iron(II) ions present (Figure 2.17), thereby allowing the spectrophotometric determination of iron(II) content in solution.

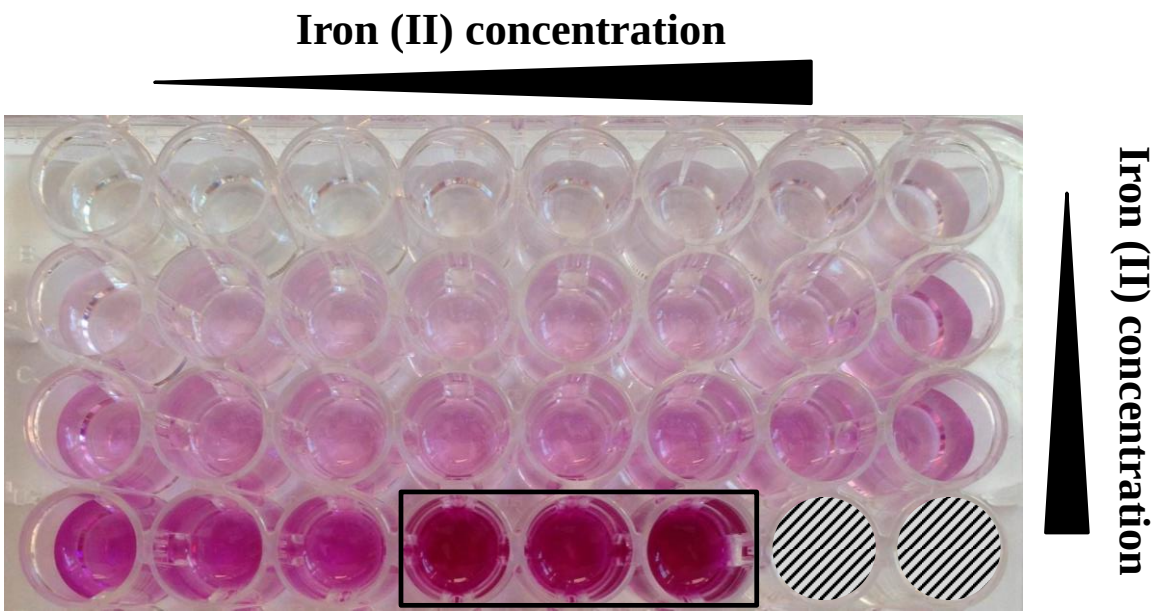

Figure 2.17. Example of the magenta coloured complexes formed following the addition of iron(II) to Ferrozine. Iron(II) concentration is increased from left to right (top to bottom 0-1 mM). Each iron concentration is presented in triplicate.

In addition to iron(II) content, this technique can be utilized to determine the total iron content of a given solution, through the addition of an iron reducing agent such as hydroxylamine hydrochloride. The addition of this reducing agent results in the reduction

of iron(III) ions to an iron(II) state, allowing Ferrozine to bind. Hence iron(II) content as a proportion of total iron content for a solution can be determined through Ferrozine assay.

2.4.1 Determination of iron(II) content

Crystalline iron-oxides such as magnetite do not bind effectively to Ferrozine, as their crystal structure can prevent their constituent iron atoms from forming complexes with the iron reagent (see *Section 2.4.4*). To counteract this, all sample suspensions/solutions were digested in hydrochloric acid prior to Ferrozine addition to destroy iron(oxide) crystal structure enabling Ferrozine binding. This digestion step also allowed the release of iron from any structure from which it is bound (e.g. Aβ), further facilitating Ferrozine binding. This process is described below.

50 µL of the sample solutions were removed and digested in 75 µL of 0.5 M hydrochloric acid (HCl) and 25 µL of deionized water (dH$_2$O). 50 µL of the digested iron solutions were then added to 785 µL of 2 mM Ferrozine™ solution (50 mM HEPES buffer) in a 48 well cell culture plate, and the absorbance read at 562 nm using a BioTek plate reader. A plate reader was used for absorbance readings as large numbers of samples can be measured simultaneously using this instrument.

2.4.2 Determination of total iron content

50 µL of sample solutions were removed and concurrently digested and reduced in 75 µL of 0.5 M HCl and 25 µL of 6.25 M hydroxylamine hydrochloride (NH_2OH•HCl). A concentrated reducing agent was employed to ensure complete iron reduction to an iron(II) state. 50 µL of the digested/reduced solutions were added to 785 µL of 2 mM Ferrozine solution. Absorbance was read at 562 nm.

Absorbance values were compared to those obtained from iron standards (see below), allowing the molarity of iron solutions to be calculated. Iron(II) concentration as a percentage of total iron content were determined from these resulting molarity values.

2.4.3 Preparation of iron standards

In order to determine the molarity of iron solutions used in this thesis, standard curves showing absorbance (at 562 nm) as a function of iron(II) concentration were created. Iron standard curves were prepared before each experiment to ensure values were correct for the time of examination. Iron solutions ranging in concentration from 0-1 mM were prepared from iron(II) ethylenediammonium sulfate tetrahydrate and iron(III) chloride, representing iron(II) and iron(III) standards respectively. These iron solutions were then digested and reduced as described above and absorbance was read at 562 nm. Typical examples of iron(II) and iron(III) standard curves are shown in Figure 2.18a and 2.18b respectively. A small, positive absorption offset can be seen at 0 M iron content, arising from background absorbance of 562 nm light by the solvents used in the Ferrozine assay. This background absorbance was constant throughout all Ferrozine measurements and was subtracted from absorption values obtained from iron solutions/suspensions.

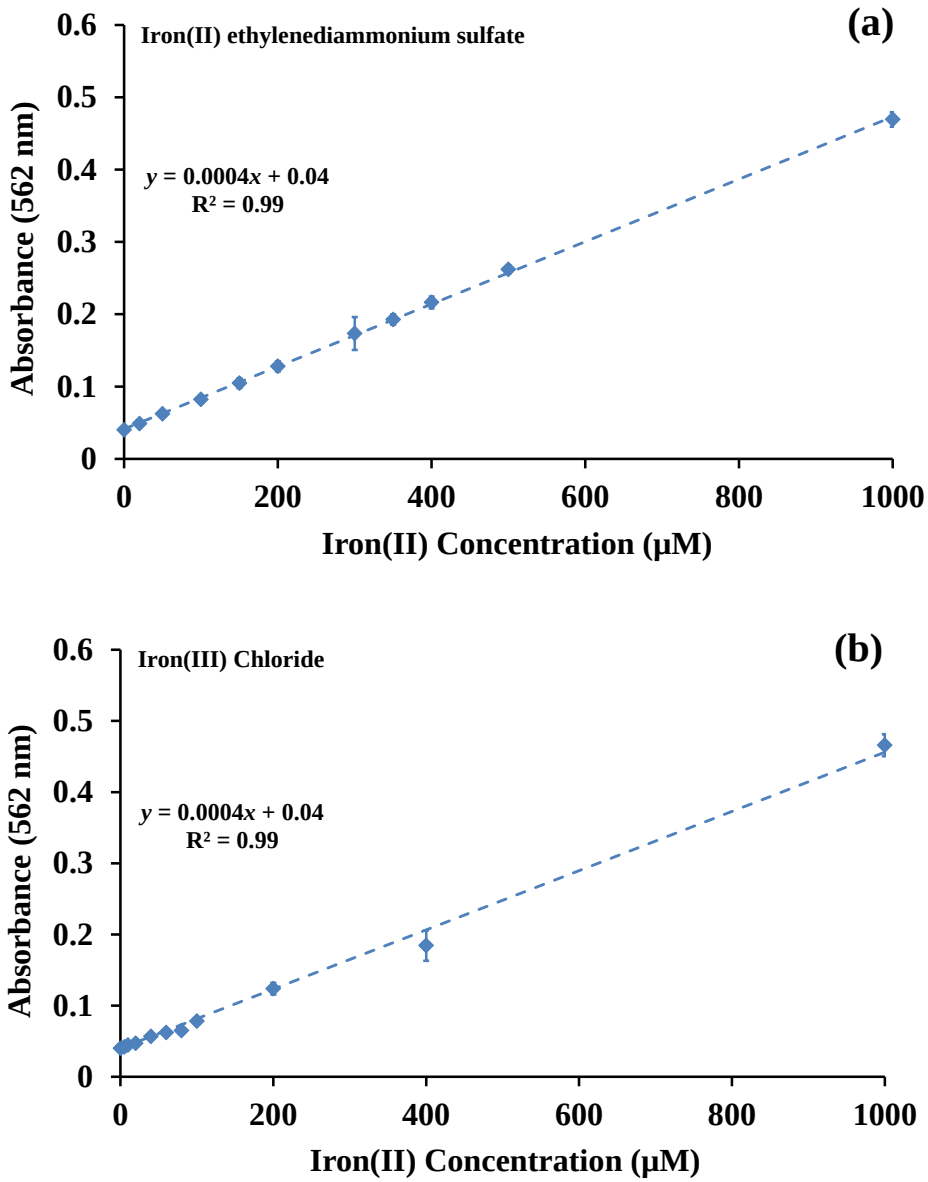

Figure 2.18. Example standard curves showing absorbance (562 nm) values with respect to iron(II) concentration for **(a)** reduced iron(II) ethylenediammonium sulfate tetrahydrate and **(b)** reduced iron(III) chloride standards. Gradients and R^2 values are provided for each curve. Blue dashed lines show the linear trend of the curves. Error bars show standard deviation (n=3).

2.4.4 Variation in acid digestion times

As is demonstrated in Figure 2.19a, when crystalline iron phases such as 6-line ferrihydrite and magnetite (and to a lesser extent 2-line ferrihydrite) are added to Ferrozine (following incubation with an iron reducing agent), only a limited amount of Ferrozine binding is achieved, with respect to their total iron content. Therefore for the iron(II) quantification assays used in this thesis, a 0.5 M HCl acid treatment was employed to allow the complete binding of Ferrozine to the iron content of these minerals.

Depending upon the iron phase used, and the crystallinity of said phase, varying periods of HCl digestion are required to enable efficient Ferrozine binding. As a general rule, the more crystalline an iron phase, the longer (time period) acid digestion will take. It was found that amorphous iron forms such as iron(III) chloride are capable of binding to Ferrozine without the need for acid digestion (as shown in Figure 2.19a; black). Efficient Ferrozine binding can be achieved with poorly crystalline iron phases such as 2-line ferrihydrite following 3-6 hours of acid digestion (Figure 2.19b; blue). However 6-line ferrihydrite requires 24 hours of HCl digestion to enable full Ferrozine binding (Figure 2.19b; red). Finally magnetite (highly crystalline) requires a minimum of 48 hours of acid digestion to enable Ferrozine binding (Figure 2.19b; green). Using these values, suitable digestion/reduction time periods were chosen for each iron type used when performing a Ferrozine assay. The minimum acid digestion time required to allow efficient Ferrozine binding was chosen to minimize the auto oxidation of any iron(II) content in the suspensions/solutions being examined.

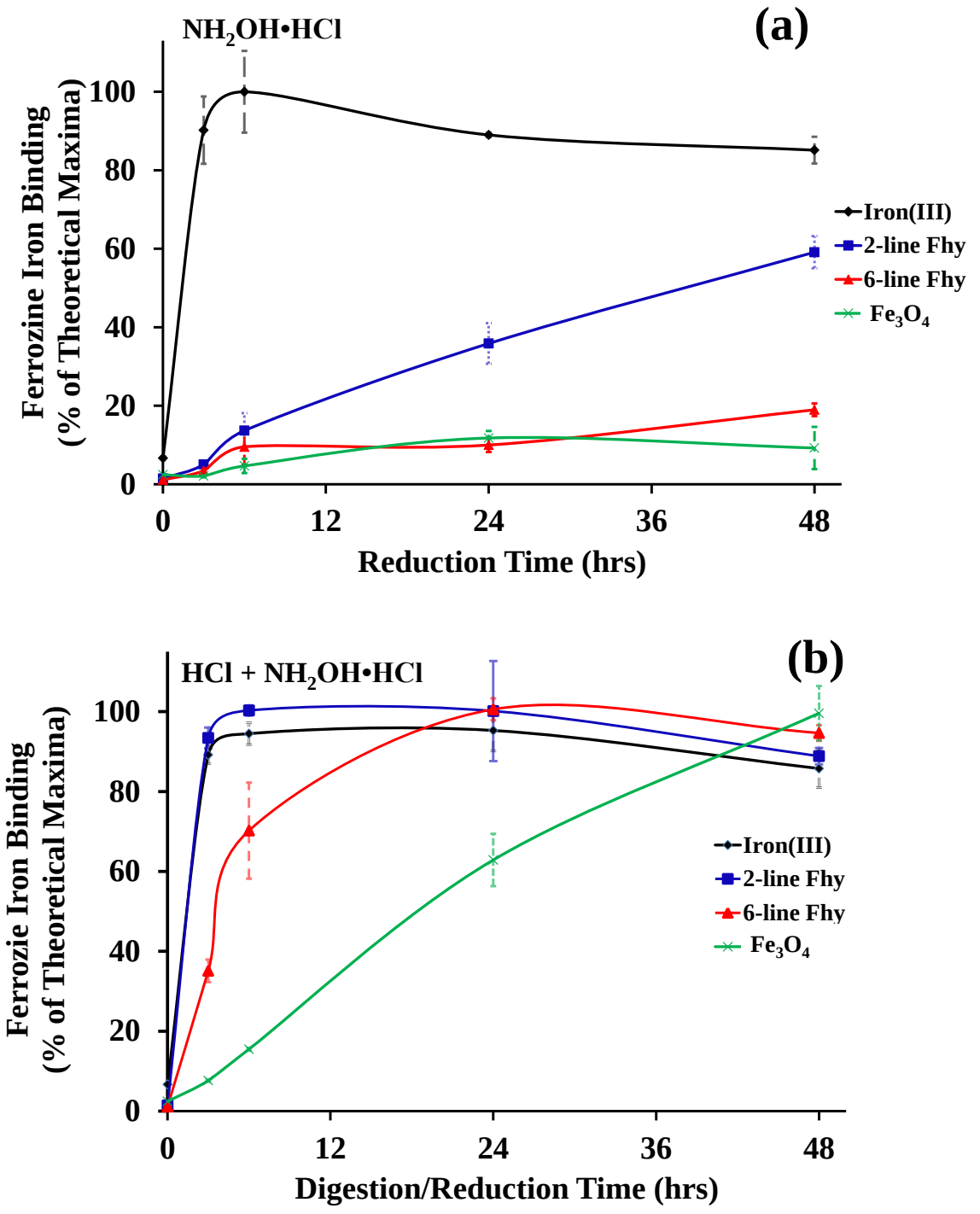

Figure 2.19. Ferrozine binding (as a percentage of the theoretical maximum) to 400 µM iron(III), 2-line ferrihydrite (Fhy), 6-line ferrihydrite, and magnetite (Fe_3O_4) suspensions, when incubated in the presence of **(a)** hydroxylamine hydrochloride (NH_2OH•HCl), or **(b)** hydrochloric acid (HCl) and hydroxylamine hydrochloride. Error bars show standard deviation (n=3).

2.5 Superconducting quantum interference device (SQUID)

To assess the magnetic moment of the sample solutions/suspensions when exposed to external magnetic field, superconducting quantum interference device (SQUID) magnetometry was conducted. SQUID magnetometry allows the detection of extremely small magnetic moments ($\leq 10^{-8}$ emu), making the technique ideal for the detection of subtle changes in the magnetic properties of a given sample material (e.g. the formation of magnetic iron oxide phases from non-magnetic precursors).

Small volumes (20 μL) of sample solution/suspension were deposited into plastic vessels for SQUID magnetometry examination. Plastic containers were sealed with molten wax before being plunged into liquid nitrogen to flash freeze solutions/suspensions, thereby maintaining solution/suspension chemistry to that of the time of sampling. Frozen samples were mounted into a Quantum Design SQUID-VSM and immediately cooled to 200K to prevent thawing. Hysteresis loops displaying the magnetic properties of sample material were created by monitoring magnetic moment (EMU) against an applied magnetic field (-5000, 5000 Oe). The magnetic response of a given material to magnetic fields is temperature sensitive. In particular, small ferromagnetic/ferrimagnetic iron oxide nanoparticles may exhibit a superparamagnetic response at room temperature, yet display magnetic coercivity when cooled beneath its blocking temperature (where nanoparticle magnetization can no longer flip during measurement). Therefore, SQUID measurements were taken in a temperature range from 200K to 10K (below the blocking temperature of the materials used), to overcome any superparamagnetic effects. Diamagnetic background signals arising from the plastic transport vessel and the solvent materials used in sample preparation were subtracted to provide the magnetic signal arising from the ferromagnetic/ferrimagnetic sample material.

2.6 Alternating current magnetic susceptometry

To determine the alternating current (AC) magnetic susceptibility of sample solutions/suspensions, measurements were performed using an AC susceptometer. AC susceptometry involves monitoring a sample material's magnetic response to the application of an oscillating magnetic field, allowing factors such as frequency dependent susceptibility to be evaluated. The principle underlying AC susceptibility measurements involves subjecting sample material to a small alternating magnetic field, then measuring the magnetic flux variation (manifesting as voltage) induced by the sample using a detection-coil system. This voltage is proportional to the sample magnetic susceptibility, providing information regarding a sample's magnetic state.

200 µL of sample solutions/suspensions were deposited into a glass vial which was then placed within an AC susceptometer. Measurements of sample susceptibility could be made in a frequency dependant manner over a frequency range of 10-250000 Hz, or as a function of time, where continual susceptibility measurements are taken at a fixed frequency. Background signals arising from glass vial containers and solvents (water, buffer etc.) were subtracted to provide true sample susceptibility values. For dilute samples (e.g < 500 µM) the frequency range was limited to 1-150 kHz due to instrument sensitivity limitations.

Chapter 3

Ferrous iron formation following the co-aggregation of ferric iron and the Alzheimer's disease peptide β-amyloid (1-42)

3.1 Introduction

As was discussed in *Chapter 1*, links have been established demonstrating the occurrence of iron accumulation in regions of AD pathology [34,39,48], including extracellular senile plaques comprised of Aβ[35,42], along with intracellular NFTs [21,22,154], both hallmark lesions of AD[18,155]. In particular, increased levels of potentially neurotoxic redox-active and potentially neurotoxic iron(II)-bearing minerals have been observed in AD tissue [36,42,105,108,113]. Additionally iron has been shown to induce Aβ to aggregate into a form capable of inducing neuronal injury [95,104]. As both oxidative stress and Aβ accumulation are recognised as early stage events in AD pathogenesis [57], the relationship between Aβ and iron may play a vital role in the onset of AD pathology.

However despite this evidence, little is known about the process of Aβ/iron interaction, and the mineral products of such interactions have not been fully characterized. Many important questions regarding the role of iron in AD pathology remain unanswered: i) what are the origins of the iron(II)-bearing minerals observed in AD tissue? ii) How does iron come to be accumulated in Aβ structures? iii) Does this co-localization of Aβ iron lead to the formation of redox-active iron forms?

In this chapter a variety of methods (described in *Section 3.2*) were utilized to examine the interaction between Aβ and synthetic ferric iron when co-incubated over a 144 hour period, in an attempt to address the questions described above. Scanning transmission x-ray microscopy (STXM) was used to visualize *localized* regions of iron and Aβ accumulation, enabling the determination of iron oxidation state when present within Aβ structures. X-ray absorption spectroscopy (XAS) and x-ray magnetic circular dichroism (XMCD) were employed to probe larger sample areas, providing information regarding the oxidation state and magnetic properties of iron following incubation with Aβ that were representative of

the sample as a whole. Additional supporting information was obtained through spectrophotometric iron(II) quantification and transmission electron microscopy (TEM) techniques. Further to this, the effect of aluminium(III) addition upon the process of Aβ/iron interaction was also assessed.

Here, TEM images displaying the effect of iron addition upon Aβ fibrillar and aggregational state are shown (*Section 3.3.1.1*). Carbon/iron STXM analysis demonstrating the accumulation of iron within Aβ structures coupled with the oxidation sate of said iron is then presented (*Section 3.3.1.2*). Evidence of iron reduction following Aβ interaction (in the presence or absence of aluminium) is provided through XAS (*Section 3.3.2*), and the quantification of Aβ mediated iron reduction is demonstrated via spectrophotometric iron(II) quantification (*Section 3.3.3*). Additionally, XMCD data displaying the magnetic properties of iron following Aβ interaction over a 144 hour period are displayed (*Section 3.3.4*). The significance of these results in understanding the role played by Aβ/iron interaction in AD is then discussed (*Sections 3.4 and 3.5*), along with the implications of these findings for future investigations (*Section 3.6*).

3.2 Materials and methods

3.2.1 Scanning transmission x-ray microscopy and transmission electron microscopy

Element specific images revealing the structure and composition of Aβ/iron(III) aggregates with a spatial resolution of approximately 20 nm were obtained by performing scanning transmission x-ray microscopy (STXM) on the PolLux beamline at the Swiss Light Source (Villigen, Switzerland). Transmission electron microscopy (TEM) was performed using a

JEOL 1230 microscope operating at 100 kV. Where both STXM and TEM were employed on the same sample membrane, the STXM measurements were performed first to exclude the effect of electron beam damage to the aggregates.

3.2.1.1 Preparation of samples

Frozen Aβ(1-42) (Bachem) was thawed and dissolved in 0.1 M NaOH to create a 1mg/mL (220 μM) stock. NaOH was used to dissolve any insoluble Aβ aggregates that may have formed during peptide storage, thereby reverting amyloid aggregation. The Aβ stock was left at room temperature for 30 minutes to ensure complete peptide dissolution before being immediately added to modified Krebs-Henseleit (KH) buffer (pH 7.4; 100 mM PIPES). Two amyloid treatments were prepared: i) To assess the co-aggregation of Aβ and iron, 18 mM iron(III) nitrate solution was added to KH buffer immediately after Aβ and resulting Aβ/iron hydroxide suspensions were left to incubate at 37°C for 96 hours before sampling. ii) In order to investigate the inclusion of iron into pre-formed Aβ structures, Aβ solutions in KH buffer were allowed to incubate for 48 hours at 37°C before the addition of 18 mM iron(III) nitrate solution. Following the addition of iron(III), Aβ/iron(III) hydroxide suspensions were allowed to incubate for a further 30 minutes before sampling. For both Aβ/iron preparations, final peptide and iron concentrations were 35 μM and 370 μM respectively. Additional Aβ solutions intended for STXM and TEM characterization of the peptide in the absence of metal addition were created by diluting the 220 μM Aβ stock with KH buffer to create a 35 μM Aβ solution.

3.2.1.2 STXM analysis

Small volumes (15 μL) of Aβ/iron(III) suspensions were deposited onto silicon nitride membranes (75nm thickness, DuneSciences), and membranes were loaded onto aluminium plates for STXM examination as previously described (*Section 2.2.1*). Not all Aβ/iron

samples were kept under anoxic conditions throughout sample transportation and loading. From the results displayed in *Section 3.3* only the aggregate shown in Figure 3.9 was kept under anoxic conditions prior to STXM examination (using the methodology described in *Section 2.2*).

Carbon mapping revealing the amyloid structure of Aβ/iron aggregates, and carbon *K*-edge (280-320 eV) x-ray absorption examination providing absorption spectra characteristic of Aβ were performed as described in *Section 2.2.2*. This process was repeated at the iron *L*-edge (700-740 eV) to reveal the iron content of these Aβ structures, along with the oxidation state of any iron present. As absorbance energies of iron are higher than those of carbon, STXM carbon analysis was conducted prior to analysis of the iron content in order to minimise x-ray induced damage to amyloid structures.

3.2.2 Electron microscopy examination

Small volumes of samples (15 µL) were deposited onto carbon/formvar coated copper TEM grids (200 mesh; Agar Scientific), and excess liquid removed using filter paper. TEM and electron diffraction were performed using a JEOL 1230 microscope operating at 100 kV.

3.2.3 X-ray absorption spectroscopy and x-ray magnetic circular dichroism spectroscopy

3.2.3.1 Preparation of iron/amyloid suspensions

Iron(III) hydroxide suspensions were prepared by diluting 18 mM iron(III) nitrate (Sigma-Aldrich) in deionized water and subsequently neutralizing to pH 7 with 1 M sodium hydroxide (NaOH), giving an iron concentration of 440 µM. Suspensions containing both 440 µM iron(III) and 440 µM aluminium(III) at pH 7 were created from 18 mM iron(III)

nitrate, and 37 mM aluminium(III) nitrate (Perkin-Elmer) in a similar manner as described above, with aluminium(III) nitrate being added after the iron(III) nitrate. All suspensions were sonicated for five minutes prior to Aβ addition to encourage a homogenous metal distribution.

A 1mg/mL (220 μM) Aβ stock was created as described previously (*Section 3.2.1.1*), before being added to the previously prepared metal suspensions. Aβ/metal suspensions were again neutralized to pH 7 following the addition of the Aβ stock, via the addition of 0.5 M hydrochloric acid (HCl). Final Aβ and metal concentrations were 35 μM and 370 μM respectively. Amyloid-free iron hydroxide suspensions were created in the same manner as above with the substitution of deionized water in place of Aβ. All Aβ/iron suspensions and amyloid-free controls were incubated at 37°C over a period of 144 hours.

3.2.3.2 XAS/XMCD measurements

Sample suspension deposition onto copper TEM grids, and mounting of grids onto aluminium probes was conducted as described in *Section 2.1* (*Figure 2.1*). Sampling was performed after 30 minutes, 48 hours and 144 hours of metal incubation with Aβ. Sample materials were kept under anoxic conditions throughout the experimental process, as described in *Section 2.1.2* (*Figure 2.4*), to prevent any changes in iron valence chemistry.

XAS and XMCD measurements were conducted on beamline 4.0.2 at the Advanced Light Source (Berkeley Laboratory, USA) and beamline I10 at Diamond Light Source (Oxfordshire, UK). Prior to spectra acquisition, two dimensional maps at a spatial resolution of 100 μm revealing areas of iron accumulation were conducted at the iron L_3 edge (see *Section 2.1.3*). Once areas of iron accumulation were identified, scans across the entire iron $L_{2,3}$ absorption edge (700-740 eV) were performed, providing information regarding both the oxidation state and the magnetic properties of the iron. However not all

iron deposits located in this way provided a sufficiently stable signal for full XAS/XMCD analysis to be performed.

X-ray absorption (XAS) spectra, revealing the oxidation state of iron in the samples, were recorded using the total electron yield method, whilst the magnetic properties were probed by analysing XMCD spectra. The latter were obtained by measuring the difference in x-ray absorption using circularly polarized x-rays, with a 0.6 T magnetic field being applied in opposing orientations along the x-ray beam direction.

3.2.4 Iron(II) quantification in suspension: Ferrozine assay

Spectrophotometric determination of the iron(II) content of Aβ/iron suspensions was achieved by performing a Ferrozine iron(II) colorimetric quantification assay [153].

Small volumes of Aβ/iron samples were removed and acid digested in 0.5 M HCl for three hours at room temperature (see *Section 2.4*). Acid digested samples were then added to 2 mM Ferrozine, and absorbance read at 562 nm. The total iron content of the Aβ/metal suspensions was recorded by adding small volumes of the sample suspension to 0.5 M HCl and 6.25 M hydroxylamine hydrochloride (an iron reducing agent), at room temperature for 3 hours. These reduced samples were then added to 2 mM Ferrozine and absorbance read at 562 nm as before. The iron(II) content of Aβ-free iron controls were assessed in the same way to provide iron(II) background levels for all iron suspensions used. Iron(II) content as a percentage of total iron content was then determined as described in *Section 2.4*.

Spectrophotometric measurements were performed as describe above on samples taken after 0, 24, 48, 72, 120 and 144 hours of metal incubation with Aβ. No iron(II)

quantification data was collected after 96 hours of incubation due to the limited amount of sample volume available.

3.2.4.1 Statistical analysis

Statistical analysis of the data obtained from iron(II) quantification in suspension was performed using a one-way analysis of variance (GraphPad Prism 6). This is a method of comparing sample means for two or more populations. The null hypothesis of equal means was rejected at the 5% confidence level.

3.3 Results

3.3.1 The co-aggregation of iron and Aβ(1-42)

3.3.1.1 Aβ/iron aggregate structure

Photographs displaying iron(III) hydroxide suspensions in the absence and presence of Aβ following 24 hours of incubation at 37°C are displayed in Figure 3.1. Where iron(III) was allowed to incubate in the absence of Aβ, iron precipitates were seen to deposit to the bottom of the sample vial forming a dense orange sediment. However when incubated with Aβ, iron hydroxide precipitates were seen to remain suspended throughout the sample medium with little sedimentation occurring. Such images suggest the addition of Aβ to stabilize iron(III) hydroxide precipitates in solution, possibly by incorporating said iron into its protein aggregate structure.

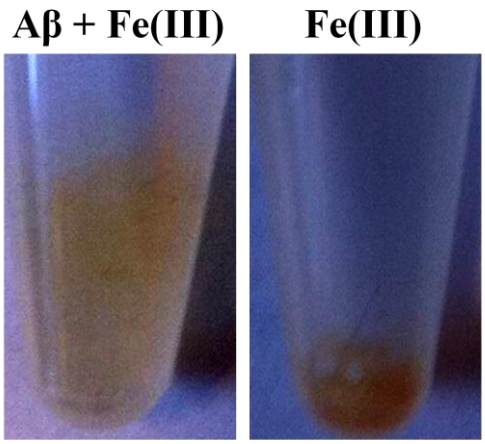

Figure 3.1. Photographs of iron(III) hydroxide suspensions in the presence (left) and absence (right) of Aβ following 24 hours of incubation at 37°C.

To investigate the effect of iron(III) addition to amyloid fibrillar structure and aggregational state TEM was performed. TEM images displaying Aβ fibrillar structures formed in the absence and presence of iron(III) hydroxide are shown in Figure 3.2 and Figure 3.3 respectively. Where Aβ was incubated in the absence of iron, small amyloid aggregates can be seen, typically ranging from 1-5 μm in diameter and comprised of fine fibril structures (Figure 3.2). Such fibril structures are consistent with those previously reported in literature for Aβ [95,156-148].

Examination of amyloid aggregates formed when incubated with iron(III) revealed the formation of structures ranging from 1-50 μm in size and containing electron dense regions, examples of which are shown in Figure 3.3. No obvious correlation between incubation time and aggregate size could be determined in these samples with both smaller (<5 μm) aggregates, and thick amorphous electron opaque regions seen in many of the samples even after only 30 min incubation. Electron diffraction patterns obtained from these Aβ/iron structures provided no evidence of the presence of crystalline material.

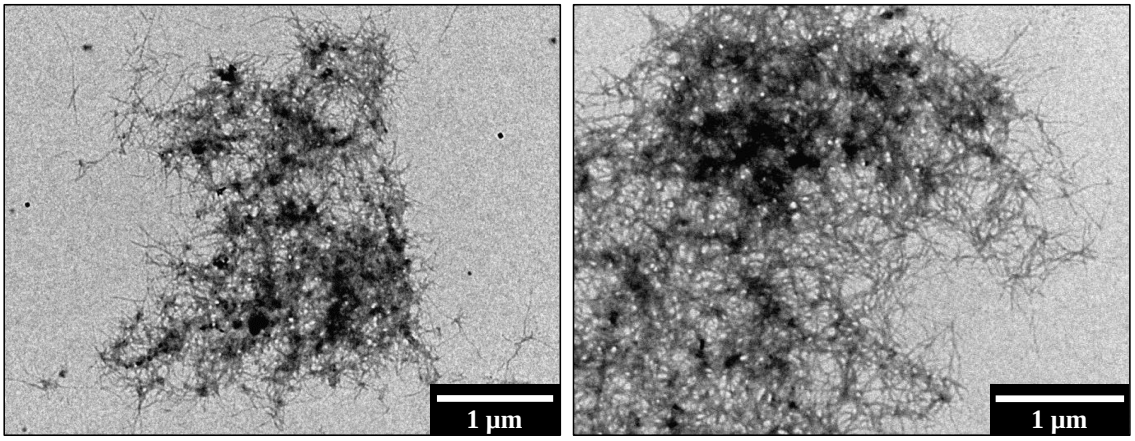

Figure 3.2. TEM images of Aβ aggregates formed in the absence of iron(III).

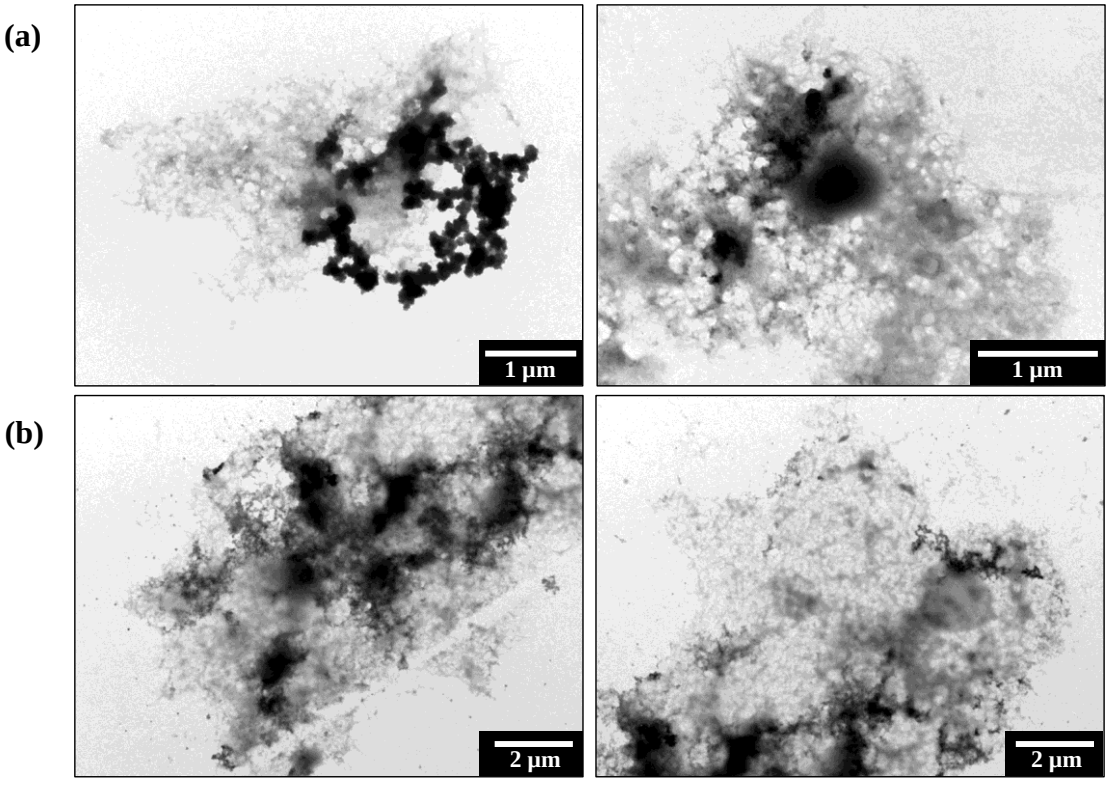

Figure 3.3. TEM images of typical Aβ structures formed following **(a)** 0.5 and **(b)** 96 hours of Aβ incubation with iron(III).

3.3.1.2 Aβ/iron aggregate elemental composition

To investigate the nature of the electron dense regions in the aggregates, scanning transmission x-ray microscopy was performed. Where Aβ and iron(III) were added simultaneously and allowed to incubate for 96 hours, carbon *K*-edge mapping of aggregates showed evidence of fine structure similar to that observed by TEM, together with dense carbon containing regions (Figure 3.4).

Aggregate x-ray absorption across the carbon *K*-edge (280-320 eV) provided spectra consistent with the calculated carbon spectrum for the amino acid sequence of Aβ(1-42) peptide (Figure 3.4f) [143]. These carbon spectra were also indistinguishable to carbon spectra collected from Aβ structures formed in the absence of iron(III) (Figure 3.4f). Characteristic features of the peptide spectrum are a low energy peak (labelled 1, Figure 3.4f) which arises from the aromatic amino acids, the dominant π* amide peak (labelled 2), and a weaker shoulder feature (labelled 3) associated with arginine. Examination of aggregate x-ray absorbance at the iron L_3-edge showed regions of iron accumulation within the amyloid structure, indicating the co-aggregation of iron with Aβ (Figure 3.4b and e). A comparison of aggregates measured by both STXM and TEM showed that many of the dense regions seen by TEM were due to accumulated iron within the aggregate (Figure 3.4d and e). Throughout all Aβ/iron samples examined, no evidence of iron accumulation was observed in the absence of Aβ structures.

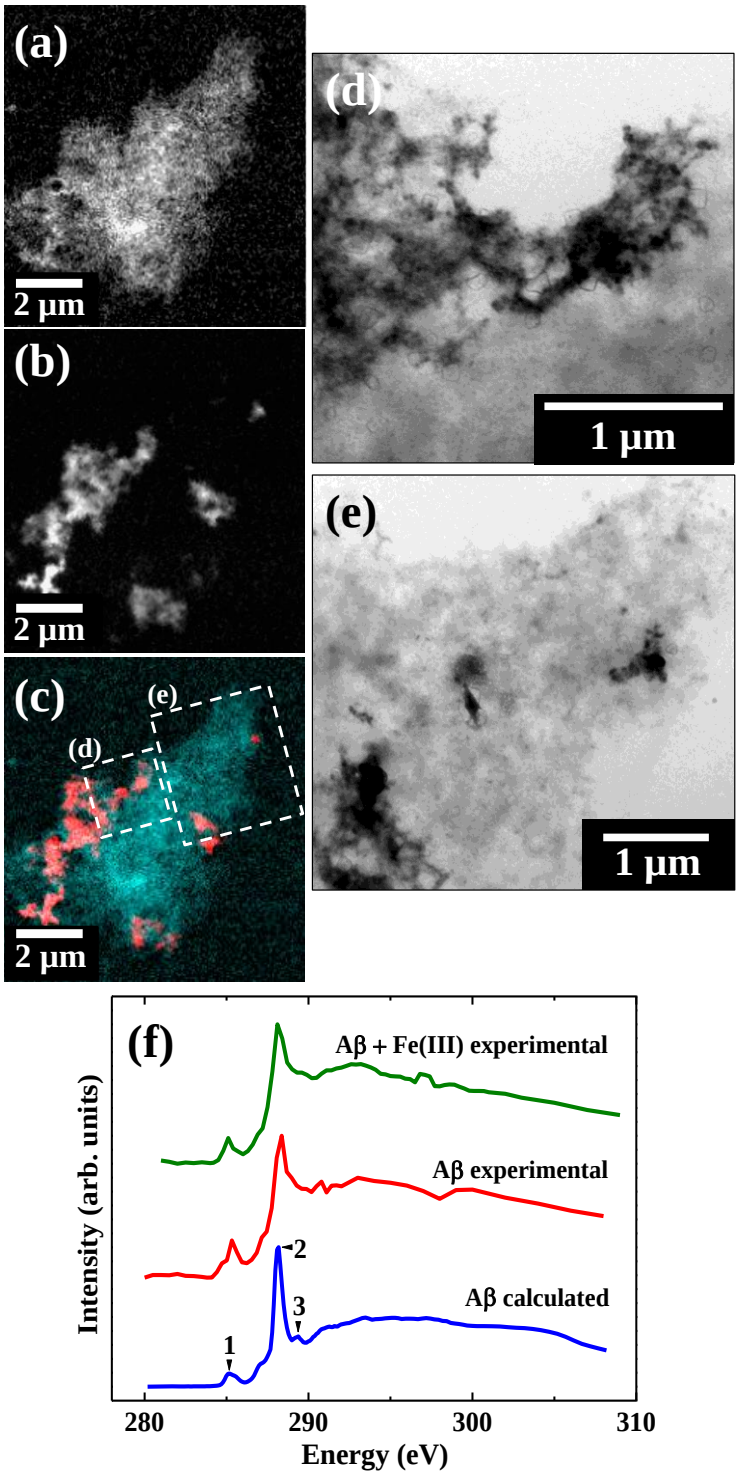

Figure 3.4. STXM and TEM images with additional carbon *K*-edge absorption spectra from a Aβ/iron aggregate formed following 96 hours of incubation. **(a)** Carbon map showing aggregate Aβ structure. **(b)** Iron map displaying the iron content of the same aggregate. **(c)** Carbon/iron composite image of the Aβ (cyan) and iron (red) content shown in (a) and (b) respectively. **(d)** and **(e)** TEM images of the Aβ aggregate as labelled in (c). **(f)** Calculated (blue) and experimental (red and green) carbon *K*-edge spectra for Aβ. Calculated spectrum was obtained using methods described in Stewart-Ornstein *et al.*[143].

Carbon *K*-edge and iron L_3-edge examination of Aβ samples allowed to incubate in KH buffer for 48 hours prior to the addition of iron(III), led to the observation of Aβ structures indistinguishable to those formed where Aβ and iron(III) were added simultaneously (Figure 3.5a). Combined STXM and TEM images of these aggregates showed them to be fibrillar in nature containing multiple areas of iron accumulation (Figure 3.5); suggesting iron had incorporated into Aβ structures that had formed prior to the addition of the metal.

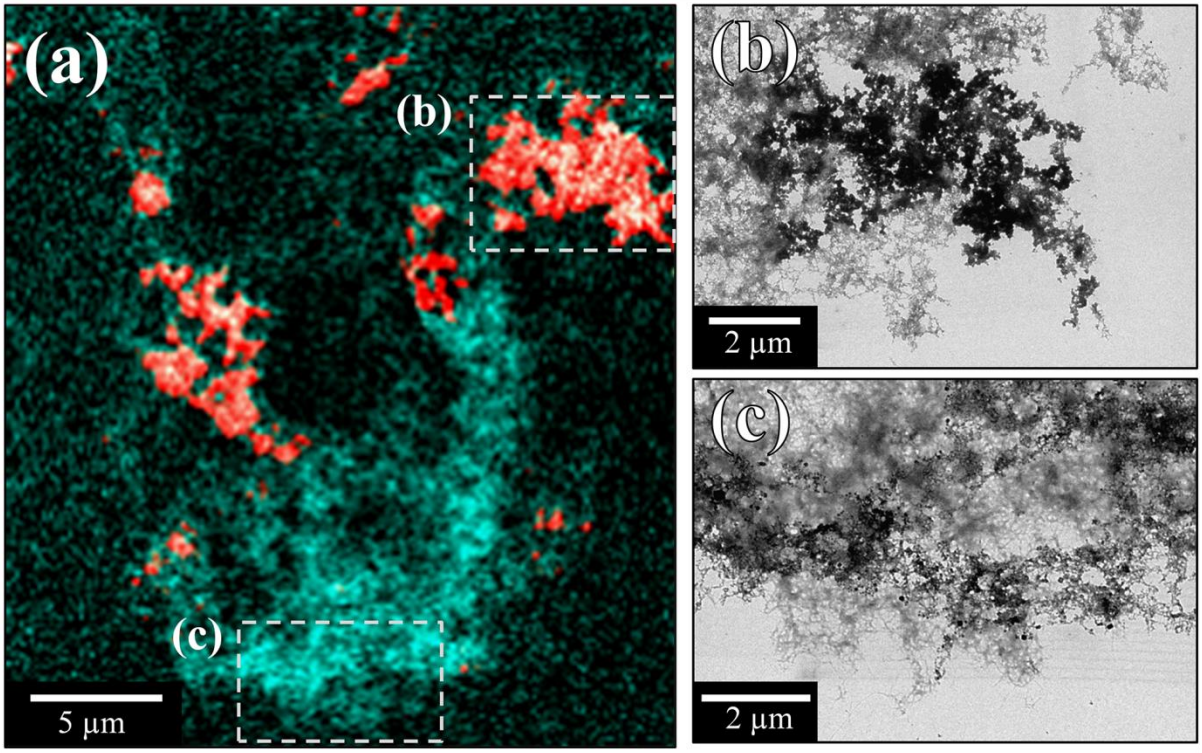

Figure 3.5. STXM and TEM images of a Aβ aggregate allowed to incubate for 48 hours prior to the addition of iron(III). **(a)** A composite image showing the Aβ (cyan) and iron (red) content of the Aβ/iron aggregate. TEM images showing the fibrillar structure of the Aβ/iron aggregate in areas of high **(b)** and low **(c)** iron content as displayed in (a).

To assess the effect of Aβ/iron co-aggregation upon Aβ structure, carbon *K*-edge spectra obtained from Aβ aggregates containing iron were compared to the carbon spectra acquired from Aβ structures with no detectable iron signal. Although no dramatic differences in

carbon *K*-edge spectra were apparent, subtle changes in the width of the π* amide peak (288 eV) were often seen, manifesting as a widening of this peak feature when Aβ was incubated with iron(III) (Figure 3.6, green). However this widening effect was also seen in carbon dense Aβ aggregates formed in the absence of iron(III) (Figure 3.6, red). Therefore this broadening of the π* amide peak appears to be a result of carbon thickness, rather than changes to the carbon structure of Aβ when incubated with iron(III). Iron is known to promote the aggregation of Aβ [95,148], resulting in the formation of carbon dense structures, explaining the frequent peak widening effect observed in Aβ structures containing iron(III).

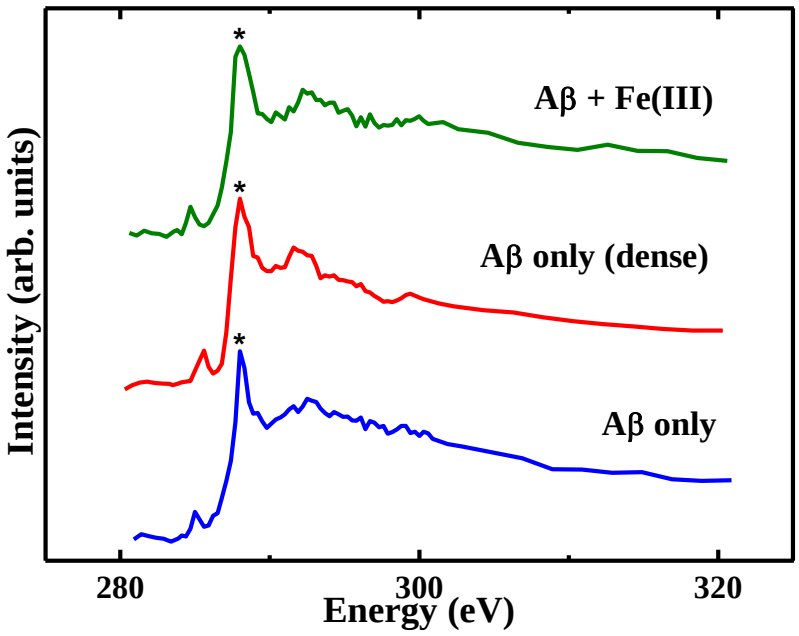

Figure 3.6. Carbon *K*-edge absorption spectra from amyloid aggregates comprised of thin Aβ (blue; observed following 48 hours of incubation in the absence of iron), dense Aβ (red; 0.5 hours incubation in the absence of iron) and Aβ + iron(III) (green; 48 hours of incubation in the presence of iron). Asterisks (*) indicate the position of the π* amide peak at 288 eV.

3.3.1.3 Iron oxidation state following co-aggregation with Aβ

STXM examination of iron accumulations incubated in the absence of Aβ at the iron $L_{2,3}$-edge provided iron absorption spectra characteristic of a pure iron(III) mineral (see *Section 1.4* ; *Figure 1.9* for reference iron(III) spectra). No enhancements to Fe^{2+} features at either the L_3 edge (708eV) or L_2 edge (721 eV) were apparent, indicating no reduction to have taken place (Figure 3.7).

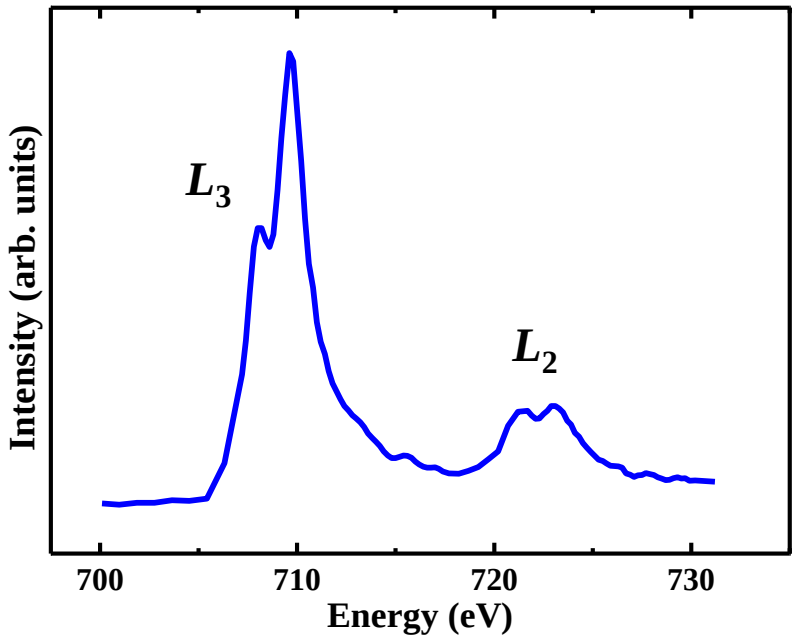

Figure 3.7. STXM iron $L_{2,3}$-edge absorption spectra recorded from deposits of iron(III) recorded in the absence of Aβ.

Where iron regions are too thick/dense to allow the transmission of x-rays, a saturation of signal at the iron L_3 peak region can occur. For iron(III) minerals this results in an apparent increase in the low energy Fe^{3+} feature at 708 eV with respect to the dominant Fe^{3+} feature at 709.5 eV, which can be mistaken as an increase in Fe^{2+} content (as is illustrated in Figure 3.8; blue). To determine between occurrences of iron signal saturation and genuine cases of iron reduction, the iron L_2 edge was examined. As the L_2 region x-ray absorption

intensities are much lower than that of the L_3 region, signal saturation is less likely to occur. Therefore where genuine iron(II)-bearing phases are present, increases in Fe^{2+} cation features at both the iron L_3 (708 eV) and L_2 (721 eV) regions are apparent (see Figure 3.8 red, for an iron(II) reference spectra). In cases of iron x-ray absorption saturation increases in Fe^{2+} features may be apparent at the L_3 edge but not at the L_2 edge (Figure 3.8; blue). Further to this, where pure iron(II) phases are present, a shift in iron L_3 peak energy from 709.5 eV to 708 eV is observed, with the dominant Fe^{3+} feature at 709.5 eV disappearing (Figure 3.8; red).

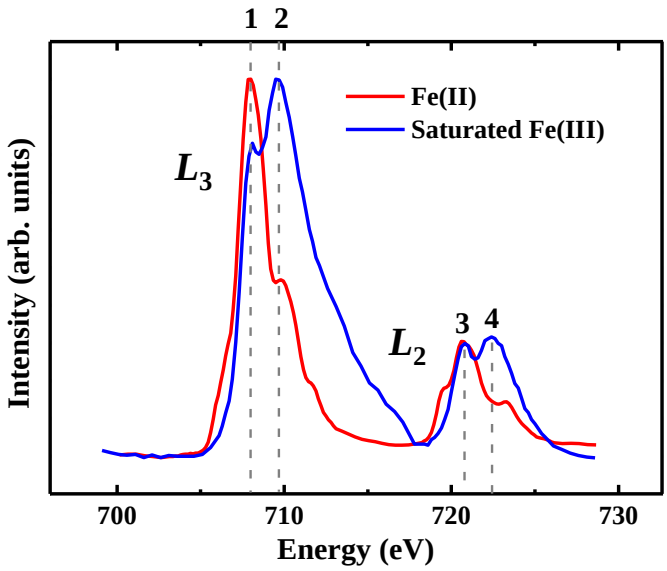

Figure 3.8. Iron $L_{2,3}$-edge absorption spectra recorded from a dense deposit of iron(III) resulting in saturation of signal (blue), compared to a spectrum obtained from a pure iron(II) material (red). Note the saturation induced increases in 708 eV peak intensity (dashed line labelled 1) compared to 709.5 eV peak intensity (dashed line labelled 2) in the saturated iron(III) spectra (blue). These saturation effects are not apparent across the L_2 region (dashed lines 3 and 4), with absorption features being characteristic of a pure Fe^{3+} material.

Iron *L*-edge x-ray microspectroscopy examination of certain Aβ/iron structures (Figures 3.9, 3.10 and 3.11) provided iron $L_{2,3}$-edge x-ray absorption spectra displaying enhanced Fe^{2+} features compared to Aβ-free iron(III) controls.

In an aggregate formed following 96 hours of Aβ/iron incubation (which had been maintained under anoxic conditions throughout the experimental procedure), subtle enhancements in Fe^{2+}cation absorption features are apparent at the iron L_3 edge (708 eV) and L_2 edge (721 eV) compared to time-matched Aβ-free iron(III) controls (Figure 3.9d). These Fe^{2+} enhancements suggest the chemical reduction of iron localized within the Aβ aggregate. In this instance iron was found to be extensively accumulated within the Aβ structure, with multiple iron deposits several microns (ca. 2-6 μm) in diameter being recorded (Figure 3.9b and c). Although it appears that these enhancements to Fe^{2+} cation features are a result of Aβ mediated iron reduction, the subtlety of the changes to the XAS profile mean that enhancements due to iron saturation effects (as shown in Figure 3.8; blue) cannot be precluded.

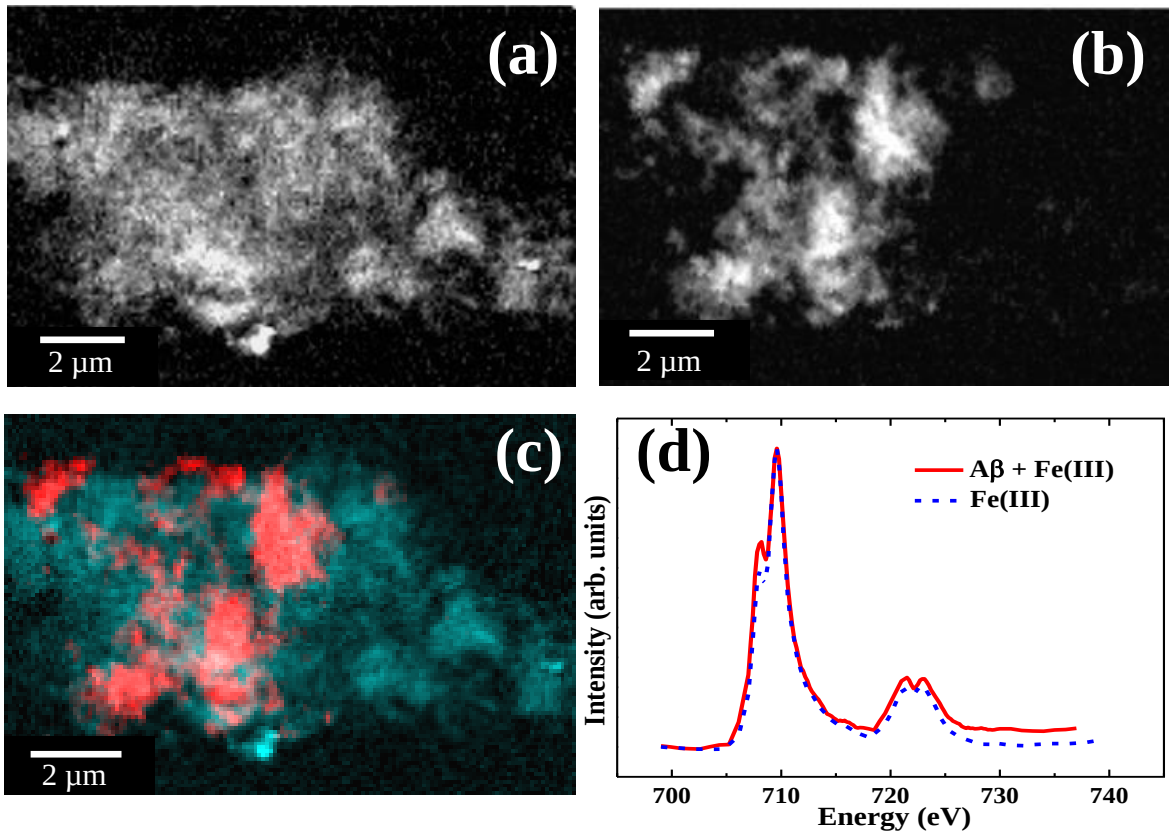

Figure 3.9. STXM images and iron $L_{2,3}$-edge spectra of an Aβ/iron aggregate formed following 96 hours of Aβ/iron(III) incubation. **(a)** Carbon map showing the Aβ structure of the aggregate. **(b)** Iron map revealing the iron content of the aggregate. **(c)** Carbon/iron composite image displaying both the Aβ (cyan) and iron (red) content shown in (a) and (b) respectively. **(d)** Iron $L_{2,3}$-edge absorption spectra obtained from this Aβ/iron structure (red), compared to a Aβ-free iron(III) control (blue dashed).

However, Aβ/iron structures (Figures 3.10 and 3.11) formed following 48 hours of iron incubation with Aβ, provided regions of iron with $L_{2,3}$ x-ray absorption spectra characteristic of chemically reduced iron phases. Surprisingly these reduction effects were observed despite the samples being exposed to aerobic environments. Carbon *K*-edge and iron L_3-edge x-ray microspectroscopy examination of these Aβ aggregates revealed multiple small concentrated areas of iron to be located within Aβ carbon structure (Figure 3.10a-c and Figure 3.11a-c). Such distributions of iron differed dramatically to those

displayed in Figure 3.9, where iron was present as large precipitates, widely spread throughout the Aβ aggregate.

Iron $L_{2,3}$-edge absorption profiles obtained from these structures demonstrated iron to be present in varied oxidation states (Figure 3.10f and Figure 3.11f). Within the Aβ/iron aggregate displayed in Figure 3.10, iron is shown to exist as iron(III) (regions 1 and 2), and also as a heavily reduced iron(II)/(III) intermediate (region 3). Iron regions from the Aβ structure shown in Figure 3.11 were found to be in a pure iron(III) state (region 1), along with a reduced iron phase reminiscent of zero-valent iron (region 2). These reduction effects were mirrored at the iron L_2-edge (720-725 eV), suggesting chemical reduction to have taken place rather than the enhancement of Fe^{2+} absorption features through saturation effects (as shown in Figure 3.8; blue). As reduced iron forms could not be formed in the absence of Aβ, the occurrence of these redox-active phases appears to be as a result of iron(III) reduction by Aβ.

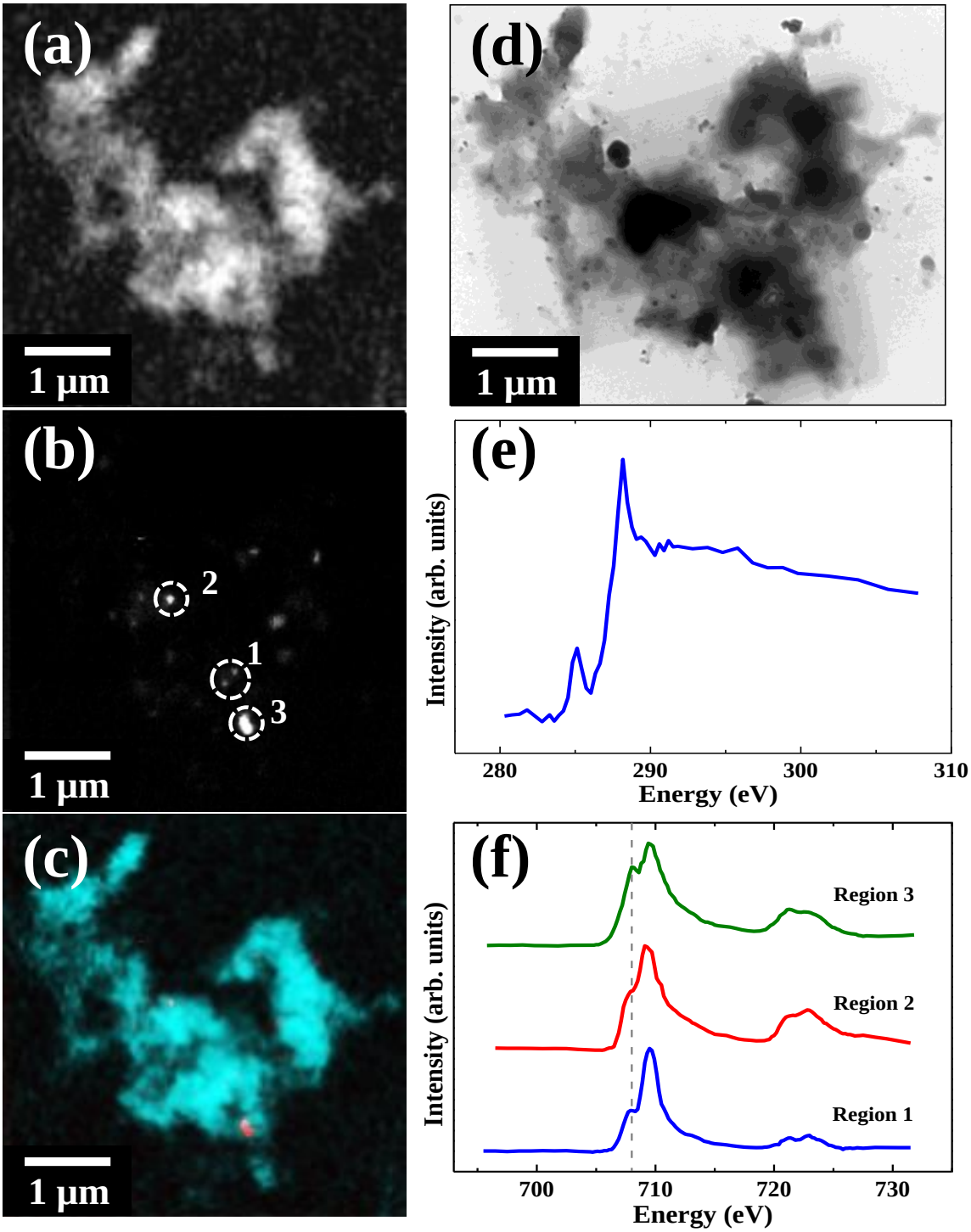

Figure 3.10. STXM and TEM images along with carbon *K*-edge and iron *L*-edge spectra of an Aβ/iron aggregate formed following 48 hours of Aβ/iron(III) incubation. **(a)** Carbon map showing the Aβ structure of the aggregate. **(b)** Iron map revealing the iron content of the aggregate. **(c)** Carbon/iron composite image displaying both the Aβ (cyan) and iron (red) content shown in (a) and (b) respectively. **(d)** TEM image of the Aβ aggregate shown in (c). **(e)** Carbon *K*-edge spectra for this Aβ aggregate. **(f)** Iron $L_{2,3}$-edge spectra of iron regions labelled in (b).

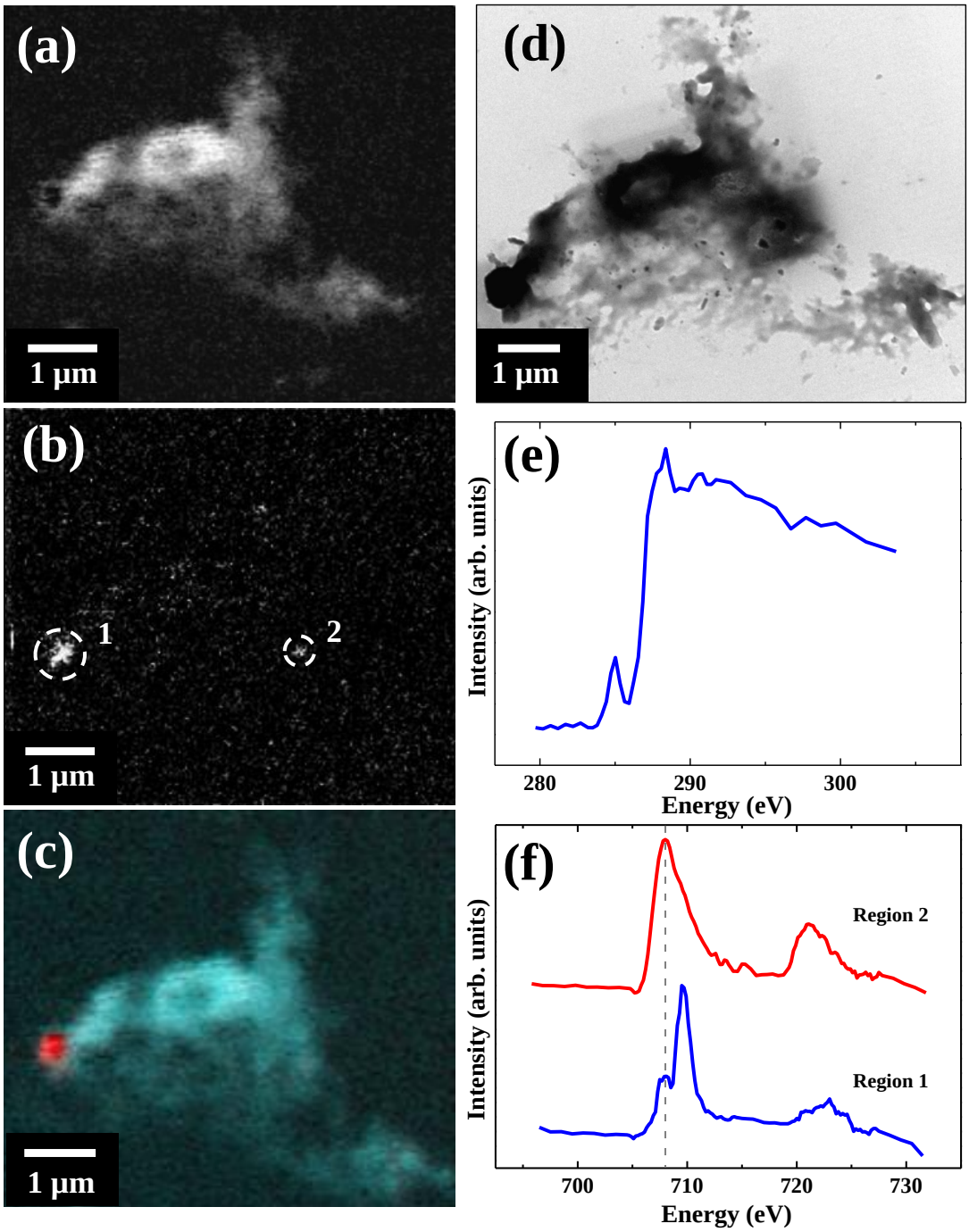

Figure 3.11. STXM and TEM images along with carbon *K*-edge and iron *L*-edge spectra of an Aβ/iron aggregate formed following 48 hours of Aβ/iron(III) incubation. **(a)** Carbon map showing the Aβ structure of the aggregate. **(b)** Iron map revealing the iron content of the aggregate. **(c)** Carbon/iron composite image displaying both the Aβ (cyan) and iron (red) content shown in (a) and (b) respectively. **(d)** TEM image of the Aβ aggregate shown in (c). **(e)** Carbon *K*-edge spectra for this Aβ aggregate. **(f)** Iron $L_{2,3}$-edge spectra of iron regions labelled in (b).

The aggregates displayed in Figures 3.10 and 3.11 both provided a strong carbon signal, and carbon *K*-edge x-ray absorbance spectra consistent with the amino acid sequence of the Aβ(1-42) peptide [143], indicating no changes to Aβ carbon structure had occurred with increased redox-active iron content (the decreased π* peak height shown in Figure 3.11e is believed to be as a result of sample thickness/density). However when these Aβ/iron structures were imaged under TEM, it was apparent that no fibrillar Aβ structure remained. Instead an amorphous structure could be seen containing several electron dense regions that correlated to the iron content observed via STXM, suggesting a possible association between the occurrence of ferrous iron phases and a disruption to Aβ fibril structure. Note also the x-ray beam induced damage to sample membranes (manifesting as darkened, striped, square regions) observed under TEM (Figures 3.10d and 3.11d). This damage occurs through the exposure of sample membranes to x-rays in the iron *L*-edge energy range, and demonstrates the requirement to examine sample materials at the lower-energy carbon *K*-edge, prior to iron *L*-edge examination.

3.3.2 X-ray absorption spectroscopy examination of iron oxidation state, following Aβ interaction

In the preceding section STXM was employed to ascertain the oxidation state of localized iron deposits. However this approach does not provide an efficient means to determine the prevailing oxidation state of iron across the entire sample area. Conversely, due to the large diameter of the x-ray beam used in XAS measurements (relative to STXM beam size), XAS provides an effective means to determine the overriding iron oxidation state of a given sample. Furthermore, associated XMCD measurements allow the magnetic state of iron materials to be elucidated (see *Section 3.3.4*). Thus when used in tandem STXM and

XAS allow the localized and generalized characterisation of iron oxidation state. In the following two sections the effect of Aβ interaction upon iron oxidation state is examined through XAS. The effect of aluminium addition (also known to accumulate in AD tissues) upon iron oxidation state following incubation with Aβ is also assessed. Aβ/iron samples were kept under strictly anoxic conditions and XAS was performed at Diamond Light Source beamline I10, and the Advanced Light Source beamline 4.0.2.

3.3.2.1 Iron(III) series

Generally, crystalline iron minerals (such as ferrihydrite, examined in *Chapter 4*, and magnetite, examined in *Chapter 6*) are not susceptible to x-ray beam induced reduction effects at the soft x-ray energy range used in this thesis. However as more amorphous iron forms were used here, the effect of the x-ray beam on these phases was explored. Repeated x-ray absorbance scans across the iron $L_{2,3}$ edge were performed, and changes in the XAS profile as a function of x-ray beam exposure were monitored. An example of this process is shown in Figure 3.12, where four successive XAS scans were performed on a ferric iron aggregate that was unstable in the x-ray beam. Despite an x-ray beam mediated reduction effect being apparent over the first three XAS scans, this reduction effect plateaued on the fourth scan with iron being present as an iron(II)/(III) intermediate, displaying that x-ray exposure alone was not sufficient to form a pure iron(II) phase. Further to this, it should be noted that due to the scanning operation mode utilized in STXM experiments, no x-ray induced beam reduction was seen to occur when examining iron aggregates under STXM (Figure 3.13).

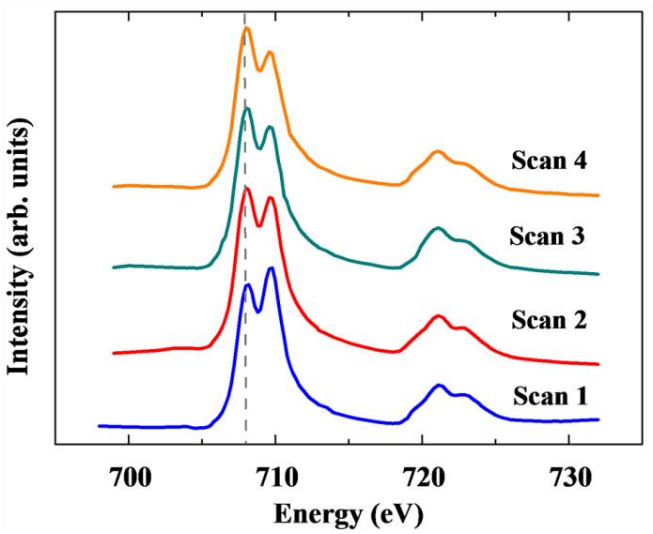

Figure 3.12. Iron $L_{2,3}$-edge x-ray absorption spectra of an unstable ferric iron aggregate following four successive XAS measurements. Fe^{2+} cation peak position is indicated by a grey dotted line at 708eV.

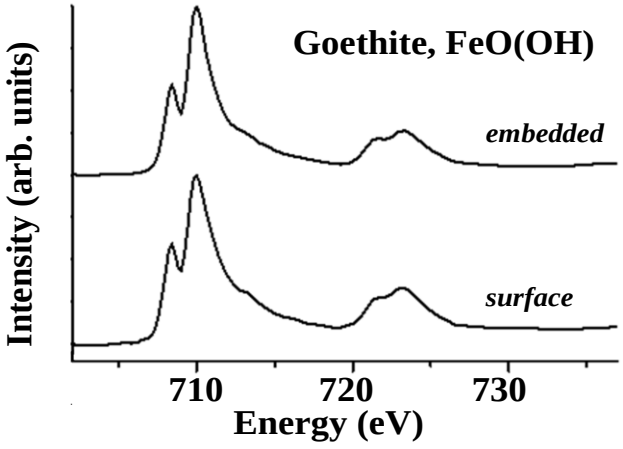

Figure 3.13. STXM iron $L_{2,3}$-edge x-ray absorption spectra obtained from a Fe(III) reference materials (goethite) when resin embedded (top), and directly exposed to the x-ray beam (bottom). No evidence of x-ray beam induced reduction was observed following prolonged periods of x-ray beam exposure.

Iron $L_{2,3}$ x-ray absorption spectra obtained from iron(III) samples maintained under anoxic conditions measured using XAS/XMCD both in the absence (a) and presence (b) of Aβ are shown as a function of time in Figure 3.14.

Where iron(III) was incubated in the absence of Aβ, the XAS spectra obtained were seen to resemble that of iron(III) references (see Figure 1.9; blue) , but with slightly enhanced Fe^{2+} features (Figure 3.14a). As the iron forms used for this experiment were amorphous in nature, this enhancement in iron(II) content is believed to be a result of x-ray beam exposure. No such x-ray beam reduction effects were observed where crystalline iron phases were examined using XAS (see *Chapters 4*, *5* and *6*).

Where Aβ was incubated with iron(III) for 30 minutes, it was not possible to obtain a sufficient signal for reliable XAS and XMCD measurements. However, following 48 hours of incubation with Aβ (Figure 3.14b), clear evidence of enhanced Fe^{2+} cation features were apparent at 708 eV, with iron appearing as an Fe^{2+}/Fe^{3+} intermediate phase (see *Chapter 1; Figure 1.10* for a calculated Fe^{2+}/ Fe^{3+} intermediate XAS spectrum). This moderate reduction effect is likely to be induced x-ray beam exposure, as progressive reduction was seen with increasing periods of beam exposure. After 144 hours of Aβ/iron incubation, iron was found to be reduced to a pure iron(II) phase (Figure 3.14b). The Fe^{2+} cation peak at 708 eV is seen to be dominant, with the Fe^{3+} features at 709.5 eV having disappeared. This reduction effect was mirrored at the iron L_2-edge. As pure iron(II) phases could not be formed in the absence of Aβ, the occurrence of this iron(II) mineral appears to be as a result of Aβ interaction with iron(III).

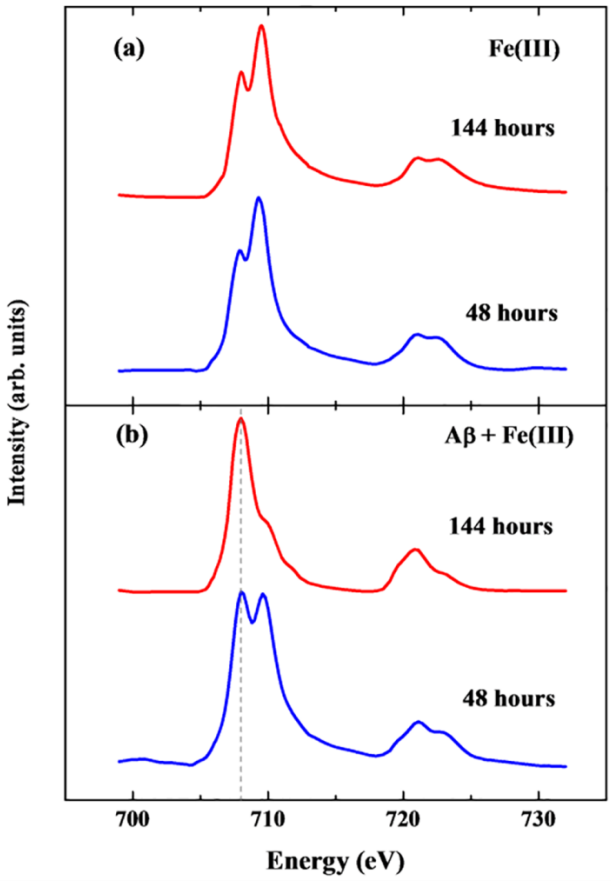

Figure 3.14. Iron $L_{2,3}$-edge x-ray absorption spectra of iron(III) in the absence **(a)** and presence **(b)** of Aβ after 48 and 144 hours of incubation. Grey dashed line at 708 eV in (b) provides a visual guide for the position of the primary Fe^{2+} cation peak.

3.3.2.2 Iron(III) and aluminium(III) series

Iron $L_{2,3}$ x-ray absorption spectra obtained from iron(III) suspensions when incubated with aluminium(III) in the presence and absence of Aβ are shown in Figure 3.15. In the absence of Aβ, no evidence of a pure iron(II) mineral was found at any of the time points examined (Figure 3.15a). Iron regions located after 144 hours of incubation (Figure 3.15a) show an iron *L*-edge spectra characteristic of a pure iron(III) mineral. However, reduced iron can be seen in the Aβ-free control sample after 30 minutes of incubation, manifesting as an enhancement in the shoulder at 708 eV. As for previously described results, this increase in Fe^{2+} cation peak intensity is thought to be due to reduction caused by exposure to the x-ray

beam. Despite this initial x-ray mediated reduction, extensive periods of x-ray beam exposure did not lead to the formation of a pure iron(II) phase.

After 48 hours of iron(III) incubation with Aβ and aluminium(III), iron $L_{2,3}$ x-ray absorption spectra of Aβ/iron aggregates (Figure 3.15b) resembled that of a pure iron(II) phase. The L_3 iron(II) peak at 708 eV had become dominant with the L_3 iron(III) peak at 709.5 eV having disappeared. This pure iron(II) form was very similar to that seen after 144 hours of Aβ/iron incubation in the absence of aluminium (Fig 3.14b), indicating that a similar reduced iron phase had been formed but over a shorter incubation time. However, this pure iron(II) phase was not maintained after 144 hours incubation, with iron reverting back to a largely iron(III) phase with some evidence of a Fe^{2+} cation content (Figure 3.15b). This subsequent oxidation of the pure iron(II) phase for longer incubation times may indicate the establishment of an iron redox cycle.

Importantly, in all cases of amyloid induced reduction stated above, iron was found to be heavily reduced upon first XAS examination (i.e. reduction did not increase as a function of x-ray exposure time). Therefore despite the iron forms used in this study being unstable in the x-ray beam, it was easily possible to separate reduction effects resulting from amyloid interaction, to those induced by x-ray beam exposure.

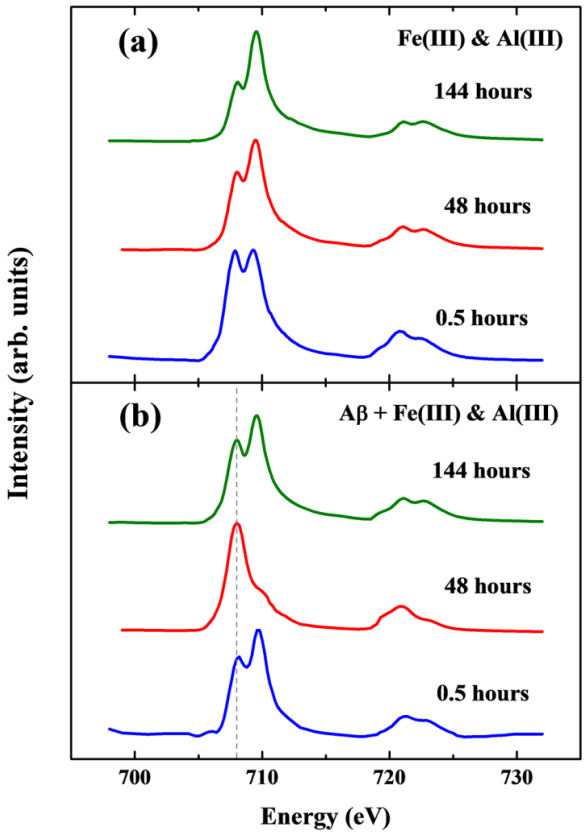

Figure 3.15. Iron $L_{2,3}$-edge x-ray absorption spectra for iron(III) aggregates containing aluminium(III) in the absence **(a)** and presence **(b)** of Aβ. Incubation times are indicated above spectra. The grey dashed line at 708eV (b) is a guide for the position of the primary Fe^{2+} cation peak.

3.3.3 Oxidative state of iron in suspension following Aβ interaction

To further investigate the reduction of iron(III) by Aβ in suspension, a spectrophotometric iron(II) quantification assay was performed. The iron(II) content of suspensions containing Aβ and iron(III), Aβ iron(III) and aluminium(III), and their Aβ-free controls is shown in Figure 3.16a and 3.16b , and respective control corrected iron(II) content are shown in Figure 3.16c and 3.16d.

The iron(II) content of all Aβ-free suspensions was found to remain consistently low throughout all time points examined (Figure 3.16a and 3.16b) with no clear evidence of

iron(II) reduction being apparent. Where iron(III) was incubated with Aβ, no significant increases in control-corrected iron(II) content were seen at the 0, 24 or 48 hour time points (Figure 3.16c). After 72 hours, iron(II) content had risen to 4% and continued to rise to 9% at the 120 hour time point and 15% after 144 hours. Although iron(III) reduction by Aβ is evidenced, redox cycling was not apparent within this time frame, an observation consistent with x-ray absorption measurements (Figure 3.14b).

In iron(III) suspensions containing Aβ and aluminium(III) an immediate conversion of iron(III) to iron(II) was observed, with control corrected iron(II) content accounting for 16% of the total iron content at time zero (Figure 3.16d). Iron(II) levels then dropped to 12% after 24 hours, before rising to 19% after 48 hours incubation. This cycling of iron(II) continued, with iron(II) content disappearing entirely after 72 hours incubation, before increasing to 25% and 42% of total iron content after 120 and 144 hours respectively. This evidence of Aβ-induced iron redox cycling when in the presence of aluminium, is entirely consistent with the XAS measurements displayed in Figure 3.15b.

These results show the reduction of iron(III) by Aβ in suspension, a result consistent with data collected via x-ray absorption spectroscopy (Figures 3.10, 3.11, 3.14 and 3.15). The addition of aluminium appears to have a catalytic effect on iron reduction by Aβ, whilst also acting to increase the reductive capacity of Aβ, enabling the redox cycling of iron.

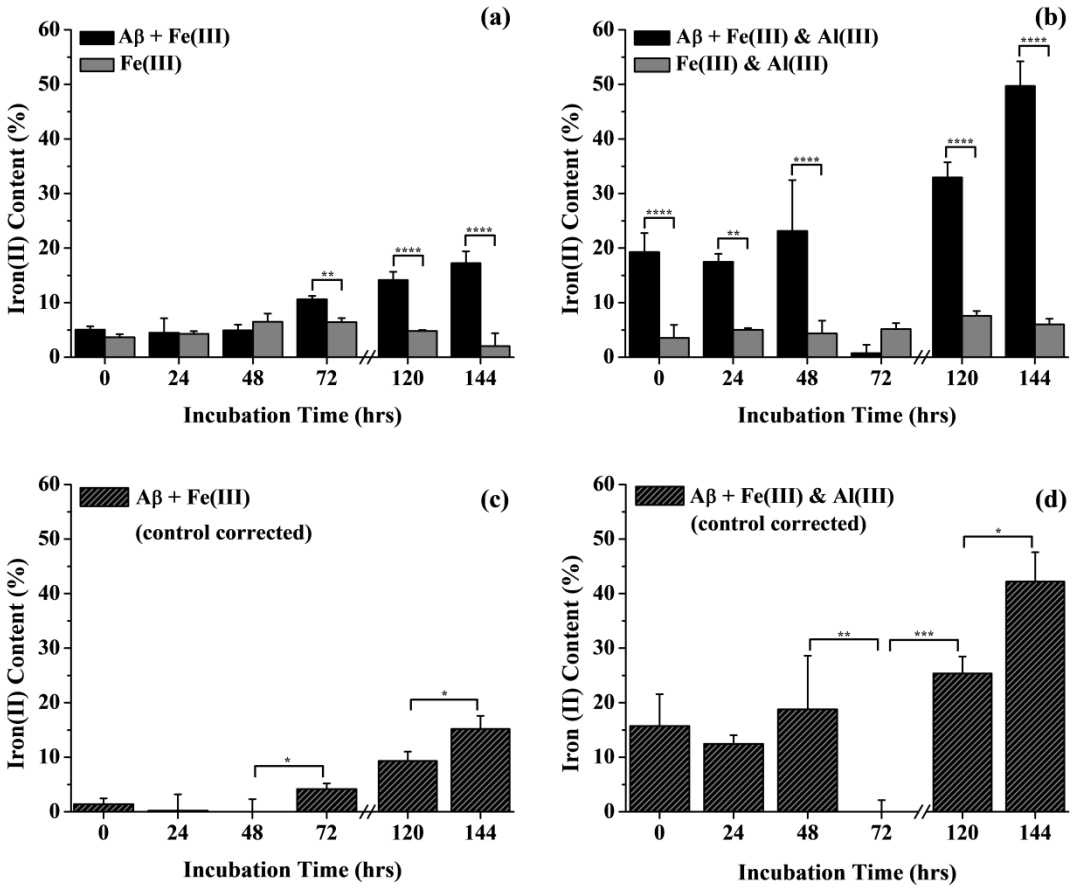

Figure 3.16. Spectrophotometric iron(II) quantification of Aβ suspensions containing iron(III) (**a** and **c**) and iron(III) and aluminium(III) (**b** and **d**). Iron(II) values as a percentage of total iron are shown for both Aβ/iron series and their Aβ-free controls in **(a)** and **(b)**. Control corrected iron(II) values of Aβ/iron suspensions as a percentage of total iron are shown in **(c)** and **(d)**. Note that measurements were not performed at 96 hours. Error bars show standard deviation (n=3); statistically significant differences in mean values for each group comparison (by one-way ANOVA) are indicated by the following levels: ***** $p < 0.05$, ****** $p < 0.01$, *** $p < 0.001$, ******** $p < 0.0001$.

3.3.4 Magnetic state of iron following Aβ interaction

XMCD measurements were conducted across the iron $L_{2,3}$ absorption edges of the samples in order to examine the magnetic state of the iron material present following Aβ interaction.

As described in *Section 1.4.1*, magnetic iron oxides such as magnetite (Fe_3O_4) generate a strong XMCD effect of 10-15%. This XMCD profile (see *Section 1.4; Figure 1.13a*) appears as three peaks across the iron L_3 region as a result of Fe^{2+} and Fe^{3+} cations occupying tetrahedral and octahedral crystal sites [137]. For titanomagnetite (*Section 1.4; Figure 1.13b*) an additional low energy positive peak is observed corresponding to Fe^{2+} cations occupying tetrahedral crystal sites [138]. The oxidation state of the mineral determines the relative intensities of these peaks, with oxidation causing an increase in Fe^{3+} cation intensity with respect to the Fe^{2+} cation peaks, and reduction causing an increase in the Fe^{2+} cation component with respect to the Fe^{3+}.

Iron $L_{2,3}$ absorption-edge XMCD examination of iron(III) and aluminium(III) either in the presence or absence of Aβ, produced spectra with no evidence of strongly magnetic material. Instead a weak magnetic signal of 1-1.5% was observed throughout all samples examined (Figures 3.17 and 3.18). Aβ-free iron(III) and aluminium(III) samples produced spectra comprised of two positive and two negative peaks (Figure 3.17a (red); peaks A-D). By comparison with XMCD spectra obtained from titanomagnetite [138], these peaks appear to arise from the presence of both Fe^{2+} cations (Figure 3.17b, peaks A and B) and Fe^{3+} cations (peaks C and D) that occupy tetrahedral and octahedral crystal sites.

The relative intensities of the peaks A-D shown in Figure 3.17 reflect the oxidation state of magnetic Fe cations. XMCD examination of the pure iron (II) phase formed after 48 hours of Aβ incubation with iron(III) and aluminium(III) showed dramatic enhancement of the Fe^{2+} cation features, with no evidence of Fe^{3+} cations on either the tetrahedral or octahedral sites being apparent (Figure 3.17b). This XMCD signal is consistent with the formation of a weakly magnetic pure iron(II) phase. Subsequent oxidation after 144 hours incubation can be seen as an increase in the Fe^{3+} cation XMCD features (Figure 3.17b), mirroring the behaviour seen in the XAS spectra (Figure 3.15b).

XMCD spectra obtained from the pure iron (II) phase formed following 144 hours of incubation of Aβ with iron(III) (Figure 3.18) were identical to those measured from Aβ incubations containing both iron(III) and aluminium(III) (Figure 3.17b), suggesting a similar weakly magnetic iron(II) phase to have been formed, but over a longer period of time.

It should be noted that some distortions to the XMCD peak intensities are apparent due to background x-ray absorption drift, resulting in a negative or positive slope across the XMCD profile (see Figure 3.17a (blue) and Figure 3.17b (red)). However, despite these distortions, the overall trend of the XMCD spectra remains correct and confirms the oxidation state changes observed by XAS.

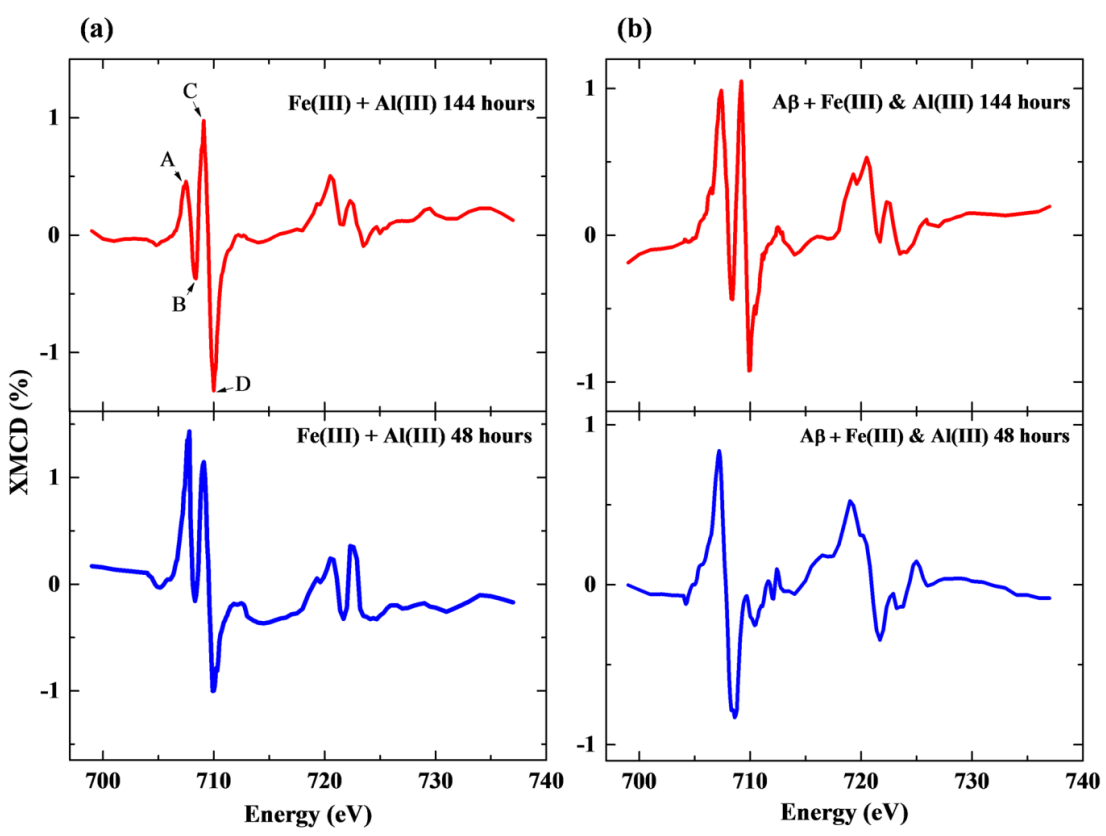

Figure 3.17. Iron $L_{2,3}$-edge XMCD spectra of iron(III) and aluminium(III) aggregates in the absence **(a)** and presence **(b)** of Aβ after 48 and 144 hours of incubation.

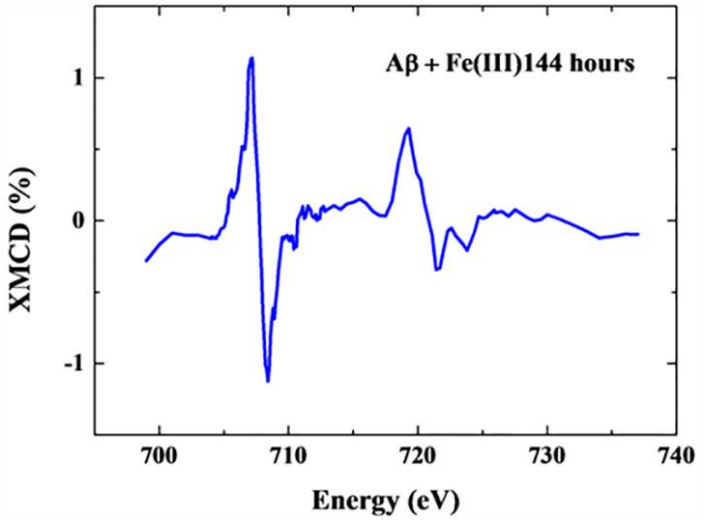

Figure 3.18. Iron $L_{2,3}$-edge XMCD spectra of iron(III) with Aβ after 144 hours of incubation.

3.4 Discussion

Through the use of multiple techniques including scanning transmission x-ray microscopy, electron microscopy, x-ray absorption spectroscopy and spectrophotometric iron(II) quantification, it was found that the AD peptide Aβ(1-42) was capable of incorporating iron(III) minerals into fibrillar aggregate structures *in vitro*, with this interaction leading to the chemical reduction of iron(III) into a pure iron(II) phase.

STXM and TEM images of structures formed following the incubation of Aβ with iron(III) revealed the presence of extensively aggregated amyloid structures containing multiple extensive areas of iron accumulation. As amyloid and iron morphology were often found to be closely correlated, and iron was only observed when co-precipitated with Aβ, these data suggest that Aβ acts to accumulate iron within its structure with possible binding of iron occurring almost immediately (after 30 mins incubation). This effect did not appear to be dependent upon the aggregation state of amyloid, with iron accumulation within Aβ

aggregates occurring where iron(III) was added to pre-formed amyloid aggregates. These findings are in agreement with those published by Jaing *et al.* who suggested Aβ to act as a metalloprotein capable of binding to iron [99].

The iron accumulation into amyloid aggregates that has been observed here may provide an explanation for the increased concentrations of iron previously witnessed in AD plaque material [35]. With iron levels being shown to be increased in the AD brain [34,49,157,158], it is entirely feasible that Aβ acts to draw iron into its structure, where it then binds to the metal. Such a process would explain observations made by Lovell *et al.* who used micro particle-induced x-ray emission analysis to show increased iron levels to exist within senile plaque material compared to surrounding brain tissue [35], and Meadowcroft *et al.* who utilized magnetic resonance imaging to show the accumulation of iron within Aβ plaques [71]. Further to this, the ability of iron to bind to amyloid provides an explanation for the increased iron levels corresponding to areas of AD pathology as witnessed in mice overexpressing Aβ [31].

Iron $L_{2,3}$-edge STXM analysis of iron identified within Aβ aggregates following air exposure, revealed the presence of two aggregates containing small dense regions of iron in a reduced state. X-ray absorption profiles from these regions were reminiscent of a reduced iron(II)/(III) intermediate along with zero valence iron (Fe^0). Interestingly not all iron found within these aggregates was reduced in nature, with some iron appearing to be present in a pure iron(III) phase. These observations indicate that iron reduction by Aβ is not ubiquitous, and may rely on a multitude of factors such as iron deposit size/surface area, aggregate morphology or interaction time. Indeed, the dense nature of the reduced iron deposits witnessed here may have prevented their complete oxidation when exposed to oxygen. In this instance, surface iron content may be in an oxidized ferric state, but the core of the iron deposit remains reduced. Furthermore, despite the carbon *K*-edge spectra

recorded from these Aβ structures being similar to that calculated for the Aβ(1-42) amino acid sequence, TEM imaging revealed the fibrillar nature of Aβ to be lost. Taken together these findings demonstrate the ability of Aβ to chemically reduce iron(III) into redox-active iron phases, with this process potentially altering Aβ fibril arrangement, resulting in the formation of an amorphous protein structure. However as only two instances of an amorphous Aβ structures containing redox-active iron were found, further validation of this hypothesis is required.

XAS examination demonstrating the prevailing oxidation state of iron precipitates maintained under anoxic conditions following incubation with Aβ, revealed the formation of a pure iron(II) mineral after 144 hours of incubation. Such data show Aβ to be capable of inducing the widespread reduction of synthetic iron(III) in the absence of any other influencing factors. These findings also provide validity to the previously described STXM results. However as XAS is not an imaging technique, no solid conclusions can be drawn with regards to amyloid structure in the presence of ferrous iron. Additional evidence of iron reduction by Aβ was provided via iron(II) quantification in suspension, where 15% of the total iron content was found to be in an iron(II) state when incubated following 144 hours of Aβ/iron incubation. The formation of pure iron(II) forms suggests Aβ to possess a strong reducing capacity upon iron, a result consistent with findings published by Khan *et al.* who showed Aβ mediated iron(III) reduction via spectrophotometric methods [96], and also Yang *et al*. who demonstrated Aβ to stabilize ferrous iron *in vitro* [124]. These observations, combined with the previously stated STXM and TEM findings, indicate that Aβ acts to accumulate iron within its structure with this interaction (binding) leading to Aβ mediated iron reduction following prolonged periods of contact.

XAS examination of Aβ aggregates containing both iron(III) and aluminium(III) led to the observation of a similar pure iron(II) phase, but formed over a shorter interaction time (48

hours) than where aluminium was absent. This catalytic effect of aluminium upon Aβ iron reduction was confirmed by iron(II) quantification assay, with the addition of aluminium leading to higher levels of iron reduction. Both XAS and iron(II) quantification assays revealed evidence of iron redox cycling where aluminium(III) was added to Aβ/iron(III) incubations, whereas no evidence of redox cycling was seen in its absence. These results show aluminium to act as an effective catalyst for the interaction of iron with Aβ, enabling the redox cycling of iron over the time period examined. These findings are also consistent with the work of Khan *et al*. who show Aβ to be capable of inducing the redox cycling of iron, with the presence of aluminium(III) appearing to potentiate the reduction of iron(III) to iron(II) [96]; and also recent investigations by Ruiperez *et al.* who show aluminium to promote the Fenton reaction by aiding the reduction of iron(III) to iron(II) [159].

The ability of Aβ to form iron(II) and zero-valent phases from iron precursors reminiscent of naturally occurring ferric iron, provides a possible origin for the redox-active iron forms previously seen within AD tissue, such as the increased levels of the iron(II) rich minerals magnetite and wüstite witnessed in pathological ferritin cores by Quintana *et al.* (2004) [108], along with the accumulation of magnetite-like material within AD plaque cores as observed by Collingwood *et al.* (2008) [36].

XMCD analysis of the magnetic state of iron in samples prepared from both amyloid incubations and amyloid-free controls, revealed iron cations in different crystal symmetry sites reminiscent of octahedral and tetrahedral coordination. The pure iron(II) phases observed by XAS, formed both with and without aluminium, were found by XMCD to contain Fe^{2+} cations arranged with opposing magnetic orientations. This implies the presence of antiferromagnetic coupling between Fe^{2+} cations on different crystal symmetry sites. As no evidence of crystalline iron forms could be obtained via electron diffraction, these pure iron(II) phases could represent an amorphous precursor for an antiferromagnetic

iron(II) mineral such as wüstite. Despite no evidence towards the formation of magnetite formation following Aβ interaction with iron(III) being observed, it is possible that the reduced iron forms witnessed here may act as a precursor for magnetite formation, or are formed in addition to magnetite biominerals in the AD brain.

3.5 Conclusions

From this study it is apparent that Aβ is capable of interacting with iron in a manner that leads to the accumulation and co-aggregation of iron within Aβ structures, resulting in the chemical reduction of redox-inactive ferric iron to a redox-active ferrous and zero-valent iron forms. With iron being abundant throughout brain tissues [46], and iron being shown to be increased in areas of AD pathology (in both human post-mortem tissue and AD transgenic models) [31,34,35], the ability of Aβ to induce the formation of redox-active iron minerals from ferric precursors would represent a significant and sustained source of reactive oxygen species capable of inducing widespread neuronal damage. The interaction of Aβ with iron could thus be an important contributor to the oxidative stress characteristic of AD, thereby playing a key role in the pathogenesis of the disorder. Furthermore the apparent ability of Aβ to reduce iron(III) to an iron(II) phase even when iron is present in a 10:1 excess of Aβ, strongly suggests that Aβ is an efficient biological iron-reducing agent. The catalytic function of aluminium(III) upon Aβ mediated iron reduction as witnessed in this study is also of vital importance. With aluminium being implicated as a promoting factor for the development of AD, including the neuropathological hallmarks of the disorder [160], any synergies existing between Aβ, iron and aluminium are likely to influence the nature of AD progression [160,161].

As pure iron(II) and zero-valence phases do not occur naturally *in vivo* [107,108], these pathological iron biominerals may represent a target for future therapies. Removal of such

forms of iron, or disruption in the ability of Aβ to interact with iron, may result in a reduction of the free radical burden associated with the AD brain and consequently a slowing of disease progression. The addition of aluminium appears to impact the reductive capacity of Aβ by increasing its ability to reduce iron(III) in suspension. Aluminium is also not naturally found within human tissues [162], and therefore its removal from brain tissue may act to reduce Aβ neurotoxicity, whilst not impacting healthy brain functions. In summary, key insights into the relationship between Aβ and iron have been made that provide valuable insights into the role played by iron in AD pathology.

3.6 Implications for further work

In this study the feasibility of utilizing advanced x-ray synchrotron techniques for the monitoring of metal oxidation/magnetic states following protein interaction, and also for the element specific imaging of protein aggregates containing areas of metal deposition has been successfully demonstrated. The results obtained here provide a platform from which further experiments can be devised examining the role of Aβ in the generation of potentially pathological redox-active iron phases. Additional development of methodology (such as improved anaerobic chambers for STXM sample transfer) coupled with the analysis of a greater number of aggregate types would act to strengthen the conclusions described above.

Although the results displayed in this chapter should not be interpreted as a 'model' for the processes that occur in the AD brain, they do provide a proof of principle (the monitoring of iron oxidation state following Aβ interaction, using synchrotron-based techniques) from

which systems more indicative of those that occur naturally can be developed (see *Chapters 4* and *5*).

Finally attention should be drawn to the batch variability witnessed in commercially available Aβ [163]. Such variability may alter the processes of Aβ/iron interaction, along with the ability of Aβ to chemically reduce iron(III) deposits, providing a further source of inhomogeneity.

Chapter 4

Evidence of redox-active iron formation following aggregation of ferrihydrite and the Alzheimer's disease peptide β-amyloid

4.1 Introduction

As described in *Chapter 1*, a link has been established between areas of iron accumulation and AD pathology [34,39,70], namely structures comprised of the AD peptide Aβ [31,35-37,42,71]. Of particular interest is the increased levels of iron(II) bearing redox-active biominerals found to be present in AD tissues compared to that of age matched disease free control tissue, due to their ability to induce oxidative stress [36,58,60,76,105,108,112,113].

In the previous chapter the ability of Aβ to accumulate (and potentially bind) amorphous iron(III) within its fibrillar structure was demonstrated, with this interaction resulting in the chemical reduction of iron(III) into pure iron(II) and zero-valent (reminiscent) iron phases. Such interactions offer an explanation for the association of iron within areas of Aβ deposition [31,35,71], possible origins to the wüstite-like material previously observed in AD tissue [108], and also provide potential precursors to magnetic iron biomineral formation.

However, within the human brain, iron is not necessarily present as an amorphous iron(III) phase, and therefore the process of Aβ/iron interaction as described in *Chapter 3*, may not be entirely representative of that occurring *in vivo*. In human tissue, iron is stored as ferrihydrite within the storage protein ferritin [129-64]. Ferrihydrite is a poorly crystalline ferric iron phase, with antiferromagnetic properties at room temperature [17]. As iron is seen to associate with regions of Aβ pathology [31,35,37,71], it reasons that iron in a ferrihydrite form, may come into contact with the amyloid peptide. With ferrihydrite being crystalline [129], this iron form could represent a precursor to the formation of the iron(II) bearing crystalline phases as seen in AD tissue [36,60,108,113], should Aβ be capable of inducing ferrihydrite reduction. Indeed, ferrihydrite has been shown to be a precursor for biogenic magnetite formation in iron(III)-reducing microbes, such as the bacteria *Geobacter sulfurreducens* [137].

At present, the interaction between Aβ and ferrihydrite has not been investigated, and the products of such processes are currently unknown. In this chapter a multidisciplinary approach is employed to examine the interaction between the AD peptide Aβ and synthetic 2-line ferrihydrite, an iron form representative of those that occur in the human brain.

XAS data demonstrating changes in the oxidation state of ferrihydrite when incubated with Aβ over a 144 hour period will be presented, along with simultaneous XMCD measurements probing changes in the magnetic properties and cation distributions of the iron mineral (*Section 4.3.1*). Additional magnetic characterization of ferrihydrite following incubation with Aβ is supplied via SQUID magnetometry (*Section 4.3.2.1*) and AC susceptometry (*Section 4.3.2.2*). Further to this, microstructural and phase analysis of Aβ/ferrihydrite structures are provided via TEM, atomic force microscopy (AFM) and STXM (*Section 4.3.3*). Iron(II) quantification assays evaluating the proportion of ferrihydrite reduced by Aβ are then displayed (*Section 4.3.4*). Additionally, electron diffraction patterns revealing alterations to the crystal structure of ferrihydrite following Aβ interaction are presented (*Section 4.3.5*). Through the use of these techniques, the iron mineral products formed through Aβ/ferrihydrite interaction are characterized. Finally, I will discuss the importance of these results in determining how Aβ/iron interactions contribute to AD pathology (*Sections 4.4 and 4.5*), and how these results complement those presented in the previous experimental chapter (*Section 4.6*).

4.2 Material and methods

4.2.1 Ferrihydrite synthesis

Ferrihydrite particles were synthesized by neutralizing 100g/L iron(III) chloride solution to pH 7 using 10 M sodium hydroxide (NaOH). The resulting ferrihydrite suspension was centrifuged at 10 000 rpm for 20 minutes and all supernatant removed. This centrifugation process was repeated six times by repeatedly suspending the ferrihydrite particles in deionized water and removing the supernatant [164].

4.2.2 Preparation of β-amyloid/ferrihydrite suspensions

Ferrihydrite suspensions (440 μM) were prepared from the ferrihydrite stock diluted with deionized water. A 220 μM Aβ stock solution was created as described in *Chapter 3*, before being added to the 440 μM ferrihydrite suspension. Ferrihydrite suspensions were sonicated for 5 minutes prior to the addition of the Aβ stock ensuring uniform ferrihydrite particle distribution. Resulting Aβ/ferrihydrite suspensions were neutralized to pH 7 with 0.5 M hydrochloric acid (HCl). Final Aβ and metal concentrations were 35 μM and 370 μM respectively. Aβ/ferrihydrite suspensions were incubated at 37°C until time of sampling. Aβ-free ferrihydrite controls were created as stated above by substituting deionized water for Aβ.

4.2.3 X-ray absorption and x-ray magnetic circular dichroism spectroscopy

Small sample volumes (15 µL) were deposited onto copper TEM grids, and grids were mounted onto copper sample holders as described in *Section 2.1*. Sampling was performed under anoxic conditions after 30 minutes, 48 hours and 144 hours of incubation at 37°C. XAS and XMCD measurements were performed on Aβ/ferrihydrite samples, and their Aβ-free controls using beamline I10 at the Diamond Light Source (Oxfordshire, UK), and beamline 4.0.2 at the Advanced Light Source (Berkeley, USA). XAS and XMCD spectra were recorded as described in *Sections 2.1.3 and 2.1.4*. To locate ferrihydrite accumulations, two dimensional iron maps were obtained as defined in *Section 2.1.3*. Detailed XAS and XMCD measurements across the iron $L_{2,3}$ absorption-edge region (700-740 eV) were conducted on areas of ferrihydrite accumulation to study both the iron oxidation and magnetic states. Not all grids provided regions of iron with sufficiently strong x-ray absorption signal to allow full XAS and XMCD analysis.

4.2.4 SQUID magnetometry

To confirm the magnetic state of ferrihydrite following incubation with Aβ, SQUID magnetometry was performed. Small volumes of Aβ/ferrihydrite suspensions (and their Aβ-free controls) were deposited into plastic tubes and flash frozen as described in *Section 2.5*. Samples were taken following 48 hours of Aβ/ferrihydrite incubation at 37°C. Hysteresis loops revealing the magnetic state of the Aβ/ferrihydrite materials were created by measuring the magnetic moment against an applied magnetic field (-5000 , 5000 Oe) at various temperatures ranging from 10-200 K to overcome the superparamagnetic properties of any nanoscale iron present. Measurements were performed using a Quantum Design SQUID-VSM. Hysteresis loops from a 370 µM magnetite nanoparticle suspension

(Sigma Aldrich <50 nm diameter) were generated as described above to provide a ferrimagnetic positive control.

4.2.5 AC susceptometry

The magnetic susceptibility of 200 μL of Aβ/ferrihydrite suspension was monitored at a frequency of 1 kHz over a 136 hours period using an AC susceptometer. Temperature was maintained at 37°C throughout data collection. Aβ-free ferrihydrite and magnetite (370 μM, synthesized *in situ* as per the Massart method [165]) suspensions were monitored at 1 kHz over a 16 hour period to provide reference values for ferrihydrite and (ferri)magnetic materials respectively. The frequency of 1 kHz was chosen, as this value lies within the detection threshold of the AC magnetic susceptometer instrumentation, when examining dilute samples (< 500 μM) as used in this thesis.

Additional susceptibility measurements were performed on 0.2 M magnetite suspensions created *in situ* by the Massart method; to demonstrate the effectiveness of this approach in monitoring the formation of magnetic iron phases from non-magnetic precursors.

4.2.6 Electron microscopy

15 μL of Aβ/ferrihydrite suspensions and their Aβ-free controls were deposited onto carbon/formvar coated copper TEM grids and excess liquid removed. Samples were taken after 30 minutes, 48 hours and 144 hours of incubation at 37°C and examined using a JEOL 1230 TEM operating at 100 kV. These samples were not exposed to the x-ray beam used in XAS/XMCD.

4.2.7 Scanning transmission x-ray microscopy

Aβ/ferrihydrite samples examined by XAS/XMCD were subsequently investigated using STXM on the PolLux beamline at the Swiss Light Source (Villigen, Switzerland).

Sample TEM grids were mounted onto stainless steel plates for STXM examination, and exposed to air throughout sample storage and transfer. Element specific images displaying the carbon and iron content of amyloid aggregates were created as previously described in *Section 2.2.2*

4.2.8 Time lapse imaging

Time lapse videos displaying the precipitation of ferrihydrite by Aβ were created using Lapse it™ time lapse software. Images were taken once a minute for a period of 8 hours. Aβ/ferrihydrite solutions were kept at 37°C throughout the imaging process.

4.2.9 Atomic force microscopy

Three dimensional topographic images of Aβ/ferrihydrite samples previously examined by TEM were generated using a Bruker BioScope Catalyst™ BioAFM. Images were to a spatial resolution of 35 nm. Three dimensional representations of Aβ/ferrihydrite surface structures were created via the use of Nanoscope analysis 1.4 software.

4.2.10 Quantification of iron(II) in suspension: Ferrozine assay

The iron(II) content of amyloid/ferrihydrite and amyloid free ferrihydrite samples was quantified in solution using a Ferrozine colorimetric assay as described in *Section 2.4* [153]. Ferrozine readings were taken after 0, 24, 48, 72, 120 and 144 hours of incubation at 37°C. No samples were taken at 96 hours due to limited sample volumes. Different Aβ

batches were used to the create Aβ/ferrihydrite solutions for iron(II) quantification, and for XAS/XMCD measurements.

4.2.10.1 Statistical analysis

Statistical analysis of iron(II) quantification data was conducted using a one-way analysis of variance (GraphPad Prism 6). This performs a hypothesis test of the equality of two or more population means. The null hypothesis of equal means was rejected at the 5% confidence level.

4.3 Results

4.3.1 Ferrihydrite oxidation and magnetic state following incubation with Aβ

Iron $L_{2,3}$ x-ray absorption spectra obtained from ferrihydrite incubated in the presence and absence of Aβ are shown in Figure 4.1, as a function of incubation time. From Figure 4.1a the Aβ-free ferrihydrite samples have x-ray absorption spectra characteristic of iron(III) minerals for all timing points, with only Fe^{3+} cation features being observed (see *Chapter 1; Figure 1.9* for reference iron(III) mineral spectrum).

After 30 minutes of Aβ/ferrihydrite incubation, XAS examination at the iron $L_{2,3}$-edges (Figure 4.1b) showed the emergence of a significant Fe^{2+} cation component as evidenced by the enhanced 708 eV feature in comparison to Aβ-free ferrihydrite (Figure 4.1a). Following 48 hours of incubation with Aβ (Figure 4.1b), ferrihydrite accumulations were found to be strongly reduced, with spectra closely resembling a pure iron(II) mineral (see *Chapter 1; Figure 1.9* for reference iron(II) spectra). This reduction effect was also mirrored at the L_2 absorption region.

Further incubation of Aβ with ferrihydrite to 144 hours (Figure 4.1b), led to the observation of a Fe^{2+} cation rich Fe^{2+}/ Fe^{3+} intermediate spectrum (see *Chapter 1; Figure 1.10* for a calculated Fe^{2+}/ Fe^{3+} intermediate XAS spectrum) . Although oxidized in comparison to the pure iron(II) mineral observed after 48 hours of incubation, ferrihydrite remained heavily reduced compared to Aβ-free ferrihydrite controls (Figure 4.1a), with a large Fe^{2+} cation peak at 708 eV, followed by a smaller but distinct Fe^{3+} cation peak at 709.5 eV.

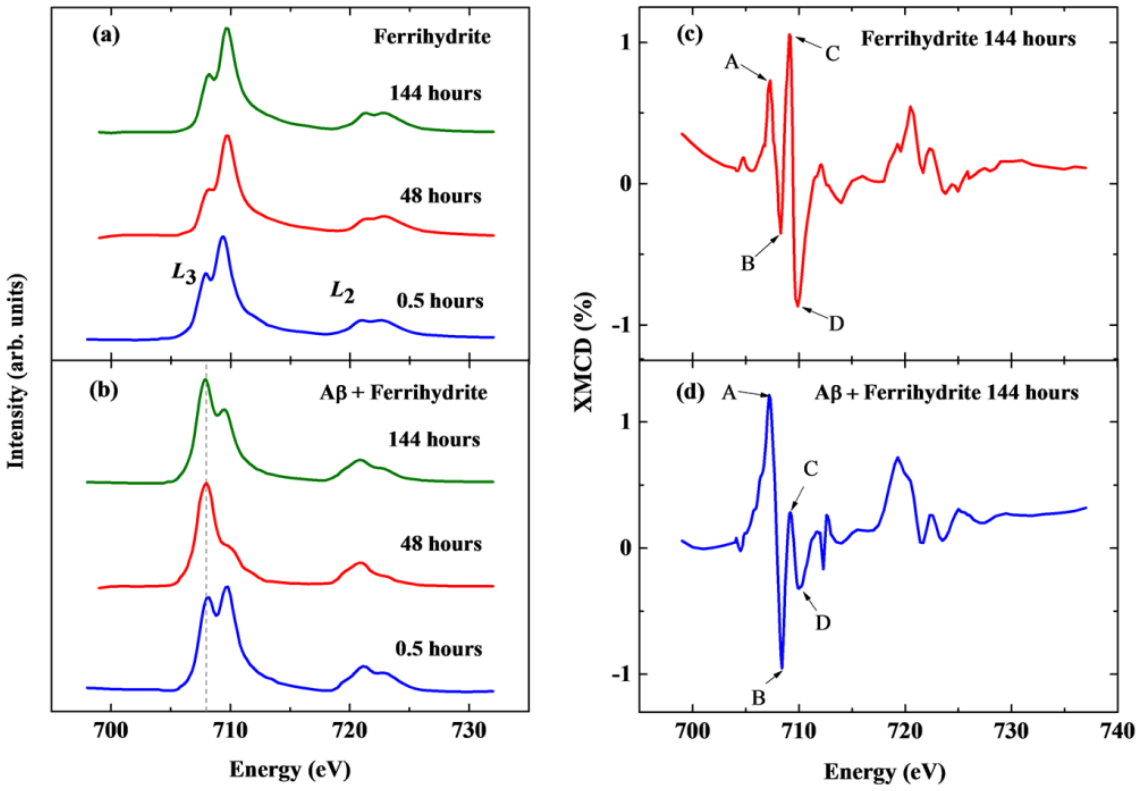

Figure 4.1. X-ray absorption spectra showing the iron $L_{2,3}$-edge of ferrihydrite aggregates incubated **(a)** in the absence of Aβ, and **(b)** in presence of Aβ. Incubation times are shown above the spectra. L_2 and L_3 regions are labelled in (a). The dashed grey line at 708 eV (b) shows the approximate position of the principle Fe^{2+} cation peak. Iron $L_{2,3}$-edge XMCD spectra of ferrihydrite aggregates after 144 hours of incubation in the absence of Aβ, and in the presence of Aβ are shown in **(c)** and **(d)** respectively.

To confirm that these reduction effects were induced by Aβ, the impact of repeated x-ray beam exposure on the samples was assessed (Figure 4.2). Only a subtle x-ray beam induced reduction effect in the Aβ-free control samples was observed (Figure 4.2a). This is likely to be a result of ferrihydrite crystalline structure, making the mineral less susceptible to x-ray beam reduction than the amorphous iron forms examined in *Chapter 4*. However Aβ/ferrihydrite samples taken after 30 minutes of incubation appeared more susceptible to x-ray beam reduction (Figure 4.2b), possibly due to destabilization of the ferrihydrite crystal structure by Aβ (refer to *Section 3.3.2.1* for further explanation of x-ray beam induced iron reduction). Despite this reduction effect, it was impossible to form pure iron(II) phases such as those seen following 48 hours of Aβ/ ferrihydrite incubation (Figure 4.1b; red), even after prolonged x-ray beam exposure.

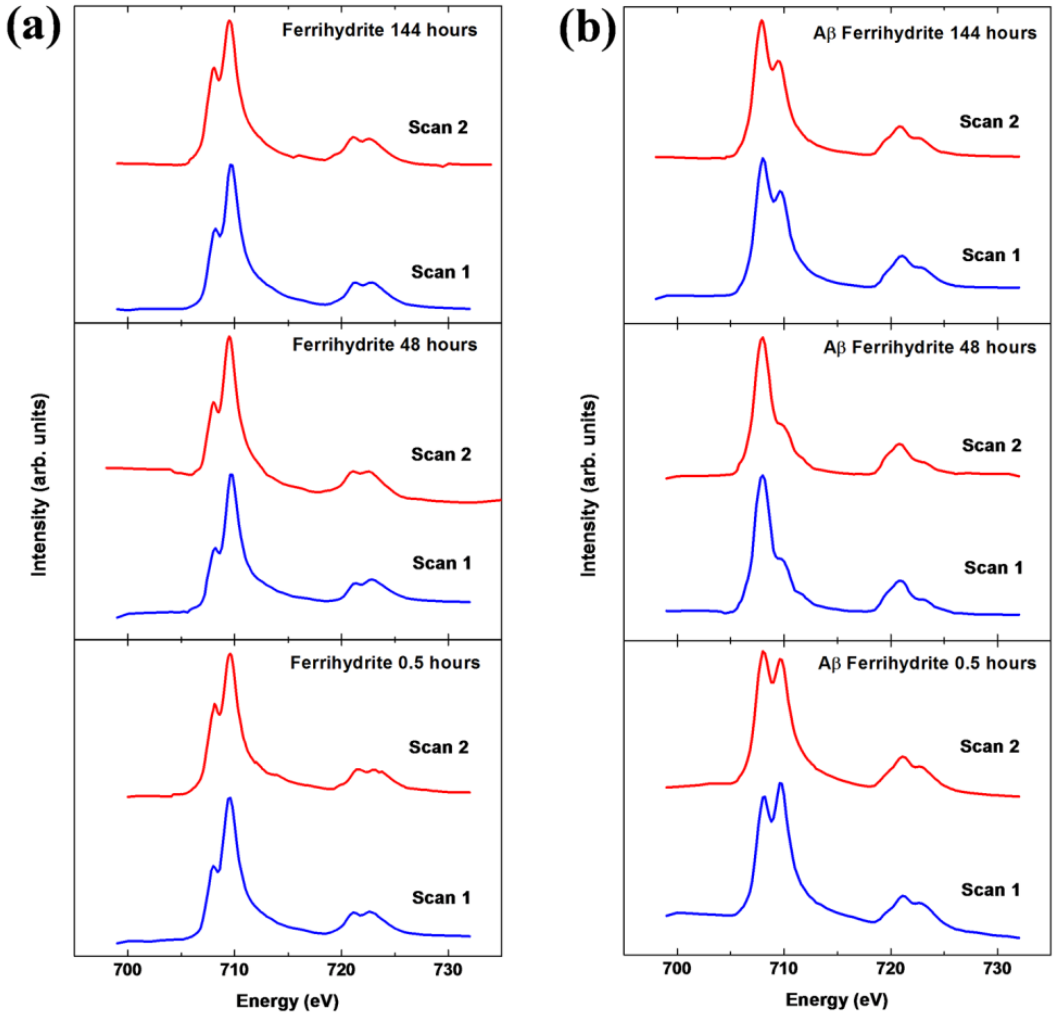

Figure 4.2. X-ray absorption spectra of the ferrihydrite iron $L_{2,3}$-edge in the absence **(a)** and presence **(b)** of Aβ, for successive XAS measurement repetitions. Scan number and incubation times are shown above the XAS spectra.

The magnetic state of the samples was probed by XMCD across the iron $L_{2,3}$ absorption edges. As described in *Chapters 1* and *3*, magnetic iron oxides such as magnetite (Fe_3O_4) generate a strong XMCD effect of 10-15% (for reference XMCD spectra refer to *Chapter 1; Figure 1.13*).

The XMCD spectrum obtained from Aβ-free ferrihydrite after 144 hours incubation is shown in Figure 4.1c. At room temperature ferrihydrite is expected to be in an antiferromagnetic or weakly ferrimagnetic state, with superparamagnetic properties due to

the nanoscale crystal size [166]. Here we observe a small (1-1.5%) XMCD effect and evidence of antiferromagnetic ordering of the cation moments, manifested as approximately equal intensity positive and negative peaks (labelled A,B,C and D). The clear energy separation of these peaks implies that the iron cations occupy two non-equivalent crystal symmetry sites, similar to the tetrahedral and octahedral sites in magnetite. The relative intensities of the XMCD peaks in Figure 4.1c suggests the presence of predominantly Fe^{3+} cations (peaks C and D), with minor contributions from Fe^{2+} cations (peaks A and B). However, the XMCD spectrum obtained from the sample incubated with Aβ (Figure 4.1d) shows a dramatic enhancement in the Fe^{2+} cation peaks (A and B), whilst preserving the antiferromagnetic ordering seen in the Aβ-free ferrihydrite.

Hence XMCD measurements confirm the iron reduction seen via XAS (Figure 4.1b), and suggest the formation of an antiferromagnetically ordered Fe(II) phase. It is possible that this phase represents a precursor for the mineral wüstite ($Fe_{1-x}O$) [167,168], although the antiferromagnetic order seen here would not be expected, as XMCD measurements were performed at room temperature and were therefore above the Néel temperature (the temperature at which antiferromagnetic spin ordering is thermally disrupted) for wüstite (~200K).

4.3.2 Magnetic characterization of Aβ/ferrihydrite suspensions

Further magnetic characterization of Aβ/ferrihydrite suspensions was achieved via SQUID magnetometry and AC susceptometry.

4.3.2.1 SQUID magnetometry

Hysteresis loops displaying the magnetic moment of Aβ/ferrihydrite suspensions following 48 hours of incubation are shown in Figure 4.3a-d. At 200 K no changes in the magnetic moment of Aβ/ferrihydrite suspensions were observed in response to a varying external magnetic field. This suggests the presence of a paramagnetic material, demonstrating there to be no ferrimagnetic/ferromagnetic component to the hysteresis loop at 200 K. However below 100 K, hysteresis loops from Aβ/ferrihydrite suspensions show evidence of magnetic moment alignment, as evidenced by the appearance of magnetic coercivity in response to an applied field. These measurements suggest a modest, soft ferromagnetic/ferrimagnetic contribution from ferrihydrite particles at temperatures below 100 K.

Hysteresis loops obtained from Aβ/ferrihydrite suspensions at 10 K (Figure 4.3e), were almost indistinguishable to those obtained from ferrihydrite reference suspensions at 10 K; demonstrating there to be no increase in magnetic iron materials following ferrihydrite incubation with Aβ. The magnetic response of these ferrihydrite suspensions were approximately 15 times smaller than that observed in concentration-matched magnetite reference suspensions (Figure 4.3f). These values are consistent with the XMCD results shown in Figure 4.1c-d, where ferrihydrite was shown to produce a XMCD effect of 1-1.5%, compared to the XMCD effect of 10-15% characteristic of strongly magnetic iron minerals, such as magnetite (*Section 1; Figure 1.13*).

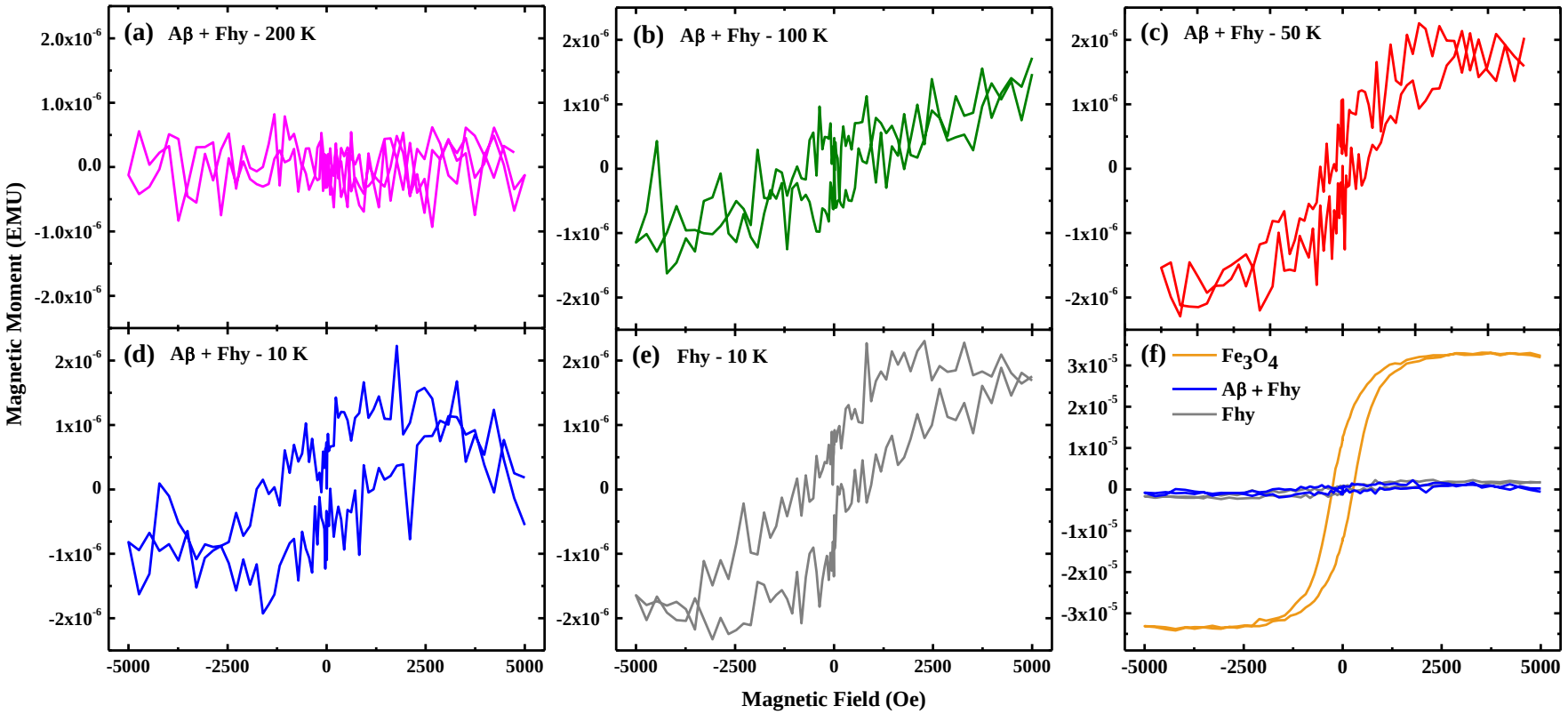

Figure 4.3. Hysteresis loops displaying the magnetic moment (EMU) versus magnetic field (Oe) of Aβ/ferrihydrite suspensions following 48 hours of incubation, along with 370 µM concentration matched ferrihydrite (Fhy) and magnetite (Fe_3O_4) references. Hysteresis loops from Aβ/ferrihydrite suspensions were obtained at **(a)** 200 K, **(b)** 100 K, **(c)** 50 K, and **(d)** 10 K. **(e)** Ferrihydrite control suspension measured at 10 K. **(f)** Magnetite suspension measured at 10K (gold), compared to Aβ/ferrihydrite (blue) and ferrihydrite (grey) suspensions as shown in (d) and (e) respectively. Note the change in vertical scale for (f).

4.3.2.2 AC susceptometry

To assess the suitability of the AC magnetic susceptometry instrumentation to detect the *in situ* formation of nanoscale ferrimagnetic/ferromagnetic materials, and to monitor the magnetic susceptibility of ferrihydrite suspensions when incubated in the presence and absence of Aβ, AC susceptibility measurements were performed.

AC susceptibility values obtained at applied magnetic field frequencies of 1 kHz, from a 0.2 M magnetite suspension created *in situ* as a function of time are shown in Figure 4.4. At the start point (time = 0), χ' and χ" susceptibility values are zero, due to the non-magnetic nature of the iron(II) and iron(III) precursors used in magnetite synthesis. However, from 2-28 minutes there is a steady increase in χ' and χ" signals, demonstrating an increase in magnetic susceptibility owing to the formation of magnetite nanoparticles. From 30 minutes onwards these values stabilize, suggesting magnetite formation to have ceased. These results demonstrate the effectiveness of AC susceptibility measurements in the monitoring of nanoscale magnetic iron mineral formation.

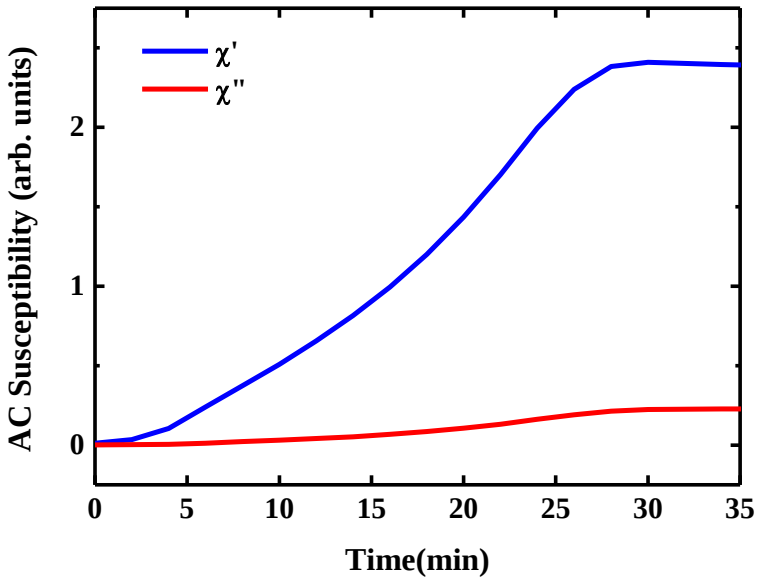

Figure 4.4. AC susceptibility measurements taken at 1 kHz, demonstrating the formation of a 0.2 M magnetite suspension over a 35 minute period, following the incubation of ferric chloride and ferrous chloride in the Massart reaction [165].

AC susceptibility values from magnetite, ferrihydrite and Aβ/ferrihydrite suspensions as a function of incubation time are displayed in Figure 4.5a, 4.5b and 4.6 respectively.

Where a 370 μM magnetite suspension was created *in situ*, time-dependent AC susceptibility measurements taken at 1 kHz, revealed a steady increase in χ' values over the first 3 hours of monitoring, corresponding to the formation of magnetite particles (Figure 4.5a). This rate of magnetite synthesis was slower than that observed in Figure 4.4, a likely result of the much lower concentrations of iron(II) and iron(III) used. Following this initial period of synthesis, a stable χ' susceptibility value was recorded until monitoring stopped following 16 hours of incubation. These steady positive χ' values are representative of a small ferrimagnetic signal, demonstrating the detection threshold of the equipment used in this experiment to be sufficiently low to successfully detect small increases in magnetic susceptibility (i.e. small amounts of magnetite formation). Furthermore, a small positive χ" value was observed throughout the period of measurement, demonstrating the presence of nanoscale ferrimagnetic/ferromagnetic particles.

In 370 μM ferrihydrite reference suspensions (Figure 4.5b), AC susceptibility measurements at 1 kHz revealed negative χ' values of approximately -1 x 10^{-3} throughout the examination period. Negative values are typical of a diamagnetic material. However, at the temperature of examination (37°C), ferrihydrite should elicit a paramagnetic response, resulting in a small positive χ' signal. This negative χ' offset appears to be induced by the diamagnetic solvent (water) used to create the ferrihydrite suspensions, thus masking the small paramagnetic signal provided by the ferrihydrite particles. Indeed, these negative χ' values are consistent with those measured from water under the same conditions (data not shown). χ" values of zero were recorded from ferrihydrite suspensions over the 16 hour

examination period, a response typical of paramagnetic and diamagnetic materials, therefore indicating no ferro/ferrimagnetic nanoparticles to be present in the ferrihydrite suspensions.

Where Aβ was incubated with ferrihydrite over a 136 hour period (Figure 4.6), magnetic susceptibility values at 1 kHz were largely similar to those obtained from ferrihydrite reference suspensions (Figure 4.5). Interestingly however, χ' values obtained from Aβ/ferrihydrite suspensions (Figure 4.6; red) reveal a subtle increase in diamagnetic signal strength over the first 48 hours of incubation (from -1×10^{-3} to -1.3×10^{-3}). Peptides are known to be diamagnetic, and β-pleated peptide structures have been demonstrated to produce substantial diamagnetic anisotropy [169]. Therefore, this increase in diamagnetic signal may correspond to the aggregation of Aβ into β-pleated fibrillar structures, before a stable aggregate size is reached following 48 hours incubation. χ" values of zero were obtained from these Aβ/ferrihydrite suspensions indicating no substantial ferromagnetic/ferrimagnetic material to have formed over the incubation period. These findings are in keeping with the XMCD and SQUID results shown in Figure 4.1d and 4.3 where no evidence of a strongly magnetic material was observed following Aβ incubation with ferrihydrite.

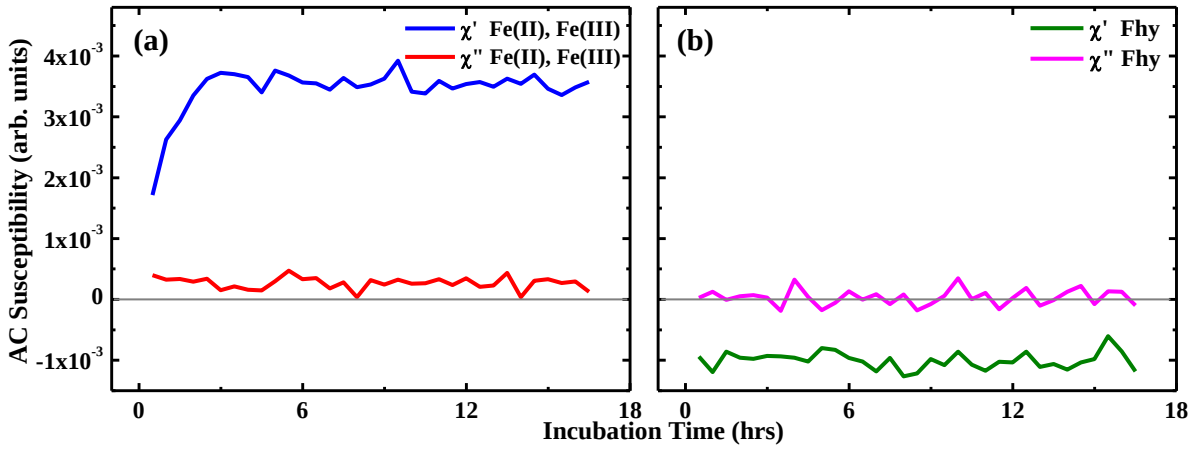

Figure 4.5. AC susceptibility values obtained from **(a)** 370 µM magnetite suspensions (Fe_3O_4; formed *in situ*) and **(b)** 370 µM ferrihydrite (Fhy) suspensions, incubated at 37°C over a 16 hour period. Measurements were taken at 1 kHz.

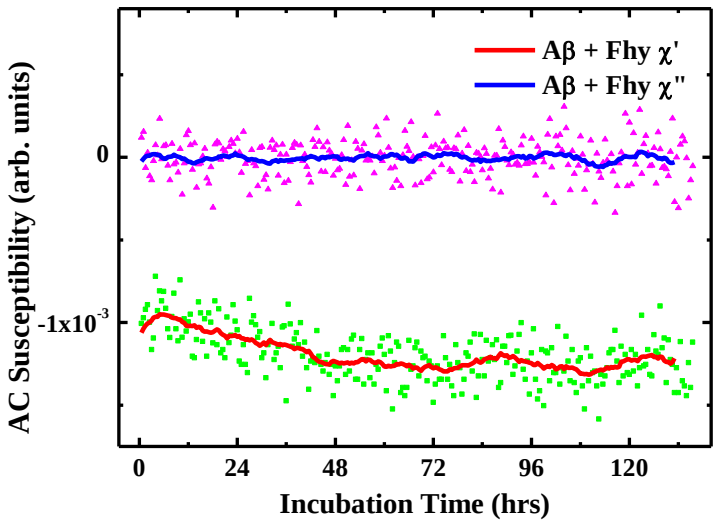

Figure 4.6. AC susceptibility values obtained from Aβ/ferrihydrite suspensions incubated at 37°C for 136 hours. Measurements were taken at 1 kHz. Symbols represent raw data, coloured lines represent smoothed data.

4.3.3 Structural characterization of Aβ/ferrihydrite aggregates

TEM and STXM images of Aβ incubated with ferrihydrite are presented in Figure 4.7. TEM examination revealed Aβ aggregates of 1-50 μm in diameter, possessing fine fibril structure integrated with dense particles of approximately 50 nm, across all time points examined (Figure 4.7a).

To investigate the origin of the dense material within fibrillar Aβ structures, element specific mapping of Aβ/ferrihydrite aggregates incubated for 30 minutes was performed using STXM. Carbon *K*-edge and iron L_3-edge STXM images of an Aβ/ferrihydrite aggregate are presented in Figure 4.7b. Carbon *K*-edge examination revealed amyloid aggregates similar in nature to those pictured using TEM (Figure 4.7a). Corresponding iron L_3-edge STXM images showed iron content to closely follow Aβ morphology, suggesting integration and possible binding of the fine ferrihydrite particles with the Aβ fibrils. In addition, larger, intense iron spots similar in size to the electron dense particles shown in Figure 4.7a can be seen scattered throughout the Aβ aggregate, suggesting that Aβ acts to bind and accumulate ferrihydrite within its structure. This correlation between Aβ and ferrihydrite content was clearly different to the Aβ/ iron(III) structures shown in *Chapter 3; Figure 3.9*, where large amorphous iron precipitates, several microns in diameter, appeared to be co-localized within Aβ aggregates, rather than being loaded into the Aβ fibrils.

This process of ferrihydrite aggregation by Aβ was further demonstrated via time lapse imaging of solutions containing Aβ and ferrihydrite (Figure 4.8). Where the peptide was incubated with ferrihydrite a clear orange precipitate can be seen to form following approximately 60 minutes of incubation, which remained suspended in the sample medium throughout the 8 hour examination period. No dense orange precipitates were observed in Aβ-free ferrihydrite suspensions.

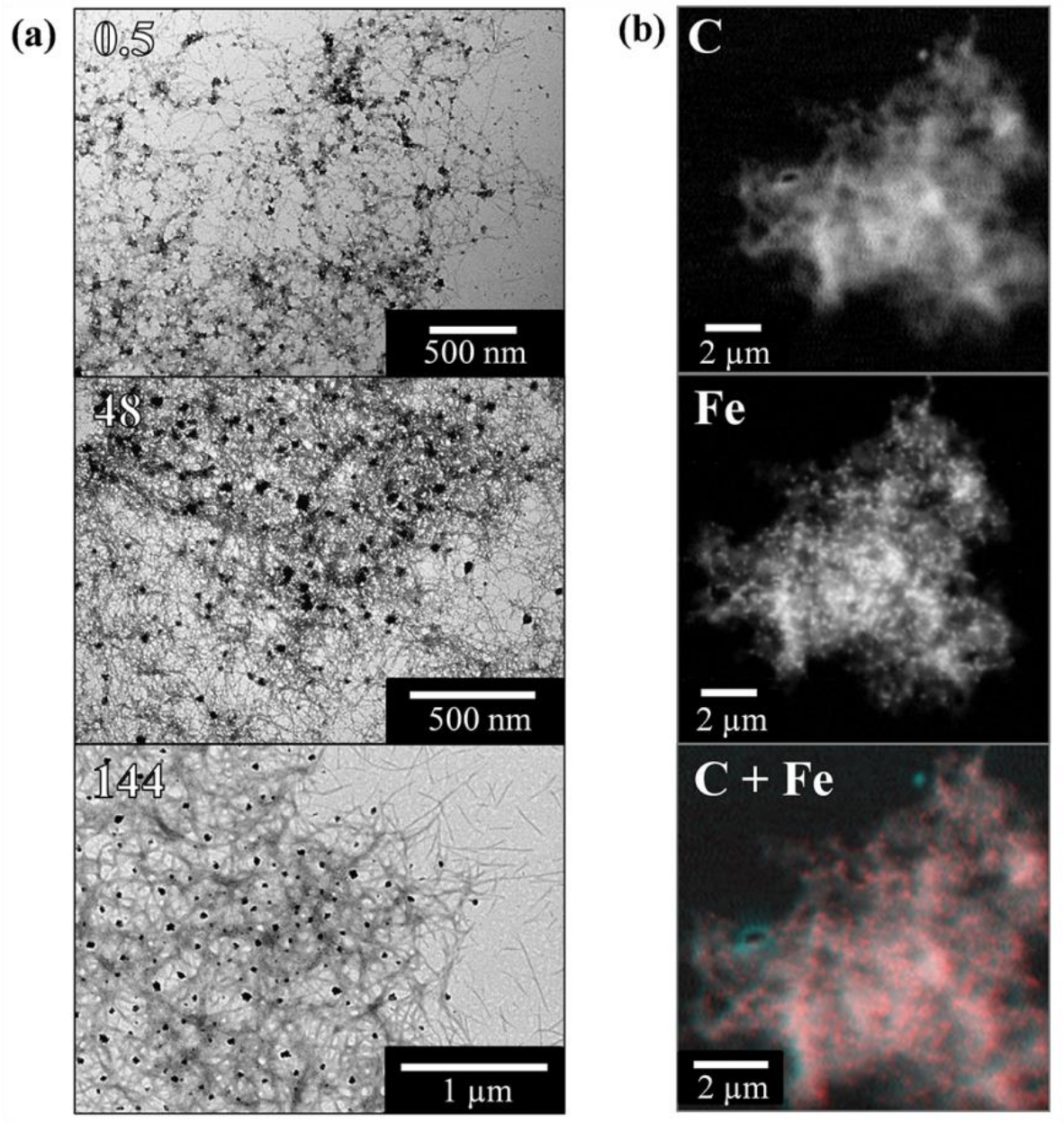

Figure 4.7. (a) Bright field TEM images and **(b)** STXM images of fibrillar amyloid structures formed following the incubation of Aβ with ferrihydrite. TEM pictures show Aβ structures present after 0.5, 48 and 144 hours of incubation. STXM images show the carbon (C) and iron (Fe) content of an Aβ/ferrihydrite aggregate along with a carbon/iron (C + Fe) composite image of the same aggregate.

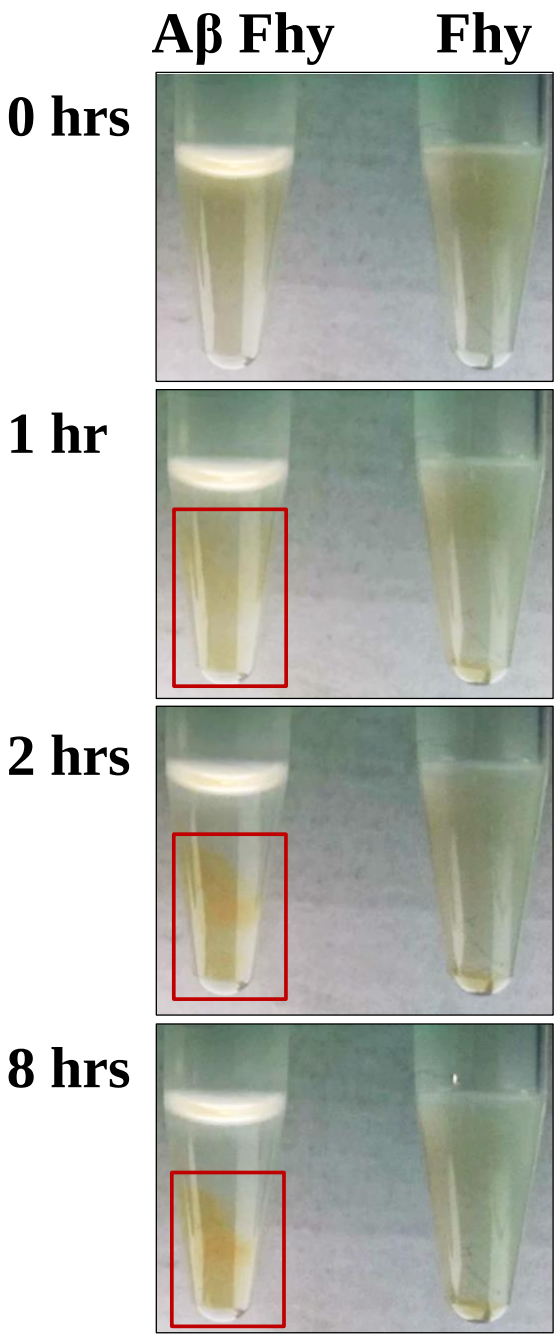

Figure 4.8. Time lapse images of ferrihydrite (Fhy) suspensions incubated in the presence (left) and absence (right) of Aβ over a 8hour period. Incubation times are shown to the left of each image. The red boxes highlight regions of ferrihydrite accumulation by Aβ.

Throughout TEM and STXM examination of Aβ/ferrihydrite structures, multiple large/dense aggregates were observed that were too thick to allow electron/x-ray transmission. Thus the morphology of dense aggregate structures could not be characterized using these approaches. As AFM is not dependent on sample thickness, this technique allows the imaging of dense structures, whilst also enabling the three dimensional morphology of Aβ/ferrihydrite aggregates to be assessed. In Figure 4.9 a preliminary AFM image of an Aβ/ferrihydrite aggregate is displayed. In this region of peptide deposition, amyloid appears to comprise a thin layer of fibrils 50-200 nm in depth, spread over a large (35 μm) area of the sample substrate. These structures are believed to be representative of those imaged via TEM and STXM as shown in Figure 4.7. Despite the majority of this aggregate possessing little depth, a region of dense material over 1.5 μm in height was observed surrounded by fibrils. As traditional fibril structures can be seen adjoining this structure, it is feasible that this dense region is comprised of the amyloid peptide, potentially loaded with ferrihydrite particles, as observed under STXM (Figure 4.7b). Such images suggest the addition of ferrihydrite to induce extensive Aβ aggregation resulting in the formation of stable three dimensional protein structures, possibly reminiscent of the insoluble Aβ plaques witnessed in AD tissue [36].

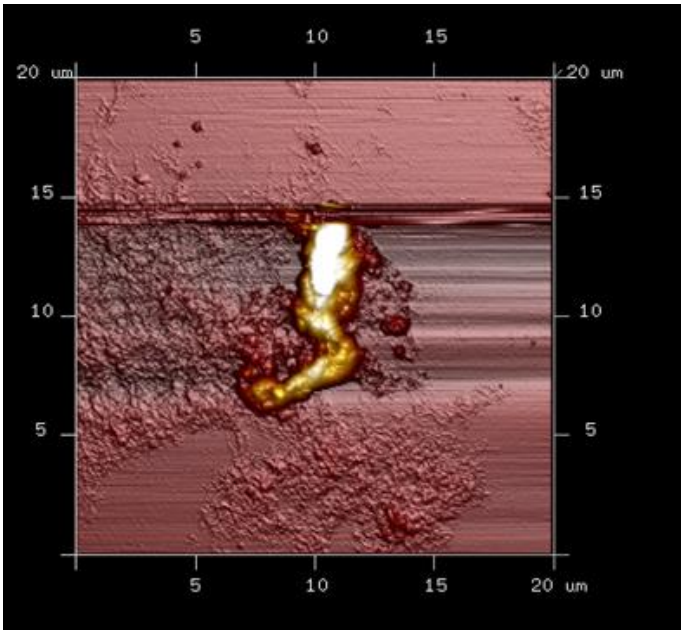

Figure 4.9. A three dimensional topographic image of an Aβ/ferrihydrite structure formed following 48 hours of incubation. Dense Aβ regions (in yellow/white) can be seen to possess significant three-dimensional structure with peak heights of over 1.5 µm.

4.3.4 Oxidative state of ferrihydrite in suspension following Aβ interaction

To further characterize the iron reduction capacity of Aβ, ferrihydrite suspensions were incubated with Aβ and their iron(II) content assessed by Ferrozine assay. The iron(II) content of Aβ/ferrihydrite and Aβ-free ferrihydrite suspensions across the 144 hour incubation time period are shown in Figure 4.10a.

Baseline iron(II) levels of the Aβ-free ferrihydrite suspensions remained constant throughout the time series, with no significant iron reduction being apparent. By examining control corrected iron(II) levels of Aβ/ferrihydrite suspensions, no iron(II) signal could be seen over the first 48 hours of Aβ/ferrihydrite incubation (Figure 4.10b), however a sharp increase in iron(II) content to 31% was observed after 72 hours. Iron(II) levels then cycled, decreasing to 13% of total iron content at 120 hours, before rising to 37% after 144 hours

incubation. These results confirm that Aβ is capable of reducing ferrihydrite to an iron(II) form and suggest the establishment of an iron redox cycle. This redox cycling could explain why the pure iron(II) formed after 48 hours of Aβ/ferrihydrite incubation became oxidized following further incubation with Aβ for 144 hours (Figure 4.1b). The peak level of ferrihydrite reduction recorded here is of a similar magnitude to where Aβ was incubated with iron(III) in the presence of aluminium (42%), and much higher than where Aβ was incubated with iron(III) alone (15%; *see Chapter 3, Figure 3.16*).

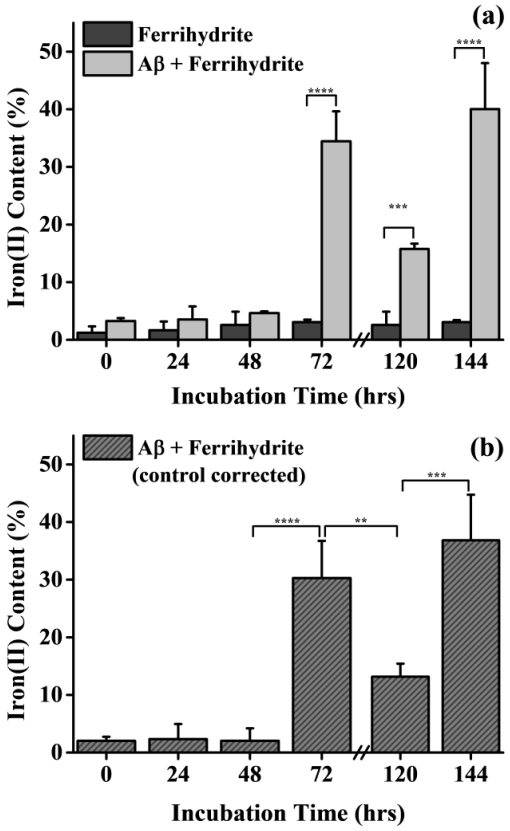

Figure 4.10. Ferrozine iron(II) quantification data showing iron(II) levels of Aβ/ferrihydrite solutions over a 144 hour incubation period. **(a)** Iron(II) content as a percentage of total iron for ferrihydrite solutions in the absence (black), and presence (grey) of Aβ. **(b)** Control corrected iron(II) content of Aβ/ferrihydrite solutions as a percentage of total iron. Sampling was not performed at 96 hours of incubation. Error bars show standard deviation (n=3); statistically significant differences in mean values for each group comparison (by one-way ANOVA) are indicated by the following levels: ** $p < 0.01$, *** $p < 0.001$, **** $p < 0.0001$.

4.3.5 Crystalline structure of ferrihydrite following Aβ interaction

In order to determine the crystalline structure of ferrihydrite following incubation with Aβ electron diffraction was performed. TEM images and selected area electron diffraction patterns from Aβ/ferrihydrite aggregates, Aβ-free ferrihydrite controls and a magnetite reference are shown in Figure 4.11. Aβ-free ferrihydrite was found to be 2-line in nature throughout all time points examined (Figure 4.11d), with broad reflections at 2.50 Å and 1.51 Å corresponding to the [110] and [300] reflections of ferrihydrite [135].

Aβ/ferrihydrite aggregates examined at the 30 minute and 144 hour incubation time points provided diffraction patterns consistent with Aβ-free ferrihydrite controls. However, analysis of Aβ/ferrihydrite aggregates after 48 hours of incubation revealed areas showing diffraction patterns with *d*-spacing values and reflection intensities reminiscent of a magnetite-like phase (JCPDS card 88-0315) (Figure 4.11b-f). In areas of modest ferrihydrite accumulation (Figure 4.11b+d), weak diffraction rings were observed at 2.55 Å, 2.11 Å, 1.52 Å and 1.22 Å corresponding to the [311], [400], [440] and [642] reflections of magnetite/maghemite. However in areas of extensive ferrihydrite accumulation (Figure 5.11c+e) stronger diffraction patterns were recorded with diffraction rings at 3.07 Å, 2.55 Å, 2.14 Å, 1,8 Å, 1.52 Å and 1.25 Å, corresponding to the [220], [311], [400], [422], [440] and [533/642] reflections of magnetite/maghemite. By comparing the diffraction pattern obtained from this Aβ/ferrihydritre region to a magnetite reference (Figure 4.11f) [170], a clear correlation can be seen.

Magnetite is a strongly magnetic mineral, a feature not consistent with the XAS/XMCD results obtained from the iron(II) phase witnessed in the Aβ/ferrihydrite series (Figure 4.1d). However the magnetite seen in these diffraction patterns could represent the oxidation product of the iron(II) phase following air exposure [171]. The broad electron diffraction rings seen in Figure 4.11e+f suggest the nucleation and subsequent crystal

growth of a nanocrystalline phase. This is consistent with the formation of a nanocrystalline iron(II) phase from the ferrihydrite precursor, and subsequent oxidation to magnetite. This process is reminiscent of the synthetic nucleation and growth of ultrafine magnetite nanoparticles [172]. Complete oxidation of the iron(II) mineral shown in Figure 4.1b following prolonged air exposure, was confirmed by repeating the XAS measurements several months later (Figure 4.12).

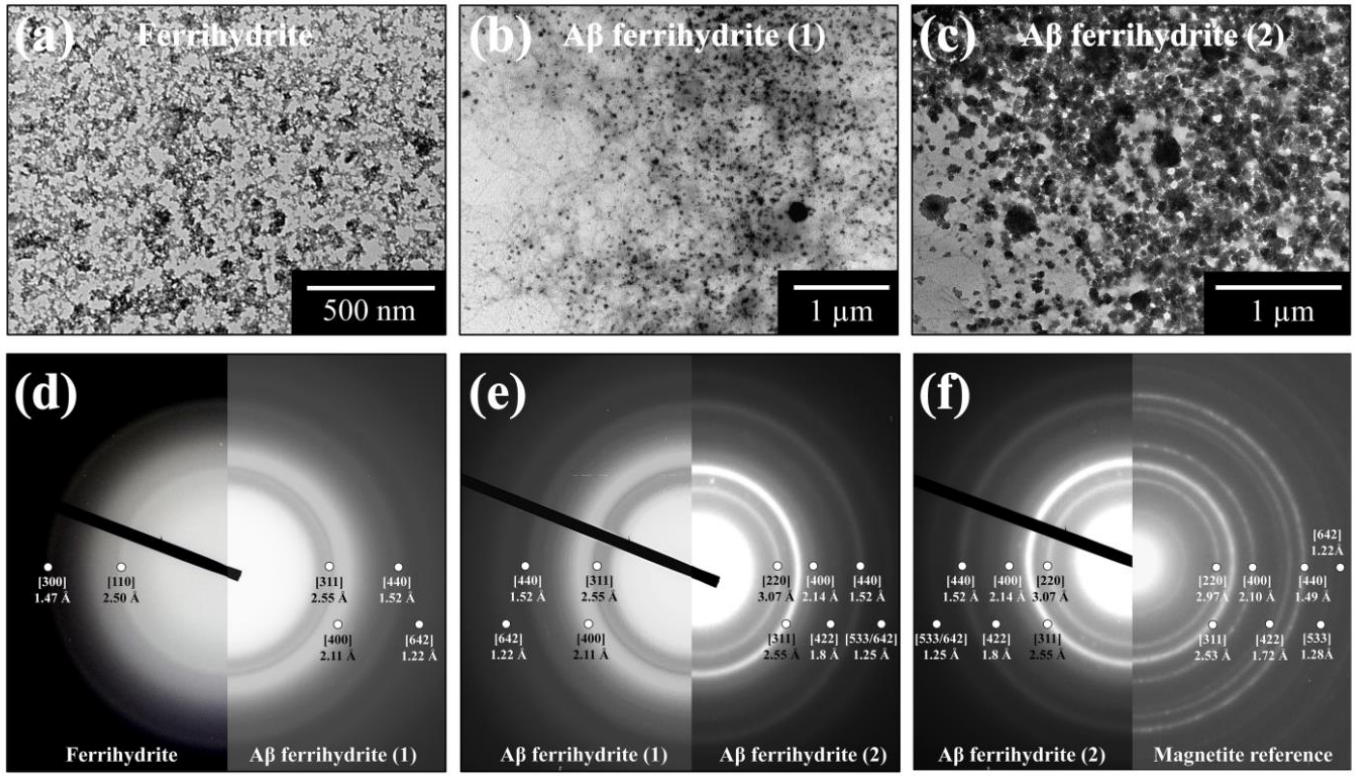

Figure 4.11. TEM images of ferrihydrite and Aβ/ferrihydrite aggregates together with selected area electron diffraction patterns obtained from these regions, following incubation for 48 hours and subsequent air exposure. **(a)** TEM image of ferrihydrite in the absence of Aβ. **(b)** TEM image of an Aβ/ferrihydrite aggregate in an area of modest ferrihydrite deposition. **(c)** TEM image of an Aβ/ferrihydrite aggregate in an area of extensive ferrihydrite deposition. **(d)** Selected area diffraction pattern from ferrihydrite accumulations shown in (a) compared to Aβ/ferrihydrite aggregates shown in (b). **(e)** Selected area diffraction patterns compared for Aβ/ferrihydrite aggregates shown in (b) and (c). **(f)** Selected area diffraction patterns compared for an Aβ/ferrihydrite aggregate shown in (c) and magnetite reference.

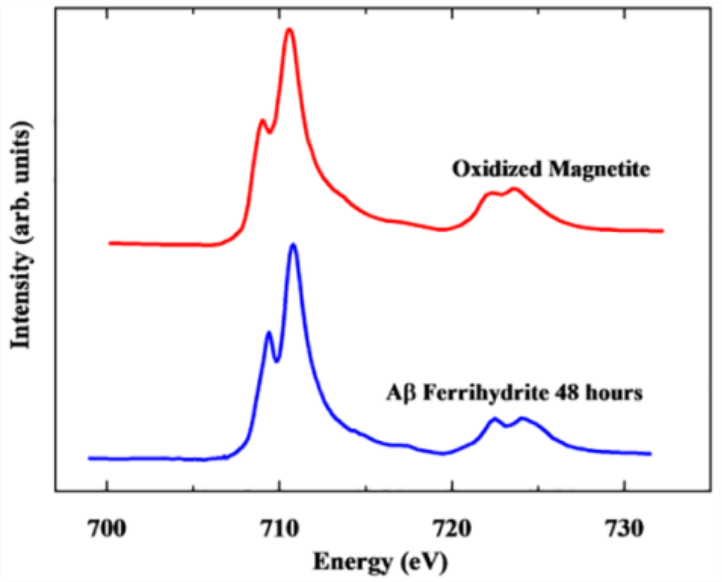

Figure 4.12. Iron *L*-edge x-ray absorption spectrum of ferrihydrite incubated with Aβ for 48 hours with subsequent prolonged air exposure, compared to an oxidized magnetite standard.

4.4 Discussion

From the use of x-ray absorption, iron(II) assay quantification, TEM and STXM techniques, it is shown that the AD peptide Aβ is capable of forming redox-active iron(II) minerals following its aggregation with the ferric mineral ferrihydrite. XAS examination revealed an iron(II) phase to be formed following 48 hours of Aβ/ferrihydrite incubation.

Concurrent XMCD analysis showed this phase to be weakly magnetic, with aniferromagnetically ordered atomic moments, suggesting the formation of an iron(II) oxide such as wüstite [167,168]. Further to this SQUID magnetometry and AC susceptometry measurements of Aβ/ferrihydrite solutions provided no evidence of a strongly magnetic material, suggesting the conversion of ferrihydrite to magnetite to *not* have occurred.

These findings are in agreement with Quintana *et al*. (2004) where a wüstite-like iron phase was observed within pathological AD ferritin [108], along with our related works where a similar iron(II) phase was formed via the interaction of Aβ and iron(III) in solution (*Chapter 3*). The results presented here suggest Aβ to be involved in the formation of the wüstite previously observed in pathological AD ferritin via reduction of ferrihydrite [108]. Iron(II) quantification assays showed evidence of ferrihydrite reduction in solution, supporting the data acquired via XAS, along with indications of ferrihydrite redox cycling by Aβ. As 37% of total iron content was found to be in an iron(II) state and ferrihydrite was in a 10:1 excess to Aβ, these results indicate that Aβ possesses a strong reductive capacity upon ferrihydrite. Such results are consistent with studies conducted by Kahn *et al* [96], and also the results displayed in *Chapter 3* where Aβ was seen to be capable of iron(III) reduction in solution. Interestingly it appears that the speed of Aβ-induced iron reduction may also be influenced by iron crystallinity, with non-crystalline iron reduction occurring after only 30 minutes of Aβ interaction (*Chapter 3, Figure 3.15d*), whereas ferrihydrite reduction required 48–72 hours (Figures 4.1 and 4.10).

Electron diffraction of Aβ/ferrihydrite aggregates revealed the presence of an iron oxide consistent with magnetite. These results provide a possible origin to the increased proportion of magnetite observed within pathological ferritin [108], along with the increased magnetite levels in AD tissue compared to disease-free controls [105,113]; and suggest that simple laboratory-based *in vitro* systems may be capable of producing bioinorganic products that are reminiscent of those that occur within tissue-based samples. Since magnetite is the oxidation product of wüstite [171], the mineral formed via Aβ/ferrihydrite interaction may have oxidized to form magnetite when exposed to air during electron

diffraction analysis. Further, the fine nanoscale crystal size of the magnetite phase observed here is consistent with its formation from the ferrihydrite precursor, and could explain the origin of ferritin-core sized iron oxide nanoparticles with a magnetite/maghemite crystal structure witnessed within AD plaque cores (Collingwood *et al.* (2008) [36]).

STXM, TEM and time lapse images suggest ferrihydrite particles integrate within Aβ fibril structures immediately after ferrihydrite addition, indicating an instantaneous interaction. In particular, STXM images show that Aβ is capable of both incorporating ferrihydrite into its fibril structure, and concentrating ferrihydrite into larger clusters. These data strongly suggest that Aβ is capable of binding ferrihydrite. On the basis of previous scientific literature, this binding may involve the formation of ternary complexes between the N-terminus of Aβ and ferrihydrite, thereby modulating the redox potential of the peptide enabling the redox cycling of ferrihydrite [98,99]. It is this interaction that is thought to induce the reduction of ferrihydrite to an iron(II) rich phase following extended periods of contact with Aβ. However it is unclear whether the iron(II) phase formed via Aβ/ferrihydrite interaction represents precursor to the magnetite previously seen in AD tissue, or whether magnetite could be formed independently of this intermediate phase.

AFM topographic imaging revealed the presence of a fibrillar Aβ aggregate with three-dimensional structure, capable of maintaining its morphology even when taken out of liquid medium. These peptide aggregates are very similar to amyloid fibrils extracted from human amyloidotic spleen [173], and somewhat resemble AD plaque material previously observed through electron tomography techniques (see Collingwood *et al.* [36]); indicating

that Aβ/ferrihydrite interaction may induce the aggregation of the peptide in a manner that is similar to AD plaque formation in the AD brain.

4.5 Conclusion

As iron is stored as redox-inactive ferrihydrite within the protein ferritin [64], the ability of Aβ to bind and reduce ferrihydrite into iron(II) phases that are known to be redox-active [114,116,117] may play a key role in the pathogenesis of AD. Iron levels are high throughout the brain [46], with the stored iron form ferrihydrite being abundant. If ferritin function is compromised in AD tissues, exposure of ferrihydrite to Aβ is likely. The apparent efficiency with which Aβ can reduce ferrihydrite suggests this interaction would represent a significant and sustained source of ROS capable of inducing widespread neuronal damage. Additionally with iron levels shown to be increased in areas of Aβ deposition in transgenic AD models overproducing Aβ [31], and in areas of AD pathology in post mortem human AD tissue, the ability of Aβ to reduce ferrihydrite is likely to be a fundamental feature of AD pathology.

From this study it is apparent that Aβ is directly capable of reducing synthetic ferrihydrite to pure iron(II) phases in the absence of any influencing factors. As iron(II) phases do not occur naturally [107,108], these iron forms associated with Aβ pathology could represent a target for iron chelation therapies, intended to lower the ROS burden in neuronal tissue, thereby inhibiting the progression of AD. The formation of iron(II) oxides in this study also suggests a biogenic origin for the wüstite and magnetite previously recorded in AD tissue providing insights into the processes of AD pathogenesis.

4.6 Additional comments and implications for further work

The results presented in this chapter represent a first time characterization of the mineral products formed through Aβ interactions with iron phases representative of those that occur in the human brain [64,129]. Importantly these findings are in agreement with, and build upon those described in *Chapter 3*, demonstrating Aβ to chemically reduce crystalline iron phases akin to those found within the storage protein ferritin. Such results indicate that Aβ may be capable of inducing redox-active iron formation in the AD brain should ferrihydrite become exposed to the disease protein, and provide a basis from which *in vitro* systems more representative of the AD brain can be developed.

Additionally this study has provided first time *in vitro* evidence of ferrihydrite induced aggregation of Aβ, and also the incorporation of ferrihydrite particles into fibrillar Aβ structures. Clear differences in the structure of Aβ/ferrihydrite structures (as shown above) can be seen when compared to aggregate structures formed through Aβ/iron(III) interaction (see *Chapter 3*). In Aβ/iron(III) structures, iron was seen to be present as amorphous dense regions, co-localized within amyloid morphology, whereas ferrihydrite was seen to both follow amyloid fibril morphology and also become aggregated into small dense clusters. These differences in Aβ/iron aggregates may arise through the differing crystal structures of the starting iron material used. Further to this, no evidence of the amorphous amyloid structures discussed in *Chapter 3* (*Figures 3.10* and *3.11*) were witnessed following Aβ/ferrihydrite incubation, even at incubation time points where iron was shown to be in an Fe^{2+} state (through XAS). Therefore it appears that the chemical reduction of ferric iron forms by Aβ does not automatically result in the loss of amyloid fibril structure.

Chapter 5

Interactions between the Alzheimer's disease peptide β-amyloid and the iron storage protein ferritin

5.1 Introduction

In the preceding chapters Aβ has been shown to chemically reduce unbound ferric iron forms into potentially pathological redox-active iron phases. These findings provide possible origins to the iron(II)-rich biominerals previously found within AD tissues [36,60,105,108,112,113]. However within biological systems iron is stored within the protein ferritin [64], and would therefore not necessarily come into direct contact with Aβ structures.

As described in *Section 1.2.1*, ferritin is a ferroxidase protein responsible for the conversion and storage of iron as redox-inactive ferrihydrite [46,64]. Despite being responsible for healthy brain iron storage, ferritin dysfunctions have been reported in multiple neurological disorders [109,122,174-177]. Furthermore, it has been suggested that disruptions to the ferroxidase function of ferritin could be responsible for the occurrence of redox-active iron minerals in AD tissues, thus contributing to oxidative burdens [58,60,107-109]. In addition to a loss of ferroxidase function, disruptions to ferritin structure can result in the exposure of its ferrihydrite core. This unbound ferrihydrite would be free to come into contact with Aβ, potentially resulting in its chemical reduction as described in *Chapter 4*. As ferritin has been shown to be accumulated within in Aβ plaque material [74,126,178], exposure of ferrihydrite to amyloid is likely should ferritin function be compromised. Moreover, as the exchange of electrons across the protein shell of ferritin (apoferritin) has been reported (Watt *et al.* [179]), Aβ may induce the chemical reduction of ferrihydrite stored within the core of ferritin even if the shell is not damaged. It is therefore feasible that alterations to ferritin structure and function could contribute to redox-active iron formation and oxidative stress in the AD brain.

How ferritin function may come to be compromised in AD tissues is unclear. Based on the results presented in *Chapter 4* and also the observation of ferritin accumulation within Aβ

plaque material in AD tissues [74,126,178], it may be possible that Aβ is capable of disrupting ferritin function, resulting in the conversion of its ferrihydrite core into a redox-active phase. To test this hypothesis, in this chapter, the interaction between Aβ and ferritin is investigated.

First, the morphology, crystal state, iron content and oxidation state of ferritin in its natural state is characterized, to ascertain the nature of ferritin's iron core (*Sections 5.2.1 and 5.3.1*). Time lapse imaging and TEM are then employed to examine ferritin aggregation by Aβ, and the effect of this interaction upon the formation of fibrillar Aβ structures (*Section 5.3.2*). These techniques are also used to examine the similarities between the chemical aggregation of ferritin by ammonium sulphate and ferritin aggregation induced by Aβ. STXM is utilized to examine the localization of ferritin's iron content within Aβ aggregates, and the oxidation state of this iron. In tandem with STXM, electron microscopy is further exploited to determine the effect of Aβ interaction upon ferritin's morphology and iron-core crystal state. Additional characterization of ferritin crystal state following interaction with Aβ is provided indirectly through XAS. Through this multidisciplinary approach, the first evidence of Aβ-mediated disruptions to ferritin structure and function is provided. This process of interaction is shown to result in the formation of redox-active iron phases, with the potential to contribute to AD pathology, as is discussed in *Sections 5.4 and 5.5*.

5.2 Materials and methods

5.2.1 Characterization of horse spleen ferritin

Concentrated horse spleen ferritin (Type I; 125mg/mL; 1% saline solution) was purchased from Sigma Aldrich.

5.2.1.1 Ferritin morphology and crystal structure

To determine the morphology and crystal structure of ferritin, 15 µL of 125 mg/mL ferritin suspension was deposited onto carbon/formvar coated TEM grids (200 mesh; Agar Scientific), and examined using a JEOL 1230 electron microscope operating at 100 kV.

5.2.1.2 Ferritin iron content

The iron content of ferritin was assessed via Ferrozine iron quantification assay. 125 mg/mL ferritin was diluted with dH$_2$O to create ferritin suspensions ranging from 0.1-1 mg/mL. Small volumes of ferritin suspensions were added to 0.5 M HCl (to release ferritin's iron core) and 6.25 M hydroxylamine hydrochloride for a period of 48 hours. Digested/reduced ferritin solutions were added to a 2 mM Ferrozine solution, and absorbance read at 562 nm. Iron concentration as a function of ferritin concentration was determined using these values [153].

5.2.1.3 Oxidation state of ferritin

To assess the oxidation state of ferritin's iron core, XAS was conducted. Small volumes of 125 mg/mL ferritin were deposited onto carbon/formvar coated TEM grids as described in *Section 2.1.2*. All sample manipulation was performed under anoxic conditions to prevent changes in iron valence state as described in *Section 2.1.2*. XAS was performed at Diamond Light Source (Oxfordshire, UK) beamline I10. Detailed XAS spectra were

collected over the iron $L_{2,3}$-edge as outlined in *Section 2.1.3*. The x-ray absorption spectrum of ferritin was recorded using the total electron yield method.

5.2.2 The interaction of Aβ and ferritin

5.2.2.1 Preparation of Aβ/ferritin suspensions

Concentrated 125 mg/mL ferritin was gently inverted multiple times to ensure uniform ferritin distribution without damaging protein structure. Ferritin was diluted in KH buffer (100 mM PIPES) to achieve a 0.7 mg/mL (440μM iron content; see *Section 5.3.1.2*) ferritin suspension.

Monomeric Aβ was thawed and dissolved in 1 mM NaOH to create a 1 mg/mL (220 μM) stock. This Aβ stock was allowed to sit at room temperature for 30 minutes to ensure complete peptide dissolution before being added to 0.7 mg/mL ferritin suspensions. Final ferritin and Aβ concentrations were 0.6 mg/mL (370 μM iron content) and 0.16 mg/mL (35 μM) respectively. Aβ-free ferritin controls were created as above, with the substitution of 1 mM NaOH for Aβ. 35 μM Aβ solutions were prepared in KH buffer as an amyloid reference. All suspensions/solutions were incubated at 37°C until the time of sampling.

To simulate the aggregation of ferritin in the absence of Aβ, additional 0.6 mg/mL ferritin suspensions were prepared through the addition of 125 mg/mL ferritin to a saturated (4 M) ammonium sulphate solution [180].

5.2.2.2 Time lapse imaging

Time lapse videos demonstrating the precipitation of ferritin by Aβ were created using Lapse it™ time lapse software. Images were taken every 5 minutes for a period of 18 hours. All suspensions were kept at 37°C throughout the imaging process.

5.2.2.3 Electron microscopy

Small volumes of Aβ/ferritin suspensions were deposited onto carbon/formvar coated copper TEM grids and excess liquid removed. Samples were taken following 0.5, 48, 96 and 144 hours of incubation at 37°C, and examined using a JEOL 1230 microscope system operating at 100 kV. Where both techniques were employed, electron microscopy was performed following STXM examination to prevent electron beam induced changes to iron chemistry [181].

5.2.2.4 Scanning transmission x-ray microscopy

15 µL of Aβ/ferritin suspensions were deposited onto silicon nitride membranes (DuneSciences 75nm thickness) and excess liquid removed using filter paper. Sampling was performed following 0.5, 48 and 144 hours of incubation at 37°C. Membranes were mounted onto stainless steel microspectroscopy plates for STXM examination as stated in *Section 2.2.1*. Carbon and iron maps revealing the biological structure and iron content of Aβ/ferritin structures were created as previously described in *Section 2.2.2*. Detailed carbon and iron x-ray absorption spectra revealing Aβ absorption profiles and iron oxidation state were created by scanning multiple energies across the carbon *K*-edge and iron *L*-edge respectively (see *Section 2.2.2*). Additional Aβ and ferritin control samples were examined to provide reference carbon *K*-edge and iron *L*-edge reference spectra. As STXM was the primary technique employed to assess iron oxidation state following Aβ interaction, conscientious effort was taken to maintain anoxic conditions throughout the handling and examination of Aβ/ferritin materials (as described in *Section 2.2.1*). Carbon *K*-edge examination was performed prior to iron *L*-edge examination to minimize x-ray beam induced damage to carbon structures.

5.2.2.5 X-ray absorption spectroscopy

For XAS/XMCD experiments, different Aβ batches were used to those in STXM experiments. 15μL of Aβ/ferritin suspensions (and their Aβ-free controls) were deposited onto carbon/formvar coated copper TEM grids, and grids were mounted onto copper sample holders as described in *Section 2.1.2*. Samples were taken under anoxic conditions following 30 minutes, 48 hours and 144 hours of incubation at 37°C. XAS measurements were performed at the iron *L*-edge using beamline I10 at the Diamond Light Source. To locate regions of ferritin deposition, two dimensional iron maps were obtained as described in *Section 2.1.3*. Detailed XAS measurements across the iron $L_{2,3}$ absorption-edge region (700-740 eV) were then conducted to assess the oxidation state of ferritin.

5.3 Results

5.3.1 Characterization of horse spleen ferritin

5.3.1.1 Ferritin morphology and crystal structure

TEM imaging of ferritin (125 mg/mL) revealed a uniform coating of circular electron dense particles approximately 12 nm in diameter spread evenly across the sample surface (Figure 5.1). Electron diffraction examination of this concentrated ferritin provided diffuse ringed diffraction patterns (Figure 5.2) and *d*-spacing values consistent with nanoscale 6-line ferrihydrite (Table 5.1)[134].

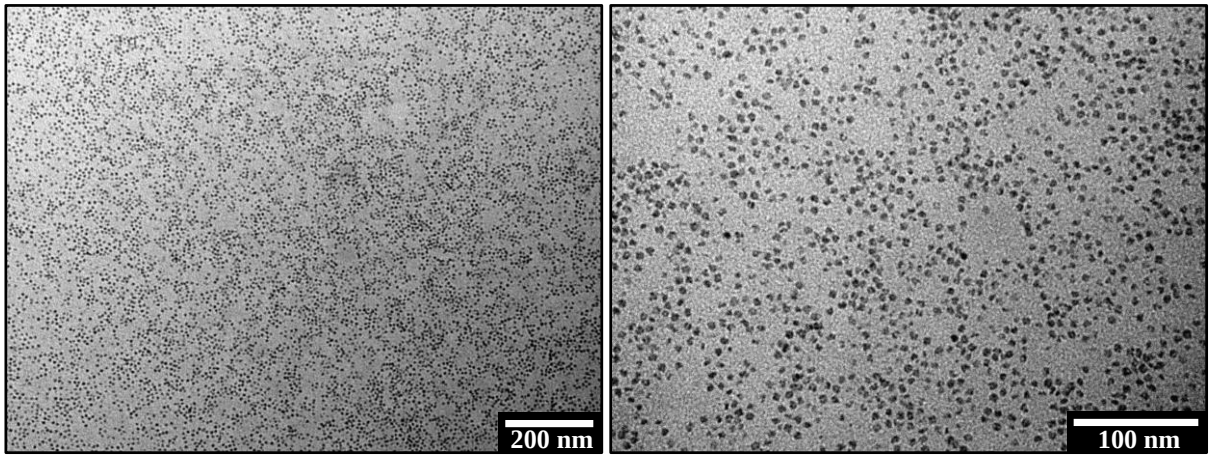

Figure 5.1. TEM images of ferritin particles (125 mg/mL)

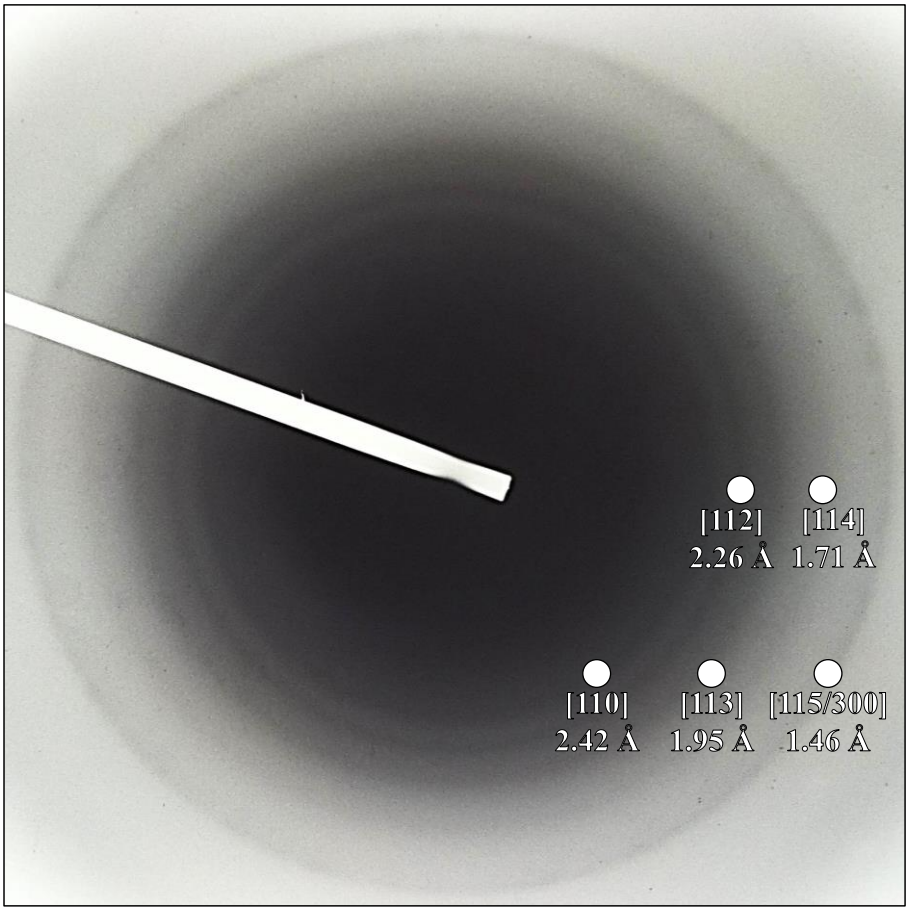

Figure 5.2. Electron diffraction patterns and *d*-spacing values obtained from ferritin particles shown in Figure 5.1.

Table 5.1. *d*-spacing values from the ringed patterns shown in Figure 5.2 compared to a ferrihydrite standard (Drits *et al.* [134])

***d*-spacing {relative intensity}**	
Ferritin (standard error)	**Ferrihydrite (hkl)**
2.42 (±0.05){100}	2.5 (110){100}
2.26 (±0.08){100}	2.24 (112){80}
1.95 (±0.08){30}	1.97 (113){35}
1.71 (±0.07){30}	1.72 (114){30}
-	1.51 (115){50}
1.46 (±0.05){70}	1.47 (300){70}

5.3.1.2 Ferritin iron content

Ferrozine iron quantification assay revealed the iron content of ferritin to be approximately 625 µM per mg/mL of the protein (Figure 5.3). For working iron concentrations used in this chapter (370 µM), ferritin was diluted to 0.6 mg/mL.

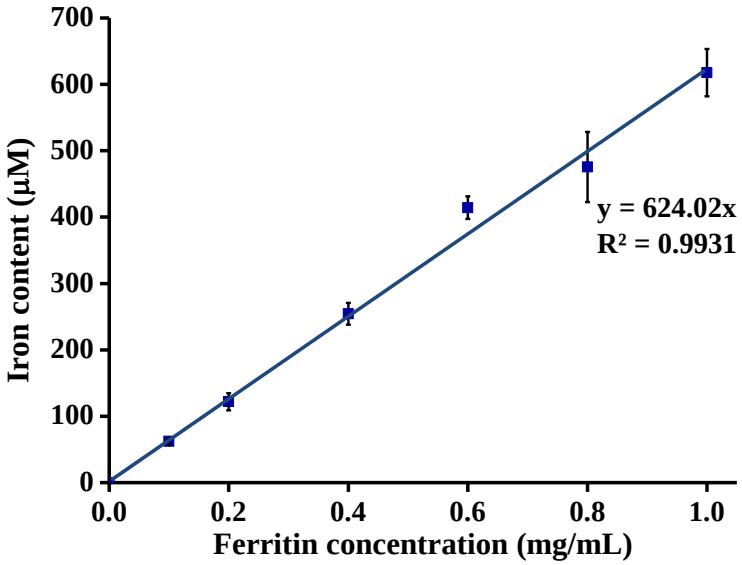

Figure 5.3. Iron content (µM) as a function of ferritin concentration (0-1 mg/mL). Error bars show standard deviation (n=3). Linear trend is indicated by the blue line.

5.3.1.3 Oxidation state

Iron $L_{2,3}$-edge XAS examination of ferritin provided absorption spectra characteristic of a pure Fe^{3+} mineral (Figure 5.4; see *Chapter 1;Figure 1.9* for reference Fe^{3+} spectra). No evidence of enhanced Fe^{2+} features was observed over successive XAS measurements, demonstrating ferritin to be stable in the x-ray beam (Figure 5.4).

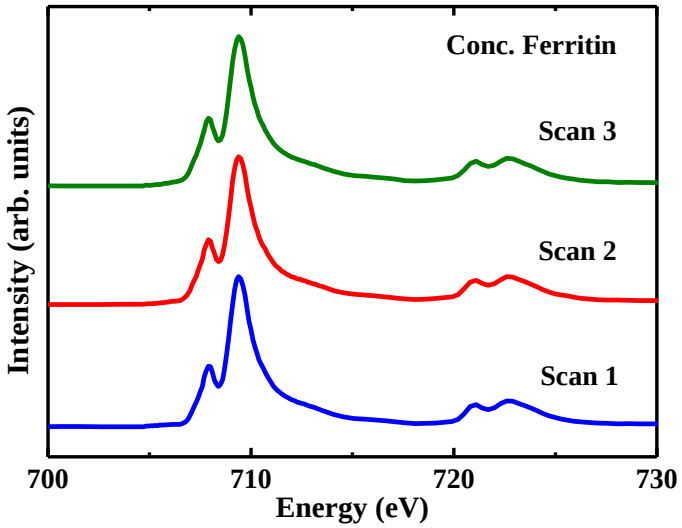

Figure 5.4. Iron $L_{2,3}$-edge x-ray absorption profiles obtained from concentrated (125 mg/mL) ferritin over three successive XAS measurements.

5.3.2 The interaction of Aβ and ferritin

5.3.2.1 Aβ-induced aggregation and disruption of ferritin structure

Time lapse images of ferritin suspensions incubated for 18 hours in the presence and absence of Aβ are shown in Figure 5.5. When incubated in the absence of Aβ, ferritin forms a stable and uniform orange/brown suspension (Figure 5.5; right). However when incubated with Aβ, dense orange precipitates are seen to form following 15-20 minutes of interaction (Figure 5.5 left), suggesting the aggregation of ferritin by Aβ. Once formed, these precipitate structures remained unchanged over the 18 hours of imaging. Precipitates

appeared similar to aggregate structures formed through the addition of ferritin to ammonium sulphate (Figure 5.6); suggesting a similar aggregation process to have occurred.

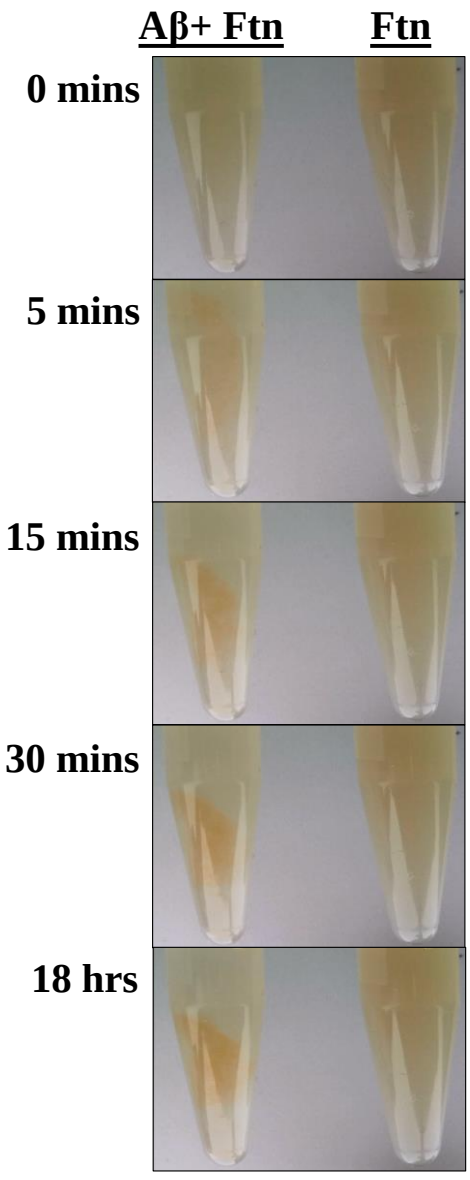

Figure 5.5. Time lapse images displaying ferritin incubated in the presence (left) and absence (right) of Aβ over an 18 hour period. Incubation times are shown to the left of each image.

Figure 5.6. Orange precipitate structures formed through the addition of ferritin to saturated ammonium sulphate

TEM images of amyloid structures formed following incubation with ferritin are shown in Figure 5.7. In comparison to ferritin-free amyloid controls (Figure 5.8), these amyloid aggregates appear to be composed of poorly defined fibril structures, containing a high concentration of electron dense particles. The size and morphology of these dense particles was consistent with that of ferritin, suggesting Aβ to accumulate ferritin within its fibrillar structure. These findings compliment time lapse imaging of Aβ/ferritin suspensions, where Aβ appeared to aggregate ferritin.

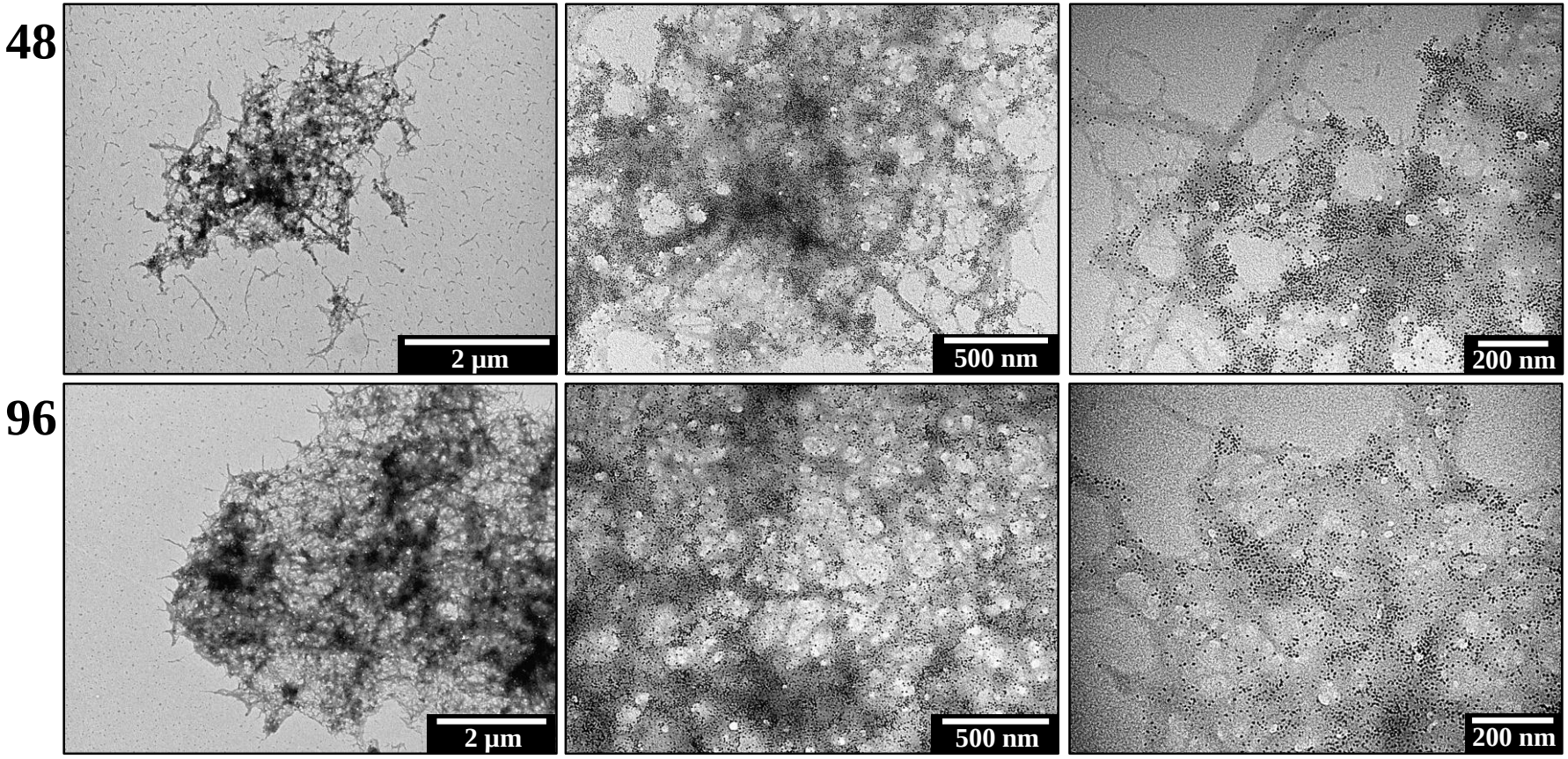

Figure 5.7. TEM images displaying typical Aβ/ferritin structures formed following 48 hours (top) and 96 hours (bottom) of Aβ incubation with ferritin.

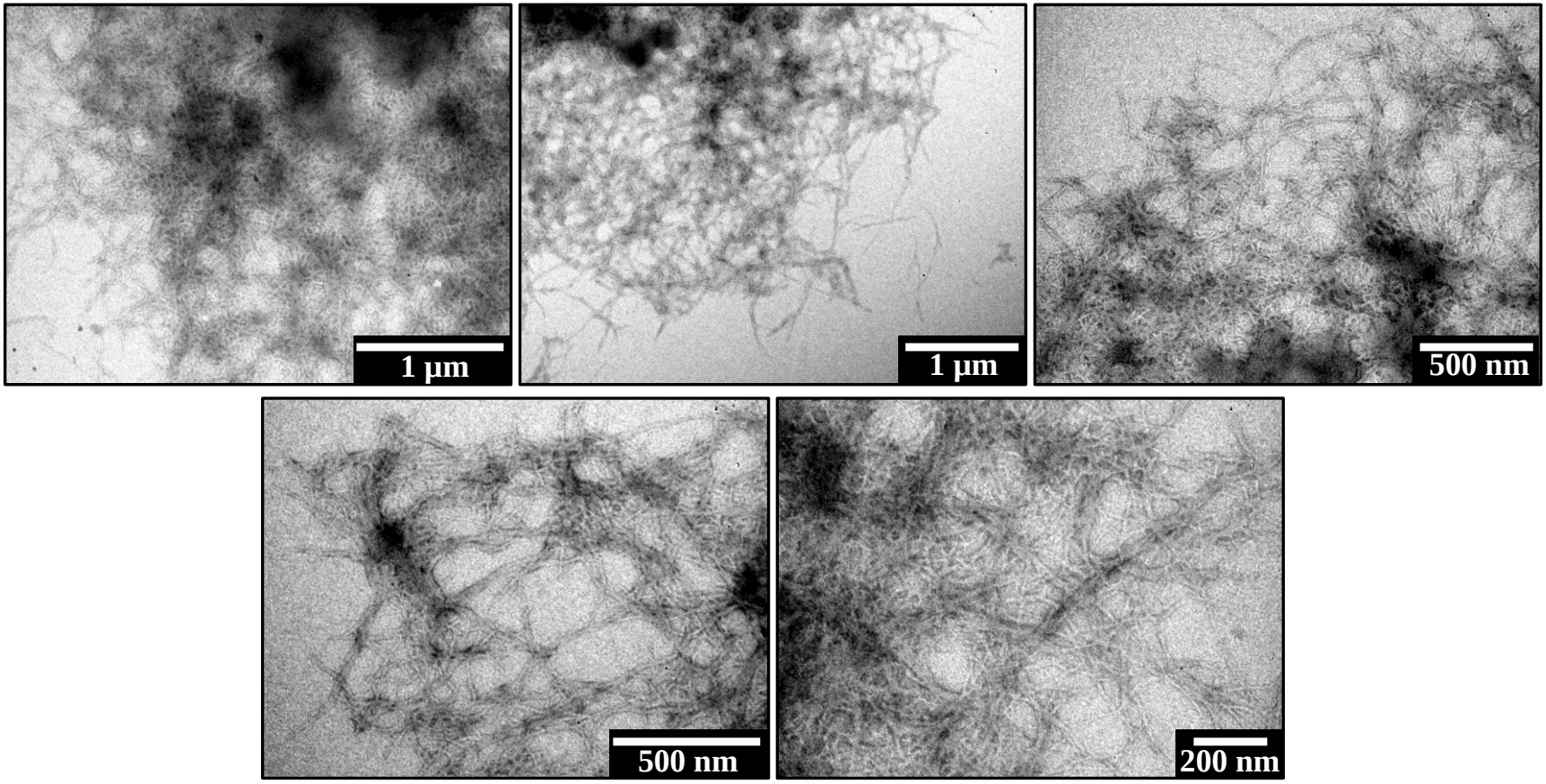

Figure 5.8. TEM images of Aβ fibril structures formed in the absence of ferritin.

To confirm that the electron dense particles shown in Figure 5.7 contained iron, and to assess the oxidation state of ferritin following incubation with Aβ over a 144 hour period; STXM was performed.

Following 0.5 hours of incubation, multiple carbon dense structures were observed throughout the sample area, an example of which is shown in Figure 5.9. Iron L_3-edge examination of the same aggregate revealed iron content to closely follow carbon morphology, suggesting the co-aggregation of Aβ and ferritin within an interaction period of 30 minutes. These observations are consistent with both time lapse imaging and TEM examinations of Aβ structures.

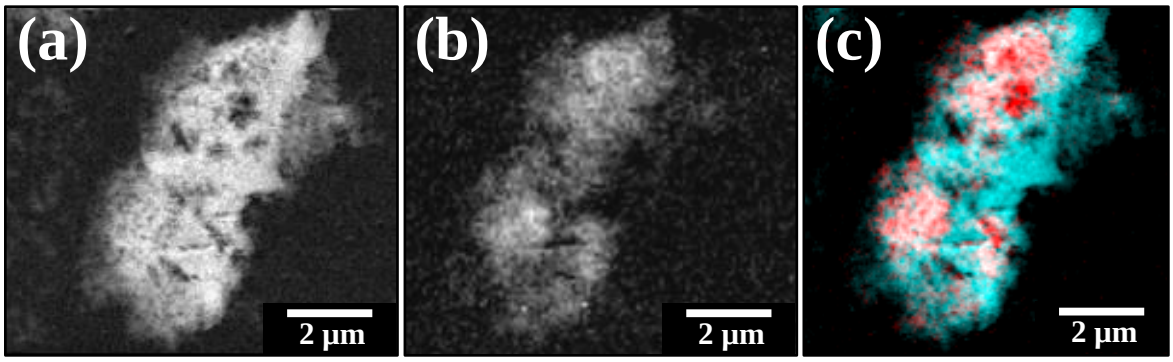

Figure 5.9. STXM images displaying the **(a)** carbon and **(b)** iron content of an Aβ/ferritin aggregate formed following 0.5 hours of incubation. **(c)** Carbon (cyan)/iron (red) composite of the images shown in (a) and (b).

STXM examination of an Aβ/ferritin aggregate formed after 48 hours of incubation again demonstrated iron and carbon content to be closely correlated (Figure 5.10). X-ray absorption examination of this aggregate over the iron $L_{2,3}$-edge provided spectra characteristic of a pure Fe^{3+} mineral, indicating no iron reduction to have taken place. TEM imaging revealed circular, electron opaque particles, extensively accumulated throughout a poorly defined fibrillar Aβ structure, suggesting ferritin morphology to be maintained (Figure 5.11).

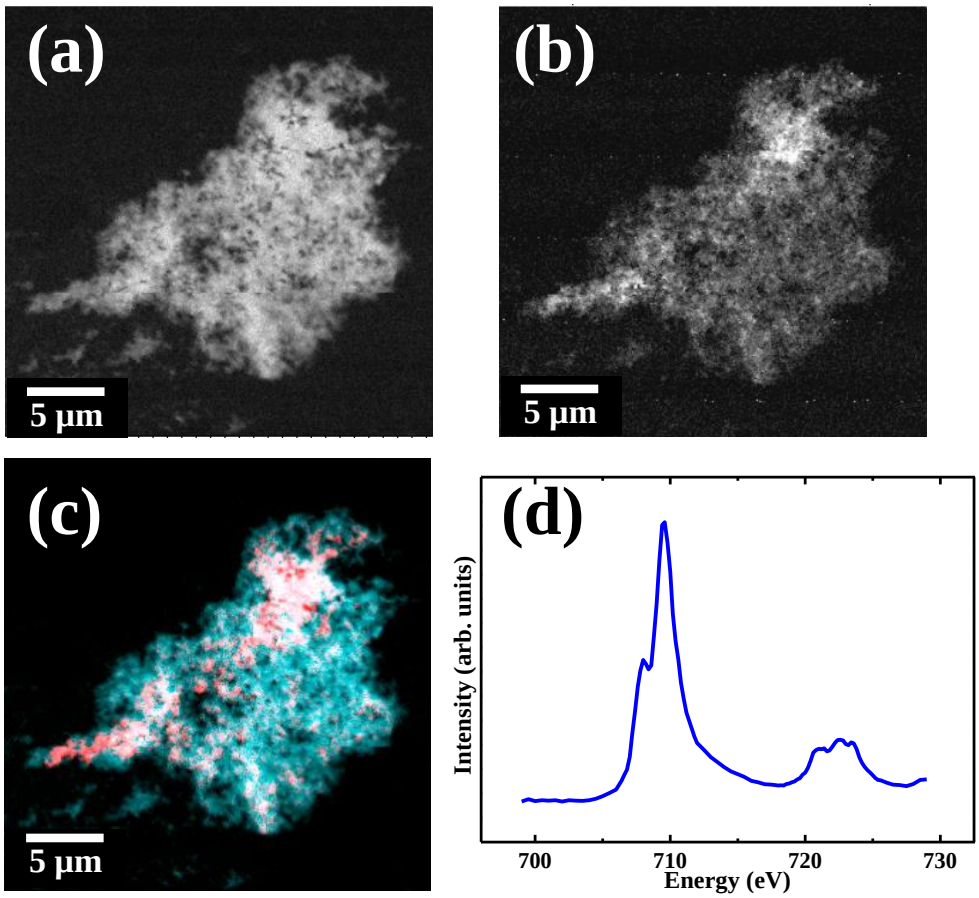

Figure 5.10. STXM images and x-ray absorption spectra from an Aβ/ferritin aggregate formed following 48 hours of incubation. **(a)** Carbon and **(b)** iron content of the aggregate. **(c)** Carbon (cyan)/ iron (red) composite of the aggregate. **(d)** Iron $L_{2,3}$-edge XAS spectra from the iron content shown in (b).

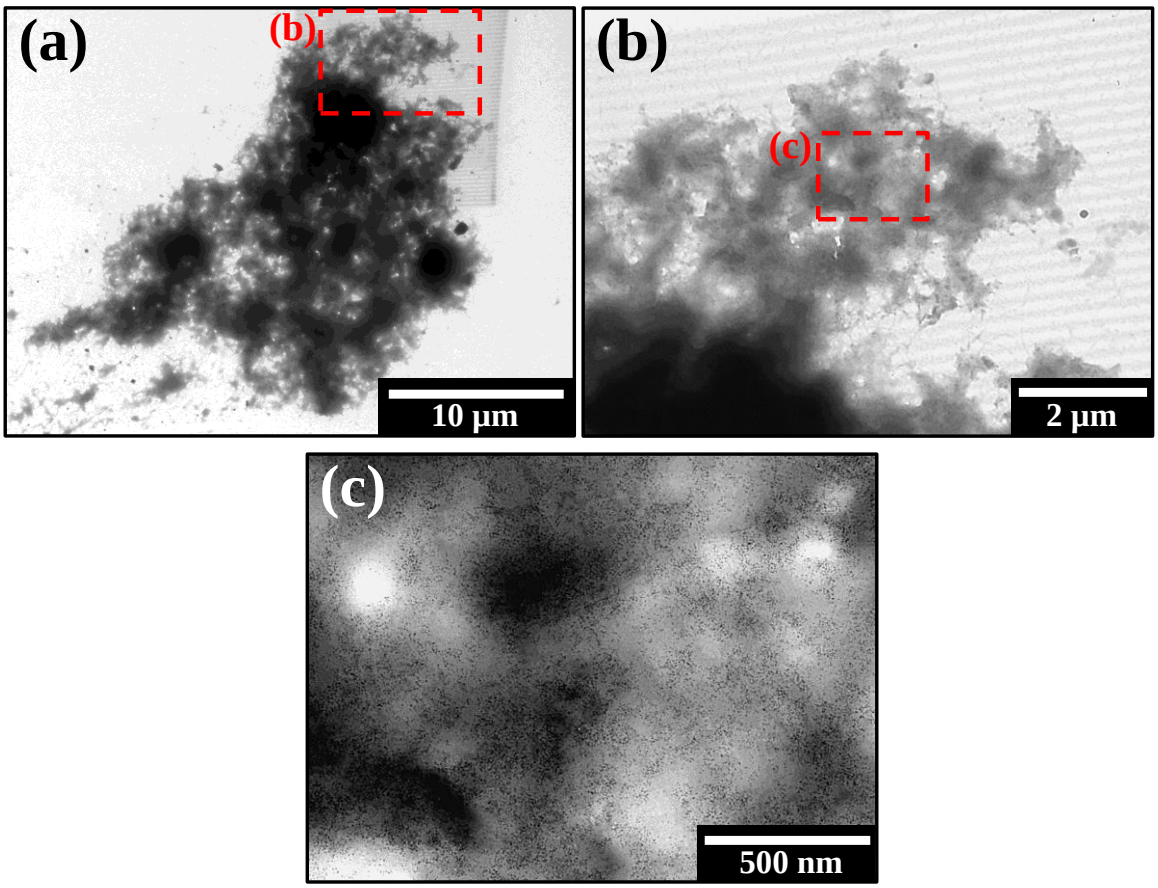

Figure 5.11. TEM images from Aβ/ferritin aggregate shown in Figure 5.10.

Surprisingly, despite this accumulation of ferritin, electron diffraction patterns from this aggregate were not consistent with 6-line ferrihydrite (Figure 5.12). Instead incomplete ringed patterns were observed, with ring arrangements characteristic of a body centred cubic (BCC) material, such as elemental (Fe^0) iron (Figure 5.13). However, despite this BCC arrangement, the calculated lattice constant (4.0 Å) and *d*-spacing values (Figure 5.12) obtained from Aβ/ferritin patterns were not consistent with lattice constant (2.87 Å) and *d*-spacing values (Table 5.2) for Fe^0.

Conversely, where ammonium sulphate was employed to chemically induce ferritin accumulation into similar density aggregates (Figure 5.14a), electron diffraction examination provided ringed diffraction patterns consistent with 6-line ferrihydrite (Figure

5.14b). Such observations suggest incubation with Aβ to alter the crystalline structure of ferritin's ferrihydrite core.

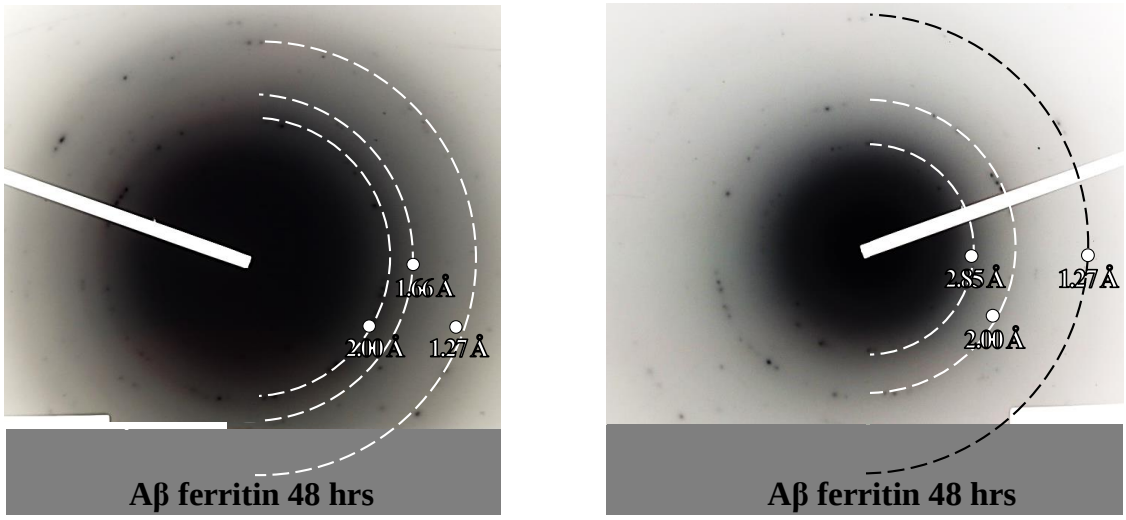

Figure 5.12. Electron diffraction patterns and *d*-spacing values obtained from the Aβ/ferritin structure shown in Figure 5.11, formed following 48 hours of incubation. Dotted lines act as a visual guide for the diffraction ring arrangements. Patterns are taken at a different exposure time to bring out the ring 2.85 Å (see right).

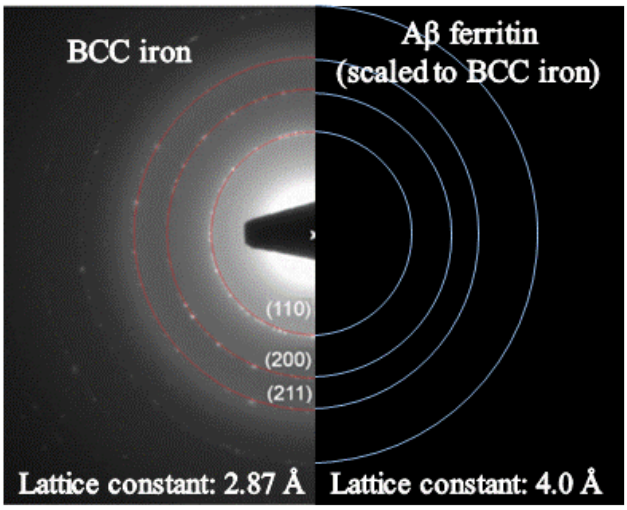

Figure 5.13. Electron diffraction patterns and lattice constant values from body-centred cubic (BCC) iron (left) [182], compared to diffraction patterns obtained from the Aβ/ferritin aggregate (right) shown in Figure 5.12. Aβ/ferritin patterns have been scaled to match that of BCC iron. The lattice constant for Aβ/ferritin was calculated using the hkl values for a BCC structure, as labelled above the innermost three rings of the BCC iron reference pattern (left).

Table 5.2. *d*-spacing values for elemental iron (Fe^0)

Iron	
Phase (hkl)	**d-spacing [intensity]**
110	2.03 [100]
200	1.43 [15]
211	1.17 [25]

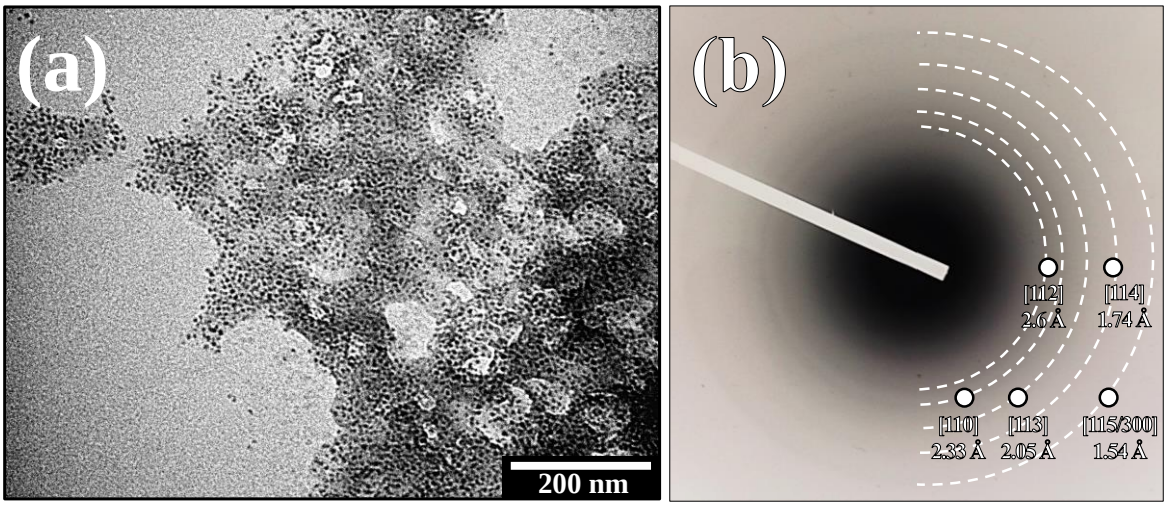

Figure 5.14. **(a)** Bright field and **(b)** electron diffraction images from ferritin aggregate structures formed through the addition of ferritin to saturated ammonium sulphate.

Further incubation of Aβ/ferritin suspensions to 144 hours led to the observation of carbon dense structures similar to those recorded after 0.5 and 48 hours of incubation; an example of which is shown in Figure 5.15. Iron L_3-edge imaging of this aggregate revealed the majority of iron to be accumulated into a single region approximately 200 nm in diameter, thus no longer following carbon morphology. XAS examination of this region over the entire iron *L*-edge provided x-ray absorption spectra corresponding to chemically reduced iron phase (Figure 5.15 d). Despite modest saturation effects at the iron L_3-edge, iron

appeared heavily reduced in comparison to time matched Aβ-free ferritin controls (Figure 5.16 and Figure 5.17), as evidenced by a downward shift in the energy of the iron L_3 peak absorbance (from 709.5 eV to 709 eV), coupled with enhanced Fe^{2+} features and diminished Fe^{3+} features at the iron L_2 edge. As no evidence of iron reduction was observed in ferritin controls (Figure 5.16; blue), these effects appear to be induced by the interaction of Aβ with ferritin.

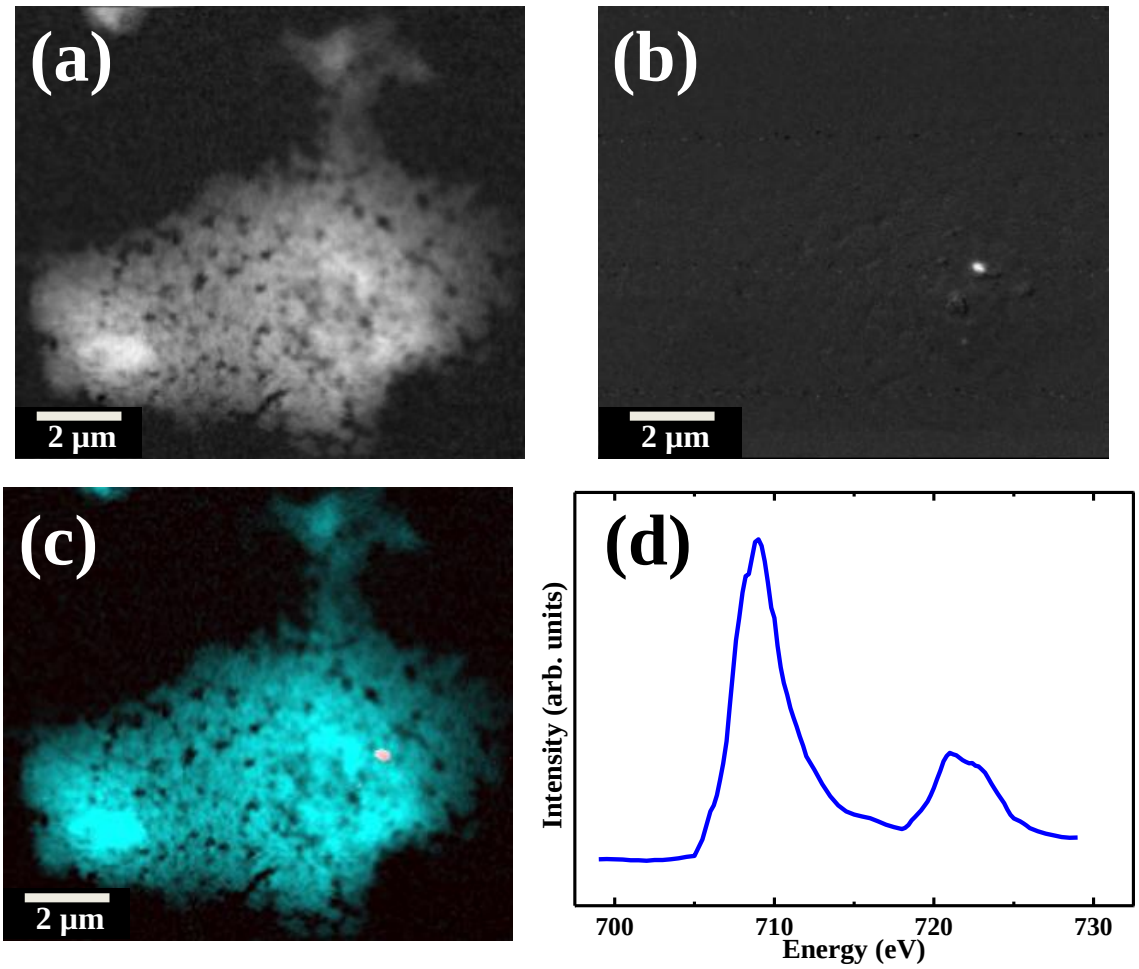

Figure 5.15. STXM images and x-ray absorption spectra from an Aβ/ferritin aggregate formed following 144 hours of incubation. **(a)** Carbon and **(b)** iron content of the aggregate. **(c)** Carbon (cyan)/ iron (red) composite of the aggregate. **(d)** Iron $L_{2,3}$-edge XAS spectra from the iron content shown in (b).

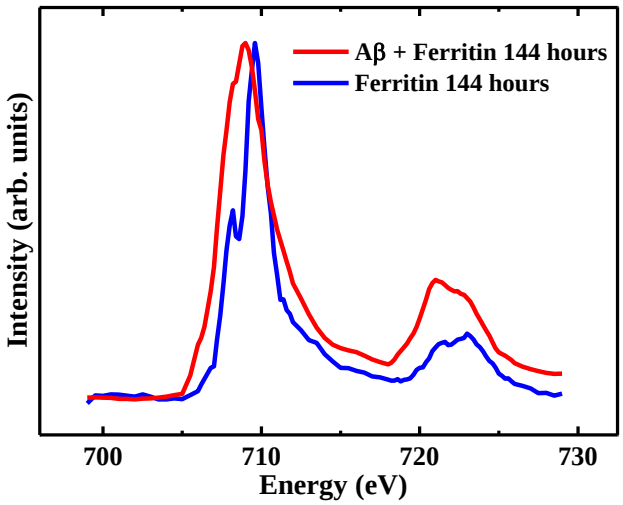

Figure 5.16. Iron $L_{2,3}$-edge x-ray absorbance spectra from ferritin incubated for 144 hours in the absence (blue) and presence (red) of Aβ. Note the downward energy shift in the primary iron L_3 peak feature (709 eV) and enhancement of Fe^{2+} features at 721 eV in the red spectrum, indicating iron reduction to have taken place.

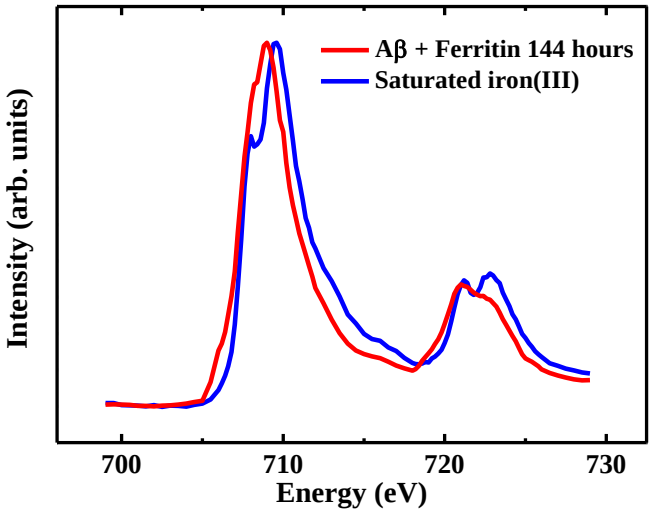

Figure 5.17. Comparisons of $L_{2,3}$-edge spectra from saturated iron(III) signal (blue) compared to the reduced iron observed following 144 hours of Aβ incubation with ferritin (red). Clear reduction effects are apparent at both the L_2 and L_3 edges of the red spectrum, indicating reduction effects to be genuine rather than manifestations of saturated x-ray absorbance signal.

TEM imaging of this aggregate revealed a largely amorphous structure, lacking any mature amyloid fibril morphology (Figure 5.18a), yet containing regions of short spiked fibrils (Figure 5.18b-c). No evidence of ferritin accumulation was found within the aggregate, suggesting ferritin structure to have been compromised, potentially resulting in the accumulation of iron as witnessed in Figure 5.15b. Examination of ferritin incubated in the absence of Aβ, demonstrated protein morphology to be maintained over the 144 incubation period (Figure 5.19), suggesting these disruptions to ferritin structure to be a result of Aβ interaction.

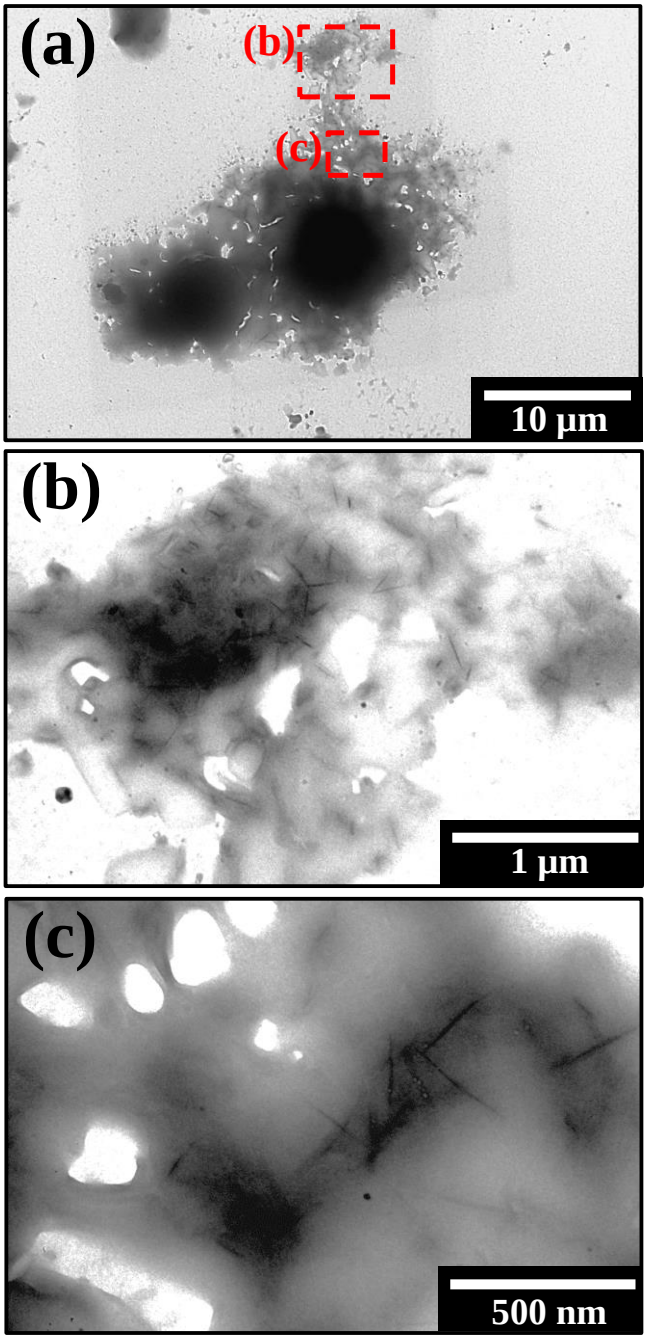

Figure 5.18 TEM images of the Aβ/ferritin aggregate shown in Figure 5.15

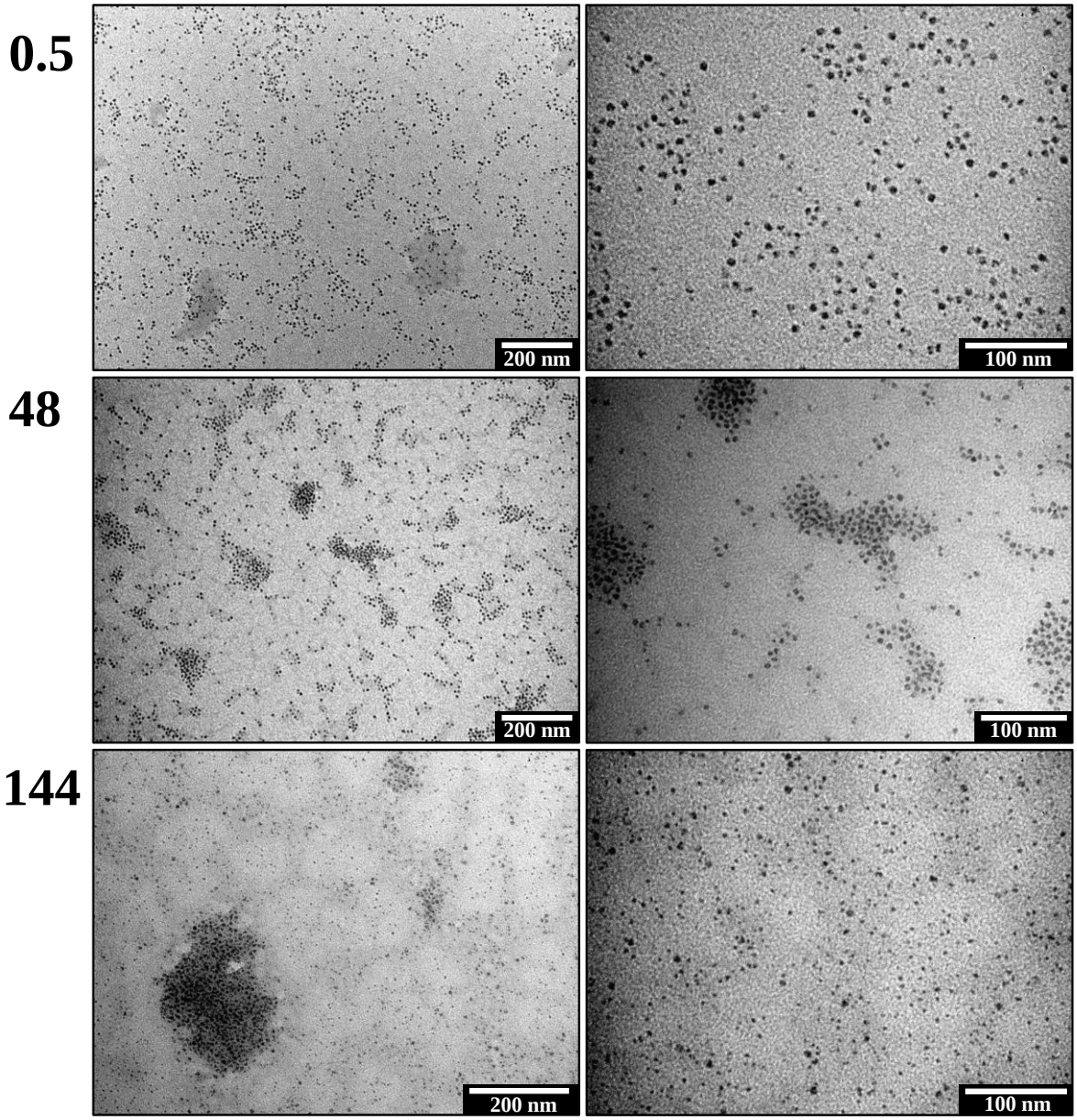

Figure 5.19. TEM images of ferritin incubated in the absence of Aβ. Incubation times in hours are shown to the left of each row.

Further TEM examination of Aβ structures formed following 144 hours of incubation with ferritin revealed the presence of multiple aggregates sharing the morphology of that shown in Figure 5.18. Electron diffraction examination of *all* (largely) amorphous structures provided diffuse ringed patterns, with BCC ring arrangements (Figure 5.20). Calculated lattice parameters and *d*-spacing values were consistent with those obtained from the

Aβ/ferritin aggregate formed following 48 hours of interaction (Figure 5.12), suggesting a similar, but more nanocrystalline phase to have formed.

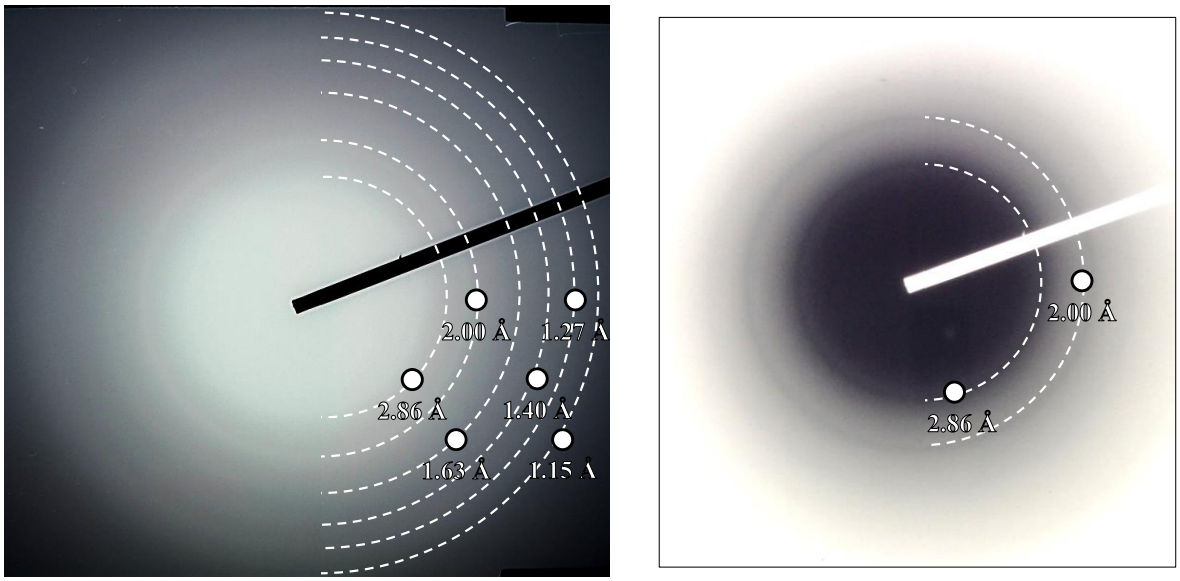

Aβ ferritin 144 hrs

Figure 5.20. Electron diffraction patterns and *d*-spacing values obtained from an Aβ/ferritin structure formed following 144 hours of incubation. Colours are inverted in the right image to bring out the inner two rings of the diffraction pattern.

Intriguingly, similar diffraction patterns to those displayed in Figure 5.20 were obtained from iron precipitates formed following the acid digestion of ferritin with 5 M HCl; as shown in Figure 5.21. These observations suggest that Aβ-mediated disruptions to ferritin structure result in alterations to the crystal structure of ferrihydrite in a similar manner to those induced chemically. Unfortunately, the exact nature of this resulting crystalline material cannot be confirmed through the data available. The crystal structure of a variety of minerals that could contribute to the patterns shown in Figures 5.20 and 5.12 were referenced, yet no positive matches were identified (as summarized in Table 5.3).

However, the sources of these patterns may include a mixed-phase and/or disordered iron material, potentially comparable to the highly disordered cubic mineral observed in

pathological ferritin cores by Quintana *et al* (2004) [108]. Alternatively, prolonged electron beam exposure may have resulted in the formation of a BCC material, from an amorphous precursor. Indeed, electron beam induced effects have previously been demonstrated by Suslick *et al*. who observed BCC iron formation following prolonged exposure of amorphous iron to an electron beam [183]. Regardless of the exact phase formed, these results clearly demonstrate Aβ to be capable of altering the crystal structure of ferritin's ferrihydrite core.

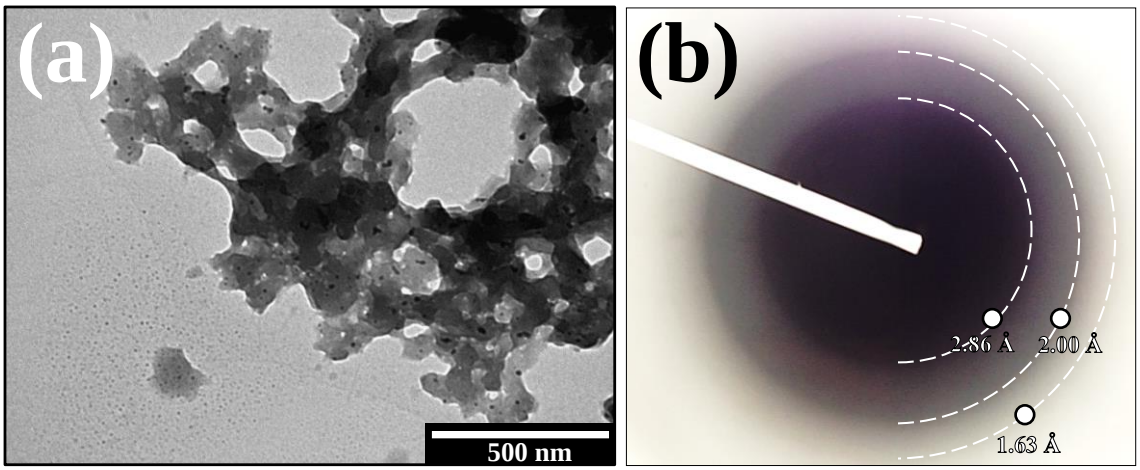

Figure 5.21. **(a)** TEM and **(b)** electron diffraction images of iron precipitates formed following the addition of 5 M HCl to ferritin.

Table 5.3. Lattice constants and cubic structures (where applicable) of various minerals compared to the crystalline material found in Aβ/ferrihydrite aggregates (Figures 5.12 + 5.20)

Cubic Minerals		
Material	**Lattice constant (Å)**	**Cubic structure**
Aβ + ferrihydrite (Figs 6.12 + 6.20)	**4.0**	**Body-centred -cubic**
Ferrite (Fe)	2.9	Body-centred-cubic
Wüstite ($Fe_{1-x}O$)	4.3	Face-centred-cubic (rock-salt)
Magnetite (Fe_3O_4)	8.4	Face-centred-cubic (hexoctahedral)
Maghemite (Fe_2O_3)	8.3	Basic cubic (tetartoidal)
Magnesioferrite ($MgFe_2O_4$)*	8.4	Face-centred-cubic (hexoctahedral)
Andradite ($Ca_3Fe_2Si_3O_{12}$)*, **	12.1	Body-centred-cubic (hexoctahedral)
Greigite (Fe_3S_4)*	9.87	Face-centred-cubic (hexoctahedral)
Sodium (Na)*ǂ	4.2	Body-centred-cubic
Disodium oxide (Na_2O)*ǂ	5.49	Face-centred-cubic (antifluorite)
Halite (NaCl)*	5.4	Face-centred-cubic (rock-salt)
Sylvite (KCl)*	6.3	Face-centred-cubic (rock-salt)
Silicon**	6.6	Face-centred-cubic (diamond)
Other minerals		
Material	**Lattice constants: *a,b,c* (Å)**	
Ferrihydrite (Fe_2O_3•$0.5H_2O$)	3.0, 3.0, 9.4	
Goethite (α-FeO(OH))	9.9, 3.0, 4.6	
Lepidocrocite (γ-FeO(OH))	12.4, 3.9, 3.1	
Feroxyhyte (δ-FeO(OH))	2.59, 2.59, 4.56	
Hematite (α-Fe_2O_3)	5.0, 5.0, 13.8	
Siderite ($FeCO_3$)*	4.69, 4.69, 15.1	
Molysite ($FeCl_3$)*	6.1, 6.1, 17.4	
Lawrencite ($FeCl_2$)*	3.6, 3.6, 17.5	
Fougerite ($Fe(OH)_2$)	3.2, 3.2, 23.9	
Butlerite ($Fe(OH)SO_4$•$2H_2O$)*	6.5, 7.4, 5.8	
Strengite ($FePO_4$•$2H_2O$)*	8,7, 9.9, 10.2	
Nierite (Si_3N_4)**	7.8, 7.8, 5.6	
Tridymite (SiO_2)**	8.7, 5.0, 8.2	
Aragonite ($CaCO_3$)*	5.0, 8.0, 5.7	
Vaterite ($CaCl_2$)*	7.3, 7.3, 25.3	

* Elemental components are constituents of KH buffer
** Elemental components are constituents of silicon membranes
ǂ Would rapidly react in water to form NaOH

It should be noted that interaction effects observed following 144 hours of Aβ incubation with ferritin were heterogeneous. Aβ aggregates containing oxidized iron (Figure 5.22) and intact ferritin (Figure 5.23) were observed in close proximity to the aggregate structure displayed in Figures 5.15 and 5.18.

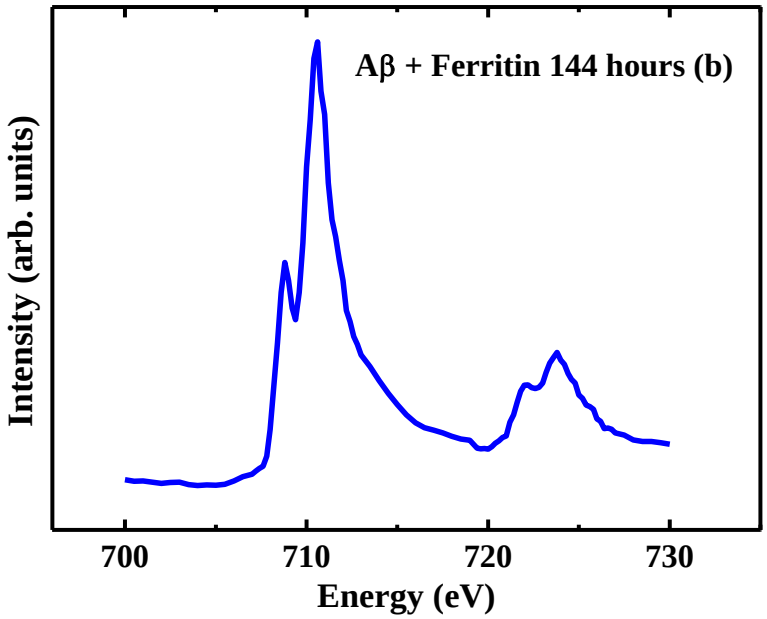

Figure 5.22. Iron $L_{2,3}$-edge STXM-XAS profile of Fe^{3+} material found within an aggregate structure in close proximity to that shown in Figure 5.15.

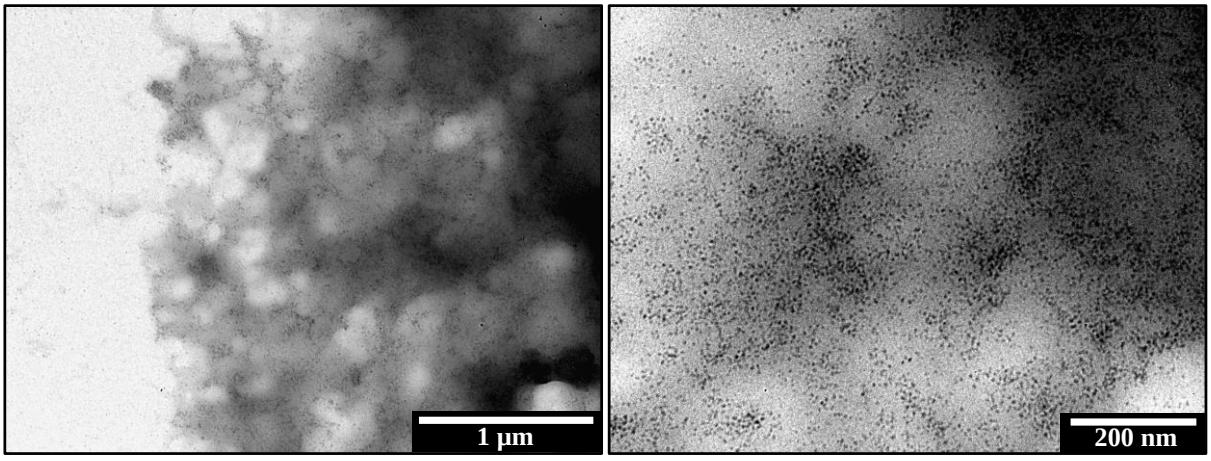

Figure 5.23. Example of an Aβ/ferritin aggregate formed following 144 hours of incubation where regular ferritin morphology is maintained

Taken together, these data suggest disruptions in ferritin structure to occur following 144 hours of incubation with Aβ, resulting in the chemical reduction of the ferritin iron core into a redox-active iron phase; and the concentration of this iron into dense nanoscale aggregates. Furthermore, this process of Aβ/ferritin interaction appears to alter the crystal structure of ferritin-derived ferrihydrite and inhibit the ability of Aβ to form mature fibril structures.

5.3.2.2 STXM carbon K-edge examination of Aβ/ferritin structures

Unfortunately, due to carbon contamination on the focusing apparatus (zone plate) of the STXM instrument during experimental time spent examining ferritin, reliable carbon *K*-edge spectra could not be obtained for this set of experiments. Despite this contamination, attempts were made to record carbon *K*-edge absorption levels from the Aβ/ferritin structures. A typical example of a Aβ/ferritin carbon spectrum is shown in Figure 5.24, compared to the carbon absorption profile for Aβ(1-42) displayed in *Chapter 3*. A low energy peak at 285 eV arising from aromatic amino acids (labelled 1) and a dominant π* peak at 288 eV (labelled 2) can be seen in both the Aβ/ferritin spectra and the Aβ spectra form *Chapter 3*, suggesting the presence of a peptide structure [143]. However a significant broadening of the π* peak at 288 eV is apparent in the Aβ/ferritin spectra, coupled with the absence of the low-intensity peak structure associated with arginine at 289.2eV (labelled 3) as seen in the Aβ spectrum from *Chapter 3*. Further to this, instrument carbon contamination prevented reference ferritin carbon *K*-edge spectra from being collected. This meant that distinctions in the absorption features of ferritin and Aβ could not be characterized. Thus despite these spectra suggesting the presence of a peptide material, this cannot be definitively confirmed to be Aβ.

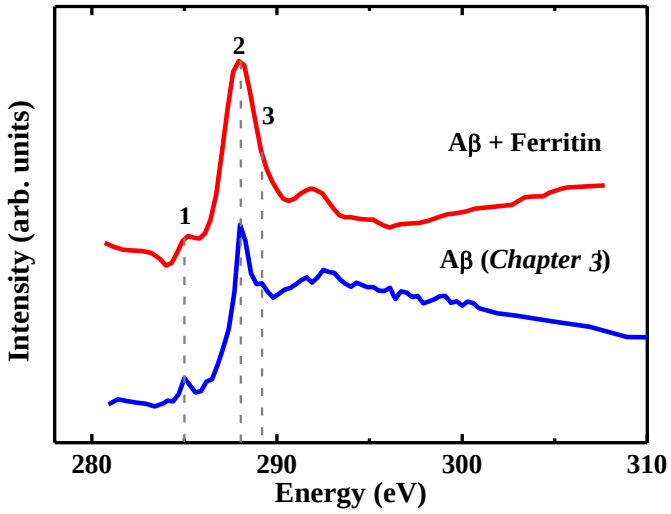

Figure 5.24. Carbon *K*-edge spectra from AB/ferritin structures (red) compared to the carbon spectra collected from Aβ(1-42) in *Chapter 3* (blue). Peptide features at 285 eV, 288 eV, and 289.2 eV are labelled 1, 2 and 3 respectively, and are highlighted by the grey dashed lines.

5.3.2.3 XAS examination of ferritin following interaction with Aβ

Iron $L_{2,3}$-edge XAS spectra obtained from ferritin (0.6 mg/mL) incubated in the absence and presence of Aβ are shown in Figures 5.25, 5.26 and 5.27. When incubated in the absence of Aβ, ferritin provided iron $L_{2,3}$-edge x-ray absorption spectra characteristic of a pure iron(III) mineral (Figure 5.25). Ferritin was found to be stable in the x-ray beam, with no enhancements to Fe^{2+} features being apparent over successive XAS measurements. These findings are in agreement with those displayed in Figure 5.4, where concentrated (125 mg/mL) ferritin was found to be in a Fe^{3+} beam stable state, and also where ferrihydrite was incubated in the absence of Aβ in *Chapter 4* (*Figure 4.1a*).

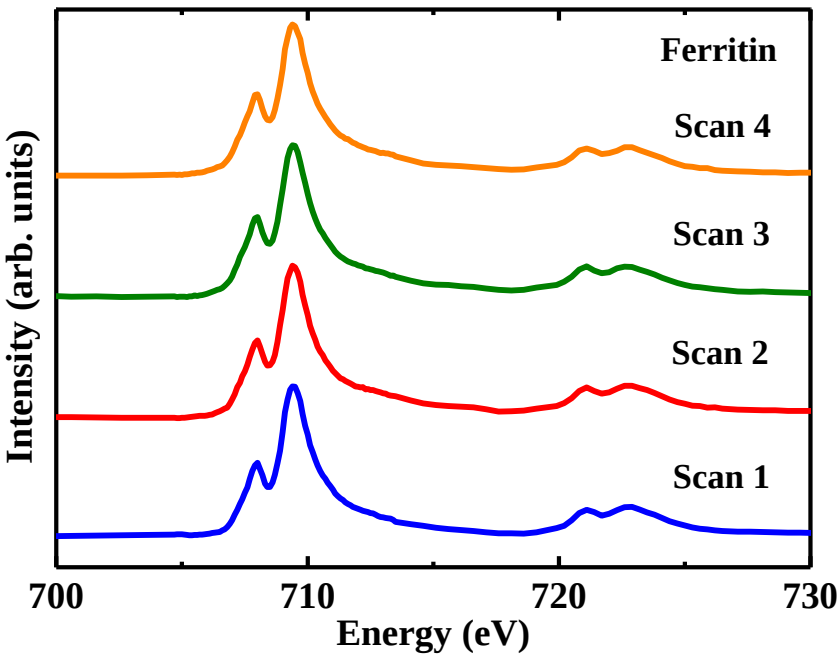

Figure 5.25. Iron $L_{2,3}$-edge x-ray absorbance spectra from successive XAS scans of a ferritin aggregate incubated in the absence of Aβ

When incubated in the presence of Aβ, initial iron L_3-edge XAS examination (labelled scan 1 in the *Figures 5.26* and *5.27*) demonstrated ferritin to remain in a Fe^{3+} state over all time points examined. However following 48 and 144 hours of incubation, successive XAS measurements of ferritin deposits over the entire iron *L*-edge resulted in enhancements to Fe^{2+} x-ray absorption features, as displayed in Figure 5.26 and 5.27 respectively.

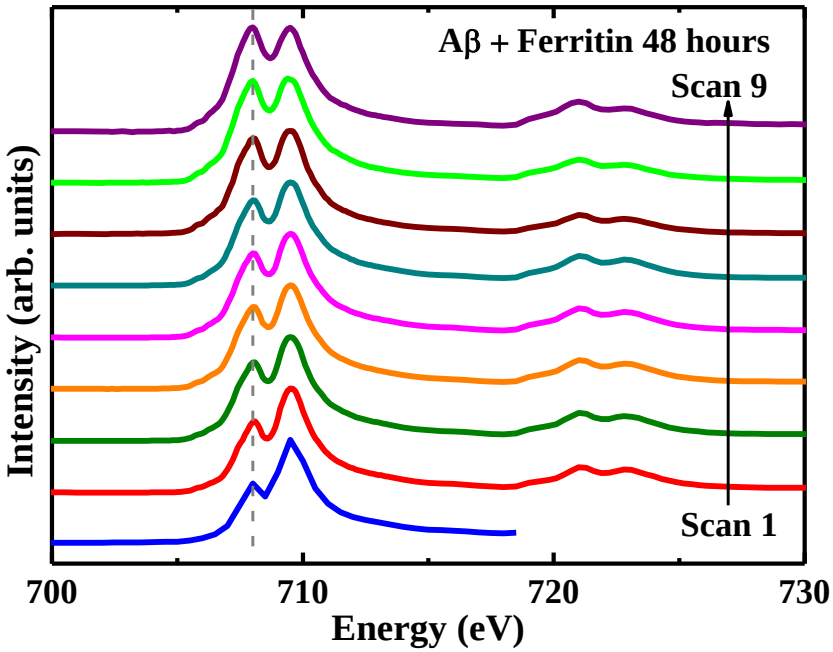

Figure 5.26. Successive iron *L*-edge XAS measurements of a beam unstable ferritin aggregate found following 48 hours of incubation with Aβ

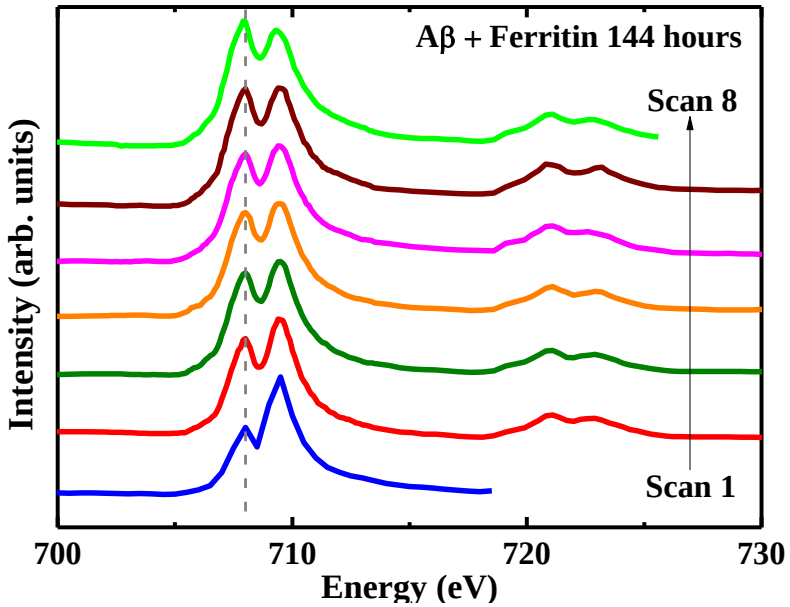

Figure 5.27. Successive iron *L*-edge XAS measurements of a beam unstable ferritin aggregate found following 144 hours of incubation with Aβ. Scan number 2 is omitted due to poor data quality.

As ferritin has shown to be stable in the x-ray beam when incubated in the absence of Aβ (Figures 5.4 and 5.25), this alteration in stability following x-ray exposure appears be a result of Aβ interaction. With crystalline iron materials typically being stable in the soft x-ray energy range used throughout this thesis, these results suggest Aβ to have altered the crystal state of ferritin's ferrihydrite core, resulting in the formation of a more amorphous iron phase susceptible to soft x-ray reduction effects. These findings support electron diffraction patterns obtained from Aβ/ferritin structures where alterations to 6-ferrihydrite crystal structure were observed (Figures 5.12 and 5.20); and also results presented in *Chapter 4*, where Aβ was seen to convert 2-line ferrihydrite into a beam unstable phase (Figure 4.2 b).

5.4 Discussion

Through the use of STXM, TEM, electron diffraction and XAS, ferritin structure is shown to be disrupted following incubation with Aβ, resulting in the conversion of ferritin's ferrihydrite core into a potentially toxic redox-active phase.

Time lapse imaging, TEM and STXM demonstrate ferritin to become accumulated within Aβ peptide structures following only 30 minutes of co-incubation at 37°C. This process resulted in a high concentration of ferritin throughout Aβ structures, with ferritin (and iron) distribution being widespread (rather than localized) within amyloid aggregates formed over the first 48 hours of co-incubation. These observations are in keeping with STXM results displayed in *Chapter 4*, where ferrihydrite was found to become accumulated and integrated throughout Aβ aggregate structures when incubated with the peptide (Figure 4.7). Corresponding iron $L_{2,3}$-edge examination of these Aβ/ferritin aggregate structures revealed iron to be in a pure iron(III) phase, suggesting no chemical reduction to

have taken place. The inclusion of ferritin within amyloid aggregates also appeared to disrupt typical amyloid fibril formation, with Aβ aggregates comprised poorly defined fibril structures typically being observed following 48-96 hours of incubation with ferritin. These aggregate structures were clearly different to Aβ structures formed through incubation with ferrihydrite, where fibrillar structure was maintained (*Chapter 4; Figure 4.7a*). This lack of fibrillar structure in Aβ/ferritin aggregates may arise through peptide/peptide interactions between the two proteins, potentially inhibiting the formation of secondary and tertiary structures required for amyloid fibril creation.

The ability of Aβ to accumulate and incorporate ferritin into its structure provide possible explanations to observations made by Grundkeiqbal *et al*. where increased levels of ferritin were recorded within senile plaque material in AD tissues [126]. However the findings reported here also contradict early electron microscopy studies by Paul *et al.* who witnessed no interaction between ferritin and amyloid fibrils taken from amyloidosis patients [184].

Prolonged incubation of Aβ with ferritin, led to the observation of Aβ aggregates where ferritin structure was absent (as shown via TEM). In these instances a complete loss of mature amyloid fibril morphology was also observed. Aβ appeared largely amorphous, albeit containing localized regions of short fibril structures. As ferritin morphology was found to be maintained in amyloid-free controls, these disruptions to ferritin structure appear to be induced through Aβ interaction. Iron L_3-edge imaging of an amorphous amyloid structure revealed iron to be concentrated into a dense spot approximately 200 nm in diameter. This distribution of iron was vastly different to earlier time points, where iron was found to be widely spread throughout Aβ structures. STXM-XAS examination across the iron $L_{2,3}$-edges revealed this iron to be heavily reduced, with features characteristic of

redox-active iron. Again, as amyloid-free ferritin controls were shown to remain in a pure iron(III) state this, reduction effect appears to be a result of Aβ interaction with ferritin.

These data suggest that Aβ acts to disrupt ferritin structure after extended periods of interaction, resulting in the reduction of the ferritin's ferrihydrite core into a redox-active phase. The capacity of Aβ to reduce 6-line ferrihydrite further demonstrates the ability of amyloid to reduce more crystalline iron materials, and is consistent with the findings presented in *Chapter 4* where Aβ was seen to reduce 2-line ferrihydrite. The ability of Aβ to reduce the ferrihydrite core of ferritin also provides a potential *in vitro* explanation to the observation of redox-active iron material within the cores of ferritin extracted from AD tissues [108].

The occurrence of reduced iron was associated with a loss of amyloid fibril structure and the accumulation of iron into a localized nanoscale deposit. Interestingly the loss of Aβ fibril structure was also associated with the appearance of chemically reduced, dense nanoscale iron deposits in Aβ aggregates formed following Aβ interaction with iron(III) hydroxide (*Chapter 3; Figures 3.10 and 3.11*). Such observations tentatively suggest that the reduction of iron may be associated with a loss of amyloid fibril structure and the formation of amorphous protein aggregates.

Further evidence of Aβ-mediated alterations to ferritin (ferrihydrite) structure was provided through electron diffraction. In the absence of Aβ, ferritin provided ringed diffraction patterns consistent with 6-line ferrihydrite. Following incubation with amyloid no evidence of 6-line ferrihydrite diffraction patterns remained. Instead Aβ/ferritin structures provided diffraction patterns consistent with a body centred cubic (BCC) crystalline material. Notably, similar BCC diffraction patterns were obtained from iron precipitates formed following the acid digestion of ferritin in hydrochloric acid. These data suggest that similar

alterations to the crystal structure of ferritin's ferrihydrite core occur where ferritin structure is disrupted after Aβ interaction, and where ferritin is disrupted chemically; highlighting the destructive nature of amyloid. The material source of these BCC patterns is currently unclear, as calculated lattice parameters (4Å) and *d*-spacing values were not consistent with BCC iron (2Å), or various other cubic iron minerals. However, it is possible that these patterns arise from a mixed-phase iron material, potentially formed through the exposure of amorphous iron material to high electron doses (as described by Suslick *et al.* [183]). Alternatively a highly disordered cubic crystalline phase, akin to the wüstite-like material recorded in pathological ferritin cores taken from AD tissues (Quintana *et al*. [108]) may have formed. Indeed the lattice parameter of wüstite (4.3 Å), is the closest of all the cubic iron minerals to the 4 Å lattice parameter recorded from Aβ/ferritin structures.

Interestingly, by comparing bright field TEM images of Aβ/ferritin aggregates to their corresponding electron diffraction patterns, ferrihydrite crystal structure appeared to become altered in Aβ structures where ferritin morphology was shown to be maintained. This suggests that Aβ may act to alter the crystal state of ferrihydrite prior to the destruction of ferritin and/or the extraction of ferrihydrite from the apoferritin protein shell. These findings support those reported in *Chapter 4*, where Aβ was shown to alter the crystal structure of 2-line ferrihydrite; although no electron diffraction evidence of magnetite was observed following Aβ/ferritin interaction. The ability of Aβ to alter the crystal structure of the ferrihydrite core whilst located within ferritin may also prove consistent with findings Watt *et al*. who reported iron electron transfer across the apoferritin protein shell [179]. Electron transfer in such a manner could allow the chemical reduction of the ferritin's iron core by Aβ (and likewise the oxidation of the peptide), without either iron or protein coming into physical contact with one and another. This

differs from natural ferritin function, where iron(II) is oxidized when it comes into contact with the ferroxidase centres located on the H-chain ferritin subunits [64].

Further indirect evidence of Aβ disruptions to the crystal structure of ferritin's ferrihydrite core were provided through XAS. Although normally stable to soft x-ray exposure, following incubation with Aβ, ferritin became unstable in the x-ray beam, resulting in x-ray induced reduction effects. These reduction traits are typical of amorphous iron phases (as demonstrated in *Chapter 3*), suggesting Aβ to have converted the ferrihydrite core of ferritin into a more amorphous form. Again, these disruptions to ferrihydrite crystal structure are consistent with results displayed in *Chapter 4*, where Aβ was shown to convert 2-line ferrihydrite into a beam-unstable state.

5.5 Conclusions

From the data presented in this chapter it appears that Aβ is capable of disrupting the structure of ferritin, resulting in the chemical reduction of its ferrihydrite core into a redox-active and potentially toxic phase. As ferritin is abundant throughout the human brain [46,64], and has been observed to accumulate in localized regions of Aβ deposition [74,126,178], this interaction process may represent a significant source of oxidative stress in AD tissues, thus contributing to the neurodegeneration associated with AD [37,38,49,53,57,78]. Furthermore, disruptions to ferritin function may detrimentally affect healthy brain functions in which iron plays a key role, resulting in further neurotoxic effects. Importantly these results suggest Aβ to be cable of chemically converting both unbound (see *Chapters 3 and 4*) and bound iron; the form in which iron exists naturally. The ability of Aβ to access the iron content of ferritin would effectively provide a limitless fuel for iron reduction, potentially allowing a sustained production of ROS and oxidative stress in AD tissues. With oxidative stress being a key characteristic of AD pathology [53,57,78], this interaction process could

represent a target for therapies intended to lower oxidative burdens and delay disease progression. Combined with the results presented in *Chapter 4*, there appear to be several avenues with which potential treatments could act to reduce amyloid-induced iron toxicity. First is the targeting of the redox-active phases, such as elemental iron and pure iron(II) phases, which do not occur naturally in the human brain. As described in *Chapters 3 and 4*, removal of these iron forms could reduce oxidative stress without disrupting healthy brain functions. Secondly the interaction of Aβ with ferritin could be targeted for inhibition. By preventing Aβ from detrimentally interacting with ferritin, the formation of redox-iron may be prevented, and the valuable function of ferritin maintained. As disruptions to ferritin have been shown to induce neurotoxic effects [122,175-177] (including the formation of aberrant tau filament structures in AD and PSP patients [123]) , maintaining ferritin function may prove of paramount importance. In summary, the findings presented in this chapter provide insights into processes of Aβ interaction with naturally occurring iron forms, which may prove vital in understanding how iron *and* Aβ contribute to the pathogenesis of AD.

5.6 Further comments

This chapter significantly builds upon the results displayed *Chapters 3* and *4* by introducing iron in a naturally occurring form; within the storage protein ferritin. These findings provide a basic *in vitro* model of how Aβ may come into contact with iron *in vivo*, whilst also further demonstrating the reductive capacity of Aβ.

The results of this study also highlight the requirement for the localized chemical imaging of bioinorganic structures, owing to the heterogeneous interaction effects observed. It is apparent that techniques such as XAS (which allow the generalized oxidative state of a material to be elucidated) do not provide the sensitivity required to understand complex

protein/protein interactions such as those occurring between Aβ and ferritin. For example, the 200 nm reduced iron deposit as detected by STXM-XAS (Figure 5.15), is unlikely to have been detected by traditional XAS techniques; where x-ray beam resolution is typically in the hundred micron range. In this instance, absorbance levels from surrounding oxidized iron regions may overwhelm any reduced iron signal, thus preventing Aβ-induced reduction effects from being detected.

The results presented here provide an intriguing insight into the process of Aβ/ferritin interaction, and highlight the need for this relationship to be examined in greater detail. Key questions remain unanswered including: *how* does Aβ act to disrupt ferritin structure; when does the reduction of ferrihydrite occur (within ferritin; or when released from ferritin); and why was reduced iron found to be accumulated into a small dense aggregate. Further to this, it is imperative to ascertain whether the accumulation of ferritin within Aβ structures is a result of generic protein/protein interactions, or whether this aggregation of ferritin is unique to Aβ. As was highlighted in previous chapters, the cytotoxic effects of these interaction processes are also of great interest. Of particular interest are: whether Aβ interaction with ferritin lead to the generation of neurotoxic compounds; and what are the effects of ferritin interaction upon Aβ neurotoxicity? Proposed experimental procedures intended to address these outstanding questions are provided in *Chapter 8; Future Work*.

Chapter 6

Disruption of magnetite crystal structure by the Alzheimer's disease peptide β-amyloid (1-42)

6.1 Introduction

Throughout *Chapters 3, 4* and *5* there has been a focus on identifying the potential origins for the increased levels of iron(II)-bearing minerals (namely magnetite and wüstite) previously recorded in Alzheimer's disease tissue [36,105,108,113]. Although these investigations have demonstrated the ability of Aβ to form pure iron(II) minerals from ferric iron precursors, no evidence of magnetic iron mineral formation has been observed as a result of Aβ interaction with naturally occurring iron forms. On the basis of these findings, it appears that Aβ is not directly capable of converting non-magnetic iron precursors into magnetic phases in the absence of any other influencing factors (such as enzymes, or metal ion catalysts), over the time period examined.

Notably, studies conducted by Galvez *et al*. report the presence of magnetite within non-diseased ferritin proteins [121], suggesting ferritin to be an amyloid-independent source of magnetic iron within brain tissues. Through iron(II) quantification techniques, this 'natural' magnetite was shown to *not* be a readily accessible source of iron(II). This observation led to the authors concluding that ferritin-derived magnetite is not a source of free toxic ferrous iron within AD tissues. As the results from *Chapter 5* indicate Aβ to be capable of disrupting ferritin structure, it is feasible for Aβ to come into contact with magnetite within the AD brain. Furthermore, with Aβ possessing a remarkable ability to alter the crystal state and oxidative state of iron (*Chapters 3,4* and *5*), amyloid may be capable of converting afore mentioned 'natural' magnetite into a source of free ferrous iron, capable of inducing ROS production thereby contributing towards AD pathology.

To date, only one study (Mir *et al.* [185]) has investigated the interaction between Aβ and magnetite, suggesting the formation of amyloid-magnetite complexes *in vitro*. However these results were far from comprehensive. Significantly, the iron mineral products and

peptide structures formed through Aβ/magnetite interaction are yet to be characterized. In this chapter, physical sciences approaches are combined with traditional microscopy techniques to examine the relationship between Aβ and synthetic, surface oxidized magnetite over a 144 hour period of interaction.

Evidence of magnetite accumulation and sequestering by Aβ is provided through TEM and element-specific STXM images (*Section 6.3.1*). Electron diffraction patterns from Aβ/magnetite structures demonstrate the effect of Aβ interaction upon magnetite crystal phase stability (*Section 6.3.2*) Aβ-mediated alterations to the magnetic and oxidative states of magnetite are then demonstrated through XMCD and XAS respectively (*Section 6.3.3*). Further magnetic characterisation displaying Aβ-induced disruption to magnetite's magnetic state is provided through SQUID magnetometry and AC susceptometry (*Section 6.3.4*). Through this multidisciplinary approach the effect of Aβ interaction upon the mineral state of magnetite is characterized for the first time.

6.2 Materials and methods

6.2.1 Preparation of Aβ/magnetite suspensions

18 mM magnetite (Fe_3O_4) stock suspensions were created through the addition of dH$_2$O to magnetite nanopowder (Sigma Aldrich < 50 nm particle size). Magnetite nanopowders were surface oxidized due to their storage in aerobic environments. Stock suspensions were sonicated for 5 minutes to ensure uniform particle size distribution and suspension stability before being added to either modified KH buffer (pH 7.4; 100 mM PIPES) or dH$_2$O to create a 440 µM magnetite suspension. These 440 µM suspensions were again sonicated for 5 minutes immediately prior to Aβ addition. Additional 440 µM maghemite (Fe_2O_3) nanoparticle suspensions were created in dH$_2$O as described above.

Synthetic Aβ(1-42) was dissolved in 0.1 M NaOH to create a 1mg/mL (220 μM) Aβ stock as described in *Chapter 3*. Aβ stock was added to 440 μM magnetite/maghemite suspensions, and the resulting Aβ/nanoparticle suspensions were neutralized (where required) to pH 7 through the addition of 0.5 M HCl. Final peptide and nanoparticle concentrations were 35 μM and 370 μM respectively.

Aβ-free magnetite/maghemite control suspensions were prepared in the same manner as described above, with the substitution dH$_2$O for Aβ. All solutions were left to incubate at 37°C until the time of sampling.

6.2.2 Electron microscopy

Electron microscopy was performed using a JEOL 1230 microscope operating at 100 kV. Samples examined under electron microscopy were not previously exposed to the x-ray beam used in XAS/XMCD or STXM.

6.2.3 Scanning transmission x-ray microscopy

To generate element specific images of Aβ/magnetite structures, STXM was performed on the Swiss Light Source PolLux beamline (Villigen, Switzerland). Aβ/magnetite suspensions were deposited onto silicon nitride membranes (75 nm thickness) and mounted onto spectromicroscopy plates as described in *Section 2.2.1*. Samples were taken after 48 hours of incubation at 37°C. Sample manipulation and examination was performed in aerobic conditions. Element specific images displaying the carbon and iron content of amyloid aggregates were created as previously described in *Section 2.2.2*. Carbon *K*-edge examination of Aβ structures was performed prior to examination at the iron *L*-edge to prevent x-ray beam induced damage to carbon structures. Different Aβ batches were used

in STXM experiments to those used in electron microscopy, XAS/XMCD, SQUID magnetometry and AC susceptibility experiments.

6.2.4 X-ray absorption spectroscopy and x-ray magnetic circular dichroism

To determine the surface oxidation state and magnetic properties of magnetite following incubation with Aβ, iron $L_{2,3}$-edge XAS and XMCD were performed. X-ray absorption events were recorded using TEY method of detection allowing a probing depth of approximately 5 nm (*see Section 1.4.1*). Small volumes of Aβ/nanoparticle suspensions were deposited onto TEM grids as described in *Chapter 2.1.2*. As described in *Section 2.1.1*, a needle point focusing magnet was used during sample preparation, inducing the concentration of magnetic material into a single 0.5-1 mm diameter aggregate at the centre of the TEM grids This aggregation allowed regions of interest to be efficiently located in XAS/XMCD experiments.

Samples were taken after 30 min, 48 hours and 144 hours of suspension incubation at 37°C. All sample preparation, transport and examination was conducted under anoxic conditions to prevent changes to magnetite valence chemistry. XAS/XMCD examination was performed at Diamond Light Source beamline I10. Two dimensional iron (L_3 -edge) maps revealing the iron content of the sample grids (*see Chapter 2; Figure 2.7d-f*) and detailed iron $L_{2,3}$–edge XAS/XMCD absorption spectra from magnetite/maghemite deposits were obtained as described in *Sections 2.1.3 and 2.1.4*. XAS spectra were recorded via the total electron yield method. XMCD spectra were obtained by recording two x-ray absorption spectra with opposed magnetic fields orientated along the x-ray beam direction. Not all iron deposits provided sufficient signal for complete XAS/XMCD analysis to be performed.

6.2.5 SQUID magnetometry

To confirm the magnetic state of magnetite following incubation with Aβ, SQUID magnetometry was performed. Small volumes (15 μL) of Aβ/magnetite suspensions (and their Aβ free magnetite controls) were deposited into sealed plastic vessels as described in *Section 2.5*. Sampling was performed following two months of incubation at 37°C. Hysteresis loops displaying the magnetic characteristics of the magnetite suspensions were created by measuring the magnetic moment against an applied magnetic field (-5000, 5000 Oe) at temperatures ranging from 5-200K (nullifying blocking effects induced by magnetite nanoparticle size). Measurements were performed using a Quantum Design SQUID-VSM.

6.2.6 AC susceptometry

The magnetic susceptibility of magnetite following long-term incubation with Aβ was also assessed via AC susceptometry. Frequency scans from 100 Hz-150 kHz were performed on Aβ/magnetite suspensions (and their Aβ-free controls) to determine the magnetic state and aggregate size of the magnetite particles. Measurements were taken following 16 months of incubation at 37°C.

6.2.7 Iron(II) quantification in solution

The iron(II) content of amyloid/magnetite and Aβ-free magnetite samples was determined in suspension using the Ferrozine colorimetric assay as described in *Section 2.4* [153]. In an attempt to allow Ferrozine iron binding, acid digestion and iron reduction times were increased to 48 hours to ensure complete digestion of magnetite (please refer to *Section 2.4.4* for the effect of iron crystal state upon Ferrozine binding). Iron(II) quantification readings were taken after 0, 24, 48, 72, 120 and 144 hours of incubation at 37°C.

6.3 Results

6.3.1 The accumulation and sequestering of magnetite nanoparticles by Aβ

To visualize the structures formed through Aβ interaction with magnetite, TEM and STXM were performed.

Examination of Aβ-free magnetite controls revealed the presence of electron dense nanoparticle aggregates typically 1-5 μM in size dispersed evenly throughout the sample grid for all time points examined (Figure 6.1).

Following 0.5 hours of Aβ/magnetite co-incubation, TEM examination revealed multiple fibrillar structures comprised of Aβ, containing regions of aggregated electron dense nanoparticles believed to be magnetite, ranging from 0.5-5 μM in diameter (Figure 6.2). Nanoparticle size and morphology was consistent with those observed in the Aβ-free magnetite controls.

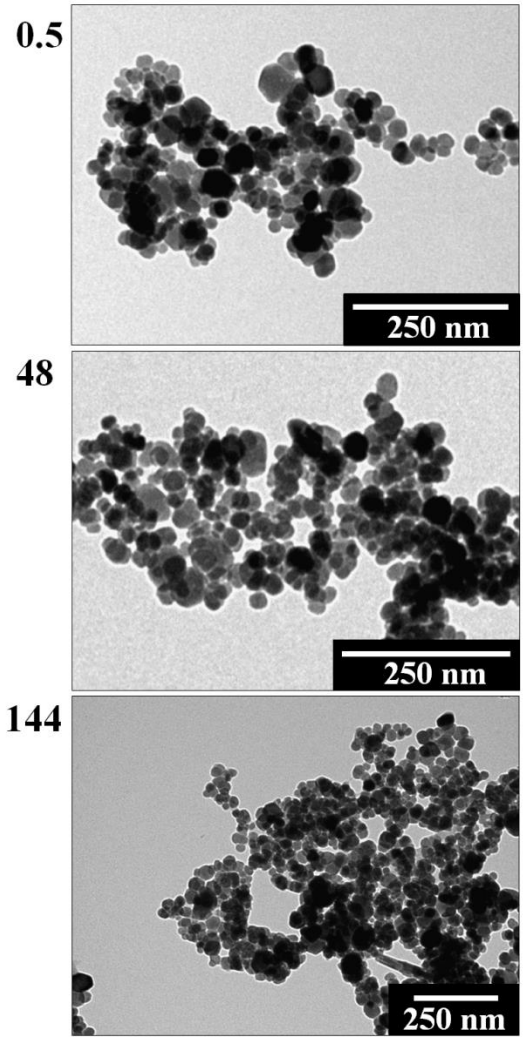

Figure 6.1. TEM images of magnetite nanoparticle aggregates in absence of Aβ. Incubation time in hours are shown to the left of each image.

TEM imaging following 48 hours of Aβ/magnetite incubation largely revealed Aβ structures containing distinct electron opaque magnetite nanoparticle regions as described for the 0.5 hour time point. However certain aggregates contained regions of nanoparticles appearing to be losing their ordered structure as if being digested by Aβ (Figure 6.2; highlighted by dashed red outlines). Further incubation to 144 hours led to the observation of Aβ aggregates containing amorphous electron dense regions integrated within fibril amyloid structures (Figure 6.2 bottom). No evidence of regular nanoparticle structure

could be seen in these regions, further indicating the destruction of magnetite nanoparticle structure by Aβ.

No clear correlations between Aβ aggregate size and incubation time were observed, with aggregate size typically ranging between 5-50 μM in diameter. Where Aβ and magnetite were incubated together, no accumulates of magnetite were observed free of Aβ structures. Following 0.5 hours of incubation, Aβ fibril structure was seen to be maintained in regions of magnetite deposition. However, in certain instances, evidence of amyloid fibril disruption was observed following 48 and 144 hours of incubation, in correlation with the occurrence of Aβ-mediated disturbances to magnetite nanoparticle structure (Figure 6.2; highlighted by solid blue outlines). These findings indicate magnetite to induce the aggregation of Aβ (in comparison to iron-free Aβ aggregates shown in *Chapter 3* and *Chapter 5*), with Aβ being capable of integrating magnetite nanoparticles into its fibrillar structure.

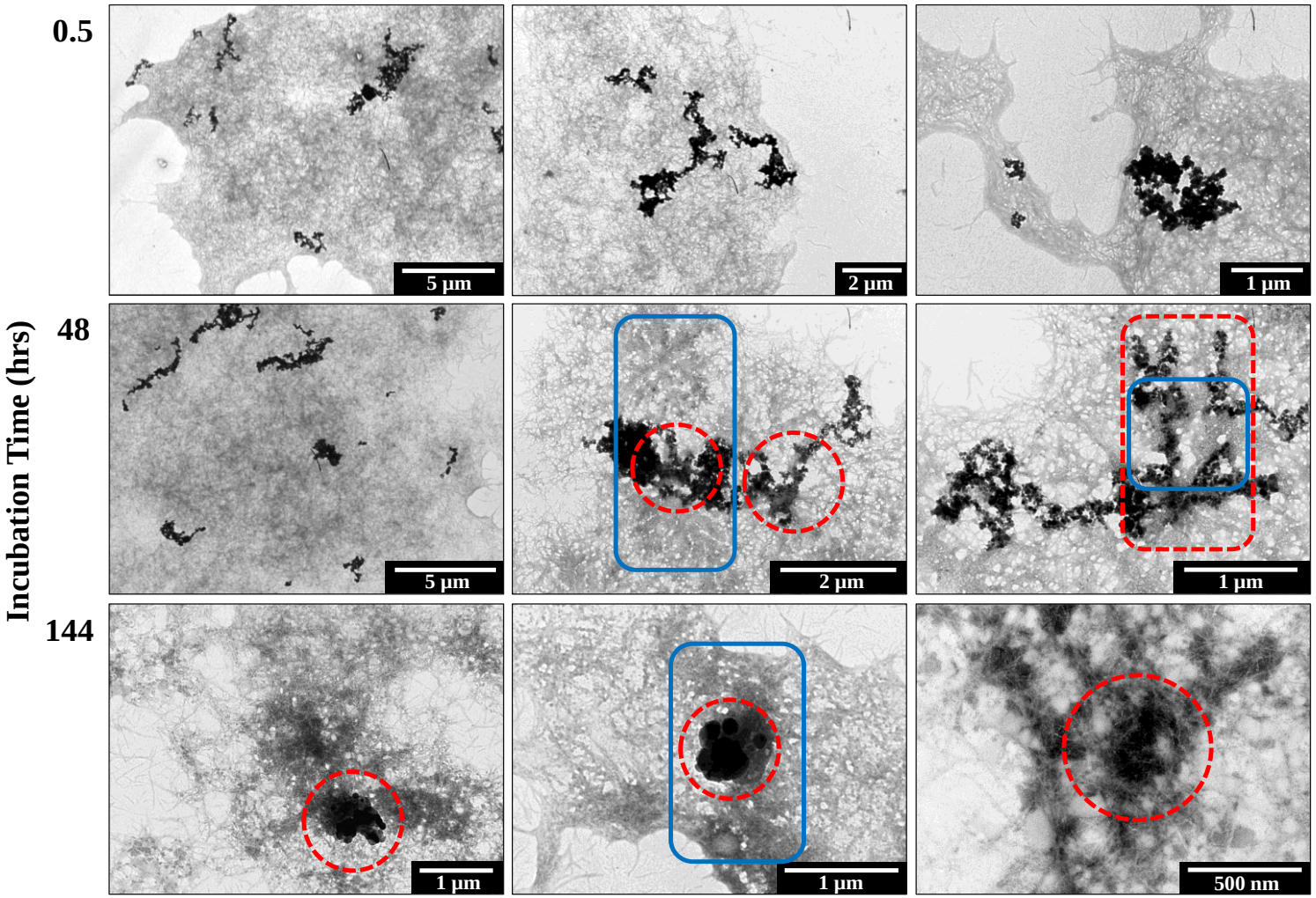

Figure 6.2. TEM images of Aβ aggregate structures formed following incubation with magnetite nanoparticles. Incubation times are displayed to the left of each row. Red dashed outlines show regions of magnetite nanoparticle disruption, blue solid outlines show amorphous Aβ regions.

To confirm that the electron dense particles found within amyloid aggregates were composed of magnetite, carbon *K*-edge and iron $L_{2,3}$-edge microspectroscopy were performed in STXM experiments. Element specific images of an Aβ/magnetite structure formed following 48 hours of incubation are displayed in Figure 6.3.

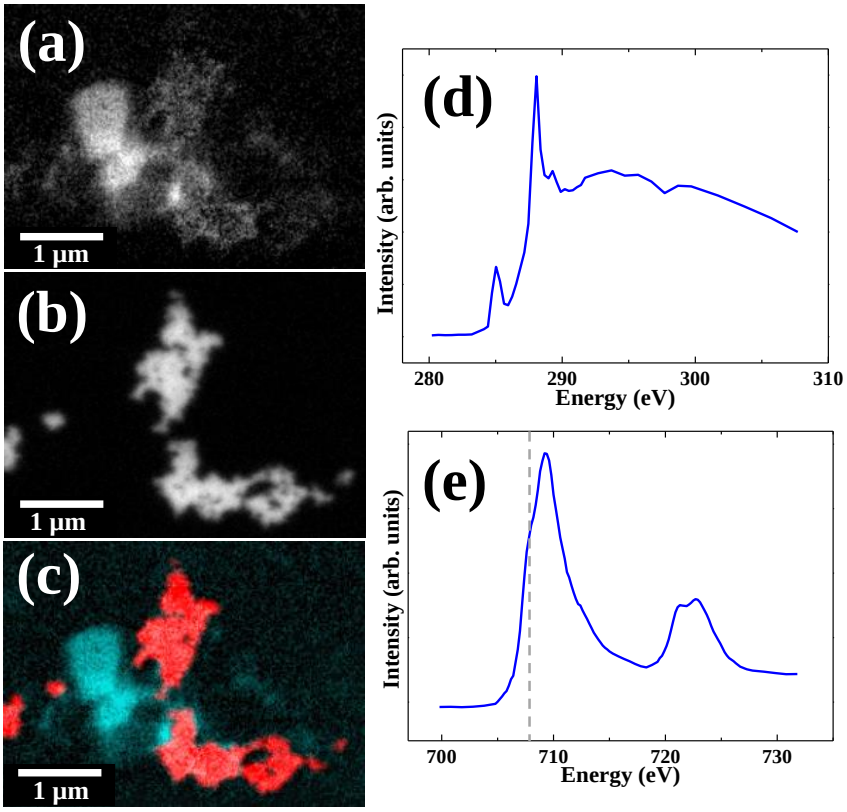

Figure 6.3. Element specific STXM images and XAS spectra from a Aβ/magnetite aggregate formed following 48 hours of incubation. **(a)** Carbon *K*-edge map revealing Aβ content. **(b)** Iron *L*-edge map of the same aggregate displaying magnetite content. **(c)** Composite image of (a) and (b). **(d)** Carbon *K*-edge XAS spectra from (a). **(e)** Iron $L_{2,3}$-edge XAS spectra from (b). The grey dotted line at 708 eV is a visual guide for the L_3-edge Fe^{2+} peak position.

Carbon *K*-edge examination of Aβ/magnetite samples (Figure 6.3a) led to the observation of multiple carbon dense structures with carbon *K*-edge x-ray absorption profiles (Figure 6.3d) consistent with the amyloid aggregates presented in *Chapter 3*, and the calculated XAS spectra for the amino-acid base sequence of Aβ(1-42) [143].

Corresponding iron L_3-edge examination revealed regions of iron accumulation within these carbon structures (Figure 6.3b), which provided iron $L_{2,3}$-edge x-ray absorption profiles (Figure 6.3f) consistent with the iron mineral magnetite (see reference magnetite XAS spectra in *Section 1.4, Figure 1.9; green*). These results confirm the co-aggregation of magnetite within Aβ structures as observed via electron microscopy (Figure 6.2). No evidence of iron accumulation was found free of Aβ structures.

6.3.2 Aβ induced alterations to magnetite crystal structure

Electron diffraction imaging of magnetite incubated in the absence of Aβ provided ringed diffraction patterns characteristic of nanopowder magnetite for all time points examined, an example of which can be seen in the left hand panels of Figure 6.4. Sharp complete rings are present at 2.97, 2.53, 2.1, 1.61 and 1.48Å corresponding to the 5 strongest reflections of magnetite: [220], [311], [400], [511] and [440] respectively (JCPDS card 88-0315). No changes to electron diffraction patterns were seen with increasing incubation time, demonstrating the crystal structure of magnetite to be maintained throughout the experimental period.

Following 0.5 (Figure 6.4 a) and 48 hours (Figure 6.4 b) of incubation with Aβ, magnetite deposits provided diffraction ring patterns indistinguishable to the Aβ-free magnetite controls. This characteristic magnetite diffraction pattern was maintained in regions where Aβ appears to be altering nanoparticle structure, such as the Aβ/magnetite aggregate shown in Figure 6.2 (middle row, right), although a diffuse background not present in the magnetite controls, can also be seen.

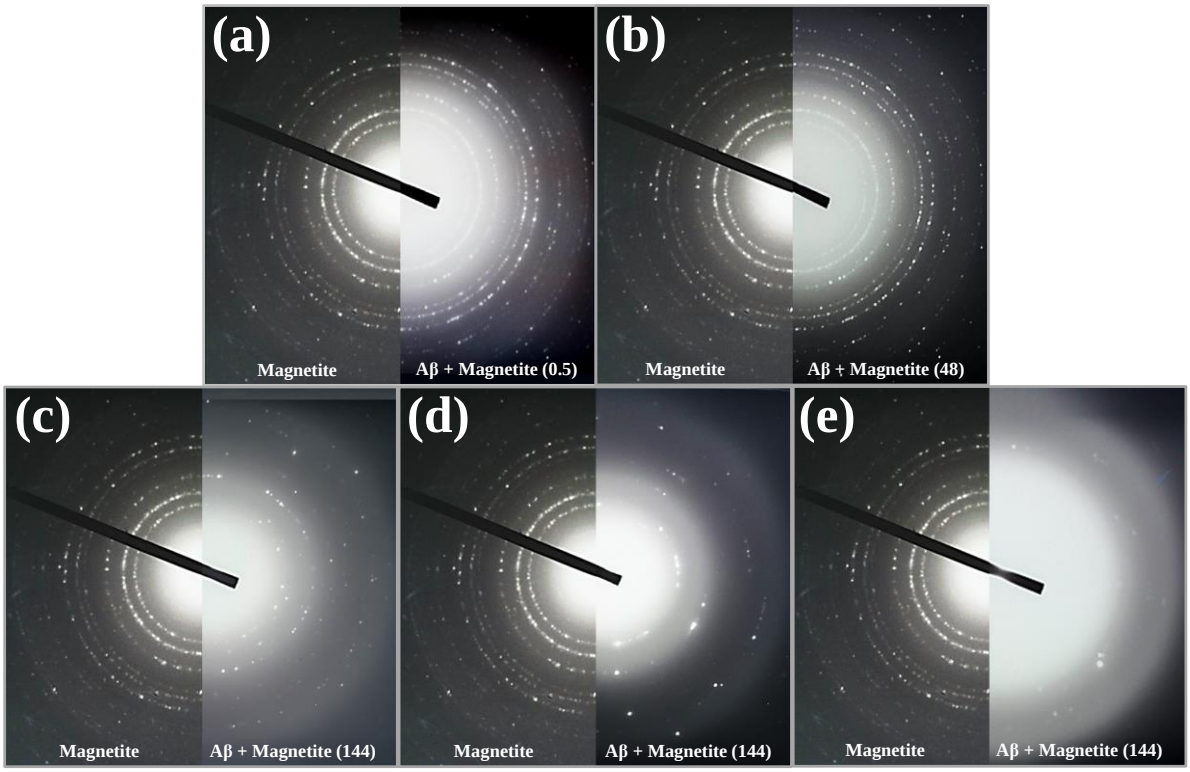

Figure 6.4. Electron diffraction patterns from a magnetite reference (left image in each panel) compared to magnetite incubated with Aβ (right image). Patters from Aβ/magnetite deposits following **(a)** 0.5 hours incubation (corresponding to Figure 6.2; top row, right), **(b)** 48 hours incubation (corresponding to Figure 6.2; middle row, central), **(c)** 144 hours (Figure 6.2; bottom, left), **(d)** 144 hours (Figure 6.2; bottom, central) and **(e)** 144 hours (Figure 6.2; bottom, right).

However, after 144 hours of incubation with Aβ, significant alterations to electron diffraction patterns obtained from magnetite deposits were observed. By comparing Figure 6.4c and Figure 6.4d (obtained from the Aβ aggregates shown in Figure 6.2; bottom row, left and Figure 6.2; bottom row, middle respectively) to magnetite references, clear disruptions to the [220], [311], [400], [511] and [440] reflections of magnetite can be seen. These diffraction rings are no longer continuous, having been replaced with incomplete spotted ring patterns. Such findings suggest Aβ to have disrupted the crystal structure of a large proportion of the magnetite nanoparticles present.

Further electron diffraction patterns shown in Figure 6.4e (corresponding to the Aβ structure displayed in Figure 6.2; bottom row, right) reveal the crystalline structure of magnetite to have been completely lost following 144 hours of incubation with Aβ. These patterns suggest the presence of a nearly amorphous iron material, a result in keeping with the bright field TEM images displayed in Figure 6.2. Taken together these results indicate Aβ be capable of altering the crystal structure of magnetite. It should also be noted that no evidence of a ferrihydrite-like material (2-line or 6-line) was observed following Aβ interaction with magnetite.

6.3.3 Oxidative state and magnetic properties of magnetite following Aβ interaction

Iron $L_{2,3}$–edge x-ray absorption spectra showing the oxidation state of magnetite incubated in the presence or absence of Aβ as a function of time are displayed in Figure 6.5.

Where magnetite was incubated in the absence of Aβ, XAS examination provided iron $L_{2,3}$-edge spectra characteristic of the pure iron(III) mineral maghemite at 0.5 and 48 hour time points (Figure 6.5a). The L_3-edge shoulder feature (708 eV) associated with magnetite is absent, being replaced by a well-defined L_3 pre-peak structure characteristic of iron(III) minerals. Further to this, the L_3 peak position is seen to shift to a higher energy (709.5 eV) than observed in magnetite references (709.2 eV), and at the L_2 edge, Fe^{3+} cation features (723 eV) are enhanced in comparison to the Fe^{2+} features (721 eV). These differences in XAS spectra are caused by magnetite nanoparticle oxidation, resulting in the formation of maghemite at the nanoparticle surface. As XAS/XMCD spectra were recorded using the TEY method, where only the outermost 5 nm of a material can be probed, this surface oxidation resulted in a Fe^{3+} cation dominated XAS spectra. Following 144 hours of

incubation, no areas of magnetite accumulation were found that provided a sufficient iron x-ray absorption signal to allow full iron $L_{2,3}$-edge XAS/XMCD analysis.

Iron $L_{2,3}$-edge XAS probing of Aβ/magnetite deposits revealed evidence of increased Fe^{2+} content following 48 and 144 hours of incubation (Figure 6.5b). As in *Chapter 3*, these modest enhancements are believed to be a result of x-ray beam induced iron reduction. Consecutive XAS scans revealed magnetite to be unstable in the x-ray beam once incubated with Aβ, with increased periods of x-ray beam exposure resulting in enhancements to Fe^{2+} cation features. Indeed, initial rapid XAS scans across the iron L_3–edge (to confirm the presence of iron) provided spectra characteristic of a Fe^{3+} mineral. However, upon full $L_{2,3}$-edge examination (in which iron deposits are exposed to the x-ray beam for prolonged periods) clear increases to Fe^{2+} content were apparent (Figure 6.6). As crystalline iron phases are typically stable when exposed to x-rays in the soft energy range (Figure 6.7), these x-ray induced reduction effects indicate Aβ to have altered the crystal structure of magnetite, resulting in the formation of an x-ray unstable iron precipitate, similar to the iron examined in *Chapter 3*. These results are entirely consistent with those obtained through electron microscopy where Aβ was shown to disrupt magnetite nanoparticle structure.

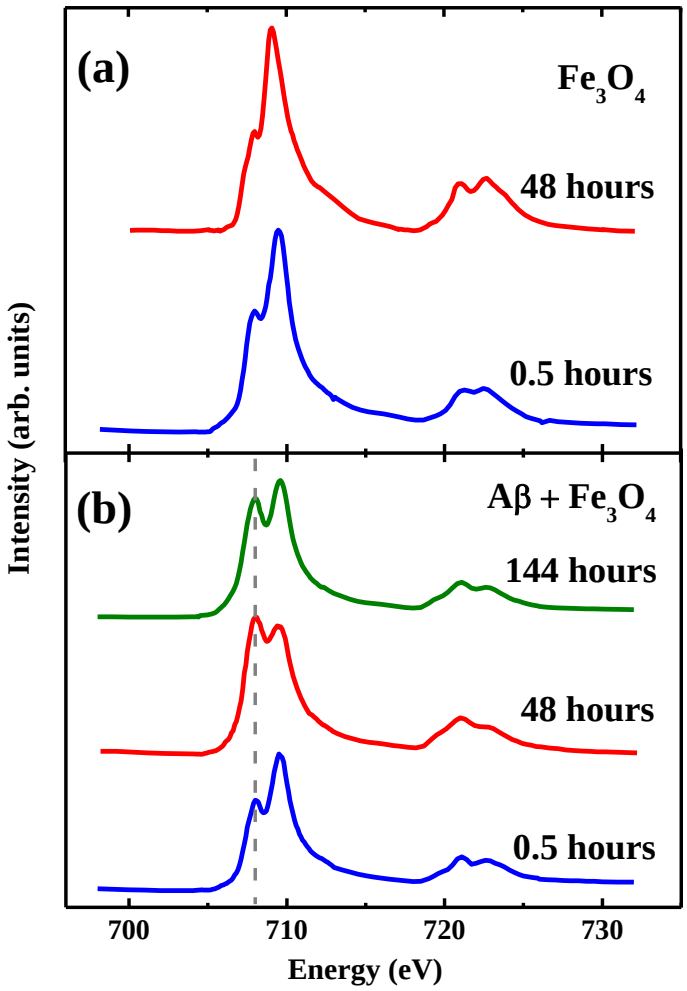

Figure 6.5. Iron $L_{2,3}$-edge XAS spectra from magnetite incubated in dH$_2$O in the absence **(a)** and presence **(b)** of Aβ. Incubation times are shown above each spectrum. The grey dotted line at 708 eV (bottom) is a visual guide for the L_3-edge Fe^{2+} peak position.

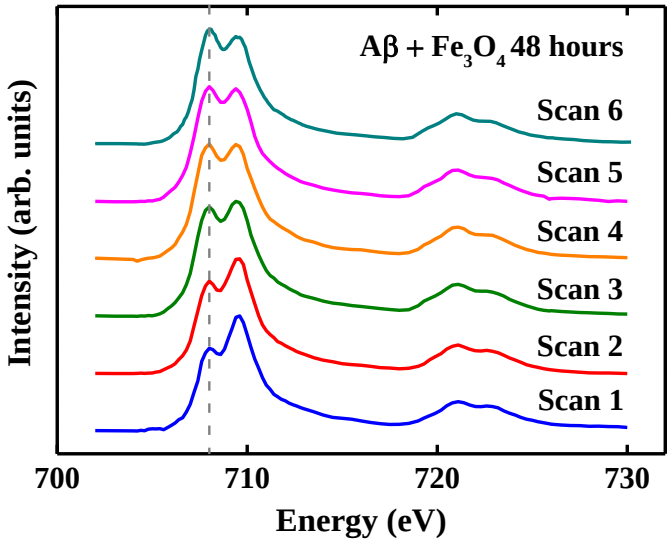

Figure 6.6. Iron $L_{2,3}$-edge x-ray absorption spectra of an x-ray unstable magnetite aggregate formed following 48 hours of incubation with Aβ. L_3 edge Fe^{2+} cation peak features (indicated by a grey dotted line at 708 eV) are shown to become enhanced following six successive XAS measurements.

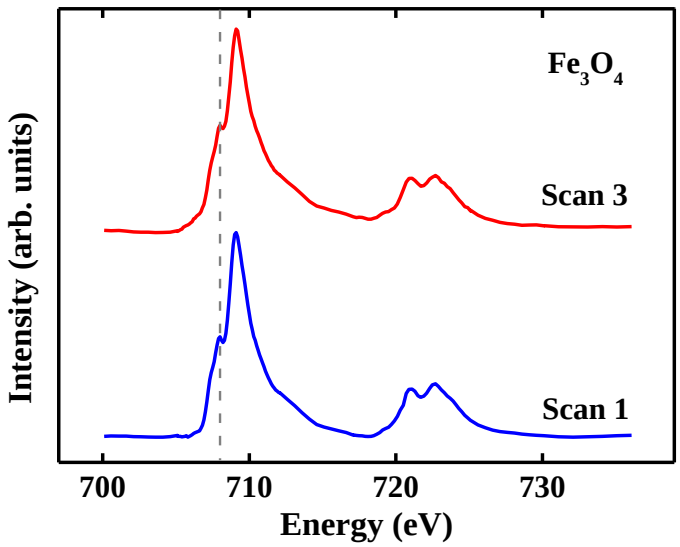

Figure 6.7. Iron $L_{2,3}$-edge x-ray absorption spectra from a magnetite aggregate stable under x-ray beam exposure. Note there is no enhancement to Fe^{2+} cation features with increasing scan number. The grey dotted line at 708 eV is a visual guide the primary Fe^{2+} L_3 peak position.

To assess the magnetic state of magnetite deposits, XMCD was performed across the iron $L_{2,3}$ absorption edges. Following 0.5 and 48 hours of incubation in the absence of Aβ, magnetite deposits provided XMCD spectra consistent with the iron(III) mineral maghemite, with strong dichroism effects of 10-15% being observed (Figure 6.8a). Increases in L_3-edge Fe^{3+} cation features in relation to L_3-edge Fe^{2+} features are apparent compared to magnetite standards (Figure 6.8c), due to the oxidized surface of the magnetite nanoparticles used. Magnetite samples prepared following 144 hours of incubation did not provide sufficient signal strength to allow full XMCD analysis.

Following 0.5 hours of incubation with Aβ, iron $L_{2,3}$-edge XMCD examination of magnetite deposits provided spectra remarkably different to that of the Aβ-free control (Figure 6.8b). XMCD spectra revealed a dramatic decrease in dichroism effects, with values of approximately 2.5% being recorded. Further to this, XMCD spectra were no longer comprised of the characteristic three-peak structure synonymous with magnetite (Figure 6.8c)[137]; instead two poorly defined negative peaks were recorded at 708.5 and 710 eV. Following 48 and 144 hours of incubation XMCD probing provided spectra with small dichroism effects of 1-1.5%, and evidence of antiferromagnetic ordering of Fe cations (Figure 6.8b). These XMCD spectra were very similar to those displayed in *Chapters 3 and 4*, suggesting a similar antiferromagnetic phase to have formed.

As was observed in the iron $L_{2,3}$-edge XAS spectra shown in Figure 6.5, XMCD spectra displayed variations in Fe^{2+} XMCD features in response to x-ray beam induced reduction. Spectra collected after 0.5 hours of magnetite incubation with Aβ show little evidence of Fe^{2+} cation components at either the L_3 or L_2 edge (Figure 6.8b; blue). However, following 48 hours of incubation with Aβ, tetrahedral Fe^{2+} XMCD features at both iron *L*-edges are significantly enhanced compared to those recorded following 0.5 hours, providing a Fe^{2+} dominated spectrum (Figure 6.8b; red). Following 144 hours of incubation Fe^{2+} cation

contributions decrease in intensity compared to those recorded at the 48 hour time point, providing an intermediate Fe^{2+}/Fe^{3+} XMCD spectra (Figure 6.8b; green).

Aβ-induced decreases in dichroism effects were observed where magnetite (Figure 6.9a) and maghemite (Figure 6.9b) nanoparticles were incubated with Aβ.

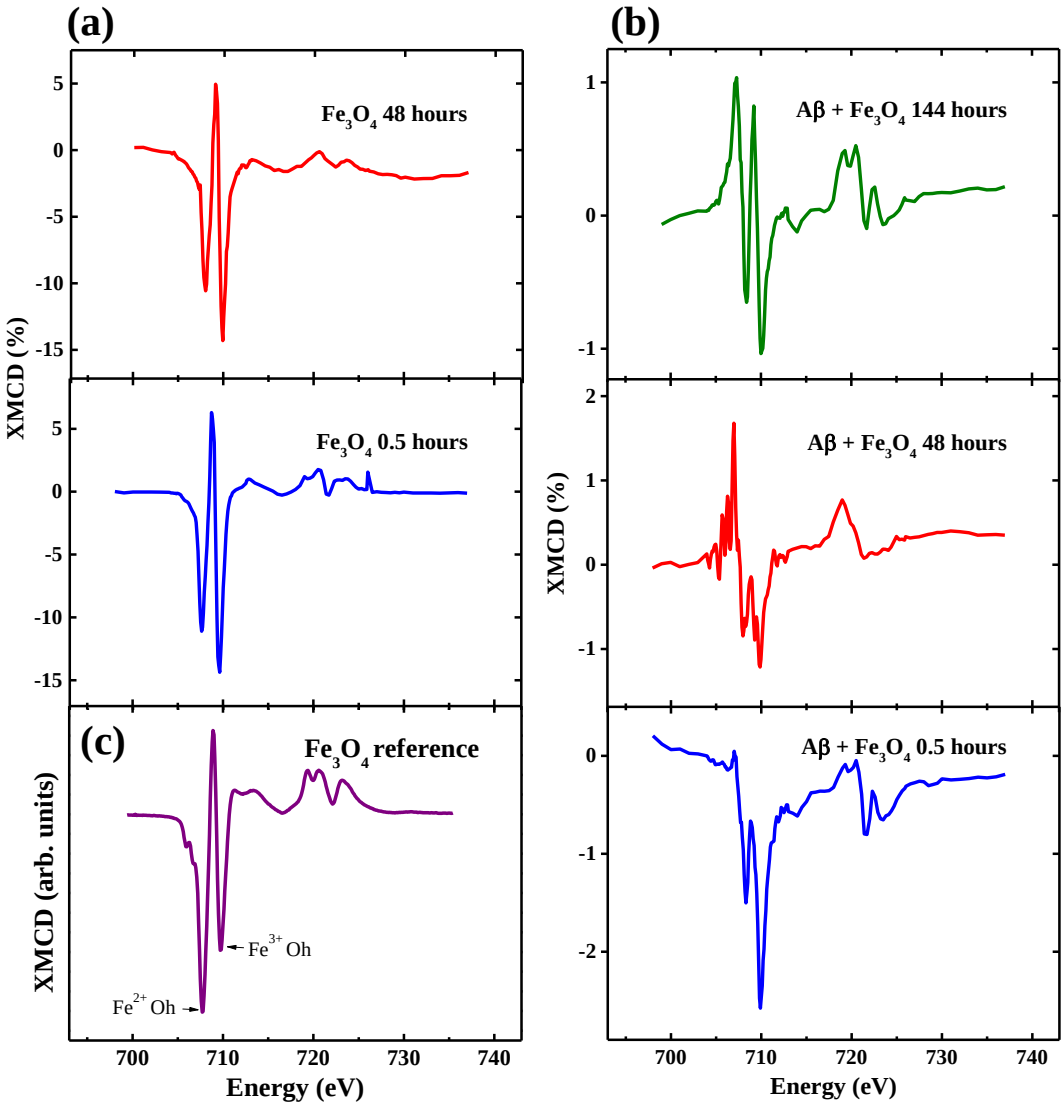

Figure 6.8. Iron $L_{2,3}$-edge XMCD spectra obtained from magnetite incubated in the absence **(a)** and presence **(b)** of Aβ. Incubation times are shown above each spectrum. **(c)** An additional magnetite reference is provided in the bottom left corner. Labels in (c) indicate the positions of the L_3-edge octahedral Fe^{2+} and Fe^{3+} cation contributions, whose ratios alter dependent upon magnetite oxidation state.

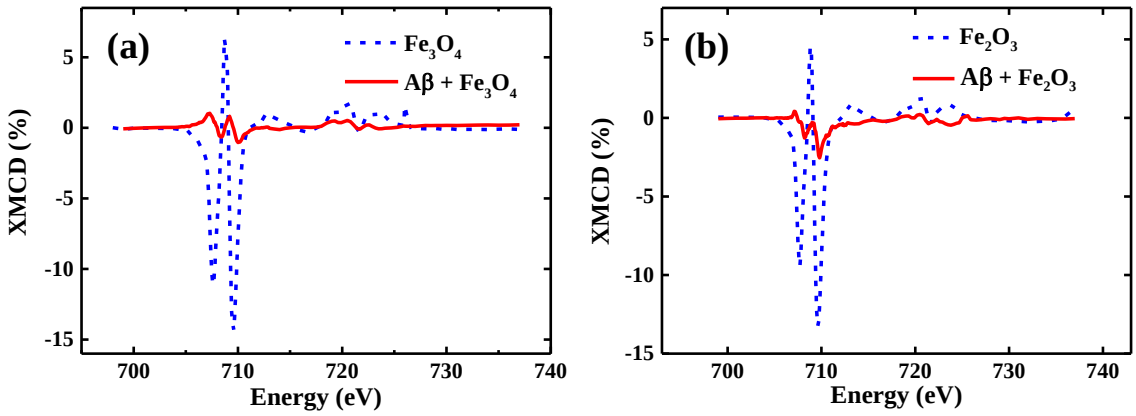

Figure 6.9. Comparisons of iron $L_{2,3}$-edge XMCD spectra obtained from magnetite (Fe_3O_4) and maghemite (Fe_2O_3) nanoparticles incubated in the absence and presence of Aβ. **(a)** Magnetite (blue; 0.5 hours incubation) and Aβ + magnetite (red; 144 hours). **(b)** Maghemite (blue; 0.5 hours) and Aβ + magnetite (red; 48 hours).

Thus XMCD measurements confirm the ability of Aβ to alter magnetite structure, resulting in the loss of magnetite's ferrimagnetic properties and the formation of a weakly magnetic antiferromagnetic material similar to those displayed in *Chapters 3* and *4*.

6.3.4 Magnetic characterisation of magnetite following Aβ interaction

To further assess the magnetic properties of magnetite following incubation with Aβ, SQUID magnetometry and AC susceptometry measurements were performed.

6.3.4.1 SQUID magnetometry

Hysteresis loops displaying the magnetic moment versus magnetic field (-5000, 5000 Oe) over a temperature range of 10-100 K from magnetite suspensions following two months of incubation in the presence or absence of Aβ are displayed in Figure 6.10.

Where incubated in the absence of Aβ, magnetite suspensions provided hysteresis loops characteristic of a ferrimagnetic material (Figure 6.10a). Magnetic moment values were consistent with magnetite references of equal concentrations (not shown) suggesting the magnetic properties of magnetite to have been maintained following the two month incubation period.

However when incubated in the presence of Aβ for two months, magnetite suspensions provided no evidence of a strongly magnetic material at any temperature examined (Figure 6.10b-c). Hysteresis loops were characteristic of a superparamagnetic material, with magnetic moment values approximately 50 times lower than Aβ-free magnetite control suspensions (Figure 6.10d). This dramatic decrease in magnetite magnetic moment following incubation with Aβ is consistent with XMCD results shown in Figure 6.8, where Aβ was shown to convert magnetite into a weakly magnetic antiferromagnetic phase.

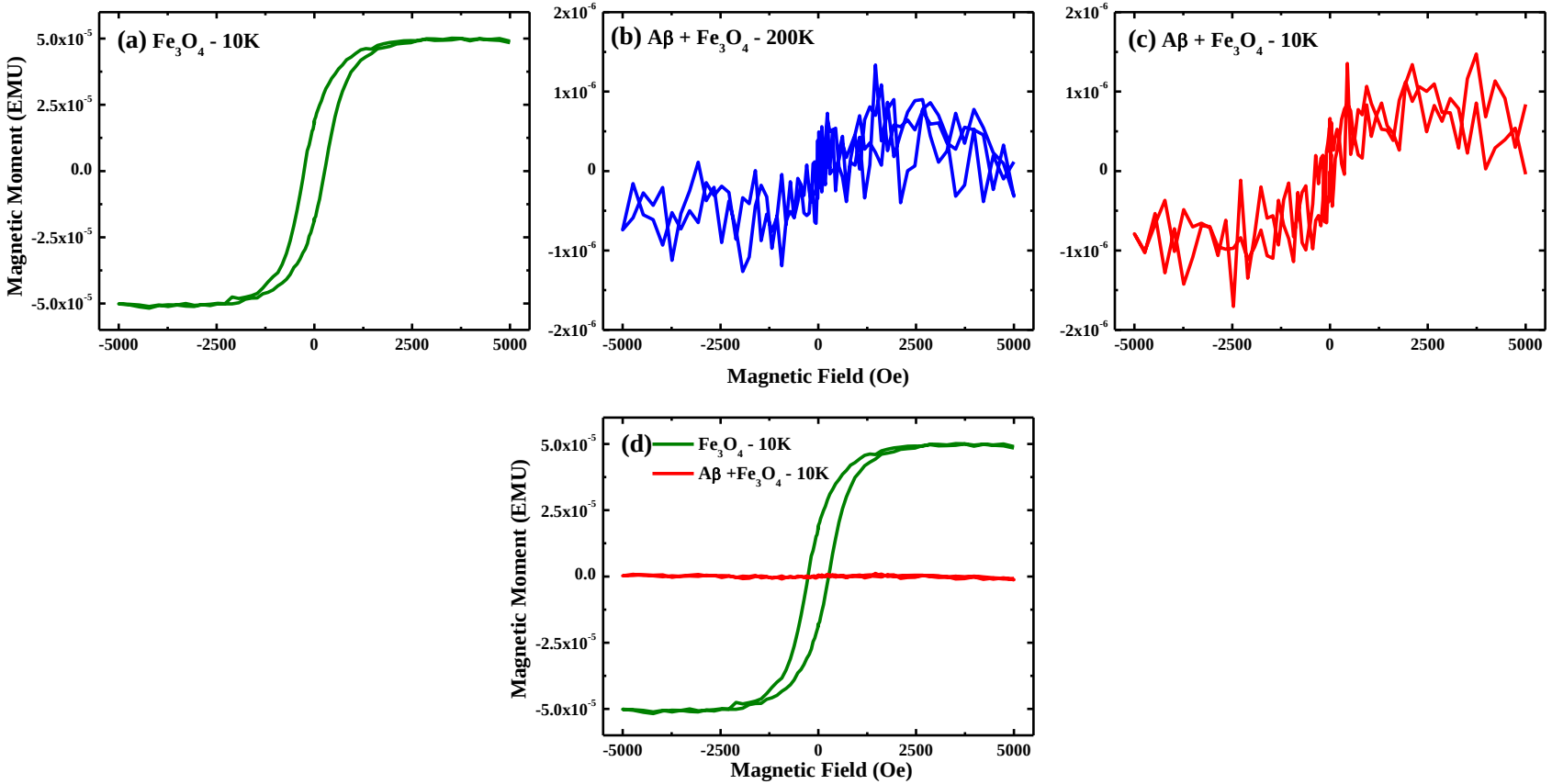

Figure 6.10. Hysteresis loops (-5000, 5000 Oe) obtained from magnetite solutions incubated for 2 months in the absence **(a)** and presence **(b)** and **(c)** of Aβ. Measurement temperatures (K) are displayed in each panel.

6.3.4.2 AC susceptometry

To confirm the magnetic properties of magnetite suspensions following 20 months of incubation in the presence or absence of Aβ, AC susceptibility measurements were taken. Results of these measurements are shown in Figure 6.11 and Figure 6.12.

In the absence of Aβ, magnetite suspensions provided positive χ' values of across the frequency range examined (Figure 6.11). These values were slightly higher to those obtained from concentration-matched magnetite references (*see Chapter 4, Figure 4.5*). This enhanced magnetic signal is believed to arise through the evaporation of water from the magnetite suspensions following extensive periods of incubation at 37°C, resulting in an increase in magnetite concentration (per μL of suspension). Regardless of the precise values, these measurements confirm magnetite suspensions to have maintained their magnetic properties following 20 months incubation in the absence of Aβ. No clear peaks in χ" values were obtained from Aβ-free magnetite suspensions, suggesting a polydisperse magnetite aggregate size distribution.

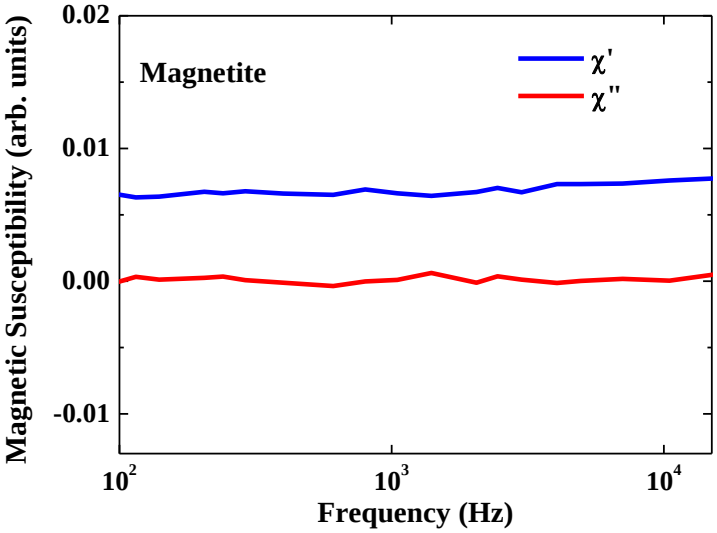

Figure 6.11. AC susceptometry measurements of magnetite suspensions incubated in the absence of Aβ for 20 months.

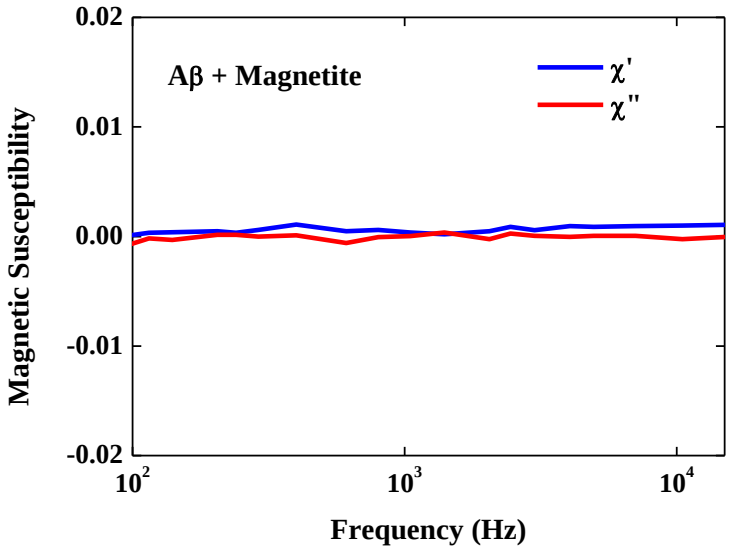

Figure 6.12. AC susceptometry measurements of magnetite suspensions incubated in the presence of Aβ for 20 months.

When incubated with Aβ for 20 months, magnetite suspensions provided small, positive χ' values (Figure 6.12) which were significantly lower than both the time-matched Aβ-free magnetite control and magnetite reference suspensions. Such decreases in χ' values

correspond to a loss of magnetic signal and suggest no ferromagnetic/ferrimagnetic material to be present. As was the case in the Aβ-free magnetite suspensions, no clear peak in χ" values was observed.

These results suggest Aβ to be capable of altering magnetite structure causing a loss in the magnetic properties of the mineral, a finding consistent with those obtained through XMCD and SQUID magnetometry.

6.3.5 Iron(II) quantification in solution: Ferrozine assay

In an attempt to quantify iron(II) levels of the Aβ/magnetite suspensions Ferrozine assays were conducted. The results of these assays (not shown) were inconclusive, due to incomplete magnetite acid digestion as indicated by erroneous total iron content values.

6.4 Discussion

Through a multidisciplinary approach incorporating electron microscopy, STXM, XAS, XMCD, magnetic susceptometry and SQUID magnetometry, Aβ is shown to be capable of sequestering magnetite nanoparticles within its fibrillar structure, with this interaction leading to the disruption of magnetite crystal structure and a loss of magnetite's ferrimagnetic properties.

Electron microscopy and STXM examination of structures formed through Aβ incubation with magnetite revealed the presence of large amyloid fibrillar structures containing regions of aggregated nanoparticles, indicating Aβ to be capable of sequestering magnetite. The affiliation of Aβ for magnetite appears to be very strong, with no evidence of magnetite being observed in the absence of the Aβ when incubated together, suggesting possible binding of magnetite by Aβ. These findings are in agreement with studies published by Mir *et al.* who found amyloid fibrils to complex with magnetite *in vitro* [185];

however the evidence presented here demonstrates this interaction process with a much improved level of clarity. Furthermore, the association between Aβ and magnetite provides another potential origin to the magnetite/maghemite material found within amyloid plaque material abstracted from AD tissues (Collingwood *et al*. (2008) [36]). *Should* physiological ferritin contain magnetite (see Galvez *et al.* [121]), Aβ could act to disrupt ferritin function (as suggested in *Chapter 5*) resulting in a release of this magnetite component, which is then sequestered by Aβ. The extensive aggregation of Aβ in the presence of magnetite indicates the iron mineral to induce amyloid aggregation in a similar manner to iron(III) as evidenced by House *et al.* [95] and in *Chapter 3* of this thesis.

Through electron microscopy, Aβ/magnetite interaction is shown to result in the destruction of magnetite nanoparticle structure. This destructive process appears to begin at the nanoparticle surface, causing disruptions to nanoparticle morphology without significantly altering the crystal structure of magnetite's core. Further interaction with Aβ sees a complete loss of magnetite core crystal structure, resulting in the formation of a largely amorphous iron phase. Magnetite was found to be in varied crystal states following the same period of incubation with Aβ, indicating nanoparticle digestion by Aβ to be non-uniform. Such observations suggest factors such as nanoparticles aggregate size and surface area to potentially alter the effect of Aβ interaction upon nanoparticle structure. As no evidence of a ferrihydrite-like material was observed following magnetite incubation with Aβ, the digestion of magnetite into an amorphous phase does not appear to pass through a ferrihydrite intermediate. Thus the phase transitions described in this chapter appear to be of a different lineage to those observed in iron reducing bacterium, where ferrihydrite acts as a precursor for magnetite formation [137].

Surprisingly the crystal state of sequestered magnetite also appears to have an effect upon the morphology of Aβ fibrils. Where nanoparticle structure was maintained, traditional amyloid fibril morphology was also observed. However, once magnetite crystal structure became disrupted, fine fibril structure was often lost in amyloid regions immediately surrounding magnetite accumulation. Amorphous Aβ/magnetite structures appear similar to those observed following Aβ interaction with iron(III) as displayed in *Chapter 3*. These observations suggest the crystal state of magnetite to be a determining factor in how Aβ physically interacts with the mineral. When in a nanoparticle form, large crystal size may prevent magnetite from becoming incorporated into amyloid structures. Conversely once magnetite crystal structure is disrupted this physical barrier is lifted, allowing (what was originally) magnetite to integrate into amyloid aggregates, forming Aβ/iron structures comparable to those shown in *Chapter 3* (*Figure 3.3*).

Iron $L_{2,3}$-edge XAS examination of Aβ/magnetite deposits suggest that Aβ is not directly capable of chemically reducing magnetite over the time period examined. However incubation with Aβ did result in magnetite becoming unstable when exposed to the x-ray beam, resulting a x-ray beam induced enhancement of Fe^{2+} content, a characteristic of amorphous iron phases (see *Chapter 3*; *Figure 3.12*). As magnetite incubated in the absence of Aβ was shown to remain stable under x-ray beam exposure, these x-ray beam induced reduction effects appear to be a result of Aβ/magnetite interaction. These findings indicate Aβ to convert crystalline magnetite into a more amorphous phase, a result consistent with bright field TEM and electron diffraction images, and the results of *Chapters 4* and *5*, where Aβ was shown to convert 2-line ferrihydrite and ferritin into a state susceptible to x-ray beam induced reduction.

Iron $L_{2,3}$-edge XMCD probing of magnetite following incubation with Aβ revealed a dramatic decrease in magnetic dichroism compared to Aβ-free magnetite controls. After

only 30 minutes of incubation with Aβ, dichroism effects were seen to decrease 5-fold, dropping from 10-15% to 2.5%. Following 48 and 144 hours of incubation with Aβ, dichroism effects continued to decrease to 1-1.5%, providing XMCD spectra reminiscent of a weakly antiferromagnetic material, consistent with those displayed in *Chapters 3* and *4*. Moreover, similar decreases in magnetic dichroism were observed when maghemite was incubated with Aβ, displaying Aβ to disrupt the structure of multiple magnetic iron phases. Moreover, the XMCD spectra and electron diffraction patterns obtained from Aβ/magnetite structures formed following 48 hours of incubation, provide a possible explanation for the nanoparticle deposits witnessed in AD plaque cores, which despite showing a crystal structure consistent with magnetite/maghemite did not possess any detectable magnetism [36].

Additional SQUID magnetometry and AC susceptometry measurements further demonstrated the magnetic properties of magnetite to be diminished following incubation with Aβ. Such a process represents a significant alteration to magnetite structure, highlighting the destructive nature of Aβ interaction upon nanoscale iron minerals.

6.5 Conclusion

Taken together these results demonstrate the remarkable ability of Aβ to both sequester and disrupt the crystal structure of magnetic iron nanoparticles, resulting in their conversion to amorphous, weakly magnetic antiferromagnetic phases. This process did not result in the chemical reduction of magnetite over the time period examined. However as Aβ is capable of chemically reducing various poorly crystalline and amorphous iron forms (please refer to *Chapters 3,4 and 5*), this "digestion" step may be a prerequisite for magnetite reduction. Thus further incubation (beyond the time-frame examined in this chapter) of digested magnetite with Aβ may result in its conversion to a pure-ferrous or

elemental (Fe^0) state as seen in *Chapters 3, 4 and 5*. Moreover, magnetite was shown to induce Aβ aggregation resulting in the formation of amyloid fibril arrangements with the potential to convey neurotoxicity (although the effect of Aβ aggregation state upon neurotoxicity is debated) [104]. Thus the interaction of Aβ with magnetite may serve to increase amyloid toxicity, along with providing potential precursors for redox-active iron formation. The observation of magnetite within physiological [121] and pathological [108] ferritin coupled with the ability of Aβ to disrupt ferritin function (*Chapter 5*), suggests that Aβ may come into contact with magnetite in the AD brain. I tentatively suggest that this relationship may prove detrimental to neuronal health through the activation of the immune system's inflammatory response, in response to the creation of insoluble amyloid structures [12]. Furthermore the ability of Aβ to destroy magnetite crystal structure, may in turn facilitate its conversion to a highly redox-active phase capable of inducing oxidative stress[49]. Thus interactions between Aβ and magnetite could play a significant role in AD pathogenesis and warrant further investigation.

6.6 Additional comments and implications for further work

The preliminary results presented in this chapter provide an interesting insight into the destructive nature of Aβ upon crystalline iron. However further characterisation of the mineral products formed following extended periods of Aβ/magnetite interaction are required to understand the relevance of this interaction process with regards to the formation of redox-active iron phases. In addition, it is imperative to determine whether the impressive amyloid aggregate structures formed in the presence of magnetite are capable of inducing cytotoxic effects that could contribute to AD pathology. Unfortunately the effects of Aβ interaction upon magnetite crystal structure/magnetic properties as

presented in this chapter have proved to be difficult to reproduce, and further more comprehensive experimentation is required to understand this relationship in a greater level of detail.

Another noteworthy finding presented in this thesis chapter, is the inability of Ferrozine to bind to magnetite. It is apparent that magnetite crystal structure must be completely destroyed for its Fe ions to freely bind with Ferrozine. Ferrozine iron(II) quantification techniques were also used by Galvez *et al.* to determine the iron(II) content of magnetite found within ferritin cores; however no acid digestion step was applied. As no detectable iron(II) signal was observed following Ferrozine addition to ferritin-derived magnetite, the authors concluded that ferritin-derived magnetite could not be a source of the toxic "free" (i.e. unbound/poorly liganded) ferrous iron observed in AD tissues. However these conclusions are extremely misleading. Although, the ferrous iron content of magnetite is not free to complex with Ferrozine, it is free to partake in redox chemistry. In fact magnetite is particularly redox-active, as demonstrated through its ability to convert hexavalent chromium, into a trivalent state [116]. Further to this, the magnetic properties of magnetite allow localized triplet state stabilization, resulting in increased free radical production [60]. If the magnetite content of ferritin was to be released in AD tissues (feasibly through the Aβ-mediated mechanisms described in *Chapter 5*), these redox-active minerals would be free to induce oxidative stresses resulting in neurotoxicity. Thus to infer that magnetite cannot be a source of ferrous iron toxicity within AD tissues, on the basis of negative Ferrozine iron(II) quantification results, is completely misconstrued.

Chapter 7

Associated investigation: Observation of iron bearing fibrillar aggregates and redox-active biominerals in Alzheimer's disease transgenic mouse cortex

7.1 Introduction

Throughout the experimental chapters of this thesis, investigations have focused on identifying how Aβ interacts with iron in simple *in vitro* systems. Findings from these studies demonstrate Aβ to be capable of chemically reducing naturally occurring iron minerals into redox-active phases capable of partaking in Fenton chemistry, potentially resulting in ROS production. However, we must establish whether similar processes of Aβ/ iron interaction can occur within *in vivo* systems displaying AD pathology. Such studies will determine whether the chemical products of *in vitro* Aβ/iron interaction are truly representative of those that occur naturally.

As described in *Chapter 1,* defining the oxidation state and magnetic properties of pathological iron deposits within AD tissues may prove vital in both the treatment and early detection of AD. Understanding the composition of pathological iron phases will influence how therapies such as iron chelators and antioxidants function, owing to the differing bonding and crystal structures of iron oxides [129]. Successfully identifying pathological iron forms will thus allow the targeting of detrimental iron without disrupting natural iron function (homeostasis). Further to this, differences in the magnetic effects of iron minerals may allow pathological iron phases to act as contrast agents in magnetic resonance imaging (MRI) of AD tissues [60], acting as a marker for AD, prior to the onset of cognitive symptoms.

In this study x-ray microspectroscopy (STXM) and electron microscopy techniques are employed to investigate the morphology and oxidative state of iron deposits located *in situ* within cortical tissue taken from an APP/PS1 transgenic mouse model, reproducing the amyloid deposition characteristic of AD. Furthermore, the localization of iron deposits with regards to regions of Aβ pathology is assessed. First, STXM images displaying the

carbon and iron content of transgenic cortical tissue are presented. Complementary high resolution TEM images of structures identified through STXM are then displayed, along with x-ray absorption profiles demonstrating the oxidation state of iron deposits located within transgenic mouse tissue. Finally, how these iron forms located *in situ* compare to the iron phases recorded in the *in vitro* experiments of *Chapters 3*, *4* and *5* will be discussed.

7.2 Materials and methods

7.2.1 Preparation of transgenic APP/PS1 mouse cortex tissues

8-9 month old APP/PS1 female transgenic mice were euthanized to obtain cortical tissues displaying AD pathology. Additional 14 month old wild type mice were euthanized as a disease-free control. Intracardial perfusion of mouse brain tissues was performed by Joe Gallagher, as described in Gallagher *et al.* (2012) [31].

7.2.2 Sectioning of mouse cortex tissue

Sectioning and embedding of mouse brain tissues for STXM and TEM examination was performed by Neil Telling. Initial coarse sections (ca. 1 mm thickness) were cut from frozen brain tissue using a sapphire blade. These coarse sections were thawed in sodium cacodylate and embedded in custom made modified epoxy resin that is suitable for STXM measurements [186]. Only 0.1 M sodium cacodylate and ethanol dehydration were employed during the embedding process to prevent any changes to iron chemistry. Semi-thin (200 nm – 1 μm) sections were cut using glass blades and deposited onto TEM copper grids or silicon nitride membranes. All STXM/TEM measurements were performed on unstained sections.

7.2.3 STXM examination of mouse cortex tissues

Copper/silicon nitride microscopy grids were mounted onto stainless steel microscopy plates for STXM examination on the soft x-ray spectromicroscopy beamline at the Canadian Light Source. Raster scans were performed across cortical tissues at the peak carbon *K*-edge absorption energy for peptide structures (288 eV), to provide images of biological structures (as described in *Section* 2.2.2). Further scans of the same regions were performed at the peak carbon *K*-edge absorption energy for epoxy resins (290 eV). These epoxy resin absorption values were subtracted from peptide values, resulting in the removal of carbon artefacts caused by the embedding material.

To identify potential iron deposits within cortical tissue whilst maintaining contrast for protein structures, raster scans at an intermediate energy (between the carbon *K*-edge and iron *L*-edge) of 350 eV were performed. Corresponding scans were then performed at the iron L_3-edge to reveal the iron content of these regions. Further high magnification scans of iron deposits were conducted at the iron L_3-edge to a spatial resolution of approximately 20 nm. Multiple scans were performed across the entire iron *L*-edge to determine the oxidation state of iron deposits as described in *Section 2.2.2*.

To determine the effect of prolonged x-ray beam exposure upon the oxidation state of embedded iron, solid suspensions of iron(III) oxyhydroxide (goethite), and nanocystalline maghemite were created in agar gels. Semi-thin sections of these iron minerals were deposited onto electron microscopy grids and examined over the iron *L*-edge as described above. To determine the effect of x-ray beam exposure on surface iron contaminants, small volumes of these iron suspensions were directly deposited onto microscopy grids and examined over the iron *L*-edge.

7.2.4 TEM imaging of cortical tissues

Complementary TEM images of structures examined under STXM were obtained utilizing a JEOL 1230 microscope system operating at 100 kV. TEM examination was performed by Neil Telling.

7.3 Results

7.3.1 Co-localization of iron within fibrillar protein structures

Examination of wild-type (WT) cortical tissue at the carbon *K*-edge provided detailed protein maps displaying extensive tissue morphology including cell bodies, cellular membranes, intracellular organelles and the extracellular matrix (Figure 7.1). Iron L_3-edge imaging of these tissues revealed infrequent (three) regions of particulate iron deposition (Figure 7.2). These iron regions were approximately 300 nm in diameter and displayed no evidence of intricate structure (Figure 7.2 d-f). Examination of iron deposits across the iron $L_{2,3}$-edge provided absorption spectra consistent with iron(III) reference materials, suggesting iron to be present in a purely ferric form (Figure 7.2g).

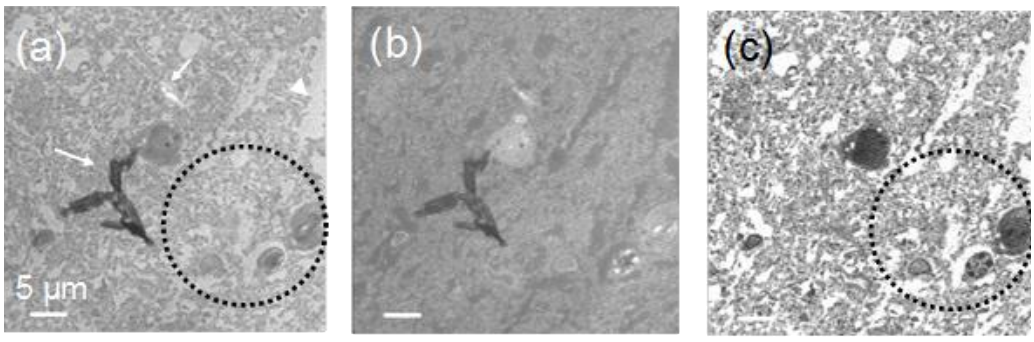

Figure 7.1. Carbon *K*-edge STXM protein maps from a WT mouse cortical tissue section. **(a)** Image taken at the π* amide protein peak (288 eV). **(b)** Image at a higher energy of 288.8 eV, showing enhanced absorption effects (darkened regions) attributed to embedding resin material (as indicated by arrowheads in (a)). Arrows in (a) show structural artefacts. Subtracting (b) from (a) provides artefact free protein images of cortical tissues **(c)**, revealing intricate details such as cellular organelles (dotted area).

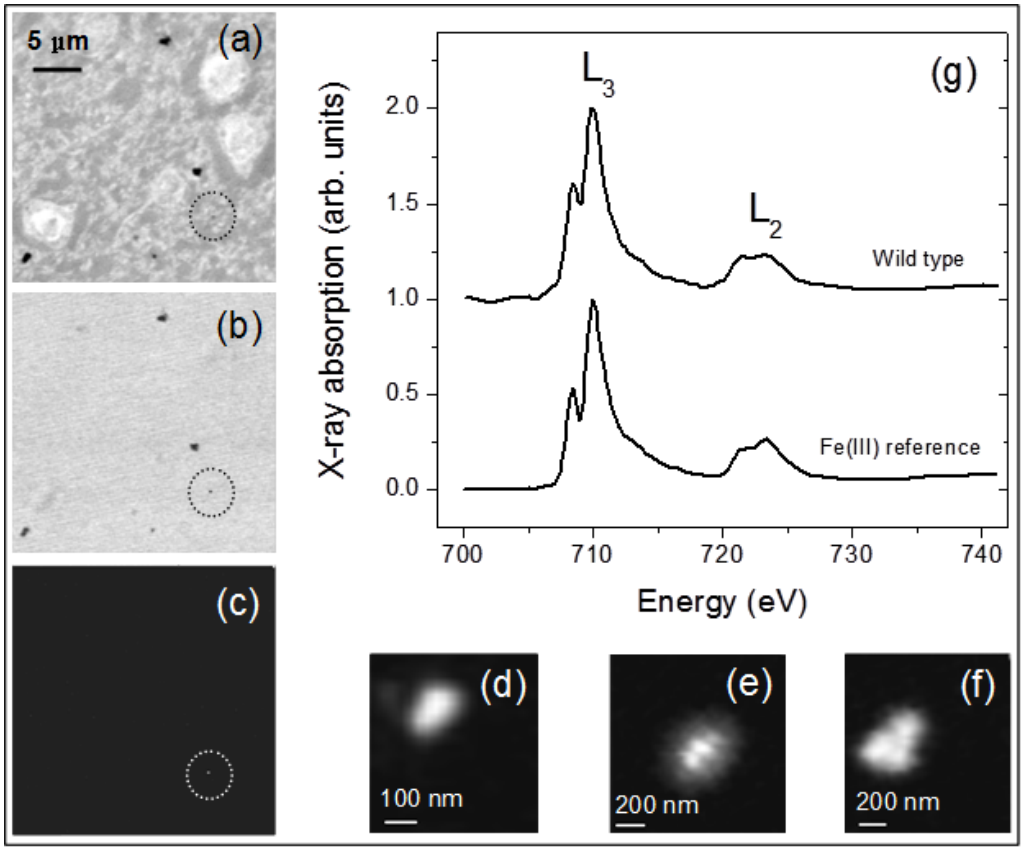

Figure 7.2. Example of iron deposits found within WT cortical tissues. **(a)** STXM image measured at 350 eV, displaying tissue structure and small dense particles. **(b)** Corresponding STXM image at the iron L_3-edge revealing the presence of multiple dense deposits within the tissue material. **(c)** Background subtracted iron L_3-edge map revealing one of the deposits shown in (b) to be comprised of iron (circled). **(d-f)** High resolution iron maps of the iron deposits found in (c), and in two other WT tissue samples. **(g)** Iron $L_{2,3}$ x-ray absorption spectra from iron deposits located within WT mouse cortical tissue compared to a goethite reference iron(III) spectra.

Carbon *K*-edge examination of transgenic APP/PS1 mouse cortical tissues revealed evidence of extensive tissue damage, although it was not clear whether this damage was pathological or due to poor tissue preservation during sample preparation (Figure 7.3). Upon Iron L_3-edge mapping of these tissues, multiple areas of iron deposition were observed, examples of which are provided in Figure 7.3. High magnification STXM iron imaging of these iron regions (Figure 7.3) revealed intricate structure to be present, bearing resemblance to the Aβ/iron structures observed using STXM as displayed in *Chapter 3*;

Figures 3.4, 3.5 and 3.9. Typical deposit size ranged from several hundred nanometers, to microns in diameter, suggesting extensive iron accumulation to have taken place. Such structures are vastly different to iron deposits located within WT cortical tissues, where iron was present in a dense particulate form.

Iron $L_{2,3}$-edge x-ray absorbance levels from the iron deposits shown in Figure 7.3 provided absorption spectra demonstrating one region (A2) to be composed of almost pure ferric iron (Figure 7.4), whilst other areas (A1 and A2) provided evidence of significant ferrous iron content compared to iron(III) reference spectra. These enhancements in ferrous iron features were not apparent in any of the iron deposits measured in WT tissues (Figure 7.2).

High magnification TEM imaging of the areas A2 and A3 revealed iron dense regions to be comprised of short, fine fibril structures, 50-150 nm in length. Such short fibril structures were consistent with Aβ structures observed following the incubation of Aβ with ferritin (*Chapter 5; Figure 5.18*), indicating that the fibril structures may be comprised of the amyloid protein. Where TEM and STXM were performed on the same aggregates, areas displaying dense fibril structures were correlated to the highest iron signal, suggesting the fibrils themselves to be loaded with iron. This differs from the short fibril structures observed following Aβ incubation with ferritin, which were shown to contain no iron (*Chapter 5; Figures 5.15* and *5.18*). For the iron deposits shown in Figure 7.2, iron oxidation state did not vary spatially across the deposit area.

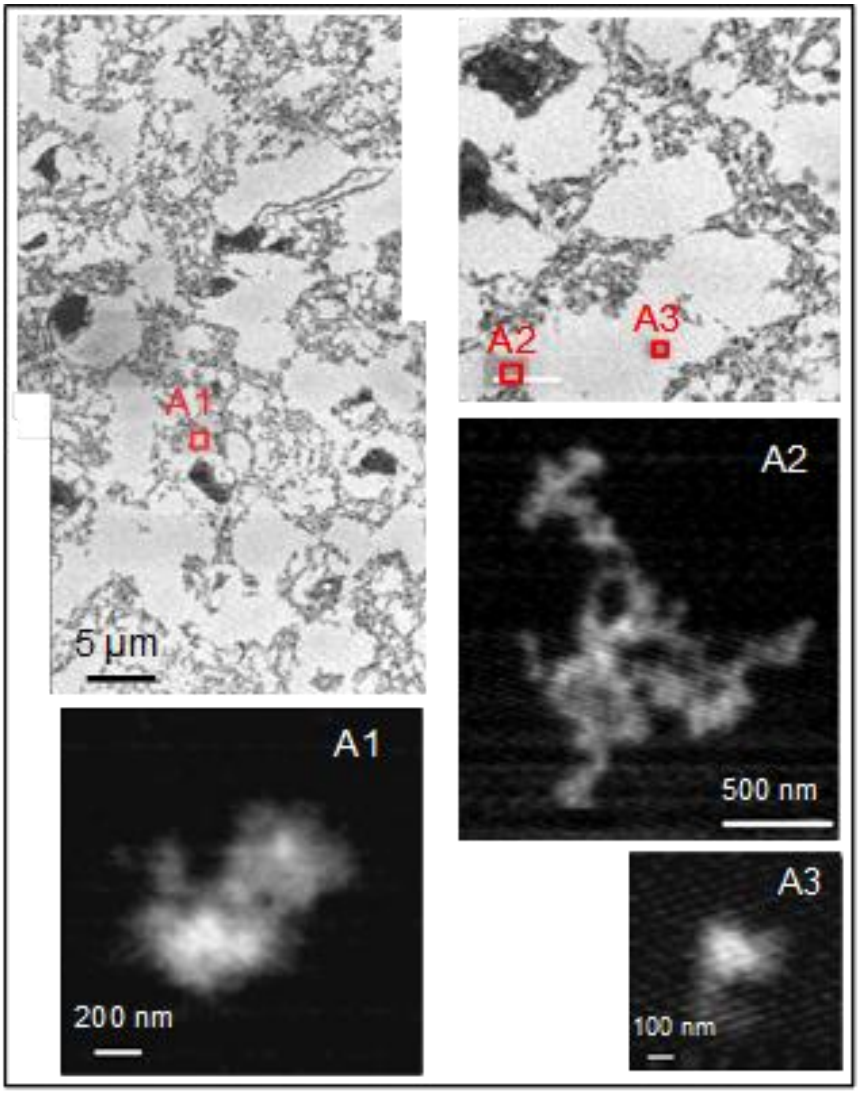

Figure 7.3. Carbon *K*-edge maps of transgenic mouse cortical tissue showing three areas of localized iron deposition (labelled A1, A2 and A3). Corresponding high resolution iron L_3 STXM maps displaying iron deposit morphology are shown below the protein maps.

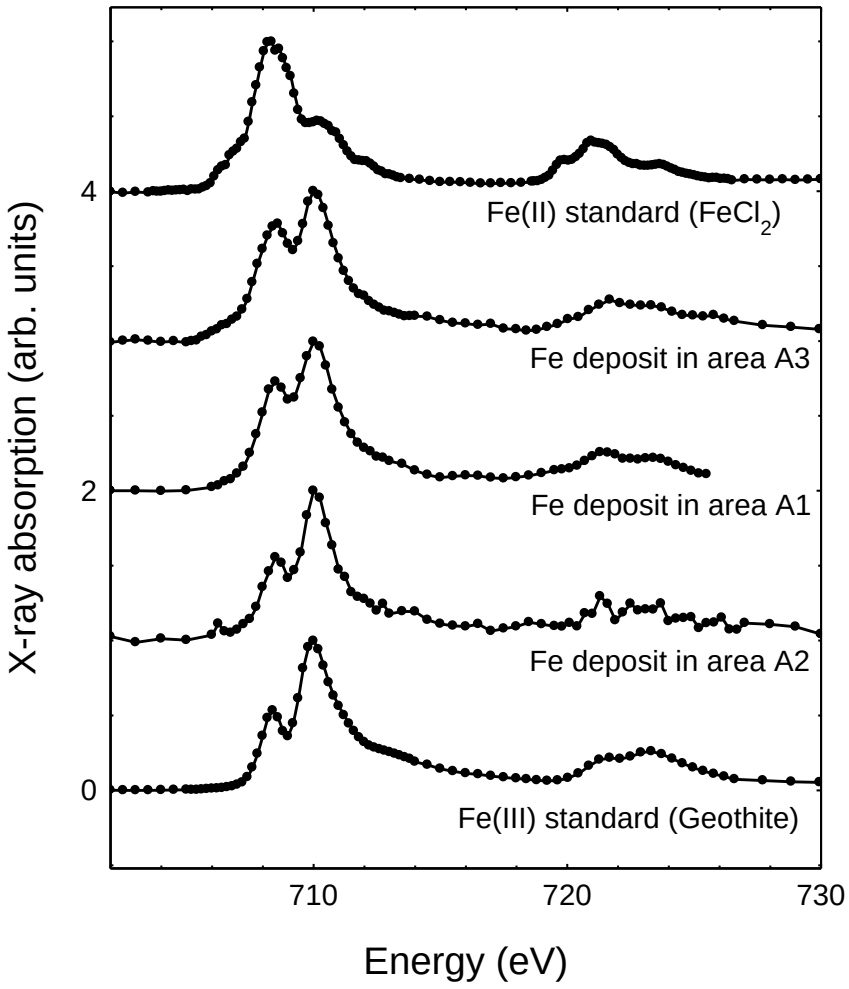

Figure 7.4. Iron $L_{2,3}$-edge x-ray absorbance spectra obtained from the iron deposits labelled A1, A2 and A3 in Figure 7.3. Increased ferrous content can be seen in the spectra from iron regions A1 and A3, as evidenced by an increase in intensities of the Fe^{2+} features at 708 eV (L_3 edge) and 721 eV (L_2 edge), with respect to the Fe^{3+} features at 709.5 eV and 723 eV respectively. Also provided are reference Fe^{2+} ($FeCl_2$) and Fe^{3+} (goethite; FeO(OH)) spectra.

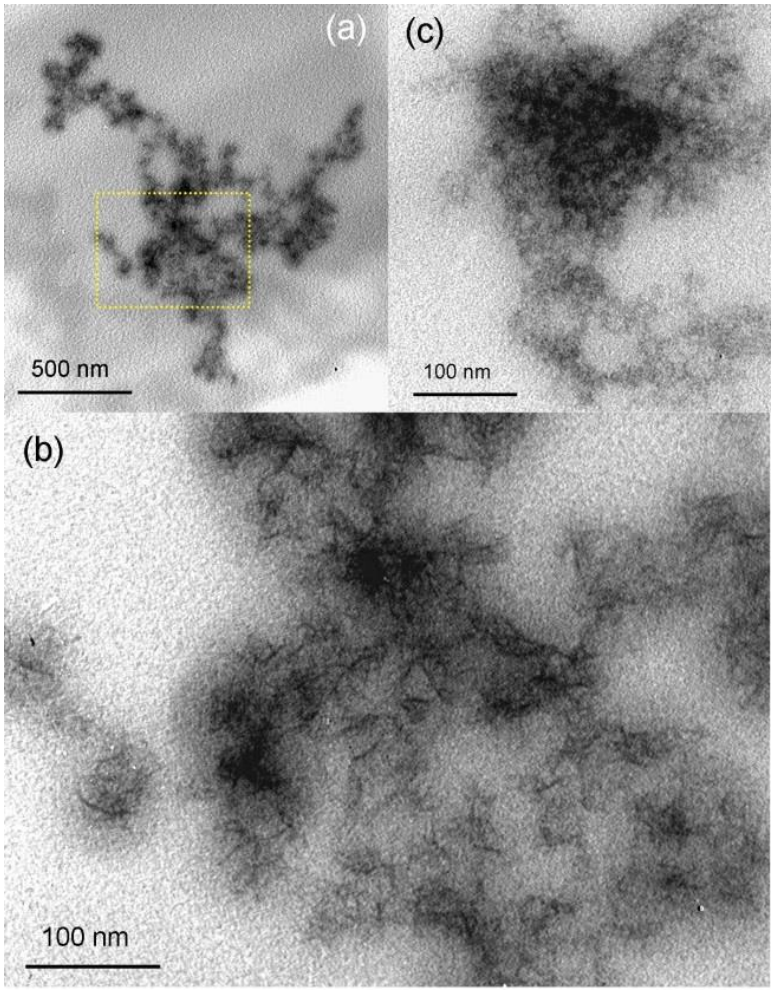

Figure 7.5. TEM images of the iron loaded cortical tissue as measured through STXM in Figure 7.2. **(a)** Region A2; **(b)** a high magnification image of the dotted area shown in (a). **(c)** Region A3. Note the similarity in fibril structure to Aβ aggregate structures formed following Aβ incubation with ferritin, as displayed in *Chapter 5* (*Figure 5.18b-c*).

7.3.2 Ferrous iron deposition in transgenic AD tissues

Examination of adjacent tissue sections to that shown in Figure 7.3, provided evidence of an iron oxide deposit (approximately 1.5 μm diameter) located within the extracellular matrix in close proximity to several neurons (Figure 7.6). Iron L_3-edge mapping of this iron deposit at the peak absorption energies for Fe^{2+} and Fe^{3+} indicated this region to contain multiple localized regions of varying oxidation states as labelled in Figure 7.6c-e. Iron $L_{2,3}$-

edge x-ray absorption spectra from these labelled regions confirm a dramatic variation in localized iron oxidation state as shown in Figure 7.6f. Iron ranged from pure ferric phase (B1), to a heavily reduced predominantly Fe^{2+} form (B4). The reduced iron found in region B4, was similar to iron *L*-edge spectra obtained from Aβ/ferrihydrite aggregates (*Chapter 4; Figure 4.1b; red*) where iron was found in a pure ferrous form reminiscent of wüstite; suggesting a similar phase may have formed *in vivo*. The multiple oxidation states of iron across this region hints towards a possible redox-cycling of iron; a result consistent with these presented in *Chapters 3 and 4*, where Aβ was demonstrated to induce the redox cycling of iron(III) and ferrihydrite *in vitro*.

As STXM is a scanning technique where samples are only exposed to the x-ray beam for milliseconds at a time, prolonged periods of STXM examination at the iron $L_{2,3}$-edge was not found to increase the ferrous content of iron(III) reference materials (when both embedded and surface exposed; Figure 7.7), variations in iron oxidation state (as shown in Figure 7.6) do not appear to be an artefact of x-ray beam reduction. It is also unlikely that variations in oxidation state are caused by co-incidental surface contamination by multiple small iron particles of differing oxidation states.

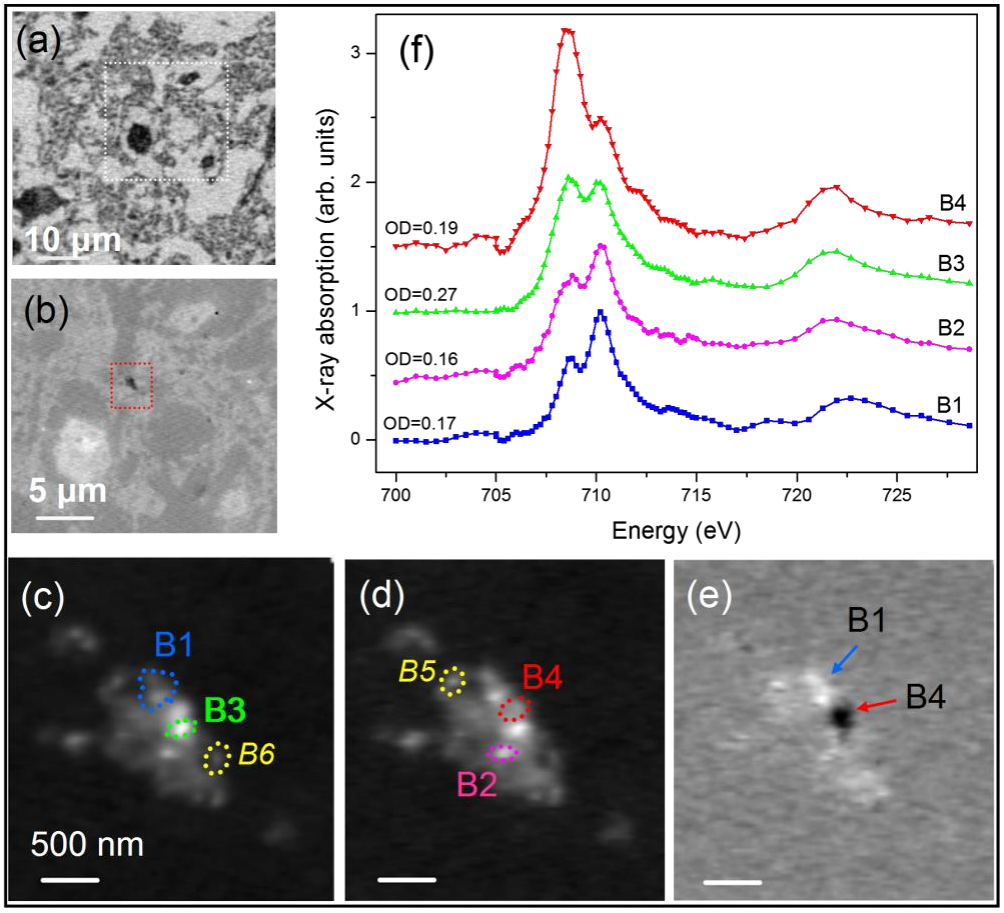

Figure 7.6. (a) Protein map of a cortical tissue section taken from transgenic APP/PS1 AD mouse tissue. **(b)** Higher resolution 350 eV image of the boxed area shown in (a), displaying protein structure and an area of iron deposition (red box). Iron L_3-edge maps taken at the **(c)** Fe^{2+} peak energy and **(d)** Fe^{3+} peak energy. **(e)** Difference map of (c) and (d), displaying localised regions of Fe^{3+} (bright contrast) and Fe^{2+} (dark contrast). **(f)** Corresponding iron $L_{2,3}$-edge x-ray absorption spectra for the iron regions labelled in (c) and (d).

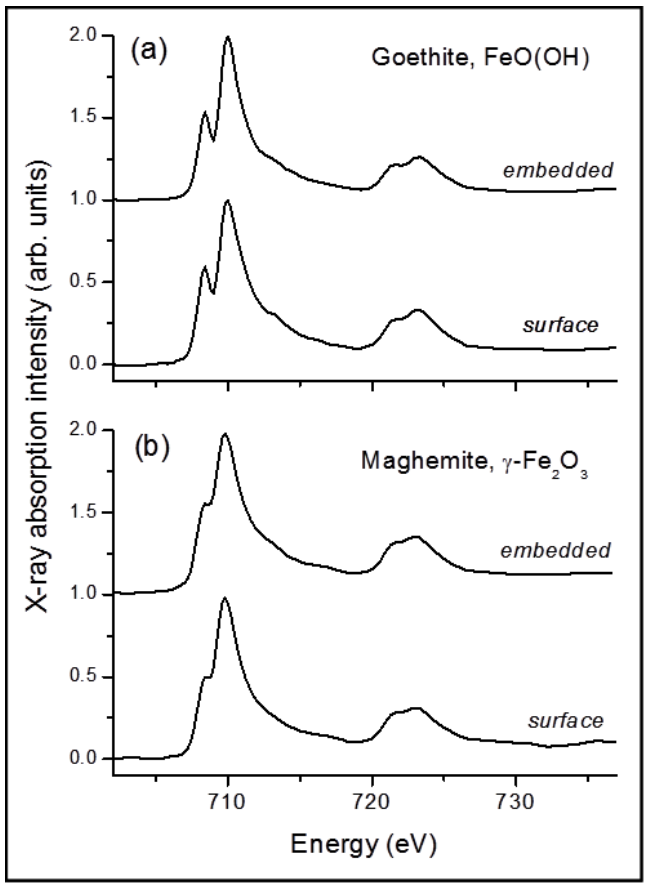

Figure 7.7. STXM iron $L_{2,3}$-edge x-ray absorption spectra obtained from iron(III) reference materials when both resin embedded, and directly exposed to the x-ray beam. Spectra were obtained from **(a)** goethite and **(b)** maghemite. No evidence of x-ray induced reduction effects were observed following prolonged periods of STXM examination.

7.4 Discussion

This study is the first to probe the nanoscale distribution, morphology and oxidation state of iron deposits within transgenic AD mouse tissue *in situ.*

STXM and TEM examination of transgenic AD mouse cortical tissue evidenced the loading of fibril structures with iron. These fibril structures strongly resemble those observed within Aβ aggregates formed following the incubation of amyloid with ferritin (*Chapter 5*); suggesting them to be comprised of Aβ. Such findings indicate there to be a link between Aβ aggregation and iron accumulation within AD tissues *in vivo*; confirming

the *in vitro* observation of iron aggregation by Aβ as described in the preceding experimental chapters. This suggests that the co-aggregation of Aβ and iron may represent a key step in the process of amyloidosis *in vivo*, and that iron may play a fundamental role in development of AD pathology.

Iron $L_{2,3}$-edge STXM x-ray absorption spectra obtained from iron oxide deposits located within transgenic mouse cortical tissue, revealed iron to be present in multiple oxidation states; ranging from redox-inactive ferric iron to predominantly ferrous, redox-active phases. The presence of redox-active phases within AD tissues is consistent with the *in vitro* experiments presented in *Chapters 3, 4* and *5*, where Aβ was shown to reduce ferric iron phases into redox-active states. This variation in iron oxide state also provides *in vivo* evidence of iron redox-cycling, as was observed following the interaction of Aβ with iron(III) hydroxide (*Chapter 3*) and 2-line ferrihydrite (*Chapter 4*) *in vitro.* As iron(II)-bearing oxides are prone to oxidation [129] and no attempts were made to prevent iron oxidation post-mortem, these results suggest that other mechanisms must be in place to prevent iron oxidation. Possible mechanisms may include the coating of iron by amyloid (as suggested by TEM imaging of Aβ/iron aggregates), or that redox-active iron is located within the core of ferritin. The latter hypothesis is supported by the results of *Chapter 5*, where the crystal structure of ferrihydrite was found to be altered whilst located within the ferritin core; and findings published by Watt *et al.* who demonstrated electron transfer and iron reduction to occur across the apoferritin cage of ferritin [179]. Indeed, as redox-active iron phases have been observed within ferritin cores isolated from AD tissues [108], ferritin may provide the basis for iron reduction *in vivo.*

7.5 Conclusions and implications

The results from this study suggest that the formation of redox-active iron phases may be associated with hallmark features of AD pathology *in vivo*. As previously described, the presence of redox-active iron oxides within AD tissues could provide a significant source of oxidative stress capable of inducing neuronal injury thereby contributing to the process of AD pathogenesis [48,49,52,157]. These redox-active phases may represent a target for the development of therapeutics (iron chelators and antioxidants) intended to reduce oxidative burdens without detrimentally affecting natural iron functions [146]. This has the potential to greatly improve current treatments intended to lower iron associated toxicity in AD patients that have provided limited success due to unforeseen long-term toxic side effects [146,187]. Differences in iron oxidation and crystal state also dramatically influence the magnetic properties of iron oxide phases. Successfully identifying pathological iron phases *in vivo* may allow pathological iron to be utilized as a contrast agent in MRI of AD tissues [60]. This in turn could allow the detection of AD onset in patients prior to the onset of cognitive and external physical manifestations. Importantly, in the context of this thesis, these results suggest a similar process of redox-iron formation to be occurring *in vivo,* to those observed within the simple *in vitro* systems presented in *Chapters 3*, *4* and *5*; further highlighting the importance of Aβ/iron interaction in the development of AD pathology.

Chapter 8

Future Work

8.1 Characterising Aβ/ferritin interaction

From the results in *Chapter 5*, it appears that Aβ has the ability to disrupt ferritin structure in a manner that results in the conversion of its redox-inactive core into a potentially toxic redox active state. However several questions remain with regards to the nature of Aβ/ferritin interaction (as highlighted in *Section 5.6*). Here I propose two experiments to further improve our understanding of Aβ/ferritin interaction.

8.1.1 The aggregation of ferritin by Aβ

To understand the level of ferritin aggregation induced by Aβ, I intend to conduct magnetic susceptibility measurements, investigating the interaction of Aβ with magnetically doped ferritin (magnetoferritin) protein.

Magnetoferritin synthesis involves the addition of iron(II) and iron(III) to apoferritin (the hollow protein cage of ferritin) in a controlled manner, as to induce magnetite formation within the protein core [188]. In theory, this method of magnetite synthesis provides a magnetically susceptible iron phase of constant diameter (8 nm), which also forms stable, uniform suspensions (ferritin is stable in suspension). Providing Aβ interacts with magnetoferritin in a similar manner to ferritin, it should be possible to monitor magnetoferritin aggregation by Aβ through the use of AC susceptometry. Stable, uniform magnetoferritin suspensions should provide a frequency-dependant χ" peak. Magnetoferritin aggregation by Aβ would induce a shift in this χ" peak value, which can be monitored by conducting multiple susceptibility measurements in a time dependant manner. However due to the small particle size of magnetoferritin, extremely high frequencies would be required to detect any shifts in χ" values. Doping magnetoferritin

with cobalt could provide a means to magnetically block these superparamagnetic particles, allowing the detection of magnetoferritin aggregation at much lower frequencies. If successful these experiments will provide a quantitative means to demonstrate the aggregation of ferritin by Aβ, providing a potential explanation to the increased ferritin loads observed within SP material in AD tissues [126].

8.1.2 The effects of albumin/ferritin interaction

To determine whether the effects of Aβ interaction upon ferritin are merely a result of generic protein-protein interactions, I intend to examine the interaction of albumin proteins with ferritin. This will involve a repeat of the experimental procedures outlined in *Chapter 5*, with the substitution of an albumin protein for Aβ. Albumins are a family of small globular proteins commonly found in the blood plasma of humans which are not inherently toxic. By conducting these investigations it should be possible to determine whether the accumulation of ferritin, and the disruptions to ferritin structure described in *Chapter 5* are specifically induced through Aβ interaction with the storage protein.

8.2 *In vitro* cellular experiments

Throughout *Chapters 3, 4* and *5*, Aβ was demonstrated to induce the conversion of naturally occurring iron phases into potentially neurotoxic redox-active forms. However, despite these observations, the role played by Aβ-induced iron reduction in AD pathogenesis remains unclear, and the chemical by-products of these interactions have not been characterized. It is of great importance to ascertain whether the products of Aβ/iron interaction convey toxic effects to cellular populations. It is also imperative to determine whether currently available AD treatments can act to reduce any harmful effects induced through Aβ/iron interactions.

To further investigate how the relationship between Aβ and naturally occurring iron (ferrihydrite and ferritin) contributes to AD pathology I intend to examine two main hypotheses:

1. The interaction of Aβ with ferrihydrite/ferritin results in the formation of cytotoxic chemical products.

Through the use of traditional biological approaches coupled with advanced synchrotron techniques I intend to characterize and quantify the chemical products formed through Aβ interaction with ferrihydrite and ferritin. Building upon this, the cytotoxic effects of these reaction products will be assessed, to determine whether the process of Aβ-mediated iron reduction is sufficient to induce the widespread neuronal death characteristic of AD.

Such studies will facilitate the identification of specific Aβ-induced iron phases that are likely to contribute to the free radical burdens and neuronal damage witnessed in AD tissues. Targeting these sources of Aβ-mediated iron cytotoxicity could result in reductions to oxidative stresses and neuronal injury without disrupting healthy brain functions.

2. Currently available AD treatments perturb the process of Aβ interaction with ferrihydrite/ferritin, and thus alter Aβ-mediated iron toxicity.

By combining methodologies from the biological and physical sciences I propose to evaluate the effectiveness of current AD therapies to disrupt and prevent Aβ-induced ferrihydrite/ferritin ROS production and toxicity. Further to this the iron mineral products and amyloid structures formed through Aβ interaction with ferrihydrite and ferritin in the presence of these treatments will be characterized.

If successful, this multidisciplinary approach will allow us to define the most efficient means to therapeutically lower Aβ-induced iron toxicity and maintain cell viability *in vitro*,

which may prove applicable to *in vivo* systems. Additionally, findings from these studies will enable further characterisation of the mechanisms underlying Aβ mediated ferritin/ferrihydrite reduction, which may prove vital in understanding how to delay/prevent AD pathogenesis.

8.3 Investigations into age-dependant redox-active iron formation in transgenic AD mice: An *in situ* study

As Aβ has been shown to induce redox-active iron formation (*Chapters 3, 4* and *5*), and redox active iron minerals have been observed in transgenic AD mice known to accumulate Aβ over time (*Chapter 7*), it is of great interest to establish *when* redox-active iron formation occurs with respect to disease progression.

I intend to achieve this by examining the brain tissues of transgenic AD mice at various points along their lifespan, for the presence of redox active iron minerals. This time-dependant approach will potentially allow us to correlate redox-active iron formation with a particular stage of AD pathology. This in turn will indicate whether redox-active iron formation is likely to contribute to AD pathogenesis, or whether these iron forms are simply a by-product of the disease process. Furthermore, this approach will enable us to establish whether magnetic iron formation occurs prior to the manifestation of clinical symptoms. This will have a significant bearing as to whether MRI techniques are a viable option for the screening and detection of AD prior to onset of cognitive decline.

These proposed *in situ* studies will utilize x-ray microspectroscopy techniques as described in *Chapter 7* to image both the biological and iron content of transgenic AD mice cortical tissues whilst characterizing iron oxidation state. Complementary electron microscopy and histological staining approaches will be employed to provide high resolution images of

tissue sections and indicators to AD pathology respectively. The outcomes of these investigations may prove integral in understanding how redox-active iron contributes to AD.

Chapter 9

Conclusions

In this thesis the role played by the AD peptide Aβ in the formation of redox-active iron phases has been investigated. Particular focus has been placed upon the effect of Aβ interaction on the oxidative and magnetic state of naturally occurring ferric iron phases, including those stored within the ferritin protein. Furthermore, first time *in situ* characterisation of iron phases within transgenic AD mouse brain tissues was presented.

Through x-ray microspectroscopy and TEM imaging, Aβ was shown to readily incorporate iron(III) oxyhydroxide precipitates into its protein aggregate structure *in vitro*, resulting in the formation of iron loaded amyloid structures (*Chapter 3*). X-ray absorbance spectroscopy and spectrophotometric iron(II) quantification demonstrated this process of interaction to chemically reduce iron(III) oxyhydroxide into a weakly-magnetic pure iron(II) phase; whilst electron diffraction suggested this reduced iron to be amorphous in nature. Furthermore, the presence of aluminium was shown to catalyse Aβ-induced iron reduction, resulting in the redox cycling of iron. Interestingly, the presence of redox-active iron may also have an effect upon Aβ fibril structure, owing to the observation of amorphous Aβ aggregates, known to contain redox-active iron. Such results demonstrate Aβ to be *directly* capable of inducing iron reduction in the absence of any other influencing factors.

Significantly, by utilizing x-ray microspectroscopy x-ray absorption spectroscopy, electron microscopy and iron(II) quantification techniques, Aβ was shown to aggregate and reduce the iron mineral ferrihydrite (*Chapter 4*). Following Aβ/ferrihydrite interaction, ferrihydrite and Aβ morphology were closely correlated, indicating the loading of ferrihydrite within Aβ fibril structures. Further to this, localized regions of ferrihydrite accumulation were observed, suggesting Aβ to act as a reservoir for ferrihydrite deposition. This aggregation process was shown to induce the reduction and redox cycling of ferrihydrite by Aβ, as demonstrated through x-ray absorption spectroscopy and iron(II)

quantification techniques. Reduced iron deposits were identified as an antiferromagnetic pure iron(II) phase reminiscent of the cubic iron mineral wüstite. These observations were supported by electron diffraction, showing the presence of the wüstite oxidation-product magnetite/maghemite, following the exposure of sample materials to oxygen. Such observations combined with those in *Chapter 3* indicate that Aβ-induced crystalline iron(II) formation may require a crystalline precursor. These findings are the first of their kind, demonstrating Aβ to induce the chemical reduction of iron forms representative of those that occur naturally within brain tissues; along with first time evidence of crystalline iron reduction by Aβ.

Further electron microscopy and x-ray spectromicroscopy-based experiments demonstrate Aβ/ferritin co-incubation to result in ferritin accumulation within amyloid structures, with this process appearing to disrupt mature Aβ fibril formation (*Chapter 5*). Following prolonged periods of interaction, ferritin structure was found to become disrupted. This resulted in the chemical reduction of ferritin-derived ferrihydrite, and the accumulation of iron into dense nanoscale deposits.

Electron diffraction patterns from Aβ/ferritin structures showed the crystal structure of ferrihydrite to be altered prior to the destruction of ferritin morphology and the reduction of ferrihydrite. The significance of this finding is two-fold. First, the alteration of ferrihydrite crystal structure whilst ferritin morphology remains intact, suggests that Aβ is capable of inducing electron transfer across the ferritin protein shell. Secondly the disruption of ferrihydrite crystal state prior to its reduction indicates that crystalline iron reduction may involve the formation of an amorphous ferric intermediate. As was the case in *Chapter 3*, the presence of redox-active iron was accompanied with a complete loss of mature Aβ fibril conformation, suggesting that redox-active iron formation may alter the ability of Aβ to form cross-β fibril arrangements. These experiments significantly build

upon those presented in *Chapters 3* and *4*, by demonstrating Aβ to be capable of reducing iron in its natural stored form. Such findings indicate Aβ to chemically reduce both bound and unbound ferric iron phases, and that Aβ itself can act to disrupt ferritin structure.

Incubation of Aβ with surface-oxidized magnetite was shown to result in a disruption to magnetite crystal structure resulting in the formation of an amorphous iron phase (*Chapter 6*). This destruction of magnetite crystallinity was found to occur following the sequestering of magnetite nanoparticles by Aβ. TEM imaging revealed this sequestering process to result in the aggregation of Aβ into large structures comprised of well-defined fibrils. Nanoparticle structure was seen to become disrupted with increasing periods of Aβ incubation, as if being digested by the peptide. Electron diffraction patterns from Aβ/magnetite structures demonstrated magnetite crystallinity to be lost following Aβ interaction, confirming the formation of an amorphous iron phase. Interestingly, initial disruptions to magnetite morphology did not correspond to a loss in crystallinity, suggesting Aβ to disrupt the surface structure of magnetite before the core.

X-ray absorption probing provided no evidence of Aβ-mediated magnetite reduction. However XMCD examination of magnetite deposits following Aβ interaction demonstrated the magnetic properties of magnetite to be significantly diminished following Aβ interaction, resulting in the formation of a weakly magnetic antiferromagnetic phase. Despite no evidence of magnetite reduction being observed in this instance, on the basis of the results presented in *Chapter 5*, the amorphous ferric species formed following Aβ/magnetite interaction may represent an intermediate phase required for the reduction of crystalline iron phases. Thus these preliminary studies show Aβ to disrupt the crystal structure of magnetic iron nanoparticles, in a manner that may facilitate their reduction by the peptide.

Taken together the *in vitro* findings of this thesis suggest that the occurrence of redox-active iron minerals within AD tissues may be inherently linked to the interaction of Aβ with both poorly liganded iron and the storage protein ferritin. This reduction process was initiated by the accumulation of ferric iron within Aβ structures, resulting in their conversion into redox-active forms. These iron phases have the potential to induce oxidative stress, and could therefore contribute to the development of AD [37,49,50,52,55,56,60,146]. Furthermore, as comparable redox-active iron phases were found to be associated with regions of AD pathology during *in situ* examination of transgenic AD mouse tissue (*Chapter 7*), a similar process of redox-active iron formation may occur *in vivo.*

Although no evidence of magnetic iron formation was observed over the time frames examined within this thesis, these results do not preclude magnetic iron formation following prolonged periods of Aβ interaction with natural iron minerals.

The identification and characterisation of redox-active iron forms associated with AD pathology as described here may prove influential in the development of treatments intended to lower iron-associated ROS burdens in AD tissues, thereby inhibiting disease progression. As these iron phases to not occur naturally [108] it may be possible to develop therapeutic agents that specifically target AD-associated iron phases, whilst maintaining iron homeostasis and neuronal health. These developments could overcome the current shortcomings of AD therapeutics such as iron chelators, which show long term toxicity through their tendency to target physiological iron stores [144-146]. Furthermore, by disrupting Aβ/iron interactions within AD tissues, redox-active iron formation may be preventable. The manner with which Aβ appears to disrupt ferritin function may also prove to be of vital importance in the development of AD; and therefore maintaining ferritin function could be a viable target in the treatment of the disorder. In light of these findings, it is

imperative to determine the toxicity conveyed by Aβ interaction with naturally occurring iron forms, and whether this relationship is likely to contribute to the pattern of neurodegeneration witnessed in AD subjects.

In summary the results of this thesis indicate the interactions between Aβ and iron to be a source of redox-active iron phases, with the potential to contribute to the pathogenesis of AD. It is hoped that these findings will improve our understanding of iron's contribution to AD, whilst providing new avenues for the development of technologies intended to combat this fatal neurodegenerative disorder.

References

1 Alzheimer's Association. 2008 Alzheimer's disease facts and figures. *Alzheimer's & dementia : the journal of the Alzheimer's Association* **4**, 110-133, doi:10.1016/j.jalz.2008.02.005 (2008).
2 Hebert, L. E., Scherr, P. A., Bienias, J. L., Bennett, D. A. & Evans, D. A. Alzheimer disease in the us population: Prevalence estimates using the 2000 census. *Archives of Neurology* **60**, 1119-1122, doi:10.1001/archneur.60.8.1119 (2003).
3 Alzheimer's Association. 2012 Alzheimer's disease facts and figures. *Alzheimer's & dementia : the journal of the Alzheimer's Association* **8**, 131-168, doi:10.1016/j.jalz.2012.02.001 (2012).
4 Waring, S. C. & Rosenberg, R. N. Genome-wide association studies in alzheimer disease. *Archives of Neurology* **65**, 329-334, doi:10.1001/archneur.65.3.329 (2008).
5 Williamson, J., Goldman, J. & Marder, K. S. Genetic Aspects of Alzheimer Disease. *Neurologist* **15**, 80-86, doi:10.1097/NRL.0b013e318187e76b (2009).
6 Rhinn, H. *et al.* Integrative genomics identifies APOE ε4 effectors in Alzheimer's disease. *Nature* **500**, 45-50, doi:10.1038/nature12415 (2013).

7 Harold, D. *et al.* Genome-wide association study identifies variants at CLU and PICALM associated with Alzheimer's disease. *Nat Genet* **41**, 1088-1093, doi:10.1038/ng.440 (2009).
8 Ma, L.-L. *et al.* Single nucleotide polymorphism rs7294919 on chromosome 12q24.22 is associated with late-onset Alzheimer's disease in Han Chinese. *Neuroscience Letters* **560**, 67-70, doi:10.1016/j.neulet.2013.12.022 (2014).
9 Mastroeni, D. *et al.* Epigenetic mechanisms in Alzheimer's disease. *Neurobiology of Aging* **32**, 1161-1180, doi:10.1016/j.neurobiolaging.2010.08.017 (2011).
10 Thompson, P. M. *et al.* Dynamics of gray matter loss in Alzheimer's disease. *Journal of Neuroscience* **23**, 994-1005 (2003).
11 Fox, N. C. *et al.* Imaging of onset and progression of Alzheimer's disease with voxel-compression mapping of serial magnetic resonance images. *Lancet* **358**, 201-205, doi:10.1016/s0140-6736(01)05408-3 (2001).
12 Ong, W. Y. & Farooqui, A. A. Iron, neuroinflammation, and Alzheimer's disease. *Journal of Alzheimers Disease* **8**, 183-200 (2005).
13 Hardy, J. & Selkoe, D. J. Medicine - The amyloid hypothesis of Alzheimer's disease: Progress and problems on the road to therapeutics. *Science* **297**, 353-356, doi:10.1126/science.1072994 (2002).
14 Hardy, J. A. & Higgins, G. A. Alzheimer's Disease - The Amyloid Cascade Hypothesis. *Science* **256**, 184-185, doi:10.1126/science.1566067 (1992).
15 Karran, E., Mercken, M. & De Strooper, B. The amyloid cascade hypothesis for Alzheimer's disease: an appraisal for the development of therapeutics. *Nature Reviews Drug Discovery* **10**, 698-U1600, doi:10.1038/nrd3505 (2011).
16 Mucke, L. & Selkoe, D. J. Neurotoxicity of Amyloid beta-Protein: Synaptic and Network Dysfunction. *Cold Spring Harbor Perspectives in Medicine* **2**, doi:10.1101/cshperspect.a006338 (2012).
17 Tsai, J., Grutzendler, J., Duff, K. & Gan, W. B. Fibrillar amyloid deposition leads to local synaptic abnormalities and breakage of neuronal branches. *Nature Neuroscience* **7**, 1181-1183, doi:10.1038/nn1335 (2004).

18 Rogers, J. & Morrison, J. H. Quantitative morphology and regional and laminar distributions of senile plaques in Alzheimer's-disease. *Journal of Neuroscience* **5**, 2801-2808 (1985).
19 Selkoe, D. J. The cell biology of beta-amyloid precursor protein and presenilin in Alzheimer's disease. *Trends in Cell Biology* **8**, 447-453, doi:10.1016/s0962-8924(98)01363-4 (1998).
20 Fiala, J. C. Mechanisms of amyloid plaque pathogenesis. *Acta Neuropathologica* **114**, 551-571, doi:10.1007/s00401-007-0284-8 (2007).
21 Gotz, J., Chen, F., van Dorpe, J. & Nitsch, R. M. Formation of neurofibrillary tangles in P301L tau transgenic mice induced by A beta 42 fibrils. *Science* **293**, 1491-1495, doi:10.1126/science.1062097 (2001).
22 Goedert, M., Sisodia, S. S. & Price, D. L. Neurofibrillary tangles and β-amyloid deposits in Alzheimer's disease. *Current Opinion in Neurobiology* **1**, 441-447, doi:http://dx.doi.org/10.1016/0959-4388(91)90067-H (1991).
23 Butterfield, D. A. & Lauderback, C. M. Lipid peroxidation and protein oxidation in Alzheimer's disease brain: Potential causes and consequences involving amyloid beta-peptide-associated free radical oxidative stress. *Free Radical Biology and Medicine* **32**, 1050-1060, doi:10.1016/s0891-5849(02)00794-3 (2002).
24 Kay, C. J. Mechanochemical mechanism for peptidyl free radical generation by amyloid fibrils. *Febs Letters* **403**, 230-235, doi:10.1016/s0014-5793(97)00076-8 (1997).
25 Hensley, K. *et al.* A Model for Beta-amyloid Aggregation and Neurotoxicity Based on Free-radical Generation by the Peptide - Relevance to Alzheimer-Disease. *Proceedings of the National Academy of Sciences of the United States of America* **91**, 3270-3274, doi:10.1073/pnas.91.8.3270 (1994).
26 Hartmann, T. *et al.* Distinct sites of intracellular production for Alzheimer's disease A[beta]40/42 amyloid peptides. *Nat Med* **3**, 1016-1020 (1997).
27 Sisodia, S. S. & Price, D. L. Role of the beta-amyloid protein in Alzheimer's disease. *The FASEB Journal* **9**, 366-370 (1995).
28 Tay, W. M., Huang, D., Rosenberry, T. L. & Paravastu, A. K. The Alzheimer's Amyloid-β(1–42) Peptide Forms Off-Pathway Oligomers and Fibrils That Are Distinguished Structurally by Intermolecular Organization. *Journal of Molecular Biology* **425**, 2494-2508, doi:http://dx.doi.org/10.1016/j.jmb.2013.04.003 (2013).
29 Butterfield, D. A. & Boyd-Kimball, D. The critical role of methionine 35 in Alzheimer's amyloid-beta-peptide (1-42)-induced oxidative stress and neurotoxicity. *Biochimica Et Biophysica Acta-Proteins and Proteomics* **1703**, 149-156, doi:10.1016/j.bbapap.2004.10.014 (2005).
30 Nelson, R. & Eisenberg, D. Recent atomic models of amyloid fibril structure. *Current Opinion in Structural Biology* **16**, 260-265, doi:http://dx.doi.org/10.1016/j.sbi.2006.03.007 (2006).
31 Gallagher, J. J. *et al.* Modest Amyloid Deposition is Associated with Iron Dysregulation, Microglial Activation, and Oxidative Stress. *Journal of Alzheimers Disease* **28**, 147-161, doi:10.3233/jad-2011-110614 (2012).
32 Monji, A. *et al.* The relationship between the aggregational state of the amyloid-beta peptides and free radical generation by the peptides. *Journal of Neurochemistry* **77**, 1425-1432, doi:10.1046/j.1471-4159.2001.00392.x (2001).
33 Nussbaum, J. M. *et al.* Prion-like behaviour and tau-dependent cytotoxicity of pyroglutamylated amyloid-beta. *Nature* **485**, 651-655, doi:10.1038/nature11060 (2012).
34 Goodman, L. Alzheimer's disease; a clinico-pathologic analysis of twenty-three cases with a theory on pathogenesis. *The Journal of nervous and mental disease* **118**, 97-130, doi:10.1097/00005053-195308000-00001 (1953).

35 Lovell, M. A., Robertson, J. D., Teesdale, W. J., Campbell, J. L. & Markesbery, W. R. Copper, iron and zinc in Alzheimer's disease senile plaques. *Journal of the Neurological Sciences* **158**, 47-52, doi:10.1016/s0022-510x(98)00092-6 (1998).
36 Collingwood, J. F. *et al.* Three-dimensional tomographic Imaging and characterization of iron compounds within Alzheimer's plaque core material. *Journal of Alzheimers Disease* **14**, 235-245 (2008).
37 Smith, M. A., Harris, P. L. R., Sayre, L. M. & Perry, G. Iron accumulation in Alzheimer disease is a source of redox-generated free radicals. *Proceedings of the National Academy of Sciences of the United States of America* **94**, 9866-9868, doi:10.1073/pnas.94.18.9866 (1997).
38 Smith, M. A., Rottkamp, C. A., Nunomura, A., Raina, A. K. & Perry, G. Oxidative stress in Alzheimer's disease. *Biochimica Et Biophysica Acta-Molecular Basis of Disease* **1502**, 139-144, doi:10.1016/s0925-4439(00)00040-5 (2000).
39 Deibel, M. A., Ehmann, W. D. & Markesbery, W. R. Copper, iron, and zinc imbalances in severely degenerated brain regions in Alzheimer's disease: Possible relation to oxidative stress. *Journal of the Neurological Sciences* **143**, 137-142, doi:10.1016/s0022-510x(96)00203-1 (1996).
40 Leskovjan, A. C. *et al.* Increased brain iron coincides with early plaque formation in a mouse model of Alzheimer's disease. *Neuroimage* **55**, 32-38, doi:10.1016/j.neuroimage.2010.11.073 (2011).
41 Perry, G. *et al.* Adventiously-bound redox active iron and copper are at the center of oxidative damage in Alzheimer disease. *Biometals* **16**, 77-81, doi:10.1023/a:1020731021276 (2003).
42 Smith, M. A. *et al.* Amyloid-beta deposition in Alzheimer transgenic mice is associated with oxidative stress. *Journal of Neurochemistry* **70**, 2212-2215 (1998).
43 Zecca, L., Youdim, M. B. H., Riederer, P., Connor, J. R. & Crichton, R. R. Iron, brain ageing and neurodegenerative disorders. *Nature Reviews Neuroscience* **5**, 863-873, doi:10.1038/nrn1537 (2004).
44 Sayre, L. M. *et al.* In situ oxidative catalysis by neurofibrillary tangles and senile plaques in Alzheimer's disease: A central role for bound transition metals. *Journal of Neurochemistry* **74**, 270-279, doi:10.1046/j.1471-4159.2000.0740270.x (2000).
45 Dong, J. *et al.* Metal binding and oxidation of amyloid-beta within isolated senile plaque cores: Raman microscopic evidence. *Biochemistry-Us* **42**, 2768-2773, doi:10.1021/bi0272151 (2003).
46 Connor, J. R., Menzies, S. L., Burdo, J. R. & Boyer, P. J. Iron and iron management proteins in neurobiology. *Pediatric Neurology* **25**, 118-129, doi:10.1016/s0887-8994(01)00303-4 (2001).
47 Munoz, P. & Humeres, A. Iron deficiency on neuronal function. *Biometals* **25**, 825-835, doi:10.1007/s10534-012-9550-x (2012).
48 Kell, D. B. Iron behaving badly: inappropriate iron chelation as a major contributor to the aetiology of vascular and other progressive inflammatory and degenerative diseases. *Bmc Medical Genomics* **2**, doi:10.1186/1755-8794-2-2 (2009).
49 Honda, K. *et al.* Redox active iron at the center of oxidative stress in Alzheimer disease. *Letters in Drug Design & Discovery* **2**, 479-482, doi:10.2174/1570180054771545 (2005).
50 Huang, X. D., Moir, R. D., Tanzi, R. E., Bush, A. I. & Rogers, J. T. Redox-active metals, oxidative stress, and Alzheimer's disease pathology. *Redox-Active Metals in Neurological Disorders* **1012**, 153-163, doi:10.1196/annals.1306.012 (2004).

51 Huang, X. D. *et al.* The A beta peptide of Alzheimer's disease directly produces hydrogen peroxide through metal ion reduction. *Biochemistry-Us* **38**, 7609-7616, doi:Doi 10.1021/Bi990438f (1999).
52 Smith, D. G., Cappai, R. & Barnham, K. J. The redox chemistry of the Alzheimer's disease amyloid beta peptide. *Biochimica Et Biophysica Acta-Biomembranes* **1768**, 1976-1990, doi:10.1016/j.bbamem.2007.02.002 (2007).
53 Honda, K., Casadesus, G., Petersen, R. B., Perry, G. & Smith, M. A. Oxidative stress and redox-active iron in Alzheimer's disease. *Redox-Active Metals in Neurological Disorders* **1012**, 179-182, doi:10.1196/annals.1306.015 (2004).
54 Rottkamp, C. A. *et al.* Redox-active iron mediates amyloid-beta toxicity. *Free Radical Biology and Medicine* **30**, 447-450, doi:10.1016/s0891-5849(00)00494-9 (2001).
55 Castellani, R. J. *et al.* Iron: The redox-active center of oxidative stress in Alzheimer disease. *Neurochemical Research* **32**, 1640-1645, doi:10.1007/s11064-007-9360-7 (2007).
56 Kell, D. B. Towards a unifying, systems biology understanding of large-scale cellular death and destruction caused by poorly liganded iron: Parkinson's, Huntington's, Alzheimer's, prions, bactericides, chemical toxicology and others as examples. *Archives of Toxicology* **84**, 825-889, doi:10.1007/s00204-010-0577-x (2010).
57 Nunomura, A. *et al.* Oxidative damage is the earliest event in Alzheimer disease. *Journal of Neuropathology and Experimental Neurology* **60**, 759-767 (2001).
58 Dobson, J. Nanoscale biogenic iron oxides and neurodegenerative disease. *Febs Letters* **496**, 1-5, doi:10.1016/s0014-5793(01)02386-9 (2001).
59 Ke, Y. & Qian, Z. M. Iron misregulation in the brain: a primary cause of neurodegenerative disorders. *Lancet Neurology* **2**, 246-253, doi:10.1016/s1474-4422(03)00353-3 (2003).
60 Dobson, J. Magnetic iron compounds in neurological disorders. *Redox-Active Metals in Neurological Disorders* **1012**, 183-192, doi:10.1196/annals.1306.016 (2004).
61 Thomas, G. M. & Huganir, R. L. MAPK cascade signalling and synaptic plasticity. *Nat Rev Neurosci* **5**, 173-183 (2004).
62 Munoz, P. *et al.* Iron Mediates N-Methyl-D-aspartate Receptor-dependent Stimulation of Calcium-induced Pathways and Hippocampal Synaptic Plasticity. *Journal of Biological Chemistry* **286**, 13382-13392, doi:10.1074/jbc.M110.213785 (2011).
63 Ercal, N., Gurer-Orhan, H. & Aykin-Burns, N. Toxic metals and oxidative stress part I: Mechanisms involved in metal-induced oxidative damage. *Current Topics in Medicinal Chemistry* **1**, 529-539, doi:10.2174/1568026013394831 (2001).
64 Chasteen, N. D. & Harrison, P. M. Mineralization in ferritin: An efficient means of iron storage. *Journal of Structural Biology* **126**, 182-194, doi:10.1006/jsbi.1999.4118 (1999).
65 Cowley, J. M., Janney, D. E., Gerkin, R. C. & Buseck, P. R. The structure of ferritin cores determined by electron nanodiffraction. *Journal of Structural Biology* **131**, 210-216, doi:10.1006/jsbi.2000.4292 (2000).
66 Yoon, J. H. *et al.* Oxidative modification of ferritin induced by hydrogen peroxide. *Bmb Reports* **44**, 165-169, doi:10.5483/BMBRep.2011.44.3.165 (2011).
67 Gomme, P. T. & McCann, K. B. Transferrin: structure, function and potential therapeutic actions. *Drug Discovery Today* **10**, 267-273, doi:10.1016/s1359-6446(04)03333-1 (2005).
68 Wu, L. J. C. *et al.* Expression of the iron transporter ferroportin in synaptic vesicles and the blood-brain barrier. *Brain Research* **1001**, 108-117, doi:10.1016/j.brainres.2003.10.066 (2004).

69 Piñero, D. J., Hu, J. & Connor, J. R. Alterations in the interaction between iron regulatory proteins and their iron responsive element in normal and Alzheimer's diseased brains. *Cellular and molecular biology (Noisy-le-Grand, France)* **46**, 761-776 (2000).
70 Collingwood, J. F. *et al.* In situ characterization and mapping of iron compounds in Alzheimer's disease tissue. *Journal of Alzheimers Disease* **7**, 267-272 (2005).
71 Meadowcroft, M. D., Connor, J. R., Smith, M. B. & Yang, Q. X. MRI and Histological Analysis of Beta-Amyloid Plaques in Both Human Alzheimer's Disease and APP/PS1 Transgenic Mice. *Journal of Magnetic Resonance Imaging* **29**, 997-1007, doi:10.1002/jmri.21731 (2009).
72 Wan, L. *et al.* beta-Amyloid peptide increases levels of iron content and oxidative stress in human cell and Caenorhabditis elegans models of Alzheimer disease. *Free Radical Biology and Medicine* **50**, 122-129, doi:10.1016/j.freeradbiomed.2010.10.707 (2011).
73 Lei, P. *et al.* Tau deficiency induces parkinsonism with dementia by impairing APP-mediated iron export. *Nature Medicine* **18**, 291-295 (2012).
74 Connor, J. R., Menzies, S. L., St. Martin, S. M. & Mufson, E. J. A histochemical study of iron, transferrin, and ferritin in Alzheimer's diseased brains. *Journal of Neuroscience Research* **31**, 75-83, doi:10.1002/jnr.490310111 (1992).
75 Smith, M. A. *et al.* Abnormal localization of iron regulatory protein in Alzheimer's disease. *Brain Research* **788**, 232-236, doi:10.1016/s0006-8993(98)00002-x (1998).
76 Castellani, R. J. *et al.* Contribution of redox-active iron and copper to oxidative damage in Alzheimer disease. *Ageing Research Reviews* **3**, 319-326, doi:10.1016/j.arr.2004.01.002 (2004).
77 Belkacemi, A. & Ramassamy, C. Time sequence of oxidative stress in the brain from transgenic mouse models of Alzheimer's disease related to the amyloid-beta cascade. *Free Radical Biology and Medicine* **52**, 593-600, doi:10.1016/j.freeradbiomed.2011.11.020 (2012).
78 Pratico, D. Oxidative imbalance and lipid peroxidation in Alzheimer's disease. *Drug Development Research* **56**, 446-451, doi:10.1002/ddr.10097 (2002).
79 Conrad, C. C. *et al.* Oxidized proteins in Alzheimer's plasma. *Biochemical and Biophysical Research Communications* **275**, 678-681, doi:10.1006/bbrc.2000.3356 (2000).
80 Sonnen, J. A. *et al.* Free radical-mediated damage to brain in Alzheimer's disease and its transgenic mouse models. *Free Radical Biology and Medicine* **45**, 219-230, doi:http://dx.doi.org/10.1016/j.freeradbiomed.2008.04.022 (2008).
81 Nunomura, A. *et al.* RNA oxidation is a prominent feature of vulnerable neurons in Alzheimer's disease. *Journal of Neuroscience* **19**, 1959-1964 (1999).
82 Smith, M. A., Harris, P. L. R., Sayre, L. M., Beckman, J. S. & Perry, G. Widespread peroxynitrite-mediated damage in Alzheimer's disease. *Journal of Neuroscience* **17**, 2653-2657 (1997).
83 Good, P. F., Werner, P., Hsu, A., Olanow, C. W. & Perl, D. P. Evidence for neuronal oxidative damage in Alzheimer's disease. *American Journal of Pathology* **149**, 21-28 (1996).
84 Pratico, D. & Sung, S. Lipid peroxidation and oxidative imbalance: Early functional events in Alzheimer's disease. *Journal of Alzheimers Disease* **6**, 171-175 (2004).
85 Cullen, K. M. Perivascular astrocytes within Alzheimer's disease plaques. *Neuroreport* **8**, 1961-1966, doi:10.1097/00001756-199705260-00033 (1997).
86 Yoshida, T., Tanaka, M., Sotomatsu, A., Hirai, S. & Okamoto, K. Activated microglia cause iron-dependent lipid peroxidation in the presence of ferritin. *Neuroreport* **9**, 1929-1933, doi:10.1097/00001756-199806220-00003 (1998).

87 Sayre, L. M. *et al.* 4-hydroxynonenal-derived advanced lipid peroxidation end products are increased in Alzheimer's disease. *Journal of Neurochemistry* **68**, 2092-2097 (1997).
88 Markesbery, W. R. & Lovell, M. A. Four-hydroxynonenal, a product of lipid peroxidation, is increased in the brain in Alzheimer's disease. *Neurobiology of Aging* **19**, 33-36, doi:10.1016/s0197-4580(98)00009-8 (1998).
89 Castegna, A. *et al.* Proteomic identification of oxidatively modified proteins in Alzheimer's disease brain. Part 1: Creatine kinase bb, glutamine synthase, and ubiquitin carboxy-terminal hydrolase L-1. *Free Radical Biology and Medicine* **33**, 562-571, doi:10.1016/s0891-5849(02)00914-0 (2002).
90 Cai, Z. Y., Zhao, B. & Ratka, A. Oxidative Stress and beta-Amyloid Protein in Alzheimer's Disease. *Neuromolecular Medicine* **13**, 223-250, doi:10.1007/s12017-011-8155-9 (2011).
91 Dikalov, S. I., Vitek, M. P., Maples, K. R. & Mason, R. P. Amyloid β Peptides Do Not Form Peptide-derived Free Radicals Spontaneously, but Can Enhance Metal-catalyzed Oxidation of Hydroxylamines to Nitroxides. *Journal of Biological Chemistry* **274**, 9392-9399, doi:10.1074/jbc.274.14.9392 (1999).
92 Mattson, M. P. *et al.* Evidence for Excitoprotective and Intraneuronal Calcium-Regulating Roles for Sectreted Forms of the Beta-amyloid Precursor Protein. *Neuron* **10**, 243-254, doi:10.1016/0896-6273(93)90315-i (1993).
93 Burdick, D. *et al.* Assembly and aggregation properties of synthetic Alzheimer's A4/beta amyloid peptide analogs. *Journal of Biological Chemistry* **267**, 546-554 (1992).
94 Hensley, K. *et al.* Brain Regional Correspondance Between Alzheimers Disease Histopathology and Biomarkers of Protein Oxidation. *Journal of Neurochemistry* **65**, 2146-2156 (1995).
95 House, E. *et al.* Aluminium, iron, zinc and copper influence the in vitro formation of amyloid fibrils of A beta(42) in a manner which may have consequences for metal chelation therapy in Alzheimer's disease. *Journal of Alzheimers Disease* **6**, 291-301 (2004).
96 Khan, A., Dobson, J. P. & Exley, C. Redox cycling of iron by A beta(42). *Free Radical Biology and Medicine* **40**, 557-569, doi:10.1016/j.freeradbiomed.2005.09.013 (2006).
97 Huang, X. D. *et al.* Trace metal contamination initiates the apparent auto-aggregation, amyloidosis, and oligomerization of Alzheimer's A beta peptides. *Journal of Biological Inorganic Chemistry* **9**, 954-960, doi:10.1007/s00775-004-0602-8 (2004).
98 Miura, T., Suzuki, K. & Takeuchi, H. Binding of iron(III) to the single tyrosine residue of amyloid beta-peptide probed by Raman spectroscopy. *Journal of Molecular Structure* **598**, 79-84, doi:10.1016/s0022-2860(01)00807-9 (2001).
99 Jiang, D. *et al.* Ternary Complexes of Iron, Amyloid-beta, and Nitrilotriacetic Acid: Binding Affinities, Redox Properties, and Relevance to Iron-Induced Oxidative Stress in Alzheimer's Disease. *Biochemistry-Us* **48**, 7939-7947, doi:10.1021/bi900907a (2009).
100 Bousejra-ElGarah, F., Bijani, C., Coppel, Y., Faller, P. & Hureau, C. Iron(II) Binding to Amyloid-beta, the Alzheimer's Peptide. *Inorganic Chemistry* **50**, 9024-9030, doi:10.1021/ic201233b (2011).
101 Atwood, C. S. *et al.* Dramatic aggregation of Alzheimer A beta by Cu(II) is induced by conditions representing physiological acidosis. *Journal of Biological Chemistry* **273**, 12817-12826, doi:10.1074/jbc.273.21.12817 (1998).
102 Atwood, C. S. *et al.* Characterization of Copper Interactions with Alzheimer Amyloid β Peptides. *Journal of Neurochemistry* **75**, 1219-1233, doi:10.1046/j.1471-4159.2000.0751219.x (2000).

103 Bondy, S. C., Guo-Ross, S. X. & Truong, A. T. Promotion of transition metal-induced reactive oxygen species formation by beta-amyloid. *Brain Research* **799**, 91-96, doi:10.1016/s0006-8993(98)00461-2 (1998).
104 Liu, B. *et al.* Iron promotes the toxicity of amyloid β peptide by impeding its ordered aggregation. *Journal of Biological Chemistry* **286**, 4248-4256 (2011).
105 Hautot, D., Pankhurst, Q. A., Khan, N. & Dobson, J. Preliminary evaluation of nanoscale biogenic magnetite in Alzheimer's disease brain tissue. *Proceedings of the Royal Society B-Biological Sciences* **270**, S62-S64, doi:10.1098/rsbl.2003.0012 (2003).
106 Collingwood, J. F. *et al.* in *Fifth International Conference on Fine Particle Magnetism* Vol. 17 *Journal of Physics Conference Series* (ed Q. Pankhurst) 54-60 (2005).
107 Quintana, C. *et al.* Study of the localization of iron, ferritin, and hemosiderin in Alzheimer's disease hippocampus by analytical microscopy at the subcellular level. *Journal of Structural Biology* **153**, 42-54, doi:10.1016/j.jsb.2005.11.001 (2006).
108 Quintana, C., Cowley, J. M. & Marhic, C. Electron nanodiffraction and high-resolution electron microscopy studies of the structure and composition of physiological and pathological ferritin. *Journal of Structural Biology* **147**, 166-178, doi:10.1016/j.jsb.2004.03.001 (2004).
109 Quintana, C. & Gutierrez, L. Could a dysfunction of ferritin be a determinant factor in the aetiology of some neurodegenerative diseases? *Biochimica Et Biophysica Acta-General Subjects* **1800**, 770-782, doi:10.1016/j.bbagen.2010.04.012 (2010).
110 Honda, K. *et al.* Ribosomal RNA in Alzheimer disease is oxidized by bound redox-active iron. *Journal of Biological Chemistry* **280**, 20978-20986, doi:10.1074/jbc.M500526200 (2005).
111 Kirschvink, J. L., Kobayashikirschvink, A. & Woodford, B. J. Magnetite Biomineralization in the Human Brain. *Proceedings of the National Academy of Sciences of the United States of America* **89**, 7683-7687, doi:10.1073/pnas.89.16.7683 (1992).
112 Dobson, J. Investigation of age-related variations in biogenic magnetite levels in the human hippocampus. *Experimental Brain Research* **144**, 122-126, doi:10.1007/s00221-002-1066-0 (2002).
113 Pankhurst, Q., Hautot, D., Khan, N. & Dobson, J. Increased levels of magnetic iron compounds in Alzheimer's Disease. *Journal of Alzheimers Disease* **13**, 49-52 (2008).
114 Brillas, E., Sires, I. & Oturan, M. A. Electro-Fenton Process and Related Electrochemical Technologies Based on Fenton's Reaction Chemistry. *Chemical Reviews* **109**, 6570-6631, doi:10.1021/cr900136g (2009).
115 Gorski, C. A., Nurmi, J. T., Tratnyek, P. G., Hofstetter, T. B. & Scherer, M. M. Redox Behavior of Magnetite: Implications for Contaminant Reduction. *Environmental Science & Technology* **44**, 55-60, doi:10.1021/es9016848 (2010).
116 Telling, N. D. *et al.* Remediation of Cr(VI) by biogenic magnetic nanoparticles: An x-ray magnetic circular dichroism study. *Applied Physics Letters* **95**, doi:10.1063/1.3249578 (2009).
117 Cutting, R. S. *et al.* Optimizing Cr(VI) and Tc(VII) Remediation through Nanoscale Biomineral Engineering. *Environmental Science & Technology* **44**, 2577-2584, doi:10.1021/es902119u (2010).
118 Scaiano, J. C., Monahan, S. & Renaud, J. Dramatic Effect of Magnetite Particles on the Dynamics of Photogenerated Free Radicals. *Photochemistry and Photobiology* **65**, 759-762, doi:10.1111/j.1751-1097.1997.tb01921.x (1997).
119 Chignell, C. F. & Sik, R. H. Effect of Magnetite Particles on Photoinduced and Nonphotoinduced Free Radical Processes in Human Erythrocytes. *Photochemistry and Photobiology* **68**, 598-601, doi:10.1111/j.1751-1097.1998.tb02520.x (1998).

120 Wu, J., Ding, T. & Sun, J. Neurotoxic potential of iron oxide nanoparticles in the rat brain striatum and hippocampus. *Neurotoxicology* **34**, 243-253, doi:10.1016/j.neuro.2012.09.006 (2013).
121 Galvez, N. *et al.* Comparative structural and chemical studies of ferritin cores with gradual removal of their iron contents. *Journal of the American Chemical Society* **130**, 8062-8068, doi:10.1021/ja800492z (2008).
122 Curtis, A. R. J. *et al.* Mutation in the gene encoding ferritin light polypeptide causes dominant adult-onset basal ganglia disease. *Nature Genetics* **28**, 350-354, doi:10.1038/ng571 (2001).
123 Perez, M. *et al.* Ferritin is associated with the aberrant tau filaments present in progressive supranuclear palsy. *American Journal of Pathology* **152**, 1531-1539 (1998).
124 Yang, E. Y., Guo-Ross, S. X. & Bondy, S. C. The stabilization of ferrous iron by a toxic beta-amyloid fragment and by an aluminum salt. *Brain Research* **839**, 221-226, doi:10.1016/s0006-8993(99)01694-7 (1999).
125 House, E., Esiri, M., Forster, G., Ince, P. G. & Exley, C. Aluminium, iron and copper in human brain tissues donated to the medical research council's cognitive function and ageing study. *Metallomics* **4**, 56-65, doi:10.1039/C1MT00139F (2012).
126 Grundkeiqbal, I. *et al.* Ferritin is a Component of the Neuritic (Senile) Plaque in Alzheimer Dementia. *Acta Neuropathologica* **81**, 105-110 (1990).
127 Nakamura, M. *et al.* Three histidine residues of amyloid-beta peptide control the redox activity of copper and iron. *Biochemistry-Us* **46**, 12737-12743, doi:10.1021/bi701079z (2007).
128 Bishop, G. M. & Robinson, S. R. The amyloid paradox: Amyloid-beta-metal complexes can be neurotoxic and neuroprotective. *Brain Pathology* **14**, 448-452 (2004).
129 Schwertmann, U. & Cornell, R. M. in *Iron Oxides in the Laboratory* (Wiley-VCH Verlag GmbH, 2007).
130 Collingwood, J. & Dobson, J. Mapping and characterization of iron compounds in Alzheimer's tissue. *Journal of Alzheimers Disease* **10**, 215-222 (2006).
131 Regan, T. J. *et al.* Chemical effects at metal/oxide interfaces studied by x-ray-absorption spectroscopy. *Physical Review B* **64**, art. no.-214422, doi:10.1103/PhysRevB.64.214422 (2001).
132 van der Laan, G. in *15th International Conference on X-Ray Absorption Fine Structure* Vol. 430 *Journal of Physics Conference Series* (ed Z. Y. Wu) (2013).
133 van der Laan, G. & Figueroa, A. I. X-ray magnetic circular dichroism—A versatile tool to study magnetism. *Coordination Chemistry Reviews*, doi:http://dx.doi.org/10.1016/j.ccr.2014.03.018.
134 Drits, V. A., Sakharov, B. A., Salyn, A. L. & Manceau, A. Structural Model for Ferrihydrite. *Clay Minerals* **28**, 185-207, doi:10.1180/claymin.1993.028.2.02 (1993).
135 Janney, D. E., Cowley, J. M. & Buseck, P. R. Structure of synthetic 2-line ferrihydrite by electron nanodiffraction. *American Mineralogist* **85**, 1180-1187 (2000).
136 Janney, D. E., Cowley, J. M. & Buseck, P. R. Structure of synthetic 6-line ferrihydrite by electron nanodiffraction. *American Mineralogist* **86**, 327-335 (2001).
137 Coker, V. S. *et al.* XAS and XMCD evidence for species-dependent partitioning of arsenic during microbial reduction of ferrihydrite to magnetite. *Environmental Science & Technology* **40**, 7745-7750, doi:10.1021/es060990+ (2006).
138 Pearce, C. I. *et al.* Fe site occupancy in magnetite-ulvospinel solid solutions: A new approach using X-ray magnetic circular dichroism. *American Mineralogist* **95**, 425-439, doi:10.2138/am.2010.3343 (2010).

139 Cutting, R. S. *et al.* Microbial Reduction of Arsenic-Doped Schwertmannite by Geobacter sulfurreducens. *Environmental Science & Technology* **46**, 12591-12599, doi:10.1021/es204596z (2012).
140 Pan, Y. *et al.* Electron beam damage studies of synthetic 6-line ferrihydrite and ferritin molecule cores within a human liver biopsy. *Micron* **37**, 403-411, doi:10.1016/j.micron.2005.12.009 (2006).
141 Kilcoyne, A. L. D. *et al.* Interferometer-controlled scanning transmission X-ray microscopes at the Advanced Light Source. *Journal of Synchrotron Radiation* **10**, 125-136, doi:doi:10.1107/S0909049502017739 (2003).
142 Lam, K. P. *et al.* Characterizing magnetism of individual magnetosomes by X-ray magnetic circular dichroism in a scanning transmission X-ray microscope. *Chemical Geology* **270**, 110-116, doi:10.1016/j.chemgeo.2009.11.009 (2010).
143 Stewart-Ornstein, J. *et al.* Using intrinsic X-ray absorption spectral differences to identify and map peptides and proteins. *Journal of Physical Chemistry B* **111**, 7691-7699, doi:10.1021/jp0720993 (2007).
144 Liu, G., Men, P., Perry, G. & Smith, M. A. in *Free Radicals and Antioxidant Protocols, Second Edition* Vol. 610 *Methods in Molecular Biology* (eds R. M. Uppu, S. N. Murthy, W. A. Pryor, & N. L. Parinandi) 123-144 (2010).
145 Dwyer, B. E. *et al.* Getting the iron out: Phlebotomy for Alzheimer's disease? *Medical Hypotheses* **72**, 504-509, doi:10.1016/j.mehy.2008.12.029 (2009).
146 Bonda, D. J. *et al.* Role of metal dyshomeostasis in Alzheimer's disease. *Metallomics* **3**, 267-270, doi:10.1039/c0mt00074d (2011).
147 Dedeoglu, A. *et al.* Preliminary studies of a novel bifunctional metal chelator targeting Alzheimer's amyloidogenesis. *Experimental Gerontology* **39**, 1641-1649, doi:10.1016/j.exger.2004.08.016 (2004).
148 Huang, X. *et al.* Trace metal contamination initiates the apparent auto-aggregation, amyloidosis, and oligomerization of Alzheimer's Aβ peptides. *J Biol Inorg Chem* **9**, 954-960, doi:10.1007/s00775-004-0602-8 (2004).
149 Mecocci, P. & Polidori, M. C. Antioxidant clinical trials in mild cognitive impairment and Alzheimer's disease. *Biochimica Et Biophysica Acta-Molecular Basis of Disease* **1822**, 631-638, doi:10.1016/j.bbadis.2011.10.006 (2012).
150 Cole, G. M. *et al.* A rationale for curcuminoids for the prevention or treatment of Alzheimer's disease. *Current Medicinal Chemistry - Immunology Endocrine & Metabolic Agents* **3**, 15-25, doi:10.2174/1568013033358761 (2003).
151 Coker, V. S. *et al.* Harnessing the Extracellular Bacterial Production of Nanoscale Cobalt Ferrite with Exploitable Magnetic Properties. *Acs Nano* **3**, 1922-1928, doi:10.1021/nn900293d (2009).
152 Online resource. AXIS 2000 software: http://unicorn.mcmaster.ca/aXis2000.html.
153 Stookey, L. L. Ferrozine - a new spectrophotometric reagent for iron. *Analytical Chemistry* **42**, 779-&, doi:10.1021/ac60289a016 (1970).
154 Yamamoto, A. *et al.* Iron (III) induces aggregation of hyperphosphorylated tau and its reduction to iron (II) reverses the aggregation: implications in the formation of neurofibrillary tangles of Alzheimer's disease. *Journal of Neurochemistry* **82**, 1137-1147 (2002).
155 Masters, C. L. *et al.* Amyloid Plaque Core Protein in Alzheimers Disease and Down Syndrome. *Proceedings of the National Academy of Sciences of the United States of America* **82**, 4245-4249, doi:10.1073/pnas.82.12.4245 (1985).
156 Nilsson, M. R. Techniques to study amyloid fibril formation in vitro. *Methods* **34**, 151-160, doi:http://dx.doi.org/10.1016/j.ymeth.2004.03.012 (2004).

157 Bolt, H. M. & Marchan, R. Iron dysregulation: an important aspect in toxicology. *Archives of Toxicology* **84**, 823-824, doi:10.1007/s00204-010-0610-0 (2010).
158 Bush, A. I. The metallobiology of Alzheimer's disease. *Trends in Neurosciences* **26**, 207-214, doi:10.1016/s0166-2236(03)00067-5 (2003).
159 Ruiperez, F., Mujika, J. J., Ugalde, J. M., Exley, C. & Lopez, X. Pro-oxidant activity of aluminum: Promoting the Fenton reaction by reducing Fe(III) to Fe(II). *Journal of Inorganic Biochemistry* **117**, 118-123, doi:10.1016/j.jinorgbio.2012.09.008 (2012).
160 Tomljenovic, L. Aluminum and Alzheimer's Disease: After a Century of Controversy, Is there a Plausible Link? *Journal of Alzheimers Disease* **23**, 567-598, doi:10.3233/jad-2010-101494 (2011).
161 Exley, C. A molecular mechanism of aluminium-induced Alzheimer's disease? *Journal of Inorganic Biochemistry* **76**, 133-140, doi:10.1016/s0162-0134(99)00125-7 (1999).
162 Exley, C. & House, E. R. Aluminium in the human brain. *Monatshefte Fur Chemie* **142**, 357-363, doi:10.1007/s00706-010-0417-y (2011).
163 May, P. C. *et al.* Beta-amyloid Peptide in vitro Toxicity - Lot-to-Lot Variability. *Neurobiology of Aging* **13**, 605-607, doi:10.1016/0197-4580(92)90064-5 (1992).
164 Lovley, D. R. & Phillips, E. J. P. Organic-matter mineralization with reduction of ferric iron in anaerobic sediments. *Applied and Environmental Microbiology* **51**, 683-689 (1986).
165 Massart, R. Preparation of Aqueous Magnetic Liquids in Alkaline and Acidic Media. *Ieee Transactions on Magnetics* **17**, 1247-1248, doi:10.1109/tmag.1981.1061188 (1981).
166 Michel, F. M. *et al.* Ordered ferrimagnetic form of ferrihydrite reveals links among structure, composition, and magnetism. *Proceedings of the National Academy of Sciences of the United States of America* **107**, 2787-2792, doi:10.1073/pnas.0910170107 (2010).
167 Gheisari, M., Mozaffari, M., Acet, M. & Amighian, J. Preparation and investigation of magnetic properties of wustite nanoparticles. *Journal of Magnetism and Magnetic Materials* **320**, 2618-2621, doi:10.1016/j.jmmm.2008.05.028 (2008).
168 Hazen, R. M. & Jeanloz, R. Wustite (Fe1-XO) - A review of its defect structure and physical-properties. *Reviews of Geophysics* **22**, 37-46, doi:10.1029/RG022i001p00037 (1984).
169 Worcester, D. L. Structural Origins of Diamagnetic Ansiotropy in Proteins. *Proceedings of the National Academy of Sciences of the United States of America* **75**, 5475-5477, doi:10.1073/pnas.75.11.5475 (1978).
170 Muller, K. *et al.* Effect of ultrasmall superparamagnetic iron oxide nanoparticles (Ferumoxtran-10) on human monocyie-macrophages in vitro. *Biomaterials* **28**, 1629-1642, doi:10.1016/j.biomaterials.2006.12.002 (2007).
171 Park, J. C., Kim, D., Lee, C. S. & Kim, D. K. A new synthetic route to wustite. *Bulletin of the Korean Chemical Society* **20**, 1005-1009 (1999).
172 Iwasaki, T., Sato, N., Nakamura, H. & Watano, S. Mechanochemical formation of superparamagnetic magnetite nanoparticles from ferrihydrite over a wide range of pH environments. *Materials Chemistry and Physics* **140**, 596-601, doi:10.1016/j.matchemphys.2013.04.011 (2013).
173 Sipe, J. D. & Cohen, A. S. Review: History of the Amyloid Fibril. *Journal of Structural Biology* **130**, 88-98, doi:http://dx.doi.org/10.1006/jsbi.2000.4221 (2000).
174 Bartzokis, G., Tishler, T. A., Shin, I. S., Lu, P. H. & Cummings, J. L. in *Redox-Active Metals in Neurological Disorders* Vol. 1012 *Annals of the New York Academy of Sciences* (eds S. M. LeVine, J. R. Connor, & H. M. Schipper) 224-236 (2004).

175 Connor, J. R., Snyder, B. S., Arosio, P., Loeffler, D. A. & Lewitt, P. A Quantitative-analysis of Isoferritins in Select Regions of Aged, Parkinsonian, and, Alzheimers Diseased Brains. *Journal of Neurochemistry* **65**, 717-724 (1995).
176 Friedman, A., Arosio, P., Finazzi, D., Koziorowski, D. & Galazka-Friedman, J. Ferritin as an important player in neurodegeneration. *Parkinsonism & Related Disorders* **17**, 423-430, doi:10.1016/j.parkreldis.2011.03.016 (2011).
177 Dixon, S. J. *et al.* Ferroptosis: An Iron-Dependent Form of Nonapoptotic Cell Death. *Cell* **149**, 1060-1072, doi:10.1016/j.cell.2012.03.042 (2012).
178 Jellinger, K., Paulus, W., Grundke-Iqbal, I., Riederer, P. & Youdim, M. B. H. Brain iron and ferritin in Parkinson's and Alzheimer's diseases. *J Neural Transm Gen Sect* **2**, 327-340, doi:10.1007/BF02252926 (1990).
179 Watt, G. D., Jacobs, D. & Frankel, R. B. Redox Reactivity of Bacterial and Mammalian Ferritin - Is Reductant Entry into the Ferritin Interior a Necessary Step for Iron Release. *Proceedings of the National Academy of Sciences of the United States of America* **85**, 7457-7461, doi:10.1073/pnas.85.20.7457 (1988).
180 King, T. P. Separation of proteins by ammonium sulfate gradient solubilization. *Biochemistry-Us* **11**, 367-371, doi:10.1021/bi00753a010 (1972).
181 Pan, Y.-H. *et al.* Electron-beam-induced reduction of Fe3+ in iron phosphate dihydrate, ferrihydrite, haemosiderin and ferritin as revealed by electron energy-loss spectroscopy. *Ultramicroscopy* **110**, 1020-1032, doi:10.1016/j.ultramic.2010.01.008 (2010).
182 Saranu, S. *et al.* Effect of large mechanical stress on the magnetic properties of embedded Fe nanoparticles. *Beilstein Journal of Nanotechnology* **2**, 268-275, doi:10.3762/bjnano.2.31 (2011).
183 Suslick, K. S., Fang, M. M. & Hyeon, T. Sonochemical synthesis of iron colloids. *Journal of the American Chemical Society* **118**, 11960-11961, doi:10.1021/ja961807n (1996).
184 Paul, W. E. & Cohen, A. S. Electron Microscopic Studies of Amyloid Fibrils with Ferritin Conjugated Antibody. *The American journal of pathology* **43**, 721-738 (1963).
185 Mir, M., Bogachan Tahirbegi, I., Jose Valle-Delgado, J., Fernandez-Busquets, X. & Samitier, J. In vitro study of magnetite-amyloid beta complex formation. *Nanomedicine-Nanotechnology Biology and Medicine* **8**, 974-980, doi:10.1016/j.nano.2011.11.010 (2012).
186 Li, J., Hitchcock, A. P., Stoever, H. D. H. & Shirley, I. A New Approach to Studying Microcapsule Wall Growth Mechanisms. *Macromolecules* **42**, 2428-2432, doi:10.1021/ma802130n (2009).
187 Li, X., Jankovic, J. & Le, W. Iron chelation and neuroprotection in neurodegenerative diseases. *J Neural Transm* **118**, 473-477, doi:10.1007/s00702-010-0518-0 (2011).
188 Wong, K. K. W., Douglas, T., Gider, S., Awschalom, D. D. & Mann, S. Biomimetic Synthesis and Characterization of Magnetic Proteins (Magnetoferritin). *Chemistry of Materials* **10**, 279-285, doi:10.1021/cm970421o (1998).